Diss. ETH NO._18461_

Temporal and spatial evolution of a syn-orogenic extensional system: the Simplon Fault Zone (Central Alps)

A dissertation submitted to

ETH ZURICH

For the degree of
Doctor of Sciences

Presented by

Marion Campani
Master in Earth Sciences (DEA), University of Montpellier II (France)

Date of birth
29 April 1982

Citizen of France

Accepted on the recommendation of

Neil Mancktelow (ETH)
Jean-Pierre Burg (ETH)
Diane Seward (ETH)
Christian Teyssier (University of Minnesota, USA)

2009

Acknowledgements

First of all I would like to thanks Neil Mancktelow for giving me the opportunity to work on this project. Thank you Neil for the constructive discussions and the experience that you shared with me on the field. We had some really nice moments there. Thank you also for always being positive, teaching me self confidence and also for your help in these difficult past months. I also want to thanks Diane Seward for teaching me the zircon fission track method, for the constant support, nice discussions and nice moments as well that we had. I would like to thanks Jean-Pierre Burg, first to have considered my CV 4 years ago, and for his critical view on my work. It has been constructive. Thank you Christian Teyssier to be part of the committee and to review the manuscript. Thank you also for the discussions that we had in different conferences.

Many people have contributed to the accomplishment of this work: the first person that I want to thanks is Frédéric Herman who really has put a lot of his time in this work. Thank you for all your help and patience with me. This was not an easy part of my PhD! Thank you also to Wolfgang Müller in RHUL for teaching me the Rb-Sr isotope chemistry, for running the final measurements and for the nice discussions. Thank you also to have come in the field with me. I also want to thanks the group from Nice with Yann Rolland, Michel Fornari, Jean-Pierre Goudour, Loic Vacher and Michel Manetti for the lab facilities and for their help in the use of the spectrometer. Thank you Yann also to have come with me in the field and for the discussions. I would like to thanks Gabriel Courioux from the BRGM, and also Michael Maxelon, who came in Zurich to teach me the GeoModeller. A big acknowledgement goes to Ivan Guerra who did the oxygen isotope in Lausanne. I also want to thanks Michele Sapigni from ENEL power for providing us fresh cores samples. Thank you Margrith Bischof and Frowin Pirovino for all the thin sections and your support. I will not forget of course the support and help from Regula, Ingrid, Suzanne, Germaine and Farida. This project was financed by the Swiss National fund.

Now also comes people who have really been important… Thank you for the great time that we shared during this past 4 years and especially for your support and help in the last difficult months and the last foggy days….
Thank you: Jess Marion and Paola (merci les filles), Carmen, Adélie, Pauline, Estelle and Arnaud, Etienne, Sabine (my dear kondi-partner), Federica (my dear dancing-partner), Sonia, Pinar, Barbara, Leo, Ben, Erwan, krughi, Georges, Mattia, Lukas, Remco, Janne, Antoine, Thank you Eli (good luck!) and Jörg, Asghar (good luck!) and Maria, the Australian ones Wewe and Claudio, Seb and Zari, Alex and Elena, Frédéric, Oli and Raquel, Andrew, Ansgar, Galli, Marcus, Marcel and Yolanda, Gregory, Manuele, Luca, Philippe, Olivier, Pietro, France, Esther, Tamara, Mark, Alistair, Christian, Mathieu, Maarten, Ettore, Ute, Daniele, Nina, Chantal, Alessandro, Rasmus, Giuditta, Eric, Boris… Thank you to my "workoholic" officemate, thank for your patience and support until the end: Sarah, Daniela, Claudio, Negar, Pipo! Also Marietta for her nice picture of the Masera fold, Nicole and Alex, Clemens, Rohit, Marco, Steffi, Jacqueline, Monika … My previous officemate who had to support all my headaches: Jeroen… And

the dear structural group: Sébastien, Santa, Beatriz, Marc, Bettina, Luigi, Stefan, Marina, Lisa, Rolf, Brian, Nicola… Thank also to the new "team" of Neil, thanks for the discussions and the Alpine review with Jan! Good luck also to you Daniel and Luca!! Other friends that I met in conferences or in colab: Ivan, Flurin and Goeffrey in Neuchâtel-Lausanne, Martin and Nancy in RHUL, Rüdiger in Basel, Marion, Guillaume and Dimitri in Nice, PYF in Paris, Julien in Berne…. Sorry for those that I forgot…. And thank you all !!

Cette dernière partie sera en Français car elle concerne ma famille et mes amies d'enfance qui ont tous vécu au rythme de ces moments difficiles. Merci pour votre soutient: Mes Parents, ma grenouille, David et ma sœur, Eglantine, Elsa, Aline, Audrey... Merci.
The final thanks are for Pierre who did so much at the end to help me to finish in time and has supported me all the time….

Table of Contents

Abstract 1
Résumé 3
General introduction 5
I. Introduction 7
I.1. Alpine overview 7
I.2. The Simplon Fault Zone (SFZ) 11
I.3. Overview of previous studies and on-going controversies 12
I.4. Goals and methods 16
I.5. Outline of the thesis 17
II. Geochronology and cooling history of the Simplon Fault Zone 19
II.1. Introduction 19
II.2. Geological setting 20
II.2.1. The Simplon Fault Zone (SFZ) 20
II.2.2. Metamorphic history 22
II.2.3. Previous thermochronological and geochronological work 23
II.3. Field observations 25
II.3.1. The SE prolongation of the Simplon Fault Zone (SFZ) 25
II.3.2. NW section Gibidum-Visp-Rhone Valley 29
II.4. Methods and sample description 32
II.4.1. Fission-track analysis: apatite and zircon 32
II.4.2. $^{40}Ar/^{39}Ar$ analysis: white mica and biotite 32
II.4.3. Rb-Sr microsampling analysis 32
II.4.4. Oxygen- Isotope Thermometry 35
II.4.5. Petrological and chemical description of samples used for $^{40}Ar/^{39}Ar$, Rb-Sr and oxygen isotope analysis 35
II.5. Results 40
II.5.1. Fission track analysis 40
II.5.2. $^{40}Ar/^{39}Ar$ analysis 41
II.5.3. Rb-Sr analysis 45
II.5.4. Oxygen stable isotope analysis 46
II.6. Discussion 46
II.6.1. Fission-track ages and the brittle history of the Simplon Fault Zone ("Simplon Line") 46
II.6.2. $^{40}Ar/^{39}Ar$ and Rb-Sr data: cooling or neo-(re-)crystallization ages? 47
II.6.3. Absolute dating of the Simplon Fault Zone (SFZ) 50
II.6.4. Cooling ages and fault activity 50
II.7. Conclusions 52
III. Exhumation history of the Simplon Fault Zone, 2-3D thermo-kinematic modeling 53
III.1. Introduction 53
III.2. Geological constraints 54
III.2.1. The Simplon Fault Zone (SFZ) 54
III.2.2. Model of an initial low-angle detachment 56
III.2.3. Rolling hinge model 56

III.2.4. Compiled thermochronological data used in the thermo-kinematic model .. 57
III.3. Approach and methods 60
III.3.1. Thermo-kinematic model 61
III.3.2. Neighbourhood Algorithm 65
III.3.3. 3D model including topographic effect 65
III.4. Results 66
III.4.1. Model A: Initial low-angle detachment 67
III.4.2. Model B, Rolling hinge model 72
III.4.3. 3D model including the surface topography 77
III.5. Discussion 81
III.5.1. Uniform exhumation rate, *Vv* 81
III.5.2. Timing and amount of faulting on the Simplon Fault Zone 81
III.5.3. Resulting exhumation rate 83
III.5.4. Comparison of the two kinematic models 84
III.5.5. Implications for the foreland basin 85
III.6. Conclusions 86
IV. 3D geometry of the Simplon Fault Zone in the Central Alps 89
IV.1. Introduction 89
IV.2. Coupling between folding and extensional faulting 91
IV.2.1. 3D geometry of the low-angle detachment system 91
IV.2.2. Extension-orthogonal folding 91
IV.2.3. Extension-parallel folding 93
IV.2.4. The regional Alpine structural history and the SFZ overprint 94
IV.3. Chronological constraints 97
IV.3.1. Previous studies 97
IV.3.2. Results 98
IV.4. 3D geometric modeling 102
IV.5. Discussion 109
IV.5.1. Extension-parallel folding 109
IV.5.2. Extension-orthogonal folds 111
IV.5.3. Relationship to the previous *D2* deformation phase 111
IV.6. Conclusion 112
V. Discussion and conclusions 113
V.1. Loss and/or transfer of the SFZ displacement 113
V.2. Age of the SFZ 114
V.3. Kinematics of exhumation 115
V.4. Exhumation rate and relative displacement 116
V4.1. Uniform exhumation rate in the Central Alps 116
V.4.2. Rate of tectonic exhumation in the Toce Dome 116
V.5. Interplay between faulting and folding 117
V.6. Conclusions of this study 118
V.6.1. General implications 118
V.6.2. Alpine geodynamic implications 120
Appendix A: Methodology 123
Fission track methodology 123
$^{40}Ar/^{39}Ar$ methodology 123

Rb-Sr microsampling methodology 124
Oxygen isotope methodology 124
Microprobe analysis 125
Appendix B: Fission track dataset 126
Appendix C: $^{40}Ar/^{39}Ar$ analytical dataset 150
Appendix D: Probability density functions 156
References 157

Abstract

Syn- to post-collisional extension is commonly associated with the development of low-angle detachments that lead to large scale exhumation in the latter part of the orogenic history. These normal faults, with a shallow dip, typically juxtapose different structural levels of the crust that record both ductile and brittle deformation with similar kinematics. Low-angle extensional fault zones are also often affected by large scale upright folding, resulting in the exhumation of a gneiss dome with a complex geometry and therefore cannot be considered as a simple 2D structure (i.e. a classic "normal fault"). The kinematics of exhumation and the evolution of such structures are still controversial. In particular, it is debated whether the mylonitic zone in the footwall developed during progressive exhumation in a normal fault system or represents a more general feature of the middle to lower crust that was captured and exhumed by the brittle detachment. Another controversy concerns the original dip of the detachment fault, because low-angle normal faults are inconsistent with the Andersonian fault theory. Alternative models propose that exhumation occurred in a rolling hinge system, with initially high-angle seismogenic faults passively rotated to shallow dip due to isostatic rebound.

These potential models have been investigated using the Simplon Fault Zone (SFZ), in the European Central Alps, as an example. This major extensional system developed as the result of orogen-parallel extension, which has been active in the Alps since at least the Oligocene. Despite the excellent outcrop and more than 50 years of research, the age of ductile shearing in the footwall and of the ductile-to-brittle transition is still not unequivocally established. On a more regional scale, the loss and/or transfer of displacement on this fault zone is also unclear, as is the relationship to the general dextral strike-slip fault system of the Rhone and Periadriatic Faults (or "Lines"), the interplay between folding and shearing, and thus the overall geometry and kinematics of exhumation.

This thesis proposes a detailed structural study of the SFZ combined with (1) absolute dating of (micro-) structurally controlled mineral growth using $^{40}Ar/^{39}Ar$ and Rb-Sr, (2) thermochronology using apatite and zircon fission track and mica $^{40}Ar/^{39}Ar$ cooling ages, (3) inverse thermo-kinematic modeling to constrain the exhumation history and critically assess potential models for the development of low-angle detachment systems, and (4) 3D geometric modeling, to establish and represent the overall complex 3D shape of the detachment system.

A cooling history was established across the SFZ using both published and new fission-track ages combined with $^{40}Ar/^{39}Ar$ cooling ages obtained from recrystallized white mica within the high-grade Simplon mylonites. This cooling pattern, together with structural arguments, indicate important displacement on a broad mylonitic shear zone, now observed in the footwall of the SFZ, between 20 and 14 Ma. This was followed by more brittle deformation, mainly localized into a detachment fault of similar kinematics, which remained active until at least 3 Ma. An increase in the degree of this localization is observed toward the SE, reflecting different structural levels now exposed along one single detachment system. Constraints on the late distributed shearing history of the SFZ is provided by absolute dating of newly grown white mica within the neck of foliation boudinage in the SE region (Isorno Valley) at ca. 14.5 Ma. In the NW (Rhone Valley), an

overlapping age range of 14.5 to ca. 10 Ma is obtained from direct dating of synkinematic phengite that grew within phyllonites developed in the Aar massif within the footwall of the SFZ. Overall, these data indicate a direct connection of the SFZ with the Rhone Line in the Rhone Valley, probably with a similar amount of displacement. To the SE, they suggest a transfer of the SFZ as a dextral strike-slip fault into the Isorno Valley, with a subsequent loss of displacement over 20 km. A direct connection, via the Centovalli Line, to dextral movement on the Periadriatic Line, as proposed in several earlier studies, is not supported by field observations.

Inversion of the extensive thermochronological dataset across the SFZ, using thermo-kinematic models, establishes that a better fit to observations is obtained with an initial planar low-angle brittle detachment dipping 30° than with the rolling hinge model that has also been proposed for the SFZ. A good fit to the dataset requires the presence of a distributed ductile shear zone (~ 2-3 km thick) as observed in the field. This provides independent evidence that this ductile shearing and the mylonite formation in the footwall developed during exhumation on the low-angle extensional fault system in the Neogene. The onset of faulting is predicted to have been at 18 Ma, with a slip rate parallel to the fault of 2.8 mm/a, which decreased around 14 Ma to 0.7 mm/a, continuing until at least 3 Ma. The total amount of vertical relative displacement between footwall and hanging wall was around 10-15 km. Finally, a regional scale increase in the exhumation rate at ca. 4 Ma, from 0.34 mm/a to 0.68 mm/a, is established from the apatite fission-track ages. This reflects an increase of the erosion rate in response to climate changes during the Pliocene.

As reflected in the 3D geometric models, exhumation of the Toce Dome is the result of complex interplay between shearing and perpendicular folding leading to a complex geometry of the SFZ. Direct dating of the crenulation cleavage developed on the axial plane to these folds establishes that they formed at around 10 Ma and were therefore broadly coeval with the late, more brittle history of the SFZ. The Simplon mylonites clearly define a domal shape formed during shearing between 17 and 14 Ma, which is not observed for the brittle detachment itself (contrary to what would be expected in a rolling hinge model). This domal shape to the mylonites can reflect the established strain gradient into the footwall, whereas the planar detachment is consistent with a more rigid block exhumation during the late brittle history.

Overall, the Simplon Fault Zone represents a telescoped crustal section of a single major low-angle detachment fault, dipping $\leq 30^{\circ}$, which reflects a continuous history of exhumation from the ductile to the brittle field. It developed in the Neogene, from 19 to 3 Ma, with a rather slow tectonic exhumation rate (maximum 1.74 mm/a) in an overall oblique convergence setting and accommodated around 10 - 15 km of vertical tectonic displacement of the footwall.

Résumé

L'extension tardi-orogénique d'un domaine continental épaissi est généralement associée au développement de détachement permettant une exhumation généralisée de la croûte. Dans le mur de ces failles normales à faible pendage, les déformations fragiles et localisées superposent de larges zones de cisaillement ductile de même cinématique. Ces zones de failles sont souvent plissées, parallèlement et perpendiculairement à la direction principale de l'extension, et engendrent l'exhumation de dômes gneissiques présentant une géométrie complexe. De telles structures ne peuvent donc être considérées comme des failles classiques en deux dimensions. La cinématique de l'exhumation et l'évolution générale des détachements est encore très débattue. En particulier les relations entre les déformations fragiles et ductiles ne sont pas clairement établies. Il est proposé que les zones de cisaillement ductile se forment lors de l'exhumation progressive le long d'un détachement plat d'échelle crustale. D'autre models proposent au contraire que ces mylonites témoignent de déformations plus généralisée de la croûte inférieure qui sont ultérieurement 'capturées' et exhumées par un détachement fragile plus tardif. Un autre problème majeur concerne le pendage initial de telles structures, car l'initiation de faille normale à faible pendage (≤ 30°) est contraire à la théorie andersonienne des failles normales. Pour cette raison, des modèles alternatifs proposent une initiation des détachements à fort pendage ultérieurement basculés par rebond isostatique.

Ces différents models ont été testés sur l'exemple de la zone de faille du Simplon située dans les Alpes Centrales Européennes. Ce système majeur en faille normale est le résultat d'une extension généralisée syn-convergence, parallèle à la chaîne et active depuis au moins l'Oligocène. Malgré l'excellence des affleurements et plus de 50 ans de recherches menées sur cette zone de faille, l'âge de la déformation cisaillante n'est pas encore établie et reste débattue. A l'échelle plus régionale, la perte et/ou le transfert du déplacement et sa relation avec le système décrochant des failles du Rhône et de la Périadriatique sont encore contredis. D'une façon générale, la géométrie, les interactions entre plissement et cisaillement et la cinématique de l'exhumation du mur de faille restent peu contraintes.

Ce travail de thèse présente une étude structurale détaillée de la Faille du Simplon couplée avec (1) une étude de datation absolue de la déformation utilisant les méthodes $^{40}Ar/^{39}Ar$ et Rb-Sr et un contrôle (micro-)structurale direct de la croissance des minéraux datés, (2) une étude de thermochronologie combinant des ages de refroidissement $^{40}Ar/^{39}Ar$ sur micas et des ages traces de fission sur apatites et zircons, (3) une inversion des données thermochronologiques utilisant un modèle thermo-cinematique pour contraindre l'histoire de l'exhumation, et (4) une reconstitution en 3D de la zone de faille. L'histoire du refroidissement est reconstituée de part et d'autre de la faille du Simplon utilisant des ages issus de la littérature, couplés à de nouveaux âges obtenus par analyses de trace de fission et la méthode $^{40}Ar/^{39}Ar$. La discontinuité des âges de refroidissements mesurés à travers la faille suggère une activité de la faille entre 20 et 3 Ma. Une intensification de la localisation des déformations est observée le long du détachement en direction du SE reflétant différents niveaux structuraux aujourd'hui exposés le long d'un même détachement. Un transfert de la faille du Simplon dans la vallée du Rhône est clairement établi dans le NW. Dans le SE un transfert dans la vallée Isorno est décrit avec

une importante diminution de la quantité de déplacement. Les observations structurales ne suggèrent pas le prolongement du Simplon le long de la faille Periadriatic. L'âge du cisaillement tardif est contraint dans la vallée Isorno par la datation de micas blancs au sein de fentes de tension provoquées par le boudinage de la foliation entre 14 Ma (méthode $^{40}Ar/^{39}Ar$) et 14.5 Ma (méthode Rb-Sr). Dans la vallée du Rhône, des phengites syn-cinématique développées dans des phyllonites du massif de L'Aar donnent une gamme d'âges similaires entre 14.5 Ma (méthode Rb-Sr) et 14 à 10 Ma (méthode $^{40}Ar/^{39}Ar$). Ces âges correspondent à l'âge de la transition ductile-fragile dans la région du Simplon.

L'inversion des âges thermochronologiques, prédit une bonne reproduction des données avec un modèle cinématique simulant un détachement de 30°, couplée à une déformation cisaillante et intégrant l'effet de la topographie. Au contraire un modèle cinématique simulant un rebond isostatique ne permet pas la reproduction des ages en surface. Le modèle retenu dans ce travail prédit une activité de la faille à 18 Ma avec un taux de glissement de 2.8 mm/a qui diminue à 0.7 mm/a vers environ 14 Ma et continue jusqu'à 3 Ma. Le déplacement vertical total induit par l'activité de la faille est de 10 à 15 km. Finalement une augmentation du taux d'exhumation à l'échelle régional est détectée à partir des âges traces de fissions sur apatites à environ 4 Ma de 0.34 mm/a à 0.68 mm/a. Ceci reflète une augmentation du taux d'érosion en réponse à des changements climatiques au Pliocène.

Le modèle géométrique en 3D met en évidence l'exhumation du dôme du Toce résultant d'une interaction complexe entre le système extensif et la convergence. Une datation directe de la formation des rétro-plis par la méthode $^{40}Ar/^{39}Ar$ sur micas propose un âge de 10 Ma et donc un développement contemporain de l'histoire tardive et plus fragile de l'exhumation. Ceci résulte en un plissement simultané des différentes fabriques avec un axe parallèle à la direction de l'extension. Les mylonites sont clairement associées à la formation d'un dôme développé entre 17 et 14 Ma reflétant un gradient de la déformation à travers la zone de cisaillement. La déformation plus cassante (i.e. le détachement fragile) par contre ne présente pas cette géométrie et reflète une exhumation plus rigide du mur de faille.

En conclusion, la faille du Simplon représente un détachement développé avec un angle $\leq$ 30º qui résulte de l'histoire continue de l'exhumation a travers la transition ductile-fragile. Cette faille a fonctionnée durant le Néogène, entre 19 et 3 Ma présentant une vitesse d'exhumation tectonique (maximum 1.74 mm/a) relativement lente dans un contexte général de convergence oblique et a accommodé environ 10 à 15 km de déplacement vertical.

General introduction

The late evolution of orogenic belts is often associated with (1) post-collisional collapse of the thickened continental crust [e.g. *Dewey*, 1988; *Platt and Vissers*, 1989; *Malavieille*, 1993] or with (2) large scale transcurrent faulting and lateral extrusion [e.g. *Peltzer and Tapponnier*, 1988; *Ratschbacher et al.*, 1991a]. Such processes induce large scale late-orogenic extension accommodated by the development of low-angle detachment systems [e.g. *Wernicke*, 1981], which may be associated with major strike-slip faults systems (generally in transcurrent tectonic settings). Syn- to post-collisional extension has been described in many different late-orogenic histories, for example in the European Alps [*Steck*, 1980; *Mancktelow*, 1985; *Ratschbacher et al.*, 1989], the Aegean [*Lister*, 1984; *Urai et al.*, 1990; *Gautier et al.*, 1993; *Jolivet et al.*, 1994; *Avigad et al.*, 2001], the U.S Cordillera (e.g. the Basin and Range [*Davis and Coney*, 1979; *Coney and Harms*, 1984]), as well as in older orogenic domains such as the Variscan Belt (e.g. Montagne Noire and Dôme du Velay [*Vandendriessche and Brun*, 1989; *Echtler and Malavieille*, 1990; *Malavieille et al.*, 1990; *Van den Driessche and Brun*, 1992; *Burg et al.*, 1994]) or the Caledonian Belt [e.g. *Séranne and Séguret*, 1985; *Norton*, 1986; *Andersen and Jamtveit*, 1990; *Chauvet and Séranne*, 1994].

Low-angle detachment systems are common features related to exhumation in all these different orogens. They were first recognized in the 1980's in the Basin and Range province of USA [e.g. *Wernicke*, 1981], associated with the exhumation of gneiss domes or "metamorphic core complexes" [e.g. *Coney and Harms*, 1984]. These structures typically juxtapose an extensional ductile shear zone with a sub-parallel more discrete brittle detachment of shallow dip. Both ductile mylonites and brittle detachment show similar kinematics and are often associated with up-right folding parallel and perpendicular to the regional extension. This results in the exhumation of a gneiss dome with a complex 3D geometry. Evolution of low-angle detachments leading to this final domal shape has been the subject of much debate and, in particular, two major controversies remain unresolved.
(1) The exhumation history of the ductile shear zone relative to the brittle detachment. Some authors propose that the final juxtaposition of ductile mylonites against the brittle detachment is the result of a single continuous process of exhumation along the detachment [e.g. *Sibson*, 1983]. Others claim that it represents two separate events, with the later, more discrete brittle detachment exhuming a fossil ductile shear zone from depth [e.g. *Davis*, 1988; *Lister and Davis*, 1989; *Axen and Bartley*, 1997]. In this thesis, the issue is tackled by using precise geochronological methods on (micro-) structurally controlled samples to unravel the history of deformation, from ductile-to-brittle.
(2) The current shallow dip of the normal fault. There are two schools of thought: those who claim that there is good evidence that the low-angle is original [e.g. *John*, 1987; *Abbott et al.*, 2001; *Smith et al.*, 2007], and those who argue that it is not mechanically feasible to develop such a low-angle fault, that the initial orientation must have been steeper, and that the dip has subsequently changed as it passed through a "rolling hinge" [e.g. *Buck*, 1988; *Wernicke and Axen*, 1988]. This problem may be critically investigated

using a structurally controlled thermochronological study coupled with 3D geometric modeling and 2- and 3-D thermal modeling.

In addition, the interplay between upright folding and faulting and its implications for the resulting exhumation pattern of the gneiss dome has been investigated in this thesis using 3D geometric modeling together with a consideration of the geochronological relationships between folding and faulting.

This thesis critically assesses these controversies on the example of the Simplon Fault Zone (SFZ), located in the European Central Alps (Fig. I.1). The SFZ [*Mancktelow*, 1985, 1990; *Merle et al.*, 1986; *Mancel and Merle*, 1987; *Steck*, 1990] is one of several well-exposed examples of low-angle detachment systems that developed in the Alps as the result of orogen-parallel extension during the Oligo-Miocene [e.g. *Mancktelow*, 1992; *Steck and Hunziker*, 1994; *Fugenschuh et al.*, 1997]. It is associated with the exhumation of the western part of the Lepontine gneiss dome [e.g. *Steck and Hunziker*, 1994]. Despite the generally excellent outcrop conditions and more than 50 years of research, the age, kinematics and geometry of various components of this major fault system are still controversial. The major controversies general to discussions about detachment development, as summarized in (1) and (2) above, also apply to the SFZ. The relationships between the large-scale backfolds associated with the so-called Northern and Southern Steep Belts [*Milnes*, 1974] and the mylonites and brittle detachment of the SFZ also remained unresolved. It was clear that the SFZ has a complicated geometry and hence cannot be studied as a simple 2D structure (i.e. a classic normal fault), but a true 3D model of its geometry and kinematics did not exist.
This thesis presents detailed structural work coupled with geochronology, 2-3D thermo-kinematic modeling and 3D geometric modeling to fully establish the spatial and temporal evolution of the detachment system during ongoing convergence across the Alps.

I. Introduction

I.1. Alpine overview

The European Alps result from collision between the European passive margin and the Apulian microplate, controlled by the southward subduction and subsequent closure of several oceanic domains. Collision started in the middle Jurassic [*Gawlick et al.*, 1999] in the Eastern Alps with the subduction of the Meliata ocean [*Kozur*, 1989]. In the Central and Western Alps collision started in the upper Cretaceous, resulting in the subduction of the Alpine Tethys (Piedmont-Liguria and Valais) oceans [e.g. *Schmid et al.*, 2004; *Herwartz et al.*, 2008]. The current map distribution of major paleogeographic units is shown in Fig. I.1, following the interpretation of *Schmid et al.* [2004].

This continental collision produced a complex nappe stack, progressively accreted toward the external European margin. The principal shortening direction was oriented NNW-SSE in the Eastern and Central Alps and W-E in the Western Alps (Fig. I.1).

The deepest rocks seen in the Alps today are exposed within the Central Alps (Fig. I.2). In this region, SE under-thrusting of the European plate below the Apulian microplate has resulted in the development of a NW-vergent nappe stack associated with intense isoclinal folding on a kilometer scale [e.g. *Lugeon*, 1901; *Schmidt and Preiswerk*, 1908; *Argand*, 1911]. This nappe formation, the so-called *D1* phase of deformation, is followed by several phases of intense post-nappe deformation (Fig. I.2), which have been described from throughout the Central Alps [e.g. *Milnes*, 1973; *Milnes et al.*, 1981; *Grujic and Mancktelow*, 1996; *Maxelon and Mancktelow*, 2005] and can be summarized as follows.

(1) An intense tight to isoclinal refolding on a regional scale (*D2*), for example the Monte Leone and Wandfluhhorn folds, associated with prograde metamorphism. *D2* fold axes are generally SW-NE oriented, that is parallel to the trend of the orogen. *D1* and *D2* are generally interpreted to have occurred in the time span from 38 Ma to 32.5 Ma (review in *Maxelon and Mancktelow* [2005]).

(2) *D2* is followed by a phase *D3* that produced wavy to open folding of the whole tectonostratigraphy around 30-32 Ma (review in *Maxelon and Mancktelow* [2005]) and formed, for example, the Maggia steep zone separating the Toce and Ticino Subdomes [e.g. *Steck*, 1998].

(3) The last regional event *D4* is a late open backfolding developed during retrograde conditions of metamorphism and restricted to the Northern and Southern Steep Belts, producing, for example, the Berisal, Glishorn, Masera, and Vanzone folds [e.g. *Milnes*, 1974]. *D4* fold axes are SW-NE oriented. The Southern Steep Belt is considered to have developed prior to 25 Ma [*Pettke and Klaper*, 1992; *Steck and Hunziker*, 1994; *Romer et al.*, 1996; *Maxelon and Mancktelow*, 2005], whereas the Northern Steep Belt is considered to be younger and associated with the late exhumation of the external massifs, as reflected in fission-track ages [*Michalski and Soom*, 1990; *Soom*, 1990].

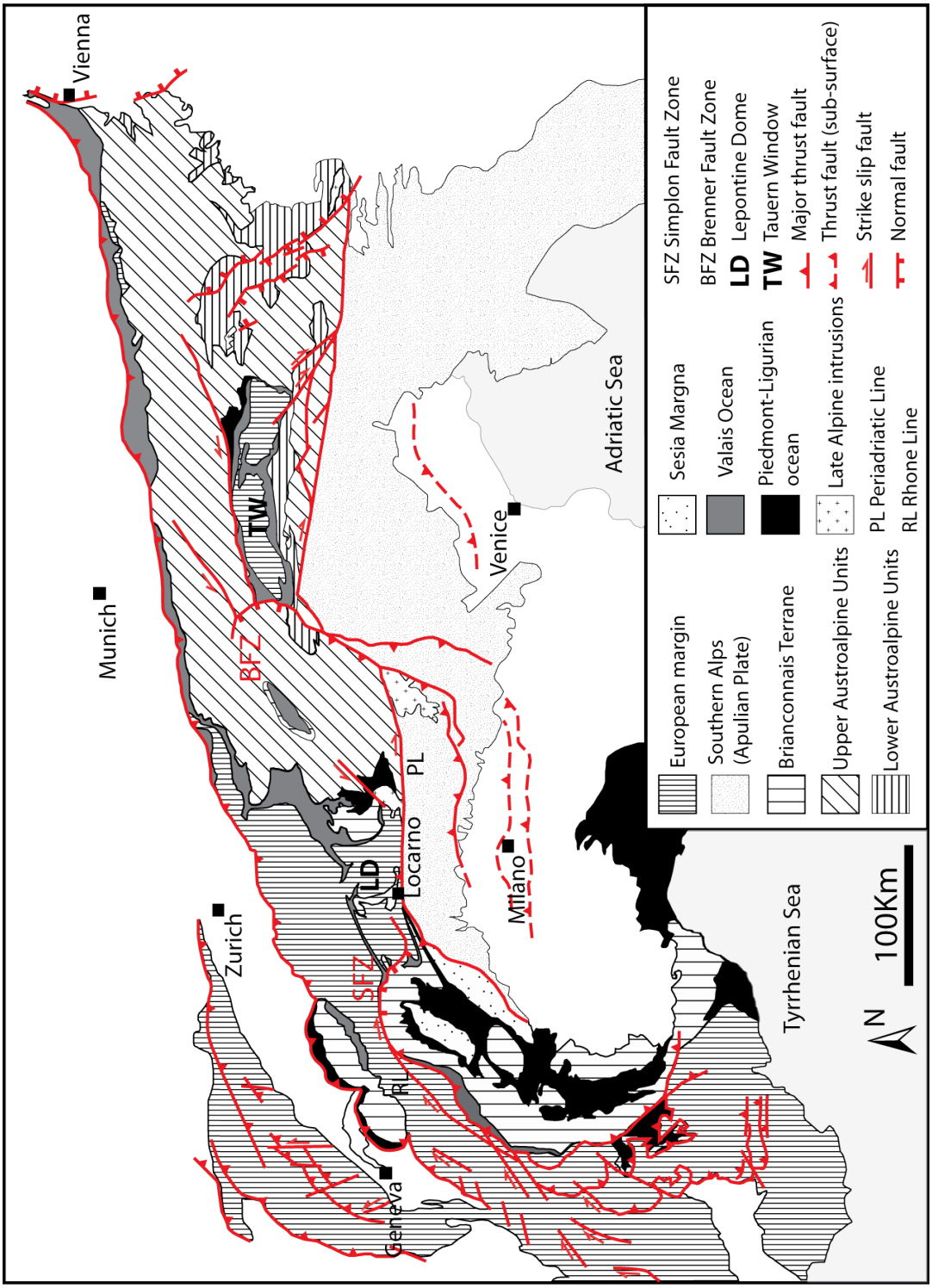

Figure I.1: Simplified tectonic map of the Alps. Principal tectonic units and discrete Neogene structures are shown from *Mancktelow and Pavlis* [1994] and *Schmid et al.* [2004]

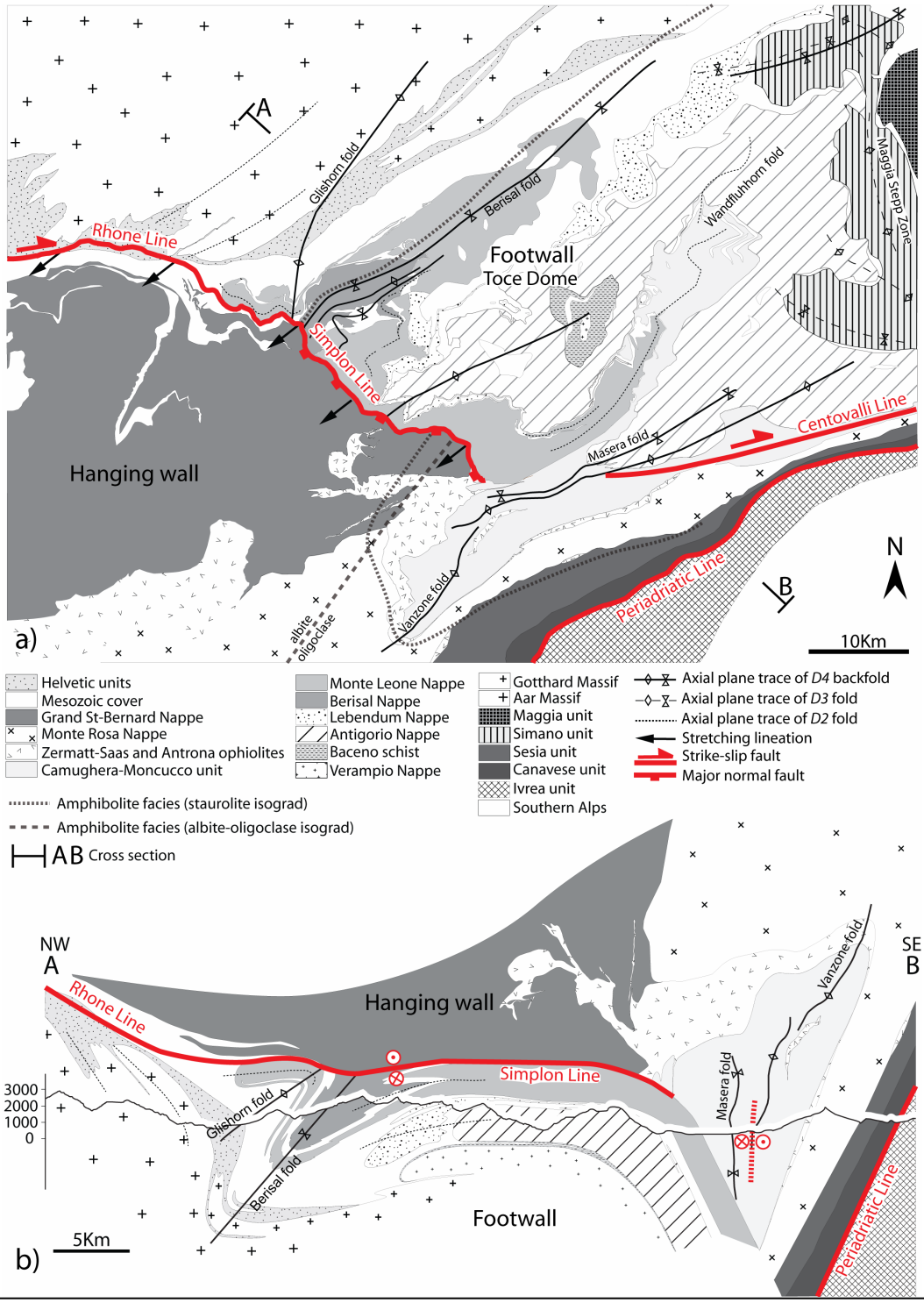

Figure I.2: The Simplon Line in the Central Alps. a) Geological map and major nappe units. Compilation from published geological maps of Visp, Brig, Simplon, Domodossola, *Keller et al.* [2005a] and *Maxelon and Mancktelow* [2005]. The greenschist/amphibolite facies boundary is drawn based on the staurolite isograd of *Niggli* [1970] to the NE of the Simplon Line, and on the albite-oligoclase isograd [*Bearth*, 1958; *Colombi*, 1989] and the staurolite isograd [*Keller et al.,* 2005b] to the SW of the Simplon Line. b) NW-SE cross section showing the major folds.

Orogen-parallel extension originally started in the Oligocene [e.g. *Steck and Hunziker*, 1994; *Nievergelt et al.*, 1996] and was strongly developed in the Neogene [e.g. *Grasemann and Mancktelow*, 1993; *Fugenschuh et al.*, 1997]. A resulting general stretching parallel to the trend of the orogen is described from the Central to the Eastern Alps [e.g. *Steck*, 1980; *Selverstone*, 1988; *Ratschbacher et al.*, 1989], being more strongly developed in the vicinity of major extensional fault zones, such as the Simplon Fault Zone [e.g. *Mancktelow*, 1985, 1990; *Steck*, 1990], the Brenner Fault Zone [e.g. *Behrmann*, 1988; *Selverstone*, 1988; *Fugenschuh et al.*, 1997], the Turba Fault Zone [*Nievergelt et al.*, 1996], and the Forcola Fault Zone [*Meyre et al.*, 1998; *Ciancaleoni and Marquer*, 2008]. Regionally, many brittle normal faults are also reported from the Western [e.g. *Bistacchi and Massironi*, 2000; *Champagnac et al.*, 2004] and Central Alps [*Wawrzyniec et al.*, 2001; *Grosjean et al.*, 2004] that are consistent with orogen-parallel extension in the Oligo-Miocene.

The Simplon and Brenner Fault Zones are two major low-angle detachment systems exposed respectively in the Central and Eastern Alps (Fig. I.1). They limit to the W and SW major gneiss domes: the Tauern Window and the Lepontine Dome respectively (Fig. I.1). It is important to note that these low-angle detachment systems, representing zones of enhanced orogen-parallel extension, occur specifically in those locations in front of the angular Apulian indenter where the width of the Alpine belt is narrowest (Fig. I.1).

The simplified Neogene tectonic map of Figure I.1 highlights the close association of normal and strike-slip faulting (mainly dextral in the Western and Central Alps, but with both senses in the Eastern Alps). Such general kinematics have been interpreted to reflect oblique convergence and overall dextral transpression [e.g. *Mancktelow and Pavlis*, 1994] and, particularly in the Eastern Alps, lateral extrusion [e.g. *Ratschbacher et al.*, 1991a, b].

I.2. The Simplon Fault Zone (SFZ)

The classic and previously most studied section of the SFZ is located geographically between Visp in the Rhone valley (Switzerland) and Domodossola in the Ossola valley (Italy) (Fig. I.3).

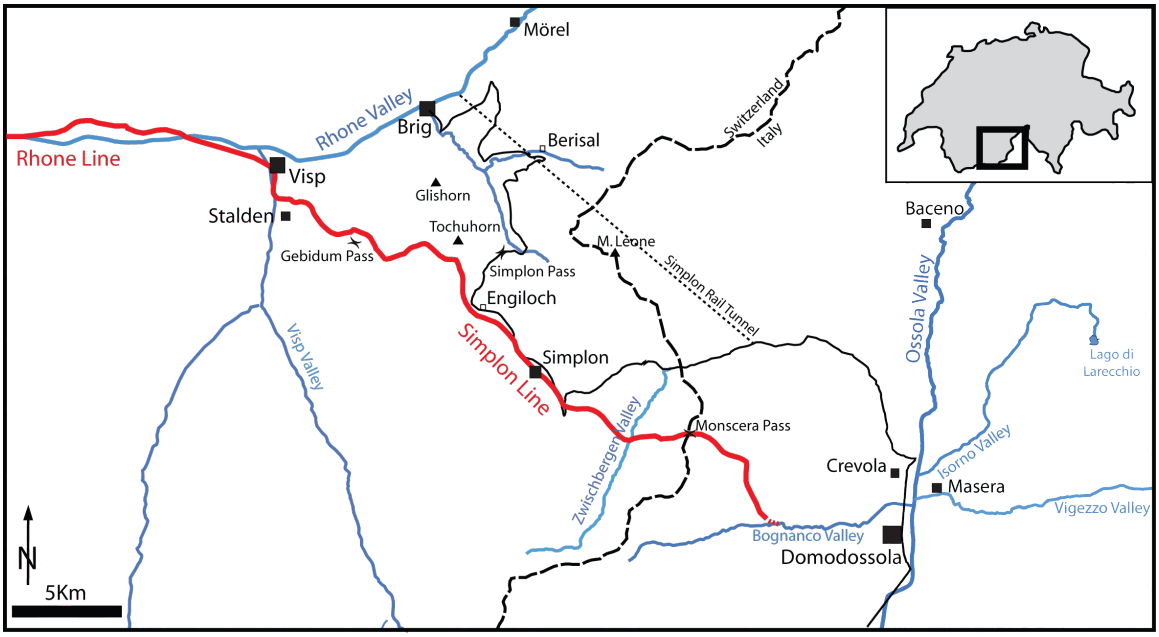

Figure I.3: Geographic location of the Simplon Fault Zone.

Along this segment, it corresponds to a major normal low-angle detachment system that strikes generally NW-SE over a length of ca. 30 km. It is situated between a major dextral strike-slip fault system, the Rhone Line [e.g. *Burkhard*, 1988], the Centovalli Line [e.g. *Schmid et al.*, 1987] and the Periadriatic Line [e.g. *Schmid et al.*, 1987] (Fig. I.2a). The SFZ forms the SW border of the "Toce" or "Simplon" Dome, which together with the "Ticino" Dome further east, comprise the regionally developed Lepontine metamorphic Dome [e.g. *Preiswerk*, 1921; *Wenk*, 1955; *Steck and Hunziker*, 1994]. Units in the Toce Dome reach upper amphibolite facies metamorphic grade but without the development of Alpine migmatites and partial melting. The SFZ represents a major discontinuity that, following *Milnes et al.* [1981], separates two main units, the upper Pennine nappes to the SW from the lower Pennine nappes to the NE.

The brittle Simplon detachment, commonly referred to in the literature as the "Simplon Line" (SL) [*Mancktelow*, 1985; *Mancel and Merle*, 1987; *Steck and Hunziker*, 1994] (Fig. I.2) consists of a narrow zone (< 10 m) of cataclasites. In some places (e.g. Zwischbergen Valley, Fig. I.3), it is also marked by a zone of foliated clay gouge that can be up to a few meters wide. In its central section (near Simplon Village Fig. I.3), the Simplon Line dips 25-30° toward the SW. The brittle detachment overprints in the footwall a broad zone of ductile mylonites. These mylonites grade over a distance of 1-2 km into less strongly overprinted units of the Lower Pennine nappes. Kinematic indicators from both the ductile and brittle components consistently show a top-down-to-SW sense of shear [*Mancktelow*, 1985, 1987, 1990; *Steck*, 1990; *Grosjean et al.*, 2004].

I.3. Overview of previous studies and on-going controversies

At the beginning of the 20th century, *Lugeon* [1901] and *Schmidt* [1906] were the first to recognize major discordances in tectono-stratigraphic units as drawn in their maps of the Central Alps. They were pioneers in establishing the existence of discontinuities such as the Simplon Line or the Periadriatic Line, although the structures themselves were not specifically distinguished.

The Simplon Line itself was first recognized in the 1950's [*Amstutz*, 1954; *Bearth*, 1956a, b], with its trace clearly indicated on the Simplon map sheet of *Bearth* [1972]. The marked change in isotopic ages across this structure, indicating a major normal component in the central region, around Simplon Village, was already established from the work of *Hunziker and Bearth* [1969]. *Steck* [1980], in a regional study from the Aar massif and the Simplon region, recognized two major stretching directions, the first related to top-to-NW nappe stacking and the second parallel to the orogen and particularly well developed in the Simplon area. He related this second fabric to a broad dextral shear zone. In later work [*Steck*, 1984, 1987, 1990, 2008; *Steck and Hunziker*, 1994], he distinguished this broad zone of movement (the "Simplon Shear Zone") from a younger and much more discrete zone of low-grade mylonite and cataclasite (the "Simplon Line"). Although real geochronological control was still lacking, he suggested that the older broad zone may be of Oligocene age, whereas the Simplon Line would be of Neogene age (Fig. I.4a, b). Note that, in his interpretation, the broad zone of Oligocene mylonites is widespread within both the footwall and hanging wall of the Simplon Line (Fig. I.4a, b) (see also *Mancel and Merle* [1987], *Schmid and Kissling* [2000] and *Schmid et al.* [2004] for similar interpretations).

In contrast, *Mancktelow* [1985, 1990, 1992] considered that both the broad zone of mylonites in the footwall and the lower-grade mylonites in the immediate vicinity of the brittle detachment fault (Simplon Line) formed part of the same system, with the same lineation and kinematics (Fig. I.4c, d). These different components in the footwall of the SFZ were taken to represent cooling, increasing localization of strain, and eventual transition to brittle behavior during progressive exhumation, lasting from 18-5 Ma [*Grasemann and Mancktelow*, 1993]. Mylonites from the hanging wall, which are abruptly transected by the detachment, were considered to be older on the basis of the markedly older isotopic mineral ages, generally annealed microstructures, and the lack of deformation of the common quartz veins [*Mancktelow*, 1990]. In contrast to the hanging wall, mylonites from the footwall preserve deformation microstructures (not annealed) and milky-white quartz veins are invariably mylonitized [*Mancktelow*, 1987, 1990].

Footwall mylonites are broadly folded around the major Berisal synform in the north [*Mancel and Merle*, 1987; *Mancktelow*, 1990, 1992] and also transected by the discrete detachment fault [*Milnes et al.*, 1981]. However the kinematics of both the folded and the transected mylonites are the same, the isotopic mineral ages are similar, and the synkinematic metamorphic conditions show a progressive decrease from amphibolite facies, though greenschist facies to near surface brittle faulting and fault gouge formation. In the model of *Mancktelow* [1990, 1992] and *Mancktelow and Pavlis* [1994], this relationship between folding and shearing was considered to represent the interplay between orogen-parallel stretching and orogen-perpendicular shortening due to continuing convergence across the Alpine chain. The alternative model of *Steck* [1984,

1987, 1990, 2008] and *Steck and Hunziker* [1994] interprets the same field relationships in terms of more distinct events over a greater time span: first major regional shearing in the Oligocene (the Simplon Shear Zone), then folding, and subsequently, in the Neogene, the development of the Simplon Line as a discrete normal fault related to exhumation of the footwall.

Therefore, although the structures are well described and recognized in the central section of the SFZ, the absolute age of such structures was still controversial (compare models in Figure I.4).

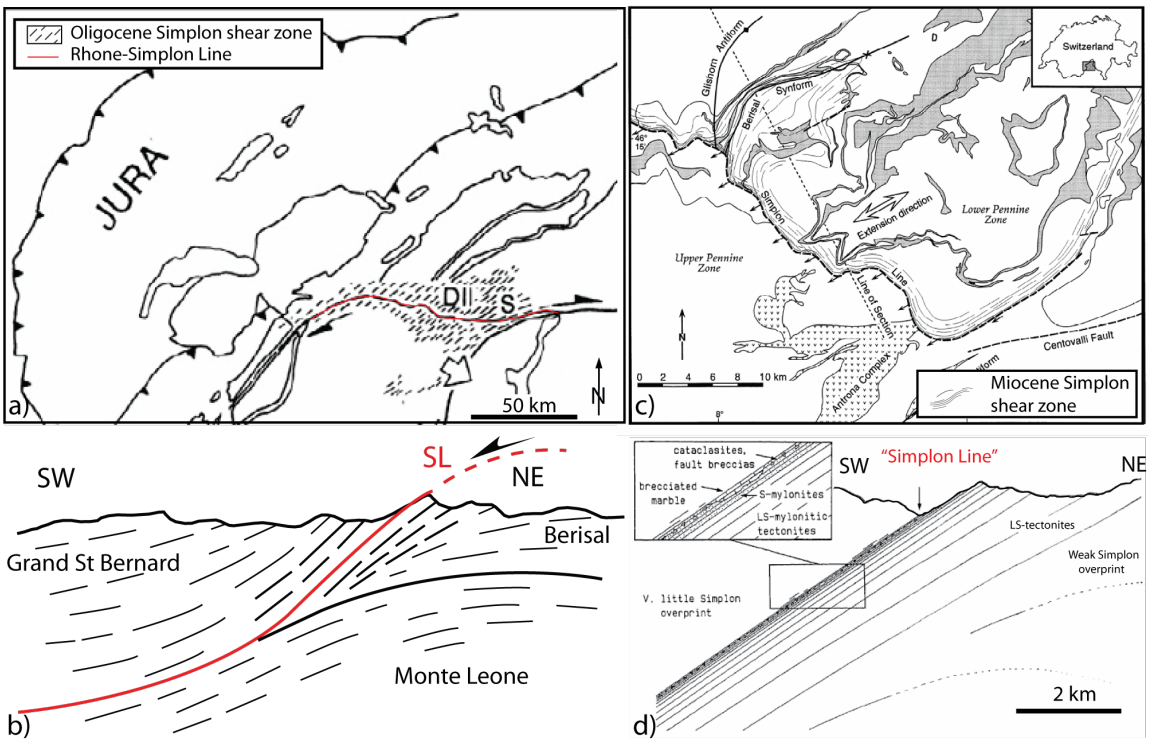

Figure I.4: The Simplon Fault Zone and the controversy with regard to its age. a) Two distinct events with an Oligocene ductile shear zone *D2* exhumed by a low-angle detachment in the late Miocene [*Steck*, 2008], b) Similar model in cross section by *Mancel and Merle* [1987]. Note that in this model the Simplon shear zone is widespread within the hanging wall of the Simplon Line. c) A continuous exhumation from ductile-to-brittle field in the Miocene by *Mancktelow and Pavlis* [1994]. d) Similar model in cross section by *Mancktelow* [1985]. The Simplon ductile shear zone is restricted to the footwall.

As noted above, one long-running controversy that is common to all examples of exhumation along low-angle detachments concerns the current shallow dip of the normal fault. Typically two models are proposed: (1) initiation of the detachment with a shallow dip [e.g. *John*, 1987; *Abbott et al.*, 2001; *Smith et al.*, 2007], and (2) initiation of the detachment at high-angle and subsequent rotation into a low dip orientation as it passes through a "rolling hinge" [e.g. *Buck*, 1988; *Wernicke and Axen*, 1988]. This controversy has recently also come to be directly relevant in considering the evolution of the Simplon and Brenner faults in the Alps [*Wawrzyniec et al.*, 1999; *Axen et al.*, 2001; *Wawrzyniec et*

al., 2001]. The rolling hinge model proposed by these authors requires a sequential development of first W-side down and then E-side down shear zones and faults in the progressively exhuming footwall (Fig. I.5a, b). On the contrary, the model of *Mancktelow* [1985] and *Grasemann and Mancktelow* [1993] implies an initial low-angle dip of the detachment of ca. 25° (Fig. I.5c, d).

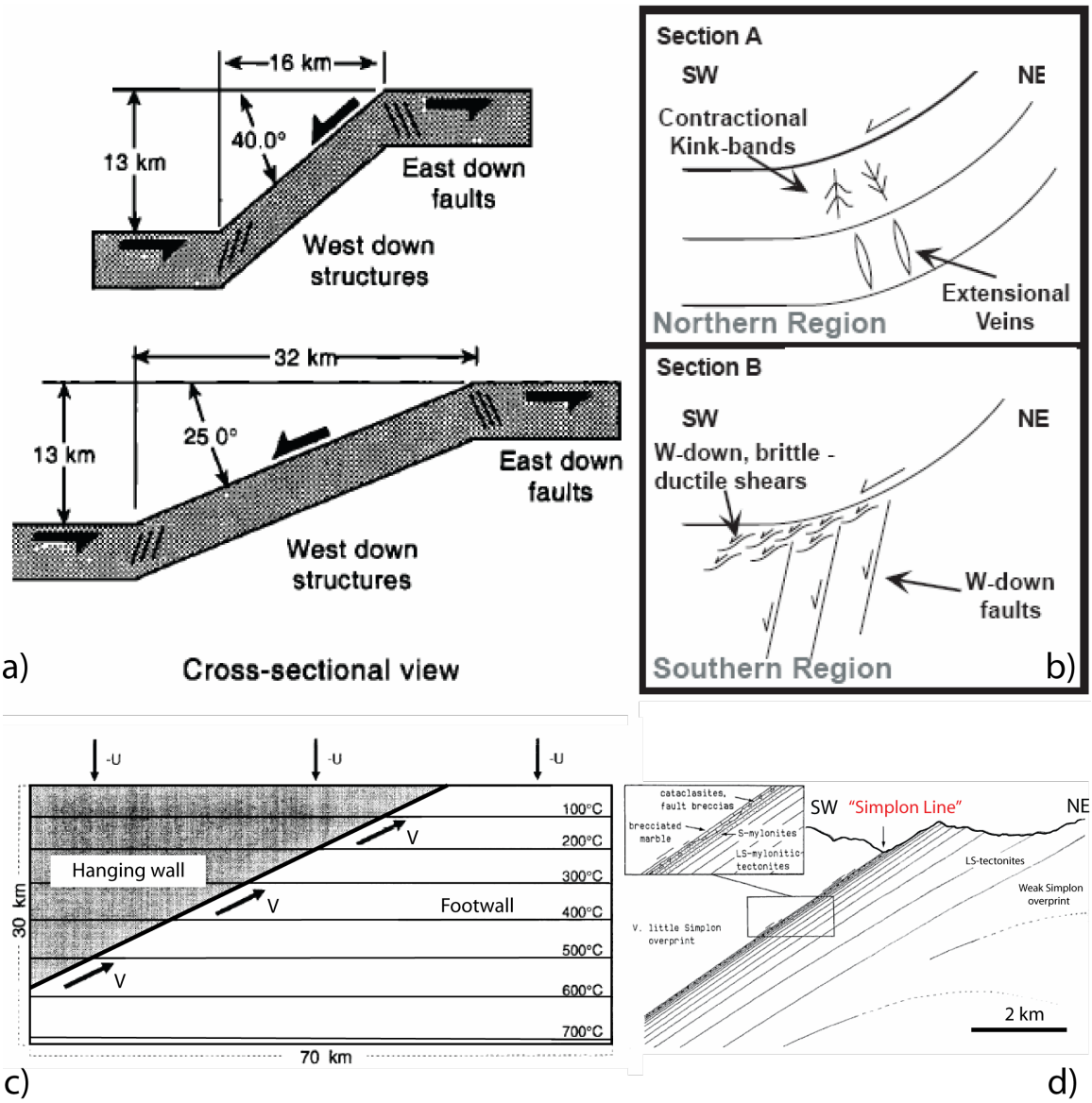

Figure I.5: Detachment geometry a) Rolling hinge model applied to the SFZ [*Wawrzyniec et al.*, 2001]. b) Rolling hinge model on the SFZ accommodated by "flexural failure" and "subvertical shear" [*Wawrzyniec et al.*, 1999]. c) Model with an initial low-angle detachment [*Grasemann and Mancktelow*, 1993]. d) Cross section assuming an initial low-angle detachment [*Mancktelow*, 1985].

The continuation of the SFZ to the SE and its possible connection to the Periadriatic Line is also controversial. Different models have been proposed and are presented in Figure I.6.
(1) A possible connection of the SFZ to the Periadriatic Line, via the Centovalli Line, [*Bearth*, 1956b; *Schmid and Kissling*, 2000; *Schmid et al.*, 2004], where clear brittle deformation was described striking E-W (Fig. I.6a).
(2) On the basis of direct field relationships, *Mancktelow* [1985, 1990, 1992], *Steck* [1987, 1990] and *Steck and Hunziker* [1994] have all argued that such a connection was impossible, and that the displacement on the Centovalli fault was in fact small. They propose a continuation of the SFZ along Val Bognanco and across the Val d'Ossola into Val d'Isorno (Fig. I.3) toward the NE and into the Toce Dome (Fig. I.6b, c).
(3) A recent model from *Keller et al.* [2006] proposes no prolongation at all of the SFZ in the SE region but rather an accommodation by backfolding (Masera and Vanzone folds) associated with anticlockwise rotation of the hanging wall (Fig. I.6d).

The continuation and/or loss of displacement to the north is also not well established. It is clear that an important component of Simplon fault movement transfers into a broad zone of dextral shearing running along the Rhone Valley and to both sides of the Mt Blanc massif [*Burkhard*, 1988; *Mancktelow*, 1990; *Steck*, 1990; *Hubbard and Mancktelow*, 1992; *Steck and Hunziker*, 1994]. However, the specific location of the SFZ between Visp and the Simplon Pass is until now not established (Fig. I.3). Besides, zones of dextral shearing are also described to the NE from Simplon-Brig along the SE border of the Aar massif, at least as far as the Grimselpass region [*Rolland*, personal communication], and the relationship of this shearing to the SFZ was also unknown.

These controversies again raise the problem of the age and correlation of structures.

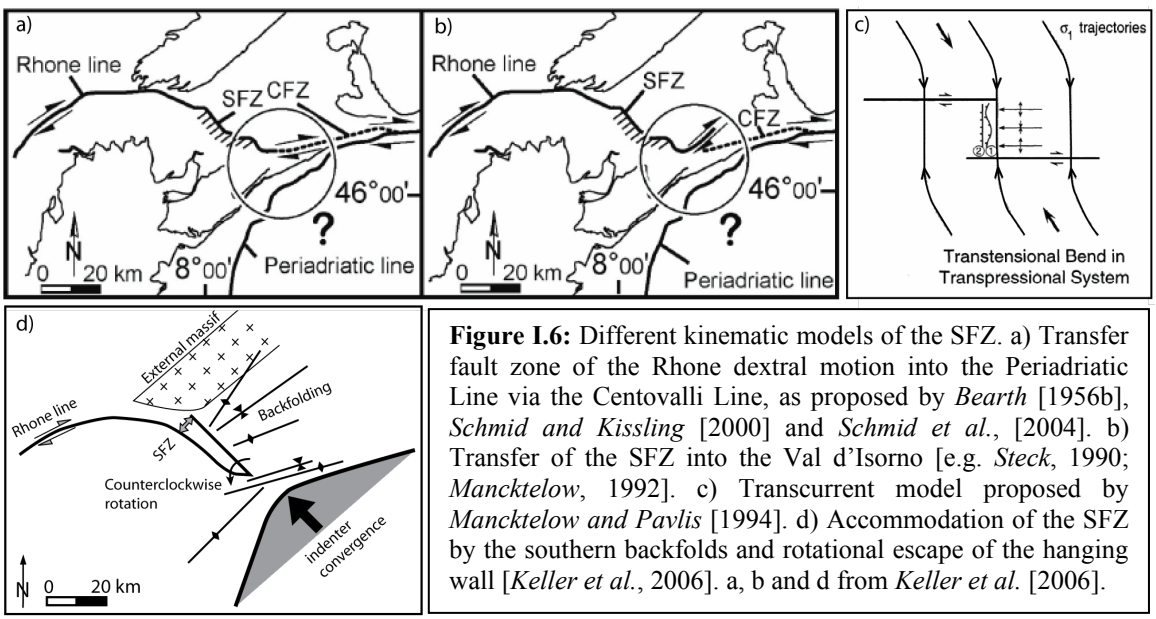

Figure I.6: Different kinematic models of the SFZ. a) Transfer fault zone of the Rhone dextral motion into the Periadriatic Line via the Centovalli Line, as proposed by *Bearth* [1956b], *Schmid and Kissling* [2000] and *Schmid et al.*, [2004]. b) Transfer of the SFZ into the Val d'Isorno [e.g. *Steck*, 1990; *Mancktelow*, 1992]. c) Transcurrent model proposed by *Mancktelow and Pavlis* [1994]. d) Accommodation of the SFZ by the southern backfolds and rotational escape of the hanging wall [*Keller et al.*, 2006]. a, b and d from *Keller et al.* [2006].

In summary, although the SFZ has been intermittently studied for more than 50 years, many regional aspects of its kinematics and spatial and temporal evolution were still matters of active debate. A better understanding of this fault zone also has important implications for the more general debate about the evolution of low-angle detachment systems developed during ongoing convergence.

I.4. Goals and methods

The **general aim** of this study was to evaluate the (still controversial) evolution of a major extensional low-angle detachment system.

The first specific aim was to determine if the juxtaposition of brittle and ductile deformation in the footwall was the result of a single continuous process of exhumation along the detachment, or due to two separate events, with the later, more discrete brittle detachment exhuming a fossil ductile shear zone from depth.

The second aim was to provide more detailed constraints relevant to the active debate on the development of the current shallow dip to the normal fault. For this purpose, we propose to characterize the cooling pattern obtained for exhumation along either an initially low-angle detachment or for a rolling hinge model by using 2- and 3-D thermo-kinematic modeling. The intention was to find a typical thermochronological signature that could be used in different settings to differentiate the two models. Such a signature can only be established in a simple model for gneissic domes exhumed along a single detachment where there is no partial melting, which would strongly influence the cooling pattern.

Many examples of low-angle detachments are not cylindrical structures but show a complex interplay between up-right folding and extensional faulting [e.g. *Yin*, 1991; *Yin and Dunn*, 1992; *Mancktelow and Pavlis*, 1994; *Avigad et al.*, 2001]. These structures have been attributed to various processes mainly implying active folding [e.g. *Chauvet and Séranne*, 1994; *Mancktelow and Pavlis*, 1994] or primary fault corrugations [*Davis and Hardy*, 1981; *Spencer*, 1985]. A final general objective was therefore to characterize the 3D geometry of a low-angle detachment system in convergent orogen in order to understand the impact of this 3D form on the resultant exhumation.

The first **regional objective** of this thesis was to establish the continuation of the SFZ to the NW and SE and to determine how displacement is either lost or transferred in these regions. The second regional objective was to establish the relative and absolute chronology of the SFZ and of the associated backfolds. A third goal was to provide new constraints on the exhumation rate and relative displacement, which first required the 3D kinematics and initial angle of the fault to be established.

Establishing the absolute dating of the deformation, through the transition in the footwall from ductile-to-brittle behavior, was critical for many of the aims of this study. This required a preliminary detailed structural, petrological and chemical study to find key samples where mineral neo- (re-)crystallization ages could be extracted. A combination of mica $^{40}Ar/^{39}Ar$ dating and Rb-Sr mircosampling dating with petrological and oxygen

stable isotope analyses was employed to obtain direct control on mineral crystallization age versus deformation.

The characterization of the exhumation history is also of major importance. The cooling history was better constrained by new apatite and zircon fission-track ages across the fault zone and a large set of mica $^{40}Ar/^{39}Ar$ cooling ages from the high-grade region (Fig. I.2a). The resulting cooling history was then used to establish the thermal history in the central region of the SFZ and extract the exhumation history across the fault zone. This approach could be used because the SFZ is clearly developed under retrograde P-T conditions from the peak regional metamorphic event. To achieve this, a 2-3D numerical thermo-kinematic model (Pecube, [*Braun*, 2003]) was used. This was coupled with a formal inversion algorithm (Neighbourhood Algorithm, [*Sambridge*, 1999a, b]) to characterize the kinematics of exhumation and to quantify the relative displacement and rates of exhumation related to the SFZ. Such an approach includes the variation in the geothermal gradient due to isotherm advection and topography. It also allows a test of all possible solutions for exhumation rates over a given time range.

Finally, the 3D field geometry was modeled using the computer software GeoModeller developed by the BRGM and Intrepid Geophysics. This program facilitates modeling of foliation and brittle fault planes in 3D using a potential method [*Lajaunie et al.*, 1997; *Aug et al.*, 2004], which makes use of all structural measurements, based on detailed structural field investigation.

I.5. Outline of the thesis

This thesis is divided into three main chapters, each representing a manuscript that will be submitted for publication.

Chapter II first presents a review of the metamorphic history and of the previous geochronological studies on the Simplon region. It then characterizes, based on structural field data, the transfer and loss of displacement on the SFZ as it passes into a dextral strike-slip fault within the Isorno Valley, which crosscuts the regional *D2* Wandfluhorn fold. The transfer of the SFZ into the Rhone fault to the north, in the Rhone Valley, is also characterized. New direct dating on the ductile-brittle transition between 14.5 and 10 Ma is then presented for these different regions, based on a combination of $^{40}Ar/^{39}Ar$, Rb-Sr microsampling, and oxygen isotope methods. Finally we reconstruct the cooling pattern across the entire fault zone using new apatite and zircon fission-track ages, muscovite and biotite $^{40}Ar/^{39}Ar$ cooling ages together with a compilation of the large amount of published ages (references given in Chapter II). This cooling pattern confirms the structurally established transfer and loss of the SFZ, characterizing an increase in the degree of localization of the deformation toward the SE, reflecting different structural levels now exposed along one single detachment system. Together, these data indicate important displacement on a broad mylonitic shear zone, now observed in the footwall of the SFZ, between 20 and 14 Ma, followed by more brittle deformation, mainly localized into a detachment fault of similar kinematics, which remained active until at least 3 Ma.

Co-authors of this manuscript are N. Mancktelow (ETH), D. Seward (ETH), Y. Rolland (Univ. Nice Sophia Antipolis) and W. Müller (Royal Holloway Univ. of London).

Chapter III critically assesses two kinematic models previously proposed for the SFZ: an initial low-angle detachment and a rolling hinge. The Neighbourhood Algorithm is used to invert a large thermochronological dataset from the central region of the SFZ for the two potential models using a 2D thermo-kinematic code (Pecube). Age-pattern evolutions within the footwall for these two different models are quite different and suggest that a rolling hinge is not a valid kinematic model for the SFZ. On the contrary, a model of a low-angle detachment dipping 30° including topography could reproduce the observed thermochronological pattern. This model predicts an onset time of faulting at ca. 19 ± 4 Ma, with fault movement remaining active until at least until 3 Ma. A maximum vertical relative displacement between footwall and hanging wall of 15 km is indicated. Different solutions of exhumation rates are discussed, with a negative correlation between the time period of faulting and the fault velocity.

Co-authors of this manuscript are F. Herman (ETH) and N. Mancktelow (ETH).

Chapter IV first establishes the field geometry of interrelated faulting and folding associated with this low-angle detachment. New chronological constraints are then presented that date the onset of the Glishorn and Berisal *D4* backfolds at ca. 10 Ma, based on mica $^{40}Ar/^{39}Ar$ and confirmed with zircon fission-track cooling pattern. The 3D foliation field geometry of the SFZ, which is affected by both extension-parallel and extension-perpendicular folding, is modeled relative to the previous fabric within the footwall and hanging wall. In the central region, the Simplon mylonites reactivate or transpose the previous fabric in the vicinity of the fault zone, except in the two dextral strike-slip fault regions (Rhone and Isorno valleys), where distinct orientations are preserved. The mylonitic fabric is clearly affected by both sets of folds while the cataclastic detachment is apparently only affected by wavy extension-parallel folds. The 3D foliation field geometry of the Lepontine Dome is also presented, which reflects the strong influence of the SFZ in the exhumation of the Toce Dome.
Coupling the 3D field geometry and geochronological constraints suggests that extension-parallel folding was synchronous with the late exhumation history of the SFZ (at around ca. 10 Ma) and that the development of the extension-perpendicular domal shape was coeval with mylonite formation (17-14 Ma), reflecting a strain gradient through the shear zone. This reflects a complex interplay between folding and faulting in a low-angle detachment system developed during ongoing convergence.

Co-authors of this manuscript are N. Mancktelow (ETH) and G. Courioux (BRGM).

In **chapter V** the results of the thesis are summarized. We then discuss the different kinematic models proposed for the Central Alps and integrate the new results from this thesis into a general model of transpressive motion due to oblique convergence since the Oligo-Miocene.

II. Geochronology and cooling history of the Simplon Fault Zone

II.1. Introduction

Major low-angle (≤ 30°) normal faults juxtapose different structural levels of the crust, typically across a brittle detachment that overprints an extensional ductile shear zone showing similar kinematics. Many papers imply a single continuous process of exhumation of the footwall along a low-angle detachment that evolves from the ductile to the brittle field [e.g. *Sibson*, 1983; *Mancktelow*, 1985; *Mehl et al.,* 2005]. However, some studies have proposed an alternative model where the mylonites from the footwall are a more general feature of the extending middle crust that are "captured" and exhumed by the late detachment [e.g. *Davis*, 1988; *Lister and Davis*, 1989; *Axen and Bartley*, 1997; *Cooper et al.*, 2006]. These two models are fundamentally very different and have different implications in terms of the amount of exhumation involved along a low-angle detachment. In this paper, we investigate these potential models along a well-exposed low-angle detachment in the Central European Alps, combining detailed geochronology and thermochronology with structural, petrological and chemical analyses. Many studies have already used thermochronology to investigate the timing and rate of exhumation on low-angle detachments [e.g. *Foster et al.*, 1993; *Grasemann and Mancktelow*, 1993; *Wells et al.*, 2000; *Vanderhaeghe et al.*, 2003; *Brichau et al.*, 2006; *Mulch et al.,* 2006], generally based on the concept of cooling ages for different mineral and isotopic systems [e.g. *Wagner et al.,* 1977]. In contrast, absolute ages of deformation are rather difficult to obtain but have been acquired by dating neo-crystallized syn-kinematic minerals (usually white mica) from specific structural sites, such as strain shadows, [*Müller et al.,* 2000a] or from retrograde phyllonitic shear zones [*Dunlap*, 1997; *Kirschner et al.,* 2003; *Mulch and Cosca*, 2004; *Rolland et al.,* 2008].

The Simplon Fault Zone [*Mancktelow*, 1985, 1990; *Merle et al.,* 1986; *Mancel and Merle*, 1987; *Steck*, 1990] in the Central Alps and the Brenner Fault Zone [*Behrmann*, 1988; *Selverstone*, 1988; *Fugenschuh et al.,* 1997] in the Eastern Alps are the most prominent low-angle detachment systems developed in the European Alps. In this paper, we specifically concentrate on the Simplon Fault Zone for several reasons. (1) Overprint of the broad ductile shear zone in the footwall by a more localized brittle detachment can be studied over a strike length of many kilometers. (2) The fault zone exposes different crustal levels, as reflected by the variation in peak metamorphic grade over the region. (3) A large amount of age data (mainly cooling ages) from the area has already been published [e.g. *Hunziker*, 1969; *Hunziker and Bearth*, 1969; *Purdy and Jäger*, 1976; *Wagner et al.,* 1977; *Deutsch and Steiger*, 1985]. However, interpretations are still controversial because of the lack of structural and petrological constraint on the analyzed samples and the need for more direct dating of the deformation. (4) Two different models on the timing of exhumation of the footwall have been proposed to explain the present features of the Simplon Fault Zone. One model proposes an earlier, early Oligocene ductile shear zone that was subsequently passively exhumed in the late Miocene by a brittle detachment [*Mancel and Merle*, 1987; *Steck*, 1990; *Steck and Hunziker*, 1994] (Fig. I.4a,b). The alternative model considers the transition from ductile to brittle behavior to be relatively continuous during exhumation in the Miocene [*Mancktelow*, 1985; *Grasemann and Mancktelow*, 1993] (Fig. I.4c,d).

In this paper, we use apatite and zircon fission track, $^{40}Ar/^{39}Ar$ biotite and white mica cooling ages, and $^{40}Ar/^{39}Ar$ and Rb-Sr microsampling crystallization ages from syn-kinematic white mica to constrain the timing of the ductile shearing and the transition from ductile to brittle deformation in the Simplon Fault Zone. These geochronological data, in combination with field, microstructural and petrological observations, allow a critical analysis of the two general models for footwall exhumation along the Simplon Fault Zone.

II.2. Geological setting

II.2.1. The Simplon Fault Zone (SFZ)

The SFZ (Fig. II.1) is a major low-angle normal fault which in its central section dips 25-30° SW (region I in Fig. II.2b). Its exhumed footwall forms the Toce Dome, which together with the Ticino Dome further east, comprise the regionally developed Lepontine metamorphic Dome [e.g. *Preiswerk*, 1921; *Wenk*, 1955; *Steck and Hunziker*, 1994]. The immediate footwall of the SFZ is characterized by a transition from a broad ductile mylonitic zone to a discrete brittle detachment with identical kinematics. The mylonitic zone grades over a distance of 1-2 km into less strongly overprinted units of the Lower Pennine nappes [*Milnes*, 1974]. The brittle detachment or "Simplon Line" (SL) [*Mancktelow*, 1985; *Mancel and Merle*, 1987; *Steck*, 1987] consists of a narrow zone (< 10 m) of cataclasites overprinting the mylonites. In some places (e.g. Zwischbergen valley, Fig. I.3), it is marked by a zone of foliated clay gouge that can be up to a few meters wide. Kinematic indicators from both the ductile and brittle components consistently show a top down to the SW shear sense [*Mancktelow*, 1985, 1987, 1990; *Grosjean et al.,* 2004]. In contrast, older structures are generally well preserved in the hanging wall, showing overprinting relationships between several deformation phases that correspond well in their orientation and style to the four regional phases, *D1* to *D4* [*Milnes et al.,* 1981]. These ductile structures are non-pervasively overprinted by brittle faults. The older regionally developed fold structures and foliations [e.g. *Steck and Hunziker*, 1994; *Grujic and Mancktelow*, 1996; *Maxelon and Mancktelow*, 2005] are also observed in the footwall but are overprinted and transposed close to the detachment by the Simplon shear zone.

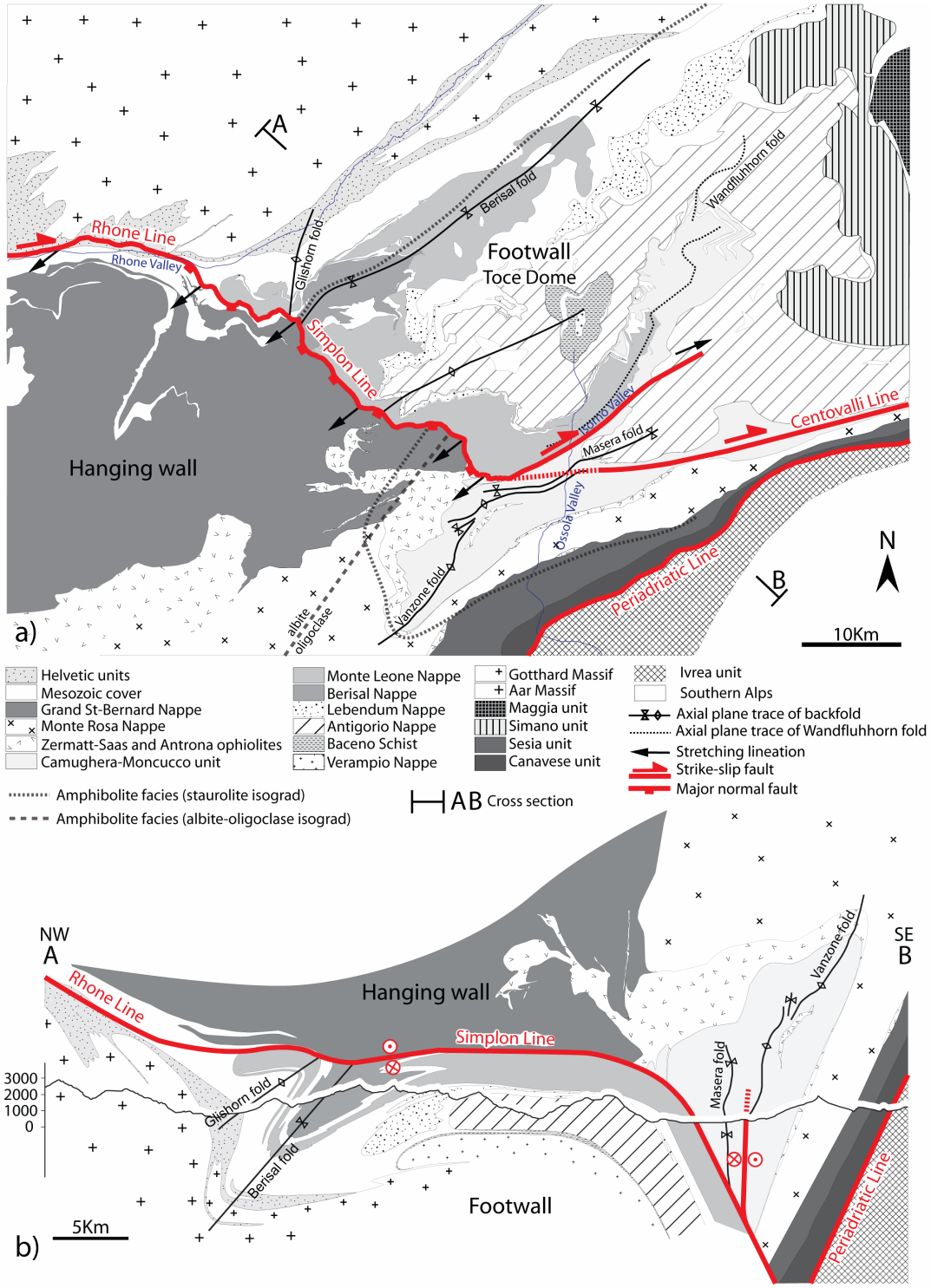

Figure II.1: Geological setting of the Simplon Fault Zone in the Central Alps. a) Geological map summarizing our own field observations and those compiled from the published geological maps of Visp, Brig, Simplon, Domodossola and *Keller et al.* [2005a]. The greenschist/amphibolite facies boundary is drawn based on the staurolite isograd of *Niggli* [1970] to the NE of the Simplon Line, and on the albite-oligoclase isograd [*Bearth*, 1958; *Colombi*, 1989] and the staurolite isograd [*Keller et al.,* 2005b] to the SW of the Simplon Line. b) NW-SE cross section perpendicular to the regional fold axes and stretching lineation and thus perpendicular to the orogen-parallel movement on the SFZ.

II.2.2. Metamorphic history

In the Central Alps, evidence is found in some nappes of an early high- to locally ultra-high pressure Alpine metamorphic event [e.g. *Lardeaux et al.,* 1982; *Chopin and Monié*, 1984; *Heinrich*, 1986; *Reinecke*, 1991]. Subsequent regional overprinting by a Barrovian style of more temperature dominated metamorphism occurs in the Penninic Alps. The associated metamorphic grade increases systematically toward the internal regions, from middle greenschist facies in the NW (Rhone Valley) to middle amphibolite facies in the SE (Ossola Valley) [*Bearth*, 1958; *Niggli and Niggli*, 1965; *Trommsdorff*, 1972; *Wenk and Wenk*, 1984]. In the lower Pennine region (i.e. NE of the SL), the Alpine metamorphism in the Mesozoic cover has been studied in detail by *Frank* [1983]. His geothermo-barometric analysis showed a systematic increase in grade from middle greenschist (400-420°C, 2-3 kbar) to middle amphibolite facies (580-620°C, 6-8 kbar) from the NW to the SE. In the upper Pennine region (SW of the SL), maximum metamorphic conditions attain ca. 620-700°C and 5 kbar in the deepest Camughera-Moncucco unit toward the south [*Keller et al.,* 2005b].

An age of ca. 38 Ma was initially proposed for the peak temperature of the amphibolite facies metamorphism, based on the earliest cooling ages on phengite Rb-Sr from the Monte Rosa and the Mischabel nappes (W of the SL), and from the Suretta nappe (eastern part of the Lepontine Dome) [*Hunziker*, 1969]. Later on, *Vance and O'Nions* [1992] dated the climax of this metamorphism, using U-Pb and Rb-Sr methods on garnet from the Mesozoic cover near the staurolite isograd in the Toce Dome. They obtained an age of ca. 30 Ma, with garnet growth requiring a time interval of 2.9 +/- 1.5 Ma. Further south, close to the Periadriatic Line (Bellinzona) (Fig. II.1), the same authors obtained Sm-Nd ages on garnet of 26.7 +/- 1.7 Ma for the peak of metamorphism. Magmatic intrusions occurring along the Periadriatic Line yield ages between 32 and 25 Ma [e.g. *Hansmann*, 1986; *Dal Piaz et al.,* 1988; *Von Blanckenburg*, 1992; *Romer et al.,* 1996]. Therefore geological and radiometric evidence are more consistent with an age around 30 Ma for the peak of amphibolite facies metamorphism, which probably lasted until ca. 26 Ma further south close to the Periadriatic Line (see review by *Gebauer* [1999]). However, a recent study carried out in the northern part of the Central Alps [*Janots et al.,* 2009], has indicated that near peak amphibolite facies conditions further into the footwall of the Simplon Fault Zone may have continued until ca. 18-19 Ma (SHRIMP U-Th-Pb on monazite and U-rich clinozoisite).

The pattern of isograds and mineral zone boundaries has been extensively described in the literature [e.g. *Trommsdorff*, 1966; *Frey et al.,* 1974; *Steck and Hunziker*, 1994; *Frey and Mahlmann*, 1999]. The SFZ offsets these isograds (Fig. II.1) and a clear jump in metamorphic grade can be observed in the central region around the Simplon village (Fig. I.3), from greenschist facies in the hanging wall to amphibolite facies in the footwall. However, across the prolongation of the SFZ toward the SE and NW, a distinct jump in metamorphic grade can no longer be observed. Ductile shearing in the footwall of the SFZ clearly postdates the peak of metamorphism and was responsible for the exhumation and associated cooling of the footwall [e.g. *Hunziker and Bearth*, 1969; *Mancktelow*, 1985; *Merle et al.,* 1986].

II.2.3. Previous thermochronological and geochronological work

The Central Alps was a very important region for the development of the thermochronological method and it was here that the fundamental concept of a "blocking temperature" for a specific mineral and isotopic system was first introduced [*Jäger*, 1965; *Jäger et al.,* 1967]. This concept was later extended by *Dodson* [1973] to the notion of a "closure temperature", influenced also by the cooling rate.

The pioneering work of Jäger and coworkers [*Jäger*, 1965; *Armstrong et al.,* 1966; *Jäger et al.,* 1967] showed that closure of the K/Ar and Rb-Sr systems on biotite occurred during post-metamorphic cooling, following isotopic resetting during the peak of Alpine metamorphism. Since then, many geochronological studies have been carried out in the Central Alps and a large number of radiometric ages were published: fission-track ages on apatite and zircon, K/Ar and $^{40}Ar/^{39}Ar$ ages on white mica and biotite, and Rb-Sr isotope ages on white mica and biotite [e.g. *Hunziker*, 1969; *Hunziker and Bearth*, 1969; *Purdy and Jäger*, 1976; *Wagner et al.,* 1977; *Frank and Stettler*, 1979; *Deutsch and Steiger*, 1985; *Michalski and Soom*, 1990; *Soom*, 1990]. All these ages have been interpreted as cooling ages.

The work of *Hunziker and Bearth* [1969] was the first to establish a marked change in biotite Rb-Sr ages across the SFZ, indicating a major normal component in the central region, with a younger age (11 Ma) in the footwall compared to the hanging wall (15-22 Ma). Further studies have confirmed this thermochronological jump in cooling ages for a range of minerals and isotopic systems (see synthesis in *Steck and Hunziker*, [1994]). There is a consistent jump between older ages in the hanging wall (from ca. 35 Ma with muscovite Rb-Sr to ca. 5 Ma with apatite fission track) to younger ages in the footwall (from ca. 20 Ma with muscovite Rb-Sr to ca. 3 Ma with apatite fission track). A recent detailed study on biotite $^{40}Ar/^{39}Ar$ cooling ages carried out by *Baxter et al.* [2002] at the contact between metapelite and amphibolite units in the central region of the SFZ, has shown a correlation of excess argon with lithology. These authors suggest that $^{40}Ar/^{39}Ar$ cooling ages should be determined on several samples from each outcrop to avoid errors introduced by local excess argon.

According to *Steck and Hunziker* [1994], the Glishorn and Berisal backfolds in the northern part of the footwall (Fig. II.1) fold the 12 Ma Rb-Sr biotite iso-age and these folds were therefore interpreted to be younger than this age. In turn, the brittle detachment (SL) was considered to be late Miocene because it crosscuts these backfolds. Most recently, in the southern and southeastern continuation of the SFZ across the Ossola valley, *Keller et al.* [2005a] showed that there is no jump recorded in the fission-track ages for zircon and apatite. Instead there is a progressive and gradual decrease in age to the north across the SFZ (from 12 Ma to 5.4 Ma with zircon and from 5.8 Ma to 2.2 Ma with apatite). In the northeastern part, across the Rhone Valley (Fig. II.1), a clear jump in cooling ages is shown by the fission-track ages [*Soom*, 1990; *Seward and Mancktelow*, 1994]. Nevertheless, almost no radiometric ages were previously available between the Rhone Valley and the central region across the SFZ and a continuation of the thermochronological jump into the Rhone Valley was not well established.

Based on the available data, two different models had been proposed for the age of the SFZ. One model proposes the lower Oligocene development of a broad extensional ductile shear zone that is not only restricted to the footwall but also covers a wide zone within the hanging wall [*Merle*, 1987; *Steck and Hunziker*, 1994] (Fig. I.4a,b). The

intrusion age (from zircon U/Pb) of 29 to 26 Ma for syn- to post-kinematic pegmatites within the interpreted prolongation of this major shear zone in the steep zone north of the Periadriatic Line provides a minimum age for this shearing event [*Romer et al.,* 1996]. However, as noted above, the thermochronological jump and crosscutting relationship of the backfolding in the footwall demonstrates Neogene activity on the brittle SL detachment. In this model, the brittle detachment is therefore considered to be a late Miocene structure that captures and exhumes the largely Oligocene "fossil" shear zone. The alternative model considers the current geometry to reflect the more-or-less continuous development during the Miocene of a major low-angle fault zone that evolves from a broad ductile shear zone to a more discrete brittle detachment as the footwall exhumes and cools [*Mancktelow*, 1985, 1990]. In this second model, the ductile shear zone directly related to this fault zone development is restricted to the footwall, with the mylonites present in the hanging wall corresponding to an older (and indeed probably Oligocene) structure.

Based on this more continuous concept, *Grasemann and Mancktelow* [1993] developed a two-dimensional thermal model using published isotopic mineral cooling ages. They concluded that the most active period for the SFZ was between 18 Ma and 15 Ma, but with a continuation until at least 5 Ma. The rapid cooling rate determined from radiometric ages in the footwall was associated with the rapid exhumation of the Lepontine metamorphic Dome. Subsequently, illite from clay-gouge marking the brittle detachment in the Zwischbergen valley (Fig. I.3) has been dated by K/Ar methods at ca. 5-7 Ma [*Zwingmann and Mancktelow*, 2004]. Muscovite from a mesothermal gold vein located in the footwall of the SFZ in the central region was dated using $^{40}Ar/^{39}Ar$ by *Pettke et al.* [1999]. These veins occur in extensional faults and fractures that crosscut the greenschist- to amphibolite metamorphic fabric of the wall rock. The muscovite gives ages of 11.6 +/- 0.1 Ma for veins crosscutting the mylonites of the SFZ and 10.6 +/- 0.3 Ma further east within the core of the Toce Dome. These ages were interpreted as crystallization ages, as they yield younger ages than the metamorphic muscovite in the immediately adjacent host rock. These ages therefore date brittle fracturing occurring between 11.6 and 10.6 Ma. The age range is consistent with the recent work of *Hetherington and Villa* [2007], who dated brittle fracturing and multistage vein-filling in the footwall Berisal unit (Fig. II.1) using $^{40}Ar/^{39}Ar$ on muscovite, with ages ranging from 6-11 Ma.

In summary, it is generally well accepted that the brittle detachment (SL) was active during the late Miocene. However, the absolute age of the broad ductile shear zone in the footwall and the time of transition to brittle deformation has not been unequivocally determined and has remained controversial. The age of mylonitic fabrics older than the Simplon mylonites in footwall and hanging wall is also relevant to this discussion and for distinguishing between the two proposed models. *Markley et al.* [1998] used $^{40}Ar/^{39}Ar$ to date syn-kinematic white mica from a low grade mylonite related by them to emplacement of the Siviez-Mischabel nappe in the hanging wall of the SFZ, at about 41-36 Ma. They noted that fine-grained white micas (20μm) from the hanging wall close to the SL detachment were partially reset at 22 Ma. They suggested that thermal reset was most likely due to increasing temperature caused by footwall exhumation, or to Oligocene magmatic activity in the lower Pennine nappes. *Hetherington and Villa* [2007] obtained $^{40}Ar/^{39}Ar$ ages of around 17 Ma for muscovite defining the main foliation in the

Berisal Unit from the SFZ footwall. They considered this to date the regional (S_2) main foliation [e.g. *Grujic and Mancktelow*, 1996; *Maxelon and Mancktelow*, 2005] and thus to represent a maximum age for the onset of the Simplon shear zone, which overprints and transposes S_2. In the Helvetic nappes north of the Rhone Valley and in the interpreted prolongation of the SFZ footwall, *Kirschner et al.* [2003] also applied $^{40}Ar/^{39}Ar$ and Rb-Sr methods to directly date syn-kinematic white micas related to nappe thrusting and established that activity or reactivation lasted until 25-15 Ma. They proposed that the Rhone (-Simplon) Line (Fig. II.1), which crosscuts the root of the Helvetics nappes (Plammis-Jägerchrüz system), was therefore active at around 17 Ma, which is similar to the 19 Ma age proposed for movement on the same structure by *Markley et al.* [1998].

II.3. Field observations

The SFZ is structurally and geomorphologically well-defined in its central part (region I in Fig. II.2b), with a corresponding marked jump in both metamorphic grade and geochronologic ages. However, its prolongation further to the NW and SE is still controversial. Detailed structural work has been carried out during this study to establish the possible continuation in these regions and to determine how displacement on this major fault zone is either accommodated or transferred. The results of this new work are summarised in Figure II.2.

II.3.1. The SE prolongation of the Simplon Fault Zone (SFZ)

In regions II and III (Fig. II.2b), the SFZ is no longer obvious. Clear structural and geomorphological evidence is missing, the foliation strike is effectively parallel in the footwall and hanging wall, there is no significant jump in metamorphic grade and apatite and zircon fission-track ages obtained across this section do not show any significant jump in central ages [*Keller et al.,* 2005a]. As a result, a continuation of the SFZ in the SE region was still controversial and different models have been proposed: 1) a continuation of the brittle SL into the E-W striking Centovalli Line (Fig. I.6a), where clear brittle deformation was described [*Bearth*, 1956b; *Schmid and Kissling*, 2000]; 2) a continuation of the SFZ (both ductile shearing and the brittle detachment) along Val Bognanco and across the Val d'Ossola into Val d'Isorno toward the NE and into the Toce Dome (Fig. I.6b) [*Mancktelow*, 1990, 1992]; 3) no prolongation at all of the SFZ in the SE region but rather an accommodation by backfolding (Masera and Vanzone folds) associated with anticlockwise rotation of the hanging wall (Fig. I.6d) [*Keller et al.,* 2006]. The footwall in the SE region (i.e. regions II and III, Fig. II.2b) is characterized by an abrupt swing of the foliation strike into an E-W orientation (region II) and then into a WSW-ENE orientation (region III), where the foliation dips steeply to the SSE (ca. 60-65° toward 155°) (Fig. II.2c) and forms part of the Southern Steep Belt [*Milnes*, 1974] (Fig. II.3a). On the foliation plane, the stretching lineation plunges W in region II and ENE in region III (Fig. II.2c), with a broad transition where the lineation is close to horizontal. This gradual change in plunge of the stretching lineation defines an overall domal shape [*Mancktelow*, 1985]. Obvious shear criteria indicating a dextral sense are well developed in these mylonites, for example sheared and boudinaged quartz veins

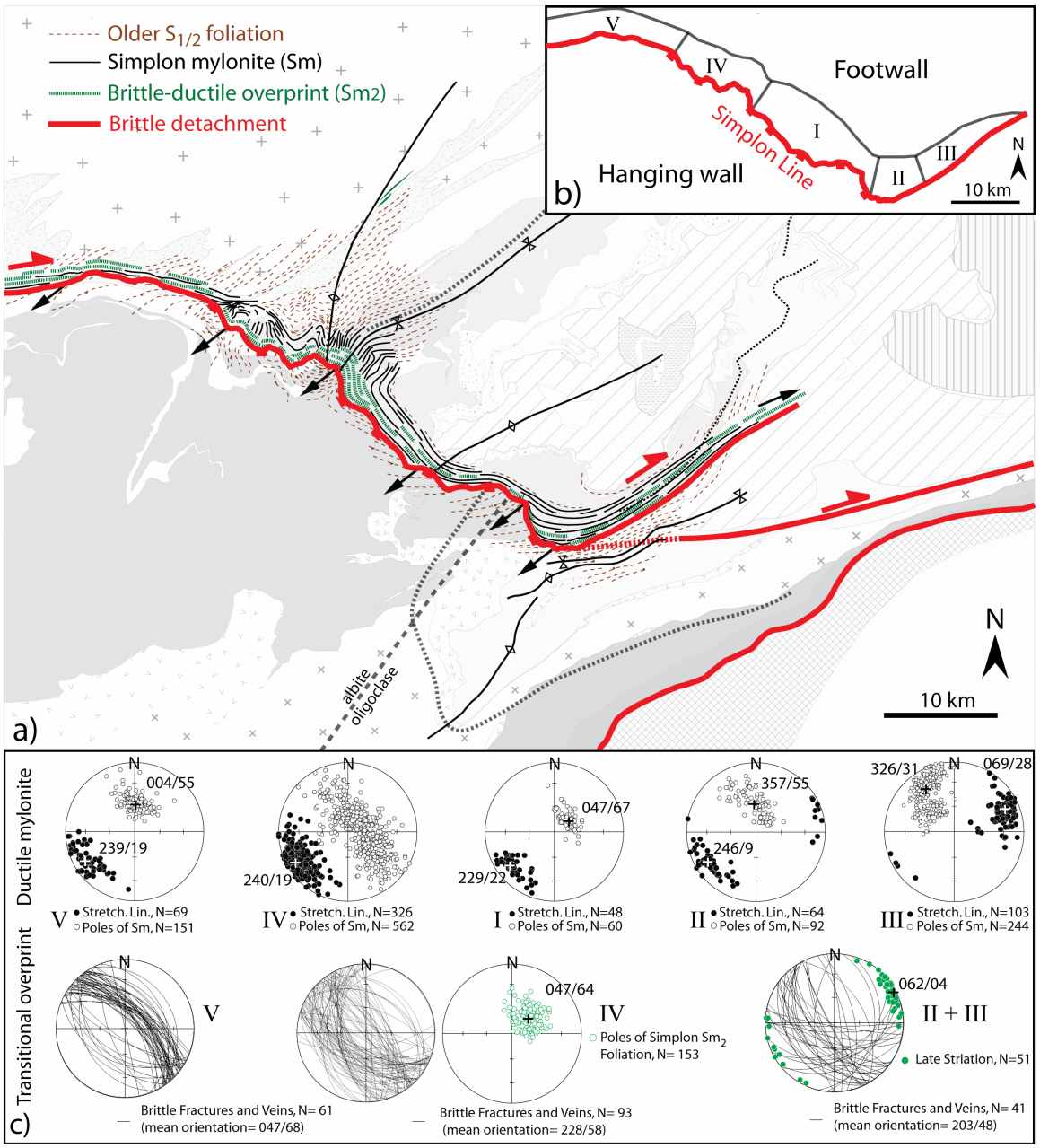

Figure II.2: a) Structural map of the Simplon Fault Zone; the legend is given in Fig. II.1. b) Subdivision into geographical regions I to V. c) Stereoplots of field measurements from the different regions; lower hemisphere, equal area projection, mean values for lineation and pole to foliation.

rotated into the foliation plane (Fig. II.3b) and shear band or C' structures [*Berthé et al.*, 1979] (Fig. II.3c).

The penetrative mylonitic overprint in the footwall here is only 100-200 m wide (Fig. II.3a). It is transitional to the north, where earlier S_2 schistosity is overprinted and transposed into the Simplon mylonitic foliation. Earlier folds are also overprinted and their axes and related intersection lineation rotated into parallelism with the Simplon stretching lineation. As first clearly established in the current study, the zone of Simplon

mylonites also crosscuts on a map scale the SE limb of the Wandfluhorn fold (Fig. II.2a), which was interpreted by *Maxelon and Mancktelow* [2005] to be a regional F2 structure. Therefore in this region, the fabrics S_2 and Sm are clearly distinct (Fig. II.2a) and cannot correspond to the same structural event. Further to the NE (near Lago di Larecchio in Fig. I.3), the penetrative mylonitic overprint progressively diminishes and the dextral shearing eventually can no longer be distinguished. In this region, there is no evidence for a continuation of the penetrative Simplon mylonites.
In region III, quartz-calcite-white mica-rich veins can be found in a range of different lithologies (Fig. II.3d). These veins vary in their geometry relative to the mylonitic foliation (Fig. II.3d,e,f,g,h). Some veins are little deformed (Fig. II.3d) and are oriented perpendicular to the stretching lineation and at a high angle to the foliation (Fig. II.3g). Such veins either have an oblique Riedel shear geometry, consistent with bulk dextral shear, or an extensional geometry related to foliation boudinage [e.g. *Lacassin*, 1988]. Others make a smaller angle to the foliation and show evidence of flanking structure development related to dextral rotation (Fig. II.3e), whereas some are more strongly sheared (in a dextral sense), boudinaged, and now effectively parallel to the foliation (Fig. II.3f). We interpret these structures as an expression of the ductile-brittle transition in this region, with the progressive development of fractures (veins) during continued dextral shearing (Fig. II.3h). Subsequent fully brittle deformation is seen as localized cataclasite zones (Fig. II.3i) and discrete brittle fractures with a clear dextral strike slip sense (Fig. II.3j). Chloritic alteration on the foliation planes is also observed (Fig. II.3k), with a nearly horizontal striation plunging 0-6° toward 060° (Fig. II.2c). Chloritic slickenfibers related to this alteration consistently show steps indicating brittle purely dextral strike-slip motion. In the NE of region III (near Lago di Larecchio Fig. I.3), the ductile dextral shearing diminishes and is replaced by a more dominant late brittle overprint. The domal shape described by the opposing plunges of the stretching lineation in the ductile mylonite is not seen in the latest brittle history, and the brittle striation is always nearly horizontal. This implies that the regional up-doming had effectively ceased before this late brittle overprint.

In the hanging wall of regions II and III, the main fabric dips shallower to the SE (Fig. II.3a). It is crosscut by the SFZ as is demonstrated in chapter IV using 3D field geometric model. In the hanging wall an open synform (Masera synform) and a tighter antiform (Vanzone antiform) are mapped on both sides of the Ossola Valley (Chapter IV). They fold the main foliation. The vertical brittle Centrovalli Line crosscuts the Vanzone antiform hinge. However, the horizontal displacement involved cannot be greater than a few hundred meters because the hinges of the Masera and the Vanzone do not show any major offset across the Centrovalli Line (Fig. II.2a). No obvious penetrative ductile shear is observed in the vicinity of the SFZ. However, further south, the southern limb of the Vanzone shows a strong dextral shearing (i.e. in the river bed of Villadossola).

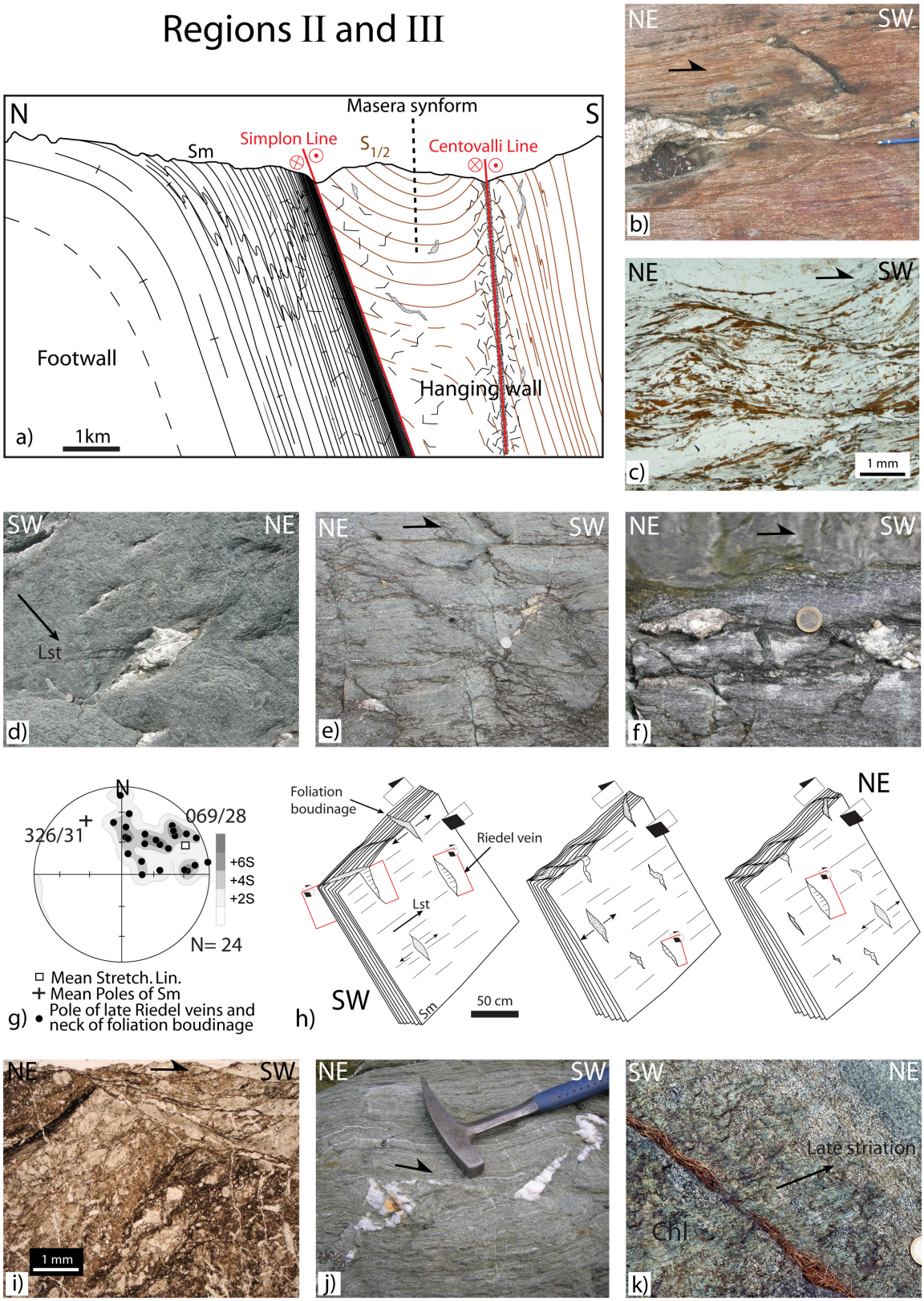
Regions II and III
N
S
Masera synform
Simplon Line
Centovalli Line
Sm
$S_{1/2}$
Footwall
Hanging wall
a)
1km
NE
SW
b)
c)
1 mm
Lst
d)
e)
f)
N
069/28
326/31
+6S
+4S
+2S
N= 24
Mean Stretch. Lin.
Mean Poles of Sm
Pole of late Riedel veins and neck of foliation boudinage
g)
Foliation boudinage
Riedel vein
Lst
Sm
50 cm
h)
i)
j)
Late striation
Chl
k)

Figure II.3, preceding page: Field observations from the SE regions II and III. a) Synthetic NS cross section through region III b) Boudinaged quartz vein affected by dextral shearing in the Simplon mylonites, region III (668371/112282). c) Shear band top-to-SW, region III (673370/116405). d) Quartz-muscovite-calcite rich veins formed in the necks of foliation boudinage within the Simplon mylonites, region III (671041/113156). e) Vein with flanking structure development related to dextral rotation, region III (671100/113274). f) Deformed vein sheared, boudinaged, and now effectively parallel to Sm, region III (671103/113241). g) Stereoplot of undeformed vein orientations; lower hemisphere, equal area projection, region III. h) Synthetic sketch summarizing the interpreted development of the quartz-muscovite-calcite rich veins during ongoing shearing, region III. i) Dextral cataclasite, region II (661998/108032). j) Brittle dextral strike slip fracture, region II (661997/108029). k) Late chlorite overprint with horizontal striation, region III (676332 /117670).

II.3.2. NW section Gibidum-Visp-Rhone Valley

In the Rhone Valley (region V, Fig. II.2b), the moderately to steeply SE-dipping "roots" of the Helvetic nappes are crosscut by a dextral shear zone with identical kinematics to the SFZ [*Steck*, 1984; *Burkhard*, 1988]. These previous studies proposed a connection of the Simplon Line (SL) with the Rhone Line, with the composite structure referred to as the Rhone-Simplon Line. However, in the intervening region IV there is no longer a clear structural discontinuity between footwall and hanging wall and the metamorphic grade to either side is similar. Thermochronological ages that could help constrain the location of SL continuation were also generally lacking.

Region IV presents a complex 3D geometry largely described in Chapter IV. The Simplon mylonites, Sm, are folded by the Glishorn and Berisal backfolds [*Steck*, 1984; *Mancktelow*, 1990, 1992] (Fig. II.2a). In region IV and V, the stretching lineation invariably effectively plunges 20° toward 240° (Fig. II.2c). The brittle fault (Fig. II.4a,b) crosscuts the folded mylonitic foliation, Sm. A narrow band of greenschist facies mylonites (with foliation Sm2), of ca. 100 m width, is concordant with the brittle detachment (Fig. II.4a,b), and transects the main folded foliation Sm (Fig. II.4c) [*Mancktelow*, 1992; *Mancktelow and Pavlis*, 1994].

In region IV, the ductile-to-brittle and brittle overprint is equally widespread within both footwall and hanging wall. Ductile-brittle shear bands with top-to-SW sense of shear are observed within both the footwall and the hanging wall (Fig. II.4d). A strong subsequent brittle overprint, with cataclasite, gouge and discrete fractures carrying slickenfibers of calcite also give a sense of displacement top-to-SW (Fig. II.4e,f).

The deformation clearly appears to be less localized than in the regions I, II and III (compare synthetic sections in Fig. II.3a and II.4a). This probably reflects different structural levels of the hanging wall along the SFZ, with region IV representing an upper structural level.

In the Rhone Valley (region V), orthogneisses of the Aar massif and its Mesozoic cover are overprinted by a 1-1.5 km wide zone of foliated phyllonites (Fig. II.4g). Obvious kinematic indicators (Fig. II.4h) show a strong dextral component to the shearing, with a stretching lineation plunging 20° toward 240° (Fig. II.2c, II.4i). In these phyllonites, fluid infiltration has been important and pervasive, as shown both by the transformation of feldspar to white mica on the grain scale and the ubiquitous presence of calcite-rich veins and sparsely distributed calcite and pyrite within the phyllonitized orthogneissic host rock. Further NE in the Rhone Valley (between Brig and Mörel Fig. I.3), a similar phyllonite developed from the Aar massif is locally observed (Fig. II.2a).

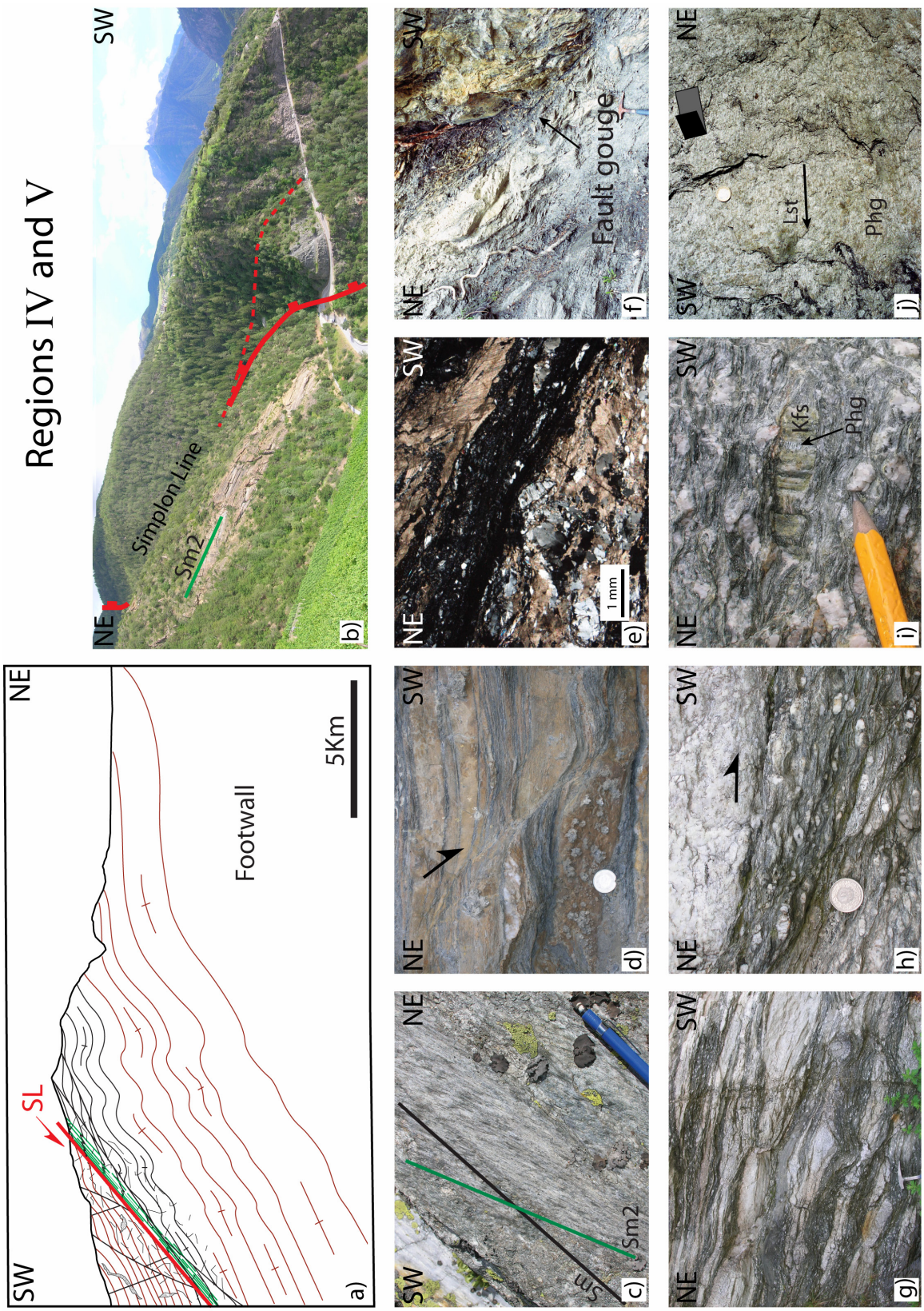
Regions IV and V
SW
NE
SL
Footwall
5Km
a)
NE
SW
Simplon Line
Sm2
b)
SW
NE
Fault gouge
f)
SW
NE
1 mm
e)
SW
NE
Kfs
Phg
i)
NE
SW
Lst
Phg
j)
NE
SW
d)
SW
NE
Sm
Sm2
c)
SW
NE
h)
NE
SW
g)

Figure II.4, preceding page: Field observations from the NW region (region V). a) Synthetic SW/NE cross section through region IV. b) SE view of the Simplon detachment in region IV (near Stalden) taken from position 634813/125484 c) Greenschist facies mylonite (Sm2) transecting the ductile Simplon mylonites (Sm), region IV (644271/121281). d) Ductile-brittle shear band with sense of shear top to the SW, region IV (630943/127014). e) Cataclasite with top-to-SW displacement, region IV (635110/125271). f) Fault gouge with top-to-SW displacement, region IV (634954/125166). g) Boudinaged foliated phyllonite developed from orthogneiss of the Aar massif, region V (633223/128447). h) Foliated phyllonite with top-to-SW shear band development, region V (633223/128447). i) Stretched feldspar porphyroclast with syn-kinematic fibrous phengite, region V (634791/129330). j) Fibrous steps indicating a dextral sense of shear (645269/132770).

Congruous brittle steps related to a horizontal lineation indicate a dextral sense of shear (Fig. II.4j). However, these structures could not be followed as a single major dextral zone of deformation further to the NE along the Rhone Valley.
As discussed above and summarised in Figure II.2, this study has established a continuation of the SFZ toward the SE in the Isorno Valley (Fig. I.3), but with decreasing overprint and displacement. A continuation of the SFZ toward the NW in the Rhone Valley is also established. However, no clear dextral deformation could be mapped further to the NE in the Rhone Valley toward the Grimsel Pass, except locally as small ductile-to-brittle dextral shear zones (Fig. II.2a). This confirms that movement on the SFZ is indeed transferred to the Rhone Line within the Rhone Valley west of Visp (Fig. I.3).

From the SE to the NW, deformation associated with the SFZ becomes less localized. Metamorphic grade also decreases to the NW (Fig. II.2a) and we interpret this as reflecting different structural levels of the detachment. Over the whole strike length of the fault zone, ductile and brittle deformation are clearly structurally interrelated, with an apparently continuous transition from ductile, to mixed brittle-ductile, to brittle behavior, while maintaining identical kinematics. Stretching lineations and striations have the same orientation, with a constant SW-NE extension direction throughout. The only exception in detail is in the SE, where the earlier ductile and brittle-ductile stretching direction outlines a broad dome, whereas the later striae maintain a relatively constant and near horizontal direction. This implies that the latest brittle dextral strike-slip movements occurred after the development of the broad Toce domal culmination in the footwall of the SFZ.

II.4. Methods and sample description

Figure II.5 shows all sample locations on the geological map, with the corresponding Swiss topographic map grid coordinates listed in Table II.1.

II.4.1. Fission-track analysis: apatite and zircon

19 samples from both the footwall and hanging wall along different sections across the fault zone were analyzed. 17 are from the NW section of the SFZ (region IV, Fig. II.5) and two from the SE (region II, Fig. II.5). Details of separation methods and analysis techniques are given in Appendix A. Because of the extremely low uranium content of most of the apatite, not all apatite samples could be analyzed and track length could not be statically measured. Most of the results from this study are therefore zircon fission-track ages.

II.4.2. $^{40}Ar/^{39}Ar$ analysis: white mica and biotite

In the footwall, a first set of samples was collected with increasing perpendicular distance from the detachment (SL), covering the transition from mylonitic rocks that were strongly affected by the Simplon shearing into the footwall protolith with little or no discernible overprint. A second set of samples was also taken parallel to the SFZ, and reflect the increase in metamorphic grade from greenschist facies in the NW (Rhone Valley) to amphibolite facies in the SE (Ossola Valley). A similar sampling approach was also used in the hanging wall, where rocks are non-pervasively overprinted by the SFZ. In total 22 samples were collected.

White mica and biotite from the matrix represented either deformed porphyroclasts separated from mylonites related to the Simplon shearing (MC111, MC287, MC288, MC289, MC302 and MC499) or annealed micas related to the older $S_{1/2}$ fabric (MC283, MC286 MC290, MC292, MC366, MC506 and MC516). In 5 others samples, large flakes of white mica were separated from foliation boudinage veins (MC22, MC36, MC276, MC291, MC346). In samples MC420, MC422, MC423 and MC430, thin aggregates of syn-kinematic newly grown white mica could be differentiated from bigger mica porphyroclasts and isolated under the binocular microscope. Methods of separation and analysis are summarized in Appendix A.

II.4.3. Rb-Sr microsampling analysis

A micro-sampling technique using rock thick sections was used [*Müller et al.,* 2000a, b], allowing Rb-Sr dating of syn-kinematic mineral growth with direct microstructural control on the relationship to the Simplon deformation. Micro-sampling was carried out on samples from the necks of foliation boudinage and on fibers growing between stretched porphyroclast related to the Simplon stretching direction (Fig. II.2c).

In three foliation boudinage samples from region III (Fig. II.3d), cogenetic single syn-kinematic white micas and calcite could be separated in direct textural contact, thus ensuring isotopic equilibrium (Fig. II.6a samples MC492, MC494, MC497). Sample MC472 from region V consists of three adjacent microsamples of syn-kinematic fibrous white mica and/or quartz-feldspar-chlorite grown between one stretched feldspar porphyroclast within a phyllonite of the Aar massif (Fig. II.6b). Microsampling and analysis methods are described in Appendix A.

	Metamorphic grade	Deformation Phase	Sample	Location	Elevation (m)	Unit	Type	Mica structure	Method
Footwall	Low-grade	Sm mylonite	MC36	633142/128177	656	Aar Massif	Phyllonite	Thin syn-kinematic Phg in Sm	$^{40}Ar/^{39}Ar$
			MC420	633077/128267	670	Aar Massif	Phyllonite	Syn-kinematic Phg in Sm and deformed Bt Porphyr.	$^{40}Ar/^{39}Ar$
			MC422	632908/128354	661	Aar Massif	Phyllonite	Thin syn-kinematic Phg in Sm	$^{40}Ar/^{39}Ar$
			MC423	633131/128697	658	Helvetic	Phyllonite	Thin syn-kinematic Phg in Sm	$^{40}Ar/^{39}Ar$
			MC472	638903/123565	1072	Aar Massif	Phyllonite	Thin Phg fiber between stretched Kfs	Rb-Sr
			MCS12	634585/125889	756	Mesozoic cover	Calc-schist	-	Fission track
			MC32	641861/123175	2603	Monte Leone	Orthogneiss	-	Fission track
			MC33	641877/123039	2606	Monte Leone	Orthogneiss	-	Fission track
			MC269	635324/125316	1029	Mesozoic cover	Sandstone	-	Fission track
			MC475	638903/123565	2273	Monte Leone	Orthogneiss	-	Fission track
		localized shear zone	MC430	645220/132778	670	Aar Massif	Phyllonite	Large undeformed Phg porphyroclasts and thin syn-kinematic Phg in matrix	$^{40}Ar/^{39}Ar$
		S1/2	MC335	640487/127471	1181	Mesozoic cover	Quartzite	-	Fission track
			MC482	637778/127174	830	Mesozoic cover	Quartzite	-	Fission track
	Medium - grade	Sm mylonite	MC302	647034/122940	1960	Berisal	Micashist	Deformed mica phorphyroclasts in Sm	$^{40}Ar/^{39}Ar$
			MCS3	646249/118442	1641	Monte Leone	Orthogneiss	-	Fission track
	High-grade	Sm mylonite	MC287	652595/112713	1406	Monte Leone	Orthogneiss	Deformed mica phorphyroclasts in Sm	$^{40}Ar/^{39}Ar$
			MC288	652728/113378	1277	Mesozoic cover	Calcschist	Deformed mica phorphyroclasts in Sm	$^{40}Ar/^{39}Ar$
			MC500	659449/108512	852	Monte Leone	Fine grained orthogneiss	-	Fission track
			MC289	660891/108102	655	Monte Leone	Fine grained orthogneiss	Deformed mica phorphyroclasts in Sm	$^{40}Ar/^{39}Ar$
			MC111	668515/111408	422	Monte Leone	Fine grained orthogneiss	Deformed mica phorphyroclasts in Sm	$^{40}Ar/^{39}Ar$
			MC499	671101/113266	710	Monte Leone	Fine grained orthogneiss	Deformed mica phorphyroclasts in Sm	$^{40}Ar/^{39}Ar$
			MC22	668302/111332	397	Monte Leone	Vein	Undeformed Ms in late neck of foliation boudinage	$^{40}Ar/^{39}Ar$
			MC276	666833/112119	419	Monte Leone	Vein	Undeformed Ms in late neck of foliation boudinage	$^{40}Ar/^{39}Ar$
			MC346	674157/119606	1406	Monte Leone	Vein	Undeformed Ms in late neck of foliation boudinage	$^{40}Ar/^{39}Ar$
			MC492	-	-	Monte Leone	Vein	Undeformed Ms in late neck of foliation boudinage	Rb/Sr
			MC494	671080/113234	692	Monte Leone	Vein	Undeformed Ms in late neck of foliation boudinage	Rb-Sr + Oxygen-Isotope
			MC497	-	-	Monte Leone	Vein	Undeformed Ms in late Riedel vein	Rb-Sr + Oxygen-Isotope
			MC498	-	-	Monte Leone	Vein	Undeformed Ms in late Riedel vein	Oxygen-Isotope
			MC291	671100/113274	710	Monte Leone	Vein	Deformed Ms in flanking structure	$^{40}Ar/^{39}Ar$
		S1/2	MC366	667203/119928	693	Baceno schist	Metapelite	Annealed mica in S1/S2	$^{40}Ar/^{39}Ar$
Hanging wall	Low-grade	S1/2	MC480	633106/126381	1152	Mesozoic Cover	Quartzite	-	Fission track
			MC481	634746/124983	902	Grand St Bernard	Paragneiss	-	Fission track
			MCS8	633787/122299	703	Mesozoic cover	Calc-schist	-	Fission track
			MC476	638814/123323	2224	Mesozoic cover	Quartzite	-	Fission track
			MC477	638758/122551	2204	Grand St Bernard	Paragneiss	-	Fission track
			MC519	641933/122507	2579	Mesozoic cover	Quartzite	-	Fission track
			MC520	642035/122277	2608	Grand St Bernard	Paragneiss	-	Fission track
			MC282	642919/122156	2357	Mesozoic cover	Quartzite	-	Fission track
			MC283	642976/122003	2357	Grand St Bernard	Paragneiss	Crenulated Ms in S1 and annealed Ms in S2	$^{40}Ar/^{39}Ar$ + Fission track
			MC286	652720/112592	1480	Grand St Bernard	Paragneiss	Annealed mica in S1/S2	$^{40}Ar/^{39}Ar$
			MC501	659008/108149	868	Camugn.-Monc.	Orthogneiss	-	Fission track
	Medium-grade	S1/2	MC290	662971/108054	504	Camug.-Monc.	Paragneiss	Annealed mica in S1/S2	$^{40}Ar/^{39}Ar$
	High-grade	S1/2	MC292	671063/113076	544	Camug.-Monc.	Paragneiss	Annealed in S1/S2	$^{40}Ar/^{39}Ar$
			MC506	668781/109542	310	Camug.-Monc.	Paragneiss	Annealed in S1/S2	$^{40}Ar/^{39}Ar$
			MC516	669466/111221	631	Camug.-Monc.	Paragneiss	Annealed in S1/S2	$^{40}Ar/^{39}Ar$

Table II.1: Sample descriptions and locations; abbreviations are taken from *Kretz* [1983].

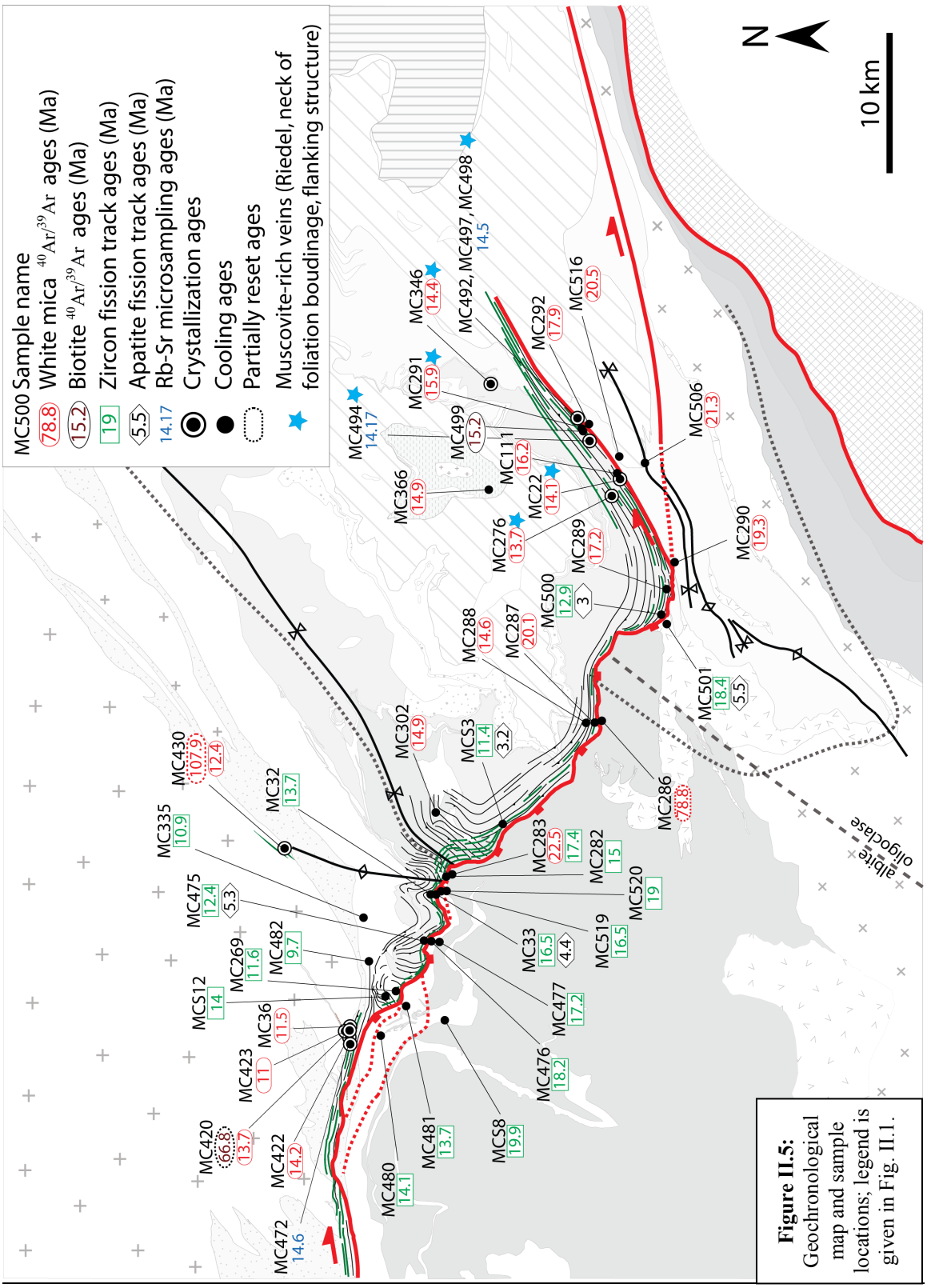

Figure II.5: Geochronological map and sample locations; legend is given in Fig. II.1.

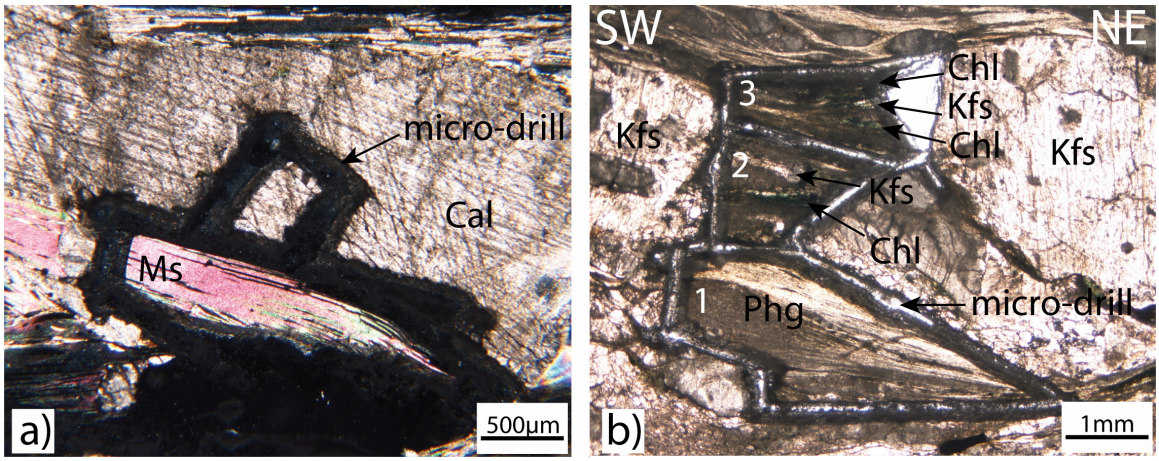

Figure II.6: Rb-Sr micro-sampling methodology. a) Micro-sampling of muscovite and calcite in textural contact from a vein in the neck of a foliation boudinage (MC492), region III. b) Micro-sampling of syn-kinematic fibrous phengite in a stretched and fractured feldspar porphyroclast (MC472), region V.

II.4.4. Oxygen- Isotope Thermometry

Stable isotope-based thermometry is based on the temperature dependent isotope fractionation between two coexisting minerals, which for the case of oxygen is generally reported as:

$$(1) \qquad 1000 \ln\alpha = \Delta_{1\text{-}2} = \delta^{18}O_1 - \delta^{18}O_2 = A\,(10^6 T^{-2}) + B$$

Where T is the absolute temperature, and A and B are calibrated coefficients. Here we use A = 3.34; B = -3.31 for the quartz-water system [*Matsuhisa et al.,* 1979] and A = 2.38; B = -3.89 for the muscovite-water system [*Friedman and O'Neil*, 1977].

Three calcite-quartz-white mica rich veins (MC494, MC497, and MC498) were chosen to analyse the stable isotopes of oxygen on coeval pairs of quartz and white mica. Further details of the method are given in Appendix A.

II.4.5. Petrological and chemical description of samples used for $^{40}Ar/^{39}Ar$, Rb-Sr and oxygen isotope analysis

Table II.1 gives a summarized structural description of the samples. All micas were first analyzed by electron probe microanalysis and the average compositions are given in Table II.2 (2 sigma errors indicate the variability in composition observed within one sample).

Samples MC302, MC287, MC288, MC289, MC111 and MC499 are typical of the middle- to high-grade Simplon mylonites in the footwall. All these samples have deformed porphyroclasts of mica defining the foliation plane and show shear bands with a sense of shear top to the SW (Fig. II.7a). White mica often forms mica fish (Fig. II.7b). Mica flakes can be quite large, with a diameter on average of ca. 400 µm to 1mm.

The sample MC366 (coming further east from the core of the Toce Dome) and samples MC286, MC290, MC292, MC506 and MC516 (from the hanging wall) do not show any overprint from the Simplon shear zone. Micas, with a diameter of ca. 200 µm to 1 mm (Fig. II.7c,d), define the old foliation plane $S_{1/2}$ and are interlayered with recrystallized quartz and plagioclase grains. Micas are annealed showing little internal deformation, and

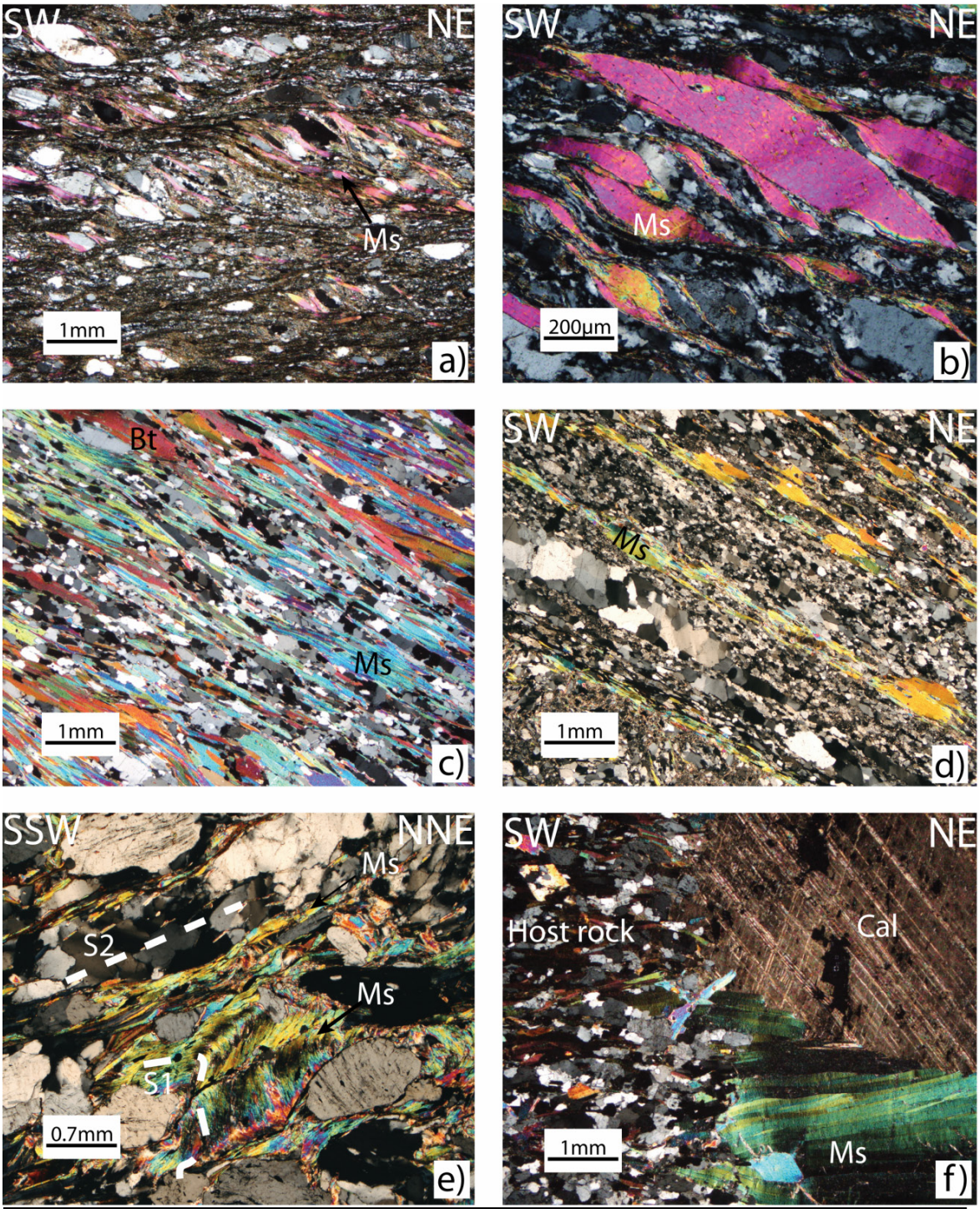

Figure II.7: Sample description. a) High-grade Simplon mylonites from region II with deformed porphyroclasts of white mica affected by shear bands with a clear sense of shear top-to-SW (MC287). b) Mica fish within the Simplon mylonites from the region II; note the undulose extinction within the mica (MC287). c) Undeformed annealed micas from a sample not affected by the Simplon shearing (MC366), within the Toce Dome. d) Undeformed annealed micas from a sample not affected by the Simplon shearing (MC286), from the hanging wall. e) Two generations of white mica (MC283), from the hanging wall. f) Boudinage of foliation within the Simplon high-grade mylonite (MC492), region III.

are clearly not markedly affected by shearing associated with the SFZ. Sample MC283 from the greenschist facies region of the hanging wall shows 2 schistosities marked by aligned white micas (Fig. II.7e). The S_1 schistosity is crenulated, with folded and kinked white micas, whereas the second schistosity S_2 defines the crenulation cleavage with new undeformed white micas growing in the axial plane. Both generations have similar diameter of i.e. 400-500 µm (Fig. II.7e). It was not possible to separate these 2 generations of micas and therefore the single micas analyzed in $^{40}Ar/^{39}Ar$ could represent either S_1 or S_2. These two phases of deformation are in any case older than the Simplon shearing.

Sample	Average	SiO_2		TiO_2		Cr_2O_3		Al_2O_3		FeO		MnO		MgO		CaO		Na_2O		K_2O		Total	
White mica			2σ		2σ		2σ		2σ		2σ		2σ		2σ		2σ		2σ		2σ		2σ
MC287	n=40	48.07	0.39	0.87	0.24	0.02	0.02	29.85	0.56	5.00	0.39	0.03	0.01	1.81	0.21	-	-	0.19	0.04	10.69	0.14	96.53	0.49
MC288	n=39	46.67	0.50	0.67	0.17	0.03	0.04	33.85	0.49	0.95	0.12	-	-	1.63	0.23	0.02	0.03	0.45	0.06	10.40	0.12	94.68	0.67
MC289	n=29	47.04	0.38	1.44	0.35	0.02	0.02	29.76	0.50	5.27	0.20	0.03	0.01	1.68	0.16	0.01	0.01	0.19	0.04	9.81	0.17	95.26	0.44
MC111	n=33	45.59	0.55	0.37	0.06	0.01	0.01	29.70	0.67	5.29	0.14	0.05	0.02	1.24	0.21	-	-	0.27	0.03	10.71	0.11	93.23	0.28
MC366	n=12	46.40	0.21	0.40	0.14	0.01	0.01	35.70	0.60	1.93	0.16	0.01	0.01	0.75	0.15	0.01	0.01	1.01	0.06	9.31	0.17	95.53	0.48
MC292	n=20	46.40	0.19	0.68	0.14	0.04	0.03	35.15	0.35	1.01	0.09	0.01	0.01	0.66	0.07	0.01	0.01	1.07	0.06	9.27	0.07	94.30	0.20
MC506	n=49	46.25	0.24	0.66	0.08	0.02	0.01	34.23	0.26	1.17	0.09	0.01	0.01	0.76	0.05	0.01	0.01	1.20	0.03	9.34	0.07	93.63	0.42
MC516	n=32	46.17	0.24	0.20	0.04	0.01	0.01	34.45	0.36	0.20	0.02	-	-	1.33	0.13	-	-	1.21	0.08	9.52	0.10	93.10	0.35
MC302	n=73	46.68	0.57	0.31	0.05	0.02	0.02	33.51	1.07	1.93	0.21	0.01	0.01	0.87	0.24	0.01	0.01	1.43	0.26	8.61	0.34	93.37	1.07
MC290	n=29	48.07	0.48	0.37	0.04	0.01	0.01	33.02	0.53	3.89	0.25	0.05	0.02	0.53	0.08	-	-	0.34	0.07	10.49	0.14	96.77	0.34
MC283	n=17	48.10	1.32	0.29	0.06	0.03	0.02	32.02	2.18	2.86	0.50	0.02	0.01	1.58	0.55	0.01	0.02	0.40	0.17	9.88	0.33	95.17	0.44
MC286	n=39	48.45	1.15	0.69	0.26	0.03	0.03	33.02	1.72	1.98	0.29	0.02	0.01	1.57	0.46	-	-	0.40	0.10	10.04	0.27	96.19	0.51
MC22	n=13	46.36	0.35	0.70	0.10	0.02	0.02	29.33	0.31	5.33	0.19	0.03	0.02	2.12	0.18	-	-	0.23	0.02	10.68	0.05	94.79	0.30
MC492	n=52	45.50	0.47	0.76	0.08	0.01	0.02	28.71	0.29	4.88	0.19	0.02	0.01	2.11	0.18	0.01	0.01	0.25	0.03	10.80	0.09	93.06	0.63
MC494	n=57	44.64	0.43	0.73	0.06	0.01	0.02	28.46	0.26	4.85	0.20	0.02	0.02	2.17	0.19	0.01	0.01	0.25	0.02	10.82	0.07	91.97	0.47
MC36	n=17	49.72	0.51	0.11	0.02	0.01	0.01	27.52	0.28	3.21	0.20	0.05	0.02	3.24	0.11	0.02	0.02	0.10	0.02	10.74	0.12	94.71	0.65
MC420	n=43	49.69	0.87	0.13	0.07	0.02	0.03	26.57	0.89	2.74	0.30	0.03	0.01	3.35	0.35	0.02	0.02	0.09	0.03	10.78	0.09	93.43	0.24
MC422	n=60	48.39	0.50	0.18	0.06	0.01	0.01	26.25	0.45	3.50	0.20	0.04	0.01	3.35	0.16	0.02	0.02	0.09	0.02	10.81	0.20	92.64	0.52
MC430	n=61	47.95	0.54	0.31	0.10	0.01	0.02	24.42	0.27	5.71	0.17	0.04	0.01	3.36	0.15	-	-	0.14	0.02	10.86	0.09	92.80	0.48
porphyroclast	n=28	47.94	0.35	0.33	0.09	0.01	0.01	24.60	0.28	5.91	0.15	0.04	0.02	3.28	0.13	-	-	0.13	0.03	10.90	0.10	93.14	0.30
MC423	n=42	46.82	0.77	0.35	0.05	0.02	0.01	32.67	0.53	1.54	0.55	-	-	1.62	0.40	0.01	0.02	0.22	0.01	10.44	0.33	93.70	0.81
Biotite																							
MC420	n=16	38.09	0.36	1.50	0.50	0.11	0.04	15.42	0.22	16.02	0.67	0.20	0.03	13.07	0.59	0.03	0.02	0.03	0.01	9.67	0.08	94.13	0.29
MC499	n=40	37.24	0.16	2.40	0.18	0.02	0.02	16.88	0.22	16.21	0.35	0.30	0.02	12.32	0.22	0.01	0.02	0.07	0.01	9.81	0.10	95.26	0.33

Table II.2: Representative mica compositions

For all these samples, white micas have muscovite compositions [*Rieder et al.,* 1998] (Table II.2). In the high-grade region, single muscovite from both footwall and hanging wall are not zoned in major elements and the Tschermak substitution [*Guidotti*, 1973] in each sample is quite small (Fig. II.8a) with a relatively homogeneous composition (MC366, MC287, MC288, MC289, MC111, MC292, MC506 and MC516). In contrast, closer to the greenschist facies region, the Tschermak substitution is more important (MC302, MC290, Fig. II.8b), and muscovites are slightly zoned in major elements. In the greenschist facies region of the hanging wall, muscovites show a clear zonation in major elements (MC283 and MC286), and the Tschermak substitution is strongly developed (Fig. II.8b). In the greenschist facies region, muscovites are therefore not homogeneous within one sample or even within one single grain (Fig. II.8b).

Samples MC22, MC276, MC291, MC346, MC492, MC494, MC497 and MC498 come from quartz-calcite-white mica-rich veins in region III, within the high-grade mylonitic (Sm) Monte Leone orthogneiss of the footwall (Fig. II.5). MC22, MC276, MC346, MC492 and MC494 are undeformed veins forming the necks of foliation boudinage. In thin section, the quartz and white mica show only slight undulose extinction (Fig. II.7f) and are otherwise undeformed. The vein MC291 is deformed and rotated in a dextral

sense toward the foliation as a flanking structure. MC497 and MC498 are veins with Riedel fault orientations coming from boulders of the Monte Leone unit, found in the Isorno river (region III). Their relation to the foliation and stretching lineation is identical to that in the immediately adjacent outcrops. In all these veins, calcite (≥ 1mm), quartz and white mica (> 1mm) are in textural equilibrium (Fig. II.7f). Similar muscovite

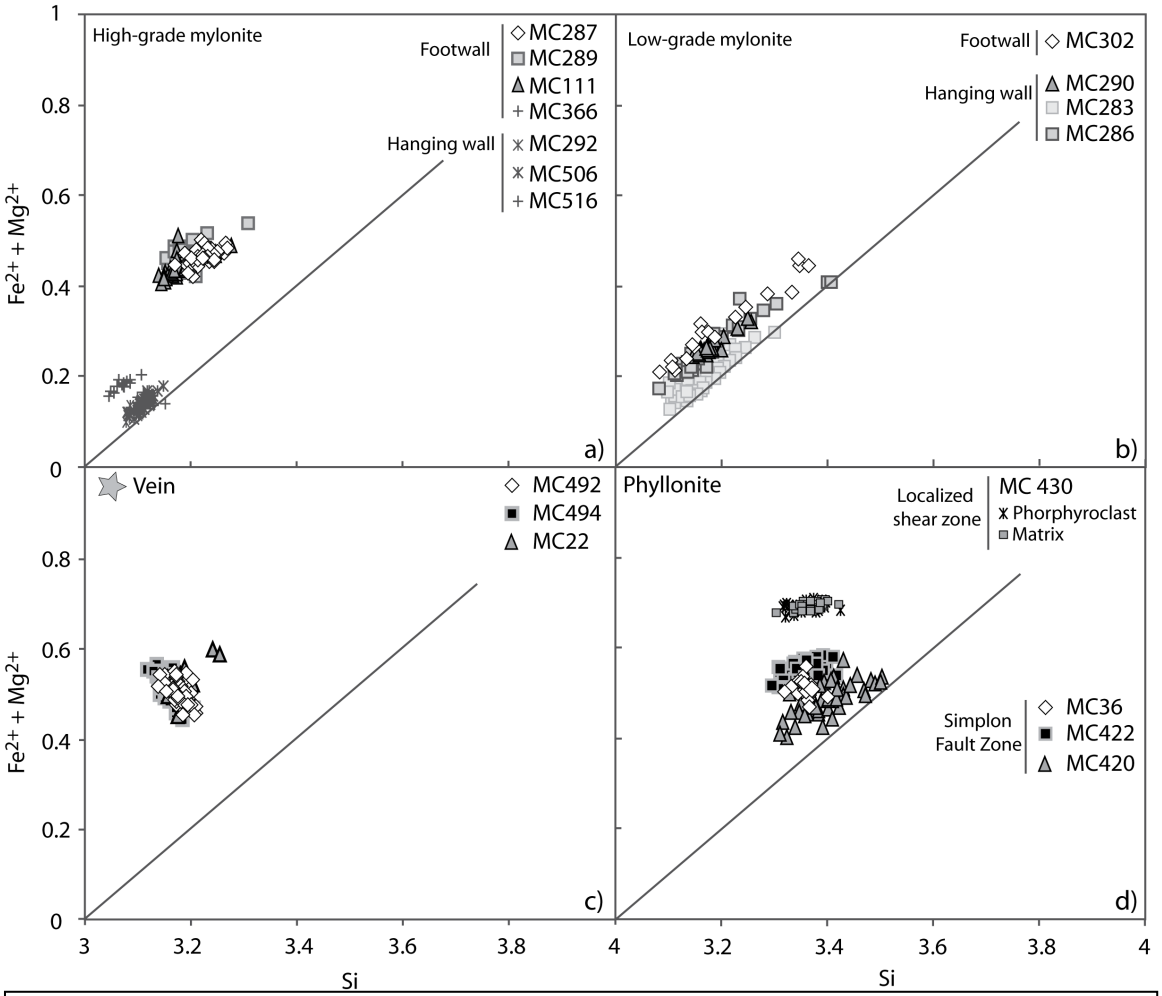

Figure II.8: Tschermak substitution for the analyzed white micas. a) Muscovites from the high-grade region. b) Muscovites from the low-grade region. c) Muscovites from veins in the neck of foliation boudinage. d) Phengites from phyllonites of the Aar massif.

compositions [*Rieder et al.,* 1998] were obtained for the three undeformed veins (MC22, MC492 and MC494, Table II.2) and there is no variation or zonation in composition within single grains (e.g. Fig. II.8c).

Samples MC36, MC420, MC422, MC423 and MC472 from the Rhone Valley (region V) are foliated phyllonites, developed from orthogneisses of the Aar Massif and its cover. White mica forms very thin flakes ca. 30-140 μm in length and 2-40 μm in width that define the foliation plane (Fig. II.9a), and develop from the destabilization of feldspar under fluid-present conditions [*Rossi et al.,* 2005; *Rolland et al.,* 2008] (Fig. II.9b). These white micas are clearly affected by dextral shearing, as indicated by overprinting shear bands (Fig. II.4h) and grow as fibers between broken porphyroclasts of feldspar (Fig.

II.9b). They are therefore interpreted to have grown syn-kinematically during dextral shearing in the footwall of the SFZ. Large porphyroclasts of biotite, with a diameter of ca. 400-700 µm, can also be found in some samples (MC420) (Fig. II.9c). Biotite is deformed, folded and kinked, and shows undulose extinction. For three analyzed phyllonites (MC36, MC420, and MC422), white micas have similar phengitic compositions [*Rieder et al.,* 1998], with the average given in Table II.2. The compositions are similar to that of phengite observed in dextral shear zones from the Grimsel Pass in the Aar massif [*Rolland,* personal communication] and from the Mont Blanc massif [*Rossi et al.,* 2005; *Rolland et al.,* 2008]. Such phengitic compositions developed under low pressure conditions probably reflect fluid-rock interaction similar to that described in *Rossi et al.* [2005]. Sample MC423 from the cover of the Aar Massif has a different composition (Table II.2) reflecting the different bulk rock composition.

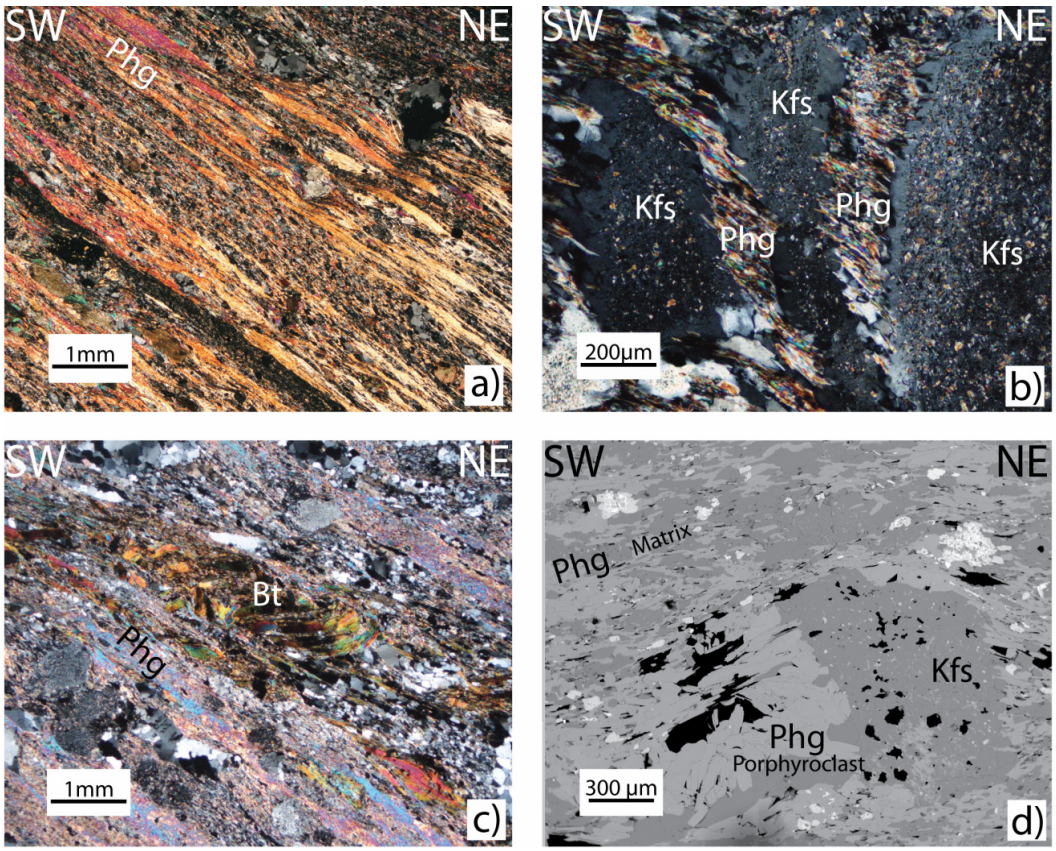

Figure II.9: Phyllonites from region V. a) Phyllonite development from orthogneiss of the Aar massif, with a matrix composed of very thin phengite (MC36). b) Fibers of phengite between broken feldspar porphyroclasts (MC36). c) Deformed porphyroclasts of biotite within the phyllonite (MC420). d) Preserved porphyroclasts of phengite within the localized phyllonite (MC430).

Sample MC430 (Fig. II.5), comes from a similar but more localized phyllonite developed from orthogneisses of the Aar Massif. Thin syn-kinematic white micas, of ca. 50-200 µm in length and 10-40 µm in width, growth within the foliation plane and as fibers between broken feldspar porphyroclasts. Their development is less pervasive than in the Rhone Valley samples. Porphyroclasts of white mica, with a diameter of ca. 100-300 µm (Fig. II.9d), can be found in the more feldspathic layers that are less affected by the

deformation and where feldspar porphyroclasts are still preserved (Fig. II.9d). Both porphyroclasts and syn-kinematic white micas have similar phengitic compositions (Table II.2). For each phyllonite, single grains show no zonation in composition, and Tschermak substitution (Fig. II.8d) shows a slight variation, mainly observed in MC420, which could be explained by a variation in P-T conditions during syn-kinematic phengite growth [*Guidotti*, 1973].

II.5. Results

II.5.1. Fission track analysis

The new fission-tracks ages are presented in Table II.3 and in Figure II.5. All ages fall within the Neogene, with apatite ages ranging from 3 to 6 Ma and zircon ages from 10 to 20 Ma. Overall, zircon central ages are younger in the footwall (9.7 to 13.7 Ma) than in the hanging wall (13.7 to 19.9 Ma). In the SE (region II), samples MC500 and MC501 show a clear jump of 5.5 Ma in zircon ages across the SL over a distance of 570 m, with ages of 12.9 Ma in the footwall and 18.4 Ma in the hanging wall (Fig. II.5). In the NW section (region IV), a similar jump in zircon ages of 5.8 Ma over 260 m is recorded, with ages of 12.4 Ma (MC475) in the footwall and 18.2 Ma (MC476) and 17.2 Ma (MC477) in the hanging wall (with these last two samples being indistinguishable within 1 sigma error) (Fig. II.5). However, except for these samples, in region IV a single clear jump in zircon ages can no longer be established. Instead, ages increase gradually toward the hanging wall.

Sample	Mineral	No. of crystals	Track density (x10^5 cm^{-2}) ρ d (counted)	ρ i (counted)	ρ s (counted)	Uranium (ppm)	P(χ^2) (Var%)	FT age ± 2σ (Ma)
MCS3	Apatite	40	14.45 (7924)	11.142 (1621)	0.131 (19)	8	2 (0.4)	3.2 ± 1.6
	Zircon	30	5.116 (1655)	40.822 (1826)	13.794 (617)	279	0 (0.3)	11.4 ± 1.8
MCS8	Zircon	20	4.688 (1655)	26.915 (884)	18.177 (597)	203	0 (0.3)	19.9 ± 3.2
MCS12	Zircon	26	4.462 (1655)	24.14 (925)	11.718 (449)	180	32 (0.1)	14.0 ± 1.8
MC32	Zircon	7	3.785 (1655)	35.476 (215)	19.8 (120)	299	84 (0)	13.7 ± 3.2
MC33	Apatite	35	11.55 (7924)	10.149 (1417)	0.222 (31)	10	8 (0.4)	4.4 ± 1.8
	Zircon	26	3.909 (1655)	28.593 (1232)	18.752 (808)	240	4 (0.2)	16.5 ± 2.0
MC269	Zircon	20	4.199 (2833)	29.669 (1138)	12.54 (481)	229	6 (0.2)	11.6 ± 1.6
MC282	Zircon	20	4.029 (2833)	21.572 (625)	11.873 (344)	172	0 (0.3)	15.0 ± 3.0
MC335	Zircon	20	3.827 (2419)	25.5 (677)	11.3 (300)	265	4 (0.3)	10.9 ± 2.2
MC283	Zircon	21	4.968 (3150)	24.198 (492)	13.083 (266)	162	31 (0.2)	17.4 ± 3.0
MC475	Apatite	20	12.003 (8084)	9.536 (780)	0.245 (20)	9	74 (0)	5.3 ± 2.4
	Zircon	21	4.581 (3150)	28.076 (595)	11.466 (243)	204	8(0.2)	12.4 ± 2.4
MC476	Zircon	28	4.014 (2419)	18.88 (626)	13.24 (439)	155	4 (0.2)	18.2 ± 3.0
MC477	Zircon	22	3.924 (2419)	20.401 (682)	13.82 (462)	170	48 (0)	17.2 ± 2.2
MC480	Zircon	20	4.592 (2777)	38.57 (896)	18.342 (426)	267	10 (0.2)	14.1 ± 2.2
MC481	Zircon	24	3.734 (2419)	17.704 (758)	10.02 (429)	152	76 (0)	13.7 ± 1.8
MC482	Zircon	22	4.312 (2777)	36.216 (759)	12.788 (268)	283	1 (0.3)	9.7 ± 2.0
MC500	Apatite	20	14.383 (8084)	15.464 (1740)	0.187 (21)	12	57 (0)	3.0 ± 1.4
	Zircon	20	5.210 (3150)	109.609 (2130)	41.734 (811)	665	23 (0.1)	12.9 ± 1.2
MC501	Apatite	21	14.043 (8084)	20.231 (2078)	0.474 (48)	16	58 (0)	5.5 ± 1.6
	Zircon	20	5.47 (3150)	79.374 (1679)	40.987 (867)	465	3 (0.1)	18.4 ± 2.0
MC519	Zircon	20	4.362 (2777)	21.796 (617)	12.717 (360)	159	84 (0)	16.5 ± 2.2
MC520	Zircon	21	4.492 (2777)	20.324 (538)	13.26 (351)	160	7 (0.2)	19 ± 3.4

Table II.3: Fission-track ages. ρs and ρi represent sample spontaneous and induced track densities; P(χ2) is the probability of χ2 for ν degrees of freedom where ν = no. of crystals−1. All ages are central ages [*Galbraith*, 1981] and are reported with a 2σ error. $\lambda D=1.55125x10^{-10}$. Ages were calculated using the recommended ζ calibration approach [*Hurford and Green*, 1983]. A geometry factor of 0.5 was used. ζ=341±6 for CN5/apatite and 130±0.6 for CN1/zircon. Uranium concentration is a broad approximation with an error minimum >20%.

II.5.2. $^{40}Ar/^{39}Ar$ analysis

$^{40}Ar/^{39}Ar$ ages are presented in Table II.4 and in Figures II.5 and II.10. Most ages are Neogene, with white mica ages ranging from 10 to 22.5 Ma, and one biotite age of 15.2 Ma. Three samples show a partial reset of older ages: the porphyroclasts of biotite (MC420) and white mica (MC430) in the Aar massif with a total release age of 67 Ma and 108 Ma respectively, and the muscovite MC286 with 79 Ma (Fig. II.5). These three samples, from the greenschist facies region, show very disturbed spectra (Fig. II.10k,l,m). The chemical analysis of Ca/K and Cl/K from $^{40}Ar/^{39}Ar$ analyses are given in Appendix C. Variations are not significant and could not be correlated to distinguish mixed ages in one single grain.

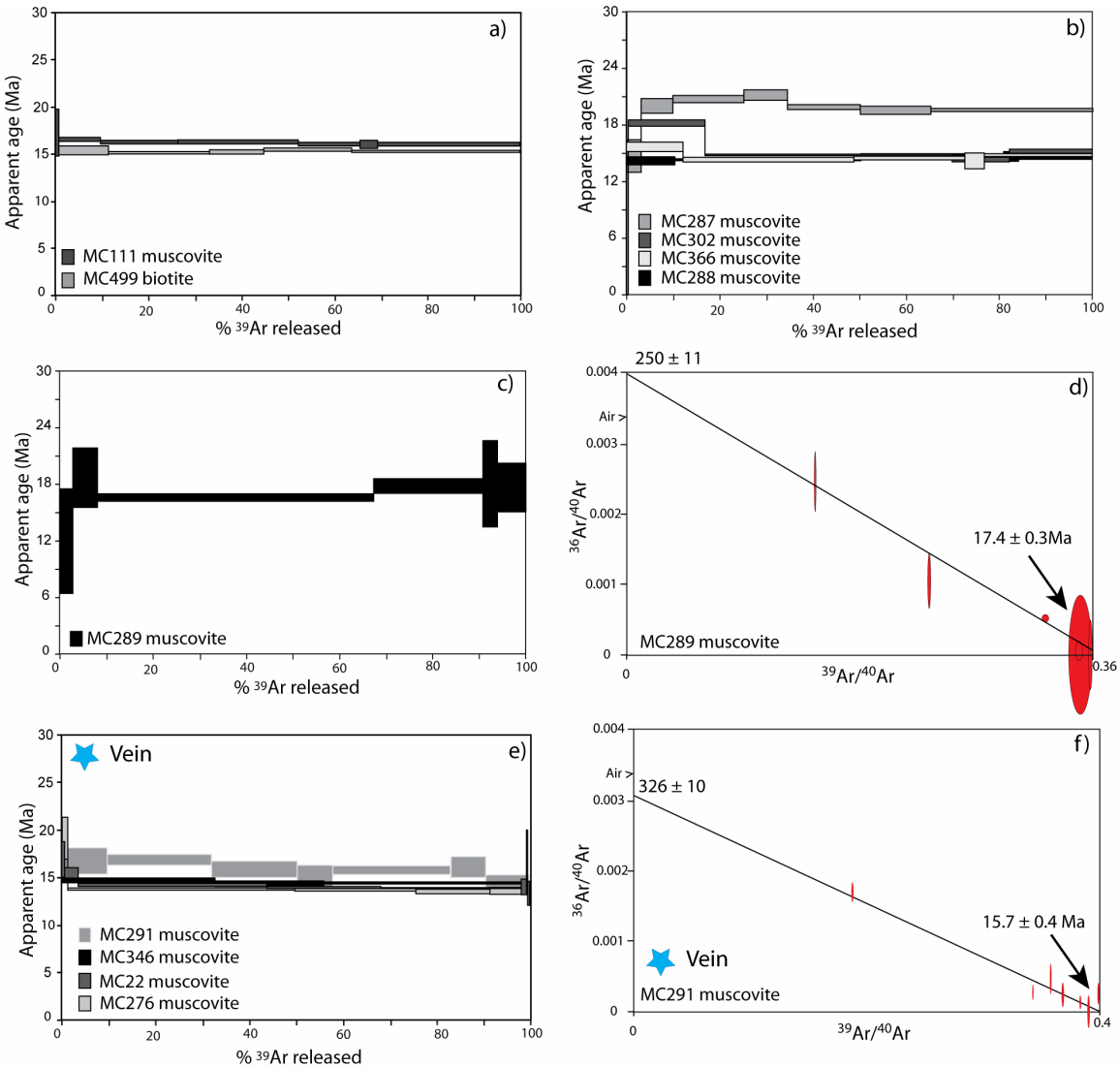

Figure II.10: $^{40}Ar/^{39}Ar$ age spectra for each sample and corresponding inverse isochron diagrams.

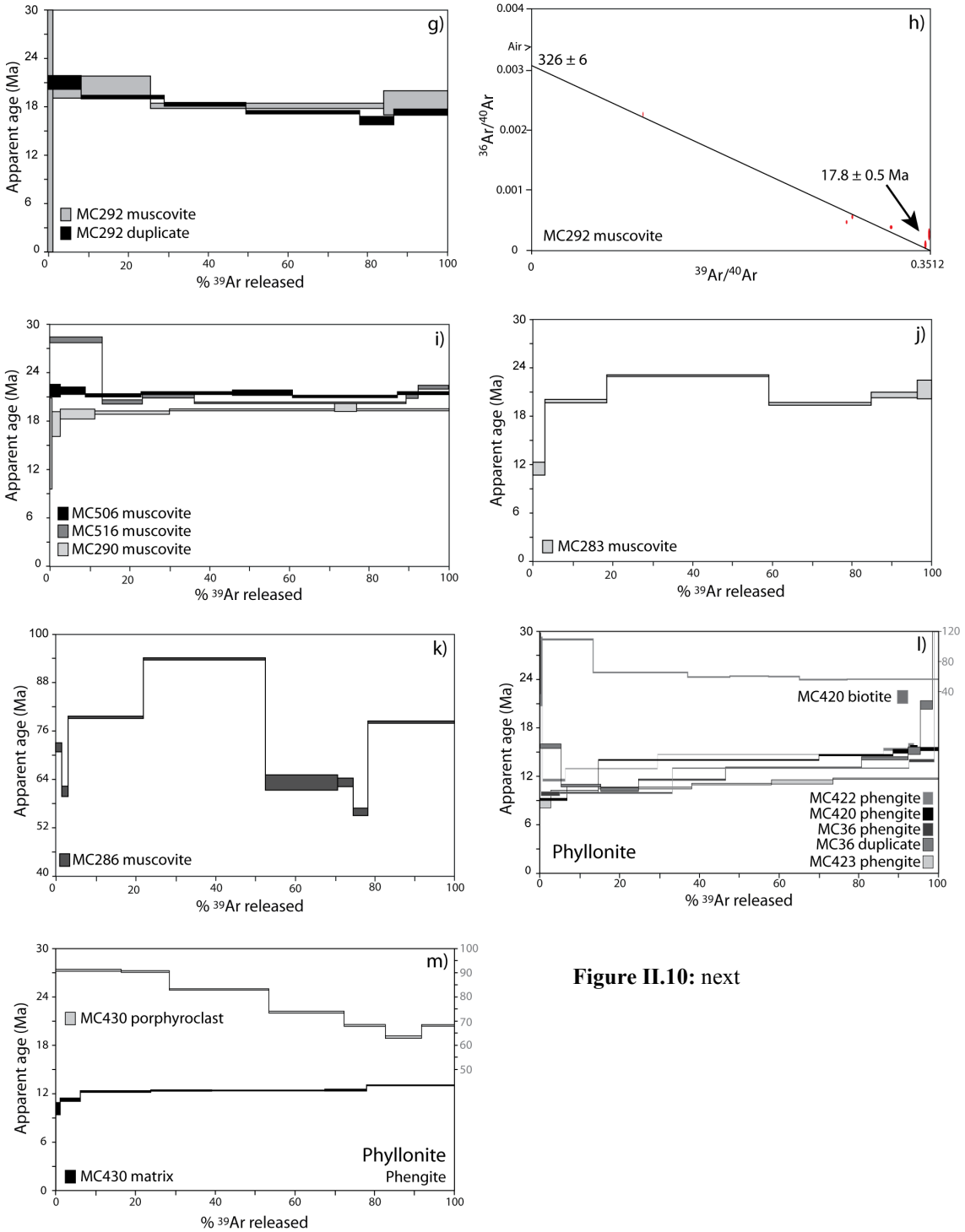

Figure II.10: next

Plateau ages are always obtained in the amphibolite facies region of both the footwall and the hanging wall (Table II.3 and Fig. II.10a,b,c,e,g,i). For three samples (MC291, MC289 and MC292), inverse isochron diagrams are also given, which confirm the plateau age with relatively high 2 sigma error (Fig. II.10d,f,h).

Except for the partially reset pre-Alpine ages (MC286, MC420 and MC430), ages are generally younger in the footwall than in the hanging wall. In the footwall parallel to the fault, ages for white mica tend to decrease from SW (20-14 Ma) to NE (14-10 Ma)

toward the greenschist facies region. In the amphibolite facies region, muscovite ages also tend to decrease from 20-17 Ma to 15-14 Ma with increasing distance from the SL. In the SE (region III), ages for three muscovites from the necks of foliation boudinage give 14 Ma (MC22, MC276 and MC346) (Fig. II.10e). The muscovite from the vein showing flanking structure development (MC291) gives a slightly older age of 15.9 Ma, which is confirmed by the inverse isochron diagram (Fig. II.10d). This age is similar to the age of 16 Ma obtained for the muscovite from the host rock (MC111). Biotite (MC499) from the host rock gives 15 Ma (Fig. II.10a), which is slightly younger than muscovite (MC111).

In the Rhone Valley (region V), 5 aggregates of very thin phengites from different phyllonites all give very similar narrow staircase spectra that increase from 10 Ma to 14 Ma (Fig. II.10l). Samples MC422, MC36 and its duplicate all have older ages for the first and final steps of the spectra. For these samples, an additional total age is given in Table II.4, calculated without the older ages, to reflect the total age of staircase spectra only. In these phyllonites, the biotite porphyroclast (MC420) gives a total release age of 66.8 Ma, and no plateau age could be calculated (Fig. II.10l).

In the localized phyllonite MC430 (Fig. II.5), the thin syn-kinematic white micas give slightly increasing staircase spectra, but a plateau age could be calculated at ~12 Ma (Fig. II.10m). On the contrary, white mica porphyroclasts from the same sample have a partially reset pre-Alpine age of 108 Ma, with very disturbed spectra (Fig. II.10m).

Sample	Mineral	$^{40}Ar/^{39}Ar$ age ± 2σ (Ma)	Description
MC22	Muscovite	14.1 ± 0.13	Plateau age
MC36	Phengite	14.2 ± 2.7	Total release age
		11.3 ± 1.2	Total age (without steps 1,8,9)
	duplicate	13 ± 2.9	Total release age
		11.9 ± 2.5	Total age (without steps 1,6,7)
MC111	Muscovite	16.2 ± 0.19	Plateau age
MC276	Muscovite	13.7 ± 0.18	Plateau age
MC283	Muscovite	22.5 ± 1.8	Total release age
MC286	Muscovite	78.8 ± 8.3	Total release age
MC287	Muscovite	20.1 ± 0.28	Plateau age
MC288	Muscovite	14.6 ± 0.15	Plateau age
MC289	Muscovite	17.2 ± 0.95	Plateau age
MC290	Muscovite	19.3 ± 0.19	Plateau age
MC291	Muscovite	15.9 ± 0.61	Plateau age
MC292	Muscovite	17.9 ± 0.47	Isochron age
MC302	Muscovite	14.9 ± 0.16	Plateau age
MC346	Muscovite	14.4 ± 0.23	Plateau age
MC366	Muscovite	14.9 ± 0.23	Plateau age
MC420	Phengite	13.7 ± 1.80	Total release age
	Biotite	66.8 ± 9.80	Total release age
MC422	Phengite	14.4 ± 0.95	Total release age
		14.2 ± 1.20	Total age (without steps 1,2)
MC423	Phengite	11 ± 0.71	Total release age
MC430	Phg Matrix	12.4 ± 0.08	Plateau age
	Phg porphyroclast	107.9 ± 19	Total release age
MC499	Biotite	15.2 ± 0.17	Plateau age
MC506	Muscovite	21.3 ± 0.18	Plateau age
MC516	Muscovite	20.5 ± 0.20	Plateau age

Table II.4: $^{40}Ar/^{39}Ar$ ages

II.5.3. Rb-Sr analysis

Rb-Sr ages are presented in Table II.5 and in Figures II.5 and II.11. In the SE (region III), two veins from the neck of foliation boudinage (MC492 and MC494) and one from a Reidel structure (MC497) all give similar ages of ca.14.5 Ma, almost identical to ages obtained with the $^{40}Ar/^{39}Ar$ method on similar veins (Fig. II.10e). Ages represent two-point Rb-Sr ages using muscovite-calcite pairs in equilibrium (Fig. II.11a,b). These results are confirmed by the isochron age (MC 492) obtained by using several measurements on muscovite-calcite pairs from the same sample (Fig. II.11c).
In the NW region (region V), the three microsamples of syn-kinematic fibrous phengite from a stretched feldspar porphyroclast do not align on an isochron, resulting in an age with a very large 2 sigma error at ca. 14.6 ± 9.5 Ma (Fig. II.11d). It is possible that isotopic equilibration was not achieved between all three microsamples, considering also the presence of small inclusions within the microsamples 2 and 3 (Fig. II.6b and Table II.5). The two-point Rb-Sr age between the microsamples 1 (pure phengite) and 2, which are in textural contact (Fig. II.11d), would be ca. 14.5 ± 0.12 Ma, comparable with ages obtained with the $^{40}Ar/^{39}Ar$ methods on the same structures (Fig. II.10l). Including microsample 3 does not significantly change the best-fit age, but markedly increases the 2 sigma error.

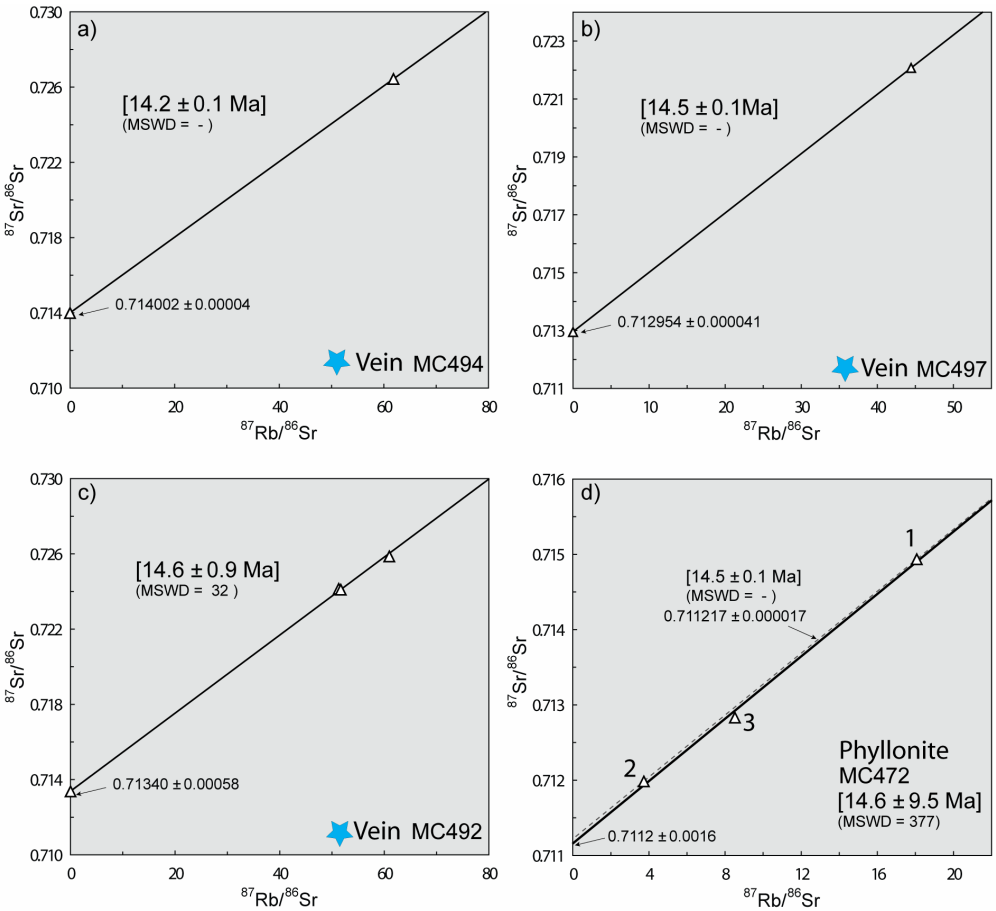

Figure II.11: Two-point and isochron Rb-Sr microsampling ages

Sample	Mineral pairs	Sample weight (µg)	Rb (ppm)	Sr (ppm)	$^{87}Rb/^{86}Sr$	$^{87}Sr/^{86}Sr$ (± 95 c.l.)		$(^{87}Sr/^{86}Sr)i$ (± 95 c.l.)	Age (Ma)
MC494	Ms	883	174.88	8.197	61.843	0.726444	± 0.000048	0.714002 ± 0.00004	14.17 ± 0.07
	Cal	67	0.53	277.8	0.00552	0.714003	± 0.000041		
MC497	Ms	720	247.74	16.15	44.435	0.722078	± 0.000049	0.714002 ± 0.00004	14.46 ± 0.10
	Cal	79	0.254	458.4	0.00160	0.712954	± 0.000042		
MC492	Ms 1	575	247.64	11.78	60.930	0.725888	± 0.000041		
	Ms 2	427	249.22	13.98	51.670	0.724102	± 0.000079	0.7134 ± 0.00058	14.58 ± 0.86
	Ms 3	397	239.07	13.51	51.289	0.724160	± 0.000053		
	Cal	49	1.000	336.4	0.00861	0.713377	± 0.000055		
MC472	1-Phg	1638	591.28	94.74	18.069	0.714937	± 0.0000097	0.7112 ± 0.0016	14.6 ± 9.5
	2-Phg+Chl+Kfs	560	275.14	213.5	3.7307	0.711985	± 0.000014		
	3-Phg+Chl+Kfs	608	397.15	135.1	8.5124	0.712833	± 0.00001		

Table II.5: Rb-Sr microsampling isotopic data

II.5.4. Oxygen stable isotope analysis

The oxygen isotope data are presented in Table II.6, with values representing averages of duplicate measurements from the same mineral separate. A temperature at equilibrium can be calculated using the isotopic fractionation factor alpha, giving temperatures of 340 ± 30 °C, 330 ± 30°C, 355 ± 20 °C for the couple quartz-white mica in MC494, MC497, and MC498 respectively.

sample	$\delta^{18}O_{qtz}$, ‰	±	$\delta^{18}O_{ms}$, ‰	±	Δqtz-ms	Temperature, °C
MC494	12.245	0.161	9.094	0.122	3.118	340 ± 30
MC497	11.228	0.006	8.01	0.296	3.187	330 ± 30
MC498	11.084	0.091	8.045	0.063	3.010	355 ± 20

Table II.6: Oxygen stable isotope data

II.6. Discussion

II.6.1. Fission-track ages and the brittle history of the Simplon Fault Zone ("Simplon Line")

In the NW section (region IV), zircon fission-track ages gradually increase toward the hanging wall (Fig. II.5). This implies a continuation of the SL not as one single discrete fracture but as a wider zone of deformation, with the brittle detachment divided into several branches. The overall relative displacement between footwall and hanging wall is similar to that in the central region [*Steck and Hunziker*, 1994], but is not localized on one single detachment. Field observations clearly support this interpretation, with a wide zone of brittle deformation observed in this region (Fig. II.4). We interpret this section to

reflect a relatively high structural level of the low-angle detachment system. Zircon fission-track ages obtained from this section imply that the fault was still active at about 11 Ma. However, our data suggest that a jump in apatite fission-track ages is not developed in this region, although we have to consider the fact that the apatite with low uranium content has a very large error and could hide any possible jump. Therefore, zircon fission-track ages do confirm a continuation of the SL in the Rhone Valley (region V), where a clear in apatite fission track has also been described [*Soom*, 1990; *Seward and Mancktelow*, 1994]. The single clear jump observed in region II confirms that the SL was still active at ca. 12 Ma and probably until around 3 Ma.

The fact that no obvious jump in fission-track ages is observed after the curve of the SL into regions II and III [*Keller et al.,* 2005a], can be interpreted in two ways. 1) In this region, the displacement on the fault does not involve any differential exhumation, as it is a purely dextral strike slip fault, as can be clearly observed in the field (Fig. II.3). 2) The fault may no longer exist, with *Keller et al*., [2006] arguing that displacement has instead been accommodated by backfolding in the Camughera-Moncucco unit. In our opinion, this second hypothesis is not tenable. Firstly, it would imply decreasing displacement along the SL toward region II. However, a similar discontinuity in zircon fission-track ages is observed along the NW-SE striking segment of the SL (with a strictly normal component) from ca. 18 to 12 Ma (Fig. II.5). The proposed geometry would also imply a rotation of the hanging wall, and there are no field observations to support such a rotation, with measured stretching lineations maintaining the same orientation (see Fig. II.2c). Besides, the Vanzone backfold is generally interpreted as being older than 25 Ma [*Pettke et al.,* 1999] and, if this is the case, then these folds could not be coeval with Neogene SL activity. We therefore interpret the lack of a jump in fission-track ages across the projected continuation of the SL toward the SE section, in regions II and III (Fig. II.2b), to reflect the change to dextral strike slip kinematics, without any significant differential exhumation between footwall and hanging wall.

II.6.2. $^{40}Ar/^{39}Ar$ and Rb-Sr data: cooling or neo-(re-)crystallization ages?

The significance of mica $^{40}Ar/^{39}Ar$ and Rb-Sr isotopic ages isotopic closure in general is highly debated and has been attributed to various factors: (1) Thermally activated isotopic diffusion, leading to the concept of a specific closure temperature for an isotopic system in a particular mineral [*Jäger*, 1965; *Jäger et al.,* 1967; *Dodson*, 1973], (2) Neo- and re-crystallization related to deformation and/or fluid-rock interaction, associated with grain size reduction and/or or interlayered mica growth [e.g. *Dunlap*, 1997; *Villa*, 1998; *Mulch et al.*, 2002; *Mulch and Cosca*, 2004]. Indeed, some studies have even shown that mica could conserve their original signature after a high temperature event [e.g. *Glodny et al.*, 2008].

In our study, in the high-grade region, deformed mica porphyrclasts from the vicinity of the fault, which are in part internally recrystallized (Fig. II.7a,b), and annealed micas from outside of the shear zone (Fig. II.7c,d) were analyzed with the $^{40}Ar/^{39}Ar$ method. Both mica types yield a similar range of ages: (1) deformed porphyroclasts related to the SFZ give ages in the range of 20.1 to 14.6 Ma (MC111, MC302, MC287, MC288, MC289, MC499 Fig. II.5) and (2) undeformed and annealed micas ages of 21.3 to 14.9 Ma (MC290, MC292, MC366, MC506 Fig. II.5). There was no evidence of internal variation in composition or zonation within any of these single grains. All these samples

from the amphibolite facies region have reached a minimum temperature of ca. 500°C at ca. 30 Ma [*Vance and O'Nions*, 1992; *Todd and Engi*, 1997]. Deformation on the SFZ postdated this metamorphic event, as shown by the retrograde paragenesis.
As similar ages are found in both deformed (in part recrystallized) and undeformed micas, we consider that cooling rather than recrystallization was responsible for the recorded $^{40}Ar/^{39}Ar$ ages. This regional metamorphism would act to re-equilibrate the major-element mica composition, anneal previous structures in old micas (Fig. II.7c,d) and result in the growth of new mica grains. Subsequently, these micas were deformed in the SFZ under rather high temperature conditions.
An alternative interpretation would be that all these micas crystallized at ages between ca. 20 and 14 Ma, as proposed by *Hetherington and Villa* [2007], who interpreted similar $^{40}Ar/^{39}Ar$ ages in the Berisal unit obtained from muscovite in the S_2 foliation as directly dating the S_2 development. In their view, S_2 would then be of Miocene age and the deformation and recrystallization of these micas in the vicinity of the fault zone would not have significantly influenced the age pattern. However, the regional S_2 fabric is generally considered to be significantly older, having developed before 26 Ma [*Steck and Hunziker*, 1994; *Grujic and Mancktelow*, 1996; *Romer et al.,* 1996]. Besides, the temperature reached by the metamorphism in this region (ca. 500°C) is well above the closure temperature of micas for the $^{40}Ar/^{39}Ar$ system given by *Dodson* [1973] and similar to the closure temperature established by *Villa* [1998]. We therefore consider these ages in the high-grade region to be cooling ages.
The closure temperature for biotite is generally considered to be on the order of 50°C lower than that of white mica and typically cooling ages yield younger ages for biotite than for white mica. In the SE section (region III) of the high-grade Simplon mylonites, biotite (15 Ma, MC499) yields a slightly younger $^{40}Ar/^{39}Ar$ age than muscovite (16-17 Ma, MC111, MC289), which would be consistent with these both being cooling ages in this region. However, muscovite from the different veins in the Isorno Valley (region III) give $^{40}Ar/^{39}Ar$ ages younger (14 Ma) than muscovite and biotite from the host rocks. Besides similar ages of ca. 14.5 Ma were obtained on such veins with the Rb-Sr microsampling method. This implies that these ages from the veins cannot be cooling ages and we interpret them as crystallization ages for the newly grown white mica in these veins, which developed in the necks of foliation boudins. This interpretation is confirmed by the equilibration temperature of 330-355°C obtained on such veins from the stable oxygen isotope analyses on quartz-muscovite. This temperature is lower (or close to) the closure temperature of white micas with the $^{40}Ar/^{39}Ar$ system given by *Dodson* [1973] (350 ± 50°C) and far below the closure temperature given by *Villa* [1998] (500°C). If white mica grows under such conditions, the age should retain the time of crystallization [e.g. *Dunlap*, 1997]. The composition of muscovite within each vein is homogeneous and thus the age of one single grain should be representative of the sample. The older, more strongly rotated and deformed vein (flanking structure) MC291, has a similar $^{40}Ar/^{39}Ar$ age to the muscovite from the host rocks (16 Ma), and this age is probably also a cooling age. These veins developed progressively during ongoing shearing and cooling through time, so the first ones should have formed at higher temperature than the last ones.

In the greenschist facies region (northwestward, in the Rhone Valley, Fig. II.1a), peak metamorphic temperatures were never more than 350°C. Pre-Alpine porphyroclasts of biotite (MC420) and white mica (MC430, MC286), from the Aar massif and the hanging wall, show very disturbed spectra, with $^{40}Ar/^{39}Ar$ ages varying between pre-Alpine and Alpine. This can either be interpreted as due to (1) the presence of a mixture of pre-Alpine white micas finely inter-mingled with some fine neo-crystallized Alpine white micas, or due to (2) a partial loss of Ar during Alpine deformation, at temperatures that were not high enough (or deformation that was not pervasive enough) to fully reset the chronometers.

The muscovite MC283 from the hanging wall seems to be almost fully reset at around 22.5 Ma, but a plateau age could not be calculated. This age is very similar to the ages observed in higher grade mylonites from the hanging wall in the SE (21-19 Ma). The result is also quite similar to $^{40}Ar/^{39}Ar$ ages found by *Markley et al.,* [1998] close to the detachment (SL) in the hanging wall from the same region. They obtained reset ages of ~22 Ma for the smaller grain size fraction (20 μm) and suggested that there was a partial loss of ^{40}Ar due to thermal advection from the exhuming footwall of the SFZ. This hypothesis could also explain our result. However such a partial reset is not observed in MC286, which is located in the central region where the maximum jump in temperature across the SL is observed (Fig. II.5) and a systematic effect due to heat transfer from the footwall cannot be verified. The results of *Markley et al.* [1998] were for small grain sizes (20μm), and thermal resetting could certainly be promoted in this case [e.g. *Dodson*, 1973].

The different age patterns obtained in the high-grade region (with young Alpine ages) compared to the low-grade region (with partially reset pre-Alpine ages) (Fig. II.5) is in good agreement with the results of *Frank and Stettler* [1979], who have suggested that the release patterns of their $^{40}Ar/^{39}Ar$ samples were controlled by the metamorphic grade. Therefore, if new mica grew under low-grade conditions, it should be possible to obtain the crystallization age [*Dunlap*, 1997]. In fact, in the Rhone Valley (region V), the very thin phengites from the phyllonite developed from orthogneiss of the Aar Massif and its cover do record Alpine $^{40}Ar/^{39}Ar$ ages (MC36, MC420, MC422, MC423, ranging from 14.2 to 11 Ma). As a result, we interpret the narrow staircase spectra between 10 and 14 Ma as a mixed age, reflecting the syn-kinematic neo-crystallization of white micas over a time period of ca. 4 Ma. Such an interpretation was already implied in interpreting similar spectra from the Helvetic Alps [*Kirschner et al.,* 2003]. The variable composition of the phengites also argues for a variation in P-T-fluid conditions during phengite growth. The staircase spectra could thus be explained by the growth of phengite over ca. 4 Ma, as retrograde P-T conditions gradually changed due to exhumation in the footwall of the SFZ. An alternative explanation could be that the phengite grew at around 14 Ma, and the younger steps are due to partial loss of ^{40}Ar [e.g. *Simon-Labric et al.*, 2009]. This partial loss could be due to either 1) late reactivation or ongoing deformation reopening the system, or 2) fluid percolation through the shear zones after or during deformation. In both cases, the syn-kinematic white mica would have an age of 14 Ma, but with evidence for deformation and fluid circulation continuing until ca.10 Ma. A comparable two-point Rb-Sr age of 14.5 Ma was obtained from syn-kinematic phengite (MC 472) within the same phyllonite of the Aar massif (Fig. II.11d).

The 12 Ma plateau age of MC430 obtained from a localized phyllonite, developed further NE in the Rhone Valley, is also considered to be a crystallization age. In fact, pre-Alpine porphyroclasts from this sample are only partially reset, with a total age of 108 Ma (Fig. II.10m).

II.6.3. Absolute dating of the Simplon Fault Zone (SFZ)

The formation ages obtained using $^{40}Ar/^{39}Ar$ and Rb-Sr methods throughout the Simplon region allow the absolute age of the Neogene deformation to be well constrained. The age of newly grown muscovite in veins developed in the necks of foliation boudins and Riedel fractures from the high-grade Simplon mylonites (region III) constrain the time for the last ductile-brittle transition during Simplon shearing in this SE region to be ca.14-14.5 Ma. In the NW, ages on syn-kinematic phengite from the dextral phyllonite shear zone in the Rhone Valley (region V) constrain the timing of the brittle-ductile transition for the Simplon-Rhone Line to be ca.10-14.5 Ma. *Markley et al.* [1998] proposed that the Rhone Line was already active at 19 Ma, and *Kirschner et al.* [2003] at 17 Ma. Our $^{40}Ar/^{39}Ar$ ages would argue that shearing has continued until at least 10 Ma.
Some localized dextral brittle shear around 12 Ma are also observed further NE in the Rhone Valley. *Rolland* [personal communication] have obtained similar ages (15 -12 Ma) for dextral localized shear zones in the Grimsel Pass. Such structures, with similar ages, can be correlated as a dextral localized shear zone network accommodating a small part of the major transcurrent tectonic setting further NE into the Rhone Valley. However it makes no doubt now of the connection between the Rhone and the Simplon Fault Zone.

II.6.4. Cooling ages and fault activity

The discontinuity in cooling ages seen across the SFZ can also provide constraints on the time of fault activity. In Figure II.12, cooling ages are plotted against horizontal distance from the Simplon Line for three different sections perpendicular to the strike of the SL in region I, region III and region IV. In this plot fission track and $^{40}Ar/^{39}Ar$ cooling ages obtained in this study are combined with a compilation of cooling ages from the literature (with references listed in the legend of Fig. II.12).
In the central section (region I), all the different thermochronometers across the SFZ present a significant jump in cooling ages, visible from 20 to 3 Ma and consistent with a normal displacement as described by *Steck and Hunzike*r [1994]. This argues for an activity of the SFZ from at least 20 to 3 Ma (Fig. II.12b).
In the SE section (region III), a slight jump in $^{40}Ar/^{39}Ar$ and Rb-Sr ages can be observed across the SFZ between 17 Ma and 14 Ma. This is attributed to a slight differential displacement between footwall and hanging wall, introduced by the regional up-doming of the footwall during penetrative ductile shearing, as indicated by the stretching lineations (Fig. II.2c). However, no significant jump in cooling ages is seen for low-temperature fission track thermochronometers after 14 Ma (Fig. II.12c). As discussed above, this is attributed to late brittle dextral strike-slip movement on the SFZ postdating the regional up-doming of the footwall, which ceased at the time of the brittle transition around 14 Ma.

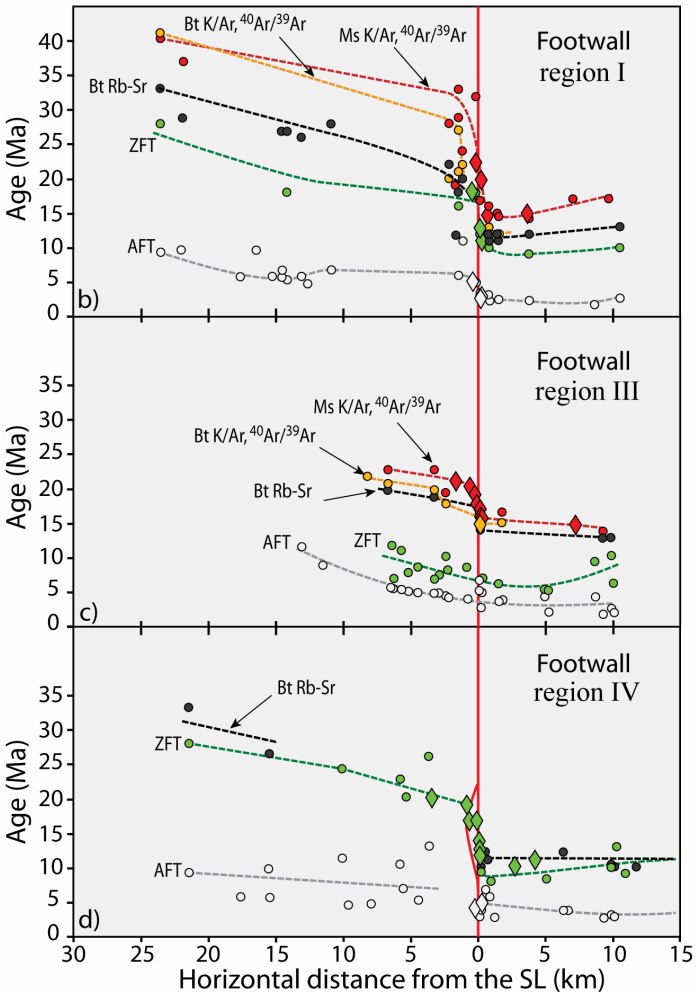

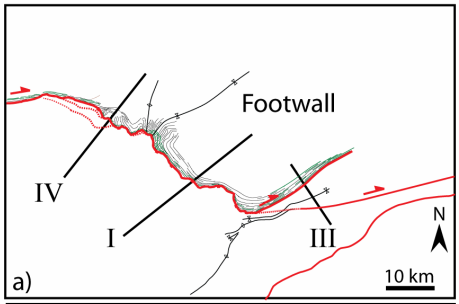

Figure II.12: Cooling age patterns across the Simplon Fault Zone. a) Location of three age-distance sections. b) Age-distance section from the central region (region I), c) Age-distance section from the SE region (region III). d) Age-distance section from the NW region (region IV). These diagrams are a compilation of new cooling ages from this study (diamonds) and published data [*Jäger et al.*, 1967; *Hunziker*, 1969; *Hunziker and Bearth*, 1969; *Purdy and Jäger*, 1976; *Wagner et al.*, 1977; *Deutsch and Steiger*, 1985; *Soom*, 1990; *Baxter et al.*, 2002; *Keller et al.*, 2005a; *Hetherington and Villa*, 2007].

One could argue that the formation of the dome could postdate the extensional ductile shear zone. However, we have strong structural arguments that the dated veins are directly related to continued penetrative ductile shear (they are themselves synthetically related with the formation of flanking structures) and represent the ductile-brittle transition, dated at ca. 14-14.5 Ma. This up-doming of the footwall can be either attributed to large scale isostatic rebound due to crustal unloading [*Spencer*, 1984; *Wernicke and Axen*, 1988; *Block and Royden*, 1990] or due to a strain gradient through the shear zone [*Davis*, 1983; *Mancktelow and Pavlis*, 1994]. This will be discussed further in following chapters.

Finally in the NW section (region IV), the different thermochronometers across the SFZ show a significant overall jump in cooling ages, mainly seen in the zircon fission-track ages and consistent with a normal displacement (Fig. II.12d). Considering the general trend of apatite fission-tracks ages, a slight jump in ages can still be distinguished between footwall and hanging wall. The younger ages observed within the footwall (14 to 4 Ma) are likely to reflect active displacement on the SFZ at this period of time, as in the central region (region I). The jump observed in zircon fission-track ages is spread over a wider zone compared to the central region (region I). This confirms that the brittle overprint in region IV is no longer localized on one discrete detachment and reflects the overall geometry of the detachment system at a higher structural level.

II.7. Conclusions

The Simplon Fault Zone (SFZ) is a major extensional ductile shear zone with a subsequent brittle overprint, in part localized on a relatively discrete detachment, the "Simplon Line" (SL), which separates the footwall and hanging wall. The regional pattern in cooling ages, together with structural arguments, indicate a direct connection between the Rhone Line, in the Rhone Valley, and the SFZ probably with a similar amount of displacement. In the SE, field and geochronological data suggest a transfer of the SFZ as a dextral strike-slip fault into the Isorno Valley, with a loss of displacement over 20 km down to a value of only 2km, which is the observed offset of the southern limb of the *D2* Wandfluhorn fold.

Identical kinematics are systematically observed for both ductile and brittle components both across and along the exposed length of the fault zone, with an increase in the deformation localization toward the SE. This probably reflects different structural levels along one single detachment system.

The discontinuity in cooling ages across the fault zone indicates a long period of fault activity between 20 and 3 Ma. Direct $^{40}Ar/^{39}Ar$ and Rb-Sr dating of footwall syn-kinematic white micas from low grade phyllonite in the Rhone Valley give ages of 14.5-10 Ma, whereas newly grown muscovite from veins in foliation boudinage necks in high-grade mylonite in the Isorno Valley give 14-14.5 Ma. These direct dating results establish that the ductile to brittle transition occurred at 14.5-10 Ma. Fission-track ages in combination with structural analyses establish that displacement along the whole fault zone has continued at lower temperature until ca. 5-3 Ma. This argues for a continuous transition from ductile shearing to a more localized zone of brittle deformation within the same geological framework, over a period of ca. 15 Ma during the Neogene. The SFZ is therefore an example of a telescoped crustal section in a single major low-angle fault, developed during continued convergence, rather than a two-stage structure involving exhumation on a brittle fault of an earlier inactive ductile shear zone.

Localized dextral brittle shear between 15 and 12 Ma also have to be considered northeastward in the Rhone Valley until at least the Grimsel Pass, accommodating a small part of the Neogene transcurrent tectonic setting.

III. Exhumation history of the Simplon Fault Zone, 2-3D thermo-kinematic modeling

III.1. Introduction

Two alternative models are currently proposed for footwall exhumation along low-angle detachments: (1) exhumation along detachments that initiated and slipped at shallow dips (≤ 30°), which is inconsistent with Andersonian fault mechanics but supported by earthquake records [e.g. *Wernicke*, 1995] and (2) exhumation through a rolling hinge system in which initially high-angle seismogenic faults are passively rotated to shallow dip due to isostatic rebound [e.g. *Spencer*, 1984; *Buck*, 1988; *Wernicke and Axen*, 1988].
Beside the major mechanical difference associated with initiation and slip of a low-angle detachment, these two models result in fundamentally different exhumation patterns, due to the different fault plane geometry (Fig. III.1). In the model of a detachment initiating and slipping at low-angle (Fig. III.1a), exhumation is achieved by the interaction between tectonics and erosion, whereas in the rolling hinge model, exhumation is mainly driven by tectonics (Fig. III.1b).
In this paper we investigate the exhumation patterns obtained for these two alternative models, using as an example a major normal fault from the European Alps. Using an extensive thermochronological dataset, we analyse the thermal history employing the 2-3D thermo-kinematic model "Pecube" [*Braun*, 2003; *Herman et al.*, 2007], coupled with a formal inversion algorithm (Neighbourhood Algorithm, [*Sambridge*, 1999a, b]).
Thermochronology is an appropriate tool to determine exhumation patterns [e.g. *Foster et al.*, 1993; *Grasemann and Mancktelow*, 1993; *Wells et al.*, 2000; *Brichau et al.*, 2006; *Mulch et al.*, 2006]. However, various studies have shown that advection compresses the isotherms near the surface, a process that must be accounted for when interpreting cooling and exhumation rates from thermochronological datasets [e.g. *Ketcham*, 1996; *Mancktelow and Grasemann*, 1997; *Braun*, 2002]. Therefore, characterization of the time-varying exhumation history on a low-angle detachment system requires a thermo-kinematic modeling approach, as used in several previous studies [e.g. *Grasemann and Mancktelow*, 1993; *Ketcham*, 1996; *Dunkl et al.*, 1998]. In addition, topography also disturbs isotherms close to the surface, which in turn must be considered when interpreting cooling ages obtained with low-temperature thermochronometers (such as apatite fission track or apatite (U-Th)/He) [e.g. *House et al.*, 1997].
We use as an example of a major low-angle detachment system the Simplon Fault Zone [*Mancktelow*, 1985, 1990; *Merle et al.*, 1986; *Mancel and Merle*, 1987; *Steck*, 1990], which is exposed in the Central Alps. Developed during Miocene orogen-parallel extension, this major structure is largely responsible for exhumation of the Toce Dome, which forms the western part of the Lepontine metamorphic Dome [e.g. *Preiswerk*, 1921; *Wenk*, 1955; *Steck and Hunziker*, 1994]. The Simplon Fault Zone is appropriate for such a study for several reasons. (1) Many cooling ages are available from a wide range of different thermochronometers, from high-temperature (white mica Rb-Sr) to low-temperature (apatite fission track) [this study and e.g. *Jäger et al.*, 1967; *Hunziker*, 1969; *Hunziker and Bearth*, 1969; *Purdy and Jäger*, 1976; *Wagner et al.*, 1977; *Soom*, 1990; *Baxter et al.*, 2002; *Keller et al.*, 2005a; *Hetherington and Villa*, 2007]. (2) Two different kinematic models for footwall exhumation have been proposed: one proposes exhumation

along an initially shallowly dipping detachment [*Mancktelow*, 1985; *Grasemann and Mancktelow*, 1993] whereas the other proposes exhumation through a rolling hinge system [*Wawrzyniec et al.*, 1999; *Axen et al.*, 2001; *Wawrzyniec et al.*, 2001]. (3) The exhumation rate in the Lepontine Dome is still controversial and argued to be either steady state [*Bernet et al.*, 2001] or reflecting periods of faster cooling in the Oligo-Miocene due to fault activity or to an increase in the regional erosion rate [*Grasemann and Mancktelow*, 1993; *Schlunegger and Willett*, 1999].
We considered two basic thermo-kinematic models for the Simplon Fault Zone example: (1) an initial low-angle detachment (model A, Fig. III.1a) or (2) a rolling hinge model (model B, Fig. III.1b). For each case, we determine the thermal history using Pecube and then compute mineral ages for the various thermochronological systems by solving the solid state diffusion. We perform a non-linear inversion of the data to constrain model parameters and to discuss their implications for the kinematics of exhumation, the timing and amount of faulting, the cooling and exhumation rates, and the relative displacement between footwall and hanging wall. We also determine constraints on possible rheological properties, on the influence of shear heating and the effect of topography.

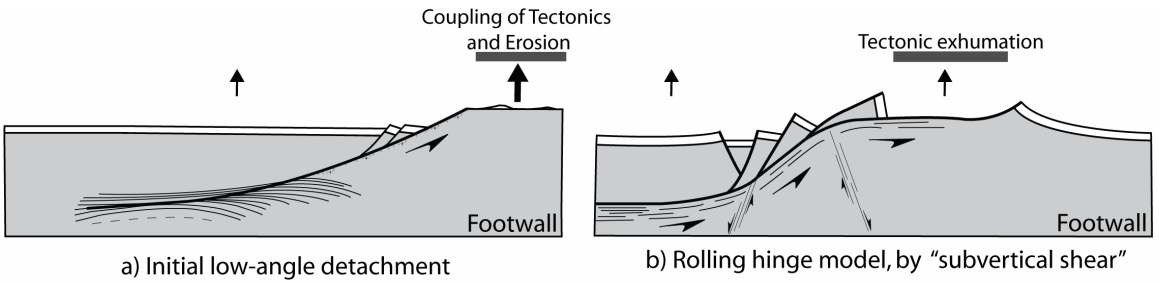

Figure III.1: Synthetic theoretical models for footwall exhumation along detachments; a) model A: initial low-angle detachment; b) model B: rolling hinge model accommodated by "subvertical shear". [e.g. *Axen and Bartley*, 1997].

III.2. Geological constraints

III.2.1. The Simplon Fault Zone (SFZ)

This study focuses on the central region of the Simplon Fault Zone (SFZ) (Fig. III.2a). This major fault zone exposes an extensional ductile shear zone with a subsequent brittle overprint, partly localized on a discrete detachment separating the footwall and the hanging wall (Chapter II). Mylonites developed in the extensional ductile shear zone grade over 1-2 km into less overprinted footwall units, but shearing is most developed over a few hundred meters immediately below the detachment [*Mancktelow*, 1985]. Unequivocal normal or "top-to-SW" shear sense criteria are observed in this zone [*Mancktelow*, 1985, 1990; *Merle et al.*, 1986; *Steck*, 1990]. The mylonites are overprinted by more brittle extensional structures, such as conjugate sets of normal brittle faults, which define a coherent paleo-stress field with horizontal SW-NE extension and near vertical compression (i.e. $\sigma 1$ vertical) [*Wawrzyniec et al.*, 2001; *Grosjean et al.*, 2004]. The discrete brittle detachment, or "Simplon Line" (SL) [*Mancktelow*, 1985; *Mancel and Merle*, 1987; *Steck*, 1987], consists of a narrow zone (< 10 m) of cataclasites, sometimes

marked by a few meters of clay gouge. In the study area, the SL dips 25-30° toward the SW, which is slightly steeper than the dip of the mylonites (22° toward 222°, Fig. III.2b). A continuous exhumation history of the footwall, from the ductile to the brittle field, is described in Chapter II, with the fault most likely active in time range between 20 and 3 Ma. The ductile-brittle transition is directly dated at around 14-14.5 Ma by $^{40}Ar/^{39}Ar$ and Rb-Sr analyses on syn-kinematic white micas (Chapter II).

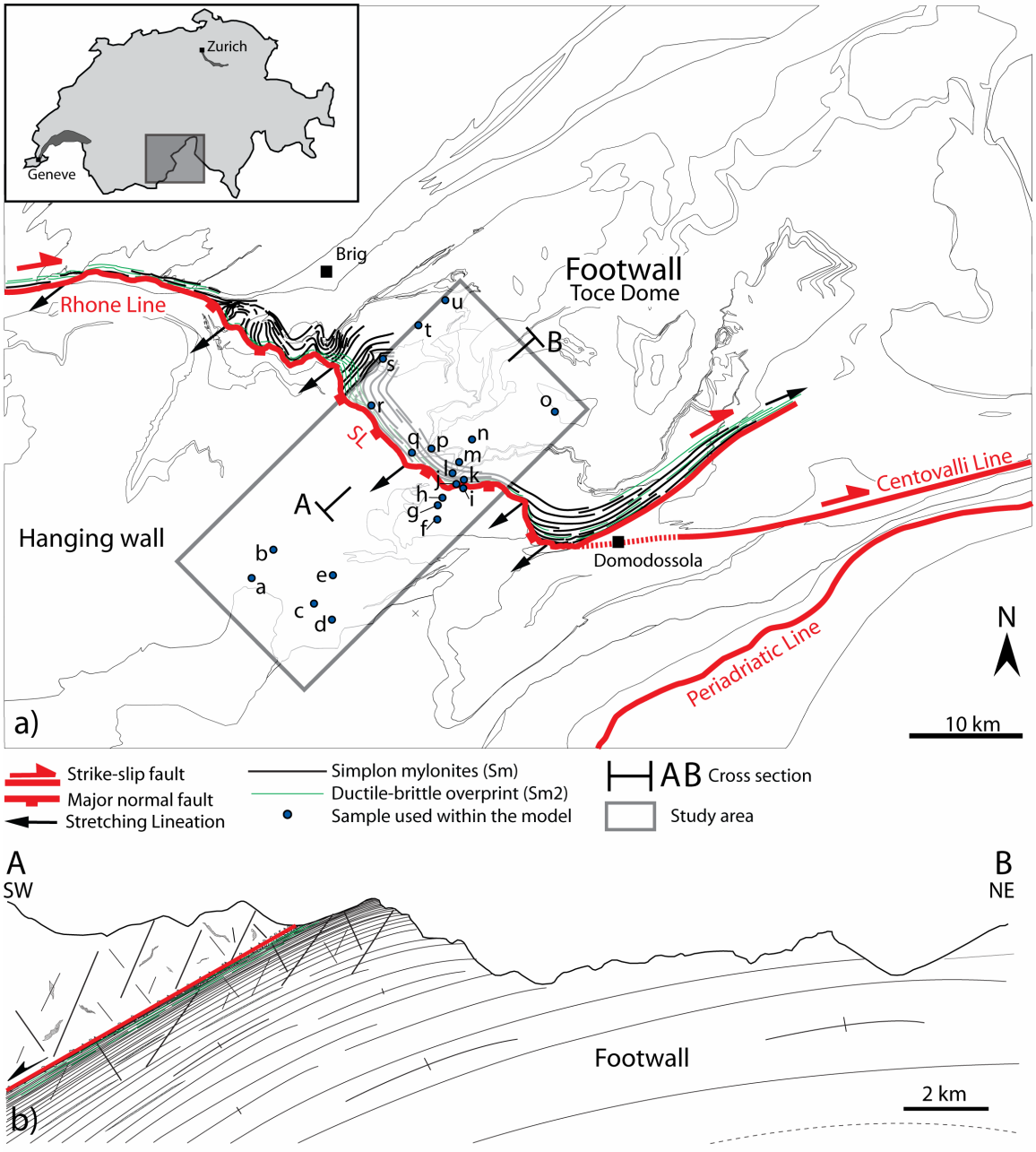

Figure III.2: Geological setting. a) Geological map with location of the study area and of the dataset; b) Cross section parallel to the transport direction illustrating the style of the Simplon deformation.

III.2.2. Model of an initial low-angle detachment

The SFZ is interpreted as a crustal scale low-angle detachment that initiated and slipped at a dip of ~25°, resulting in the exhumation of ductile mylonites developed along the same structure at greater depth [*Mancktelow*, 1985]. *Grasemann and Mancktelow* [1993] developed a 2D finite-difference thermal model of the fault history, based on published isotopic mineral cooling ages [*Hunziker*, 1969; *Hunziker and Bearth*, 1969; *Purdy and Jäger*, 1976; *Wagner et al.*, 1977; *Deutsch and Steiger*, 1985; *Soom*, 1990]. They modeled the geometry of a detachment dipping 25°, with erosion applied at the surface and an additional differential velocity applied in the footwall, parallel to the fault plane, to simulate a distributed ductile shear. They considered fault activity to start at 18 Ma, which is the time of apparently faster cooling rate observed in the footwall cooling curve. T-t histories were extracted for samples on either side of the fault, and for different scenarios and displacement histories along the fault. Using this approach, they concluded that the best fit to the known cooling curves was obtained if the most active period of the SFZ was between 18 Ma and 15 Ma, with 10 mm/a for the total relative displacement (parallel to the fault), followed by at least 5 Ma at the slower velocity of 0.4 mm/a. The corresponding exhumation rates in the footwall, for a constant fault dip of 25°, was 4.6 mm/a between 18-15 Ma and 0.6 mm/a after 15 Ma. A relatively steady-state exhumation rate for the hanging wall of 0.4 mm/a was proposed. The resultant total vertical relative displacement on the fault zone was 15 km in this model.

III.2.3. Rolling hinge model

Integrated field and fluid inclusion studies on the SFZ by *Wawrzyniec et al.* [1999], *Axen et al.* [2001] and *Wawrzyniec et al.* [2001] resulted in the recognition of several postmylonitic structures that these authors considered to be convincing arguments for the passage and deformation of the footwall through a rolling hinge system. In their model, this rolling hinge is accommodated by "flexural failure" [e.g. *Buck*, 1988; *Axen and Bartley*, 1997] in the northern region (Simplon Pass, Fig. I.3) and "subvertical shear" [e.g. *Wernicke and Axen*, 1988; *Axen and Bartley*, 1997] assisted by slip on steep faults in the central region (near Simplon Village, Fig. I.3). In this central region, early postmylonitic structures assigned to the passage through the lower hinge are represented by a set of west-down synthetic brittle fractures (dipping 80°). In the northern region, the corresponding structures are contractional kink bands and extensional veins. The lower hinge acts in steepening the detachment, which accommodates uplift of the footwall, and is also responsible for localization of the wide mylonitic zone closer to the detachment (< 50m) [*Axen et al.*, 2001]. The upper hinge is only poorly developed, and is reflected by less common antithetic east-down brittle faults (dipping 80°). Synkinematic fluid inclusions from these two sets of fractures indicate different P-T conditions for earlier and late postmylonitic structures. Early postmylonitic structures develop at conditions similar to that of the mylonite formation, that is close to peak of metamorphism conditions (T > 500°C and P~5.5-7 kbar). The later east-down structures develop at shallower crustal level (T~300°C and P~2-4 kbar) during retrograde metamorphism. These P-T conditions are obtained by intersecting isochore populations (defined from the density of the syn-kinematic fluid inclusions) and the estimated P-T path for the region [*Todd and Engi*, 1997].

III.2.4. Compiled thermochronological data used in the thermo-kinematic model

Using a 2-3D thermo-kinematic model, we aim to critically assess these two different models by inverting a compilation of the large amount of published data on cooling ages available from the Simplon area [*Jäger et al.*, 1967; *Hunziker*, 1969; *Hunziker and Bearth*, 1969; *Purdy and Jäger*, 1976; *Wagner et al.*, 1977; *Deutsch and Steiger*, 1985; *Soom*, 1990; *Baxter et al.*, 2002; *Keller et al.*, 2005a; *Hetherington and Villa*, 2007], together with new ages presented in Chapter II. This compilation includes apatite and zircon fission-track (AFT, ZFT) ages, biotite and white mica $^{40}Ar/^{39}Ar$ ages and biotite and white mica Rb-Sr ages. All these ages are listed in Table III.1. It is important to note that these ages could reflect either cooling through a closure temperature [*Jäger*, 1965; *Jäger et al.*, 1967; *Dodson*, 1973] or crystallization below a closure temperature [e.g. *Dunlap*, 1997; *Villa*, 1998; *Mulch and Cosca*, 2004]. A preliminarily assessment of geochronological data coupled with structural, petrological and chemical analyses is first needed to distinguish cooling ages from possible crystallization ages and partially reset ages (especially relevant for the $^{40}Ar/^{39}Ar$ and Rb-Sr isotopic systems). As described in Chapter II, in the central region of the SFZ (Fig. III.2a), high-grade mylonites from the footwall only yield cooling ages, as the rocks attained temperatures higher than 500°C. However, in the hanging wall, the maximum temperature conditions did not exceed 300-400°C and white mica $^{40}Ar/^{39}Ar$ and Rb-Sr ages should therefore yield either partially reset mixed ages (Chapter II) or neo-crystallization ages [*Markley et al.*, 1998]. It follows that such white mica $^{40}Ar/^{39}Ar$ and Rb-Sr ages from the hanging wall cannot be used as cooling ages in our model. AFT and ZFT ages are reset in both footwall and hanging wall (see Chapter II and [*Wagner et al.*, 1977; *Seward*, 1989; *Michalski and Soom*, 1990; *Keller et al.*, 2005a]).

No	Name	Location	Distance from the SL (m)	elevation (m)	AFT Ma (±2σ)	ZFT Ma (±2σ)	Bt Rb-Sr Ma (±2σ)	Bt $^{40}Ar/^{39}Ar$ + K/Ar Ma (±2σ)	Ms $^{40}Ar/^{39}Ar$ + K/Ar Ma (±2σ)	Ms Rb-Sr Ma (±2σ)	Ref.
a	KAW 367	637050/104900	-15156	1880	6.3 ± 1.3						4
b	KAW 377	638300/106900	-13118	1800	5.5 ± 1.1		26.1 ± 5.4				4
c	KAW 376	641900/102750	-14174	2116	5.6 ± 1.1	17.5 ± 3	26.1 ± 3				4
d	KAW 375	643150/101300	-14607	2140	6.4 ± 1.3						4
e	KAW 374	643300/106100	-10919	2678	7 ± 1.4		27.6 ± 2.2				4
f	KAW407	651460/110582	-2126	1475				20.4 ± 2.4	28.1 ± 2.6		3
g	KAW 370	651550/111300	-1448	1521	6.2 ± 1.2	16.8 ± 3		26.7 ± 2.6	32.9 ± 3		2-3-4-5
h	KAW 410	651700/111600	-1111	1501			19.7 ± 6.6	22.1 ± 2	24 ± 2.2		2-3-5
i	KAW2769	653060/112660	-115	1660	5.2 ± 1.4	17.7 ± 3.8					5
j	MC287	651460/110582	50	1406					20.1± 0.3		7
k	KAW 2770	653100/112930	152	1600	3.6 ± 1.2	11.6 ± 2			16.7 ± 0.4		5
l	KAW 357	652670/113500	793	1280	3.3 ± 1.8		12.2 ± 4.6			19 ± 5.6	1-5
m	MC 288	652728/113378	666	1277					14.6 ± 0.2		7
n	KAW 159	653960/116300	3807	830	2.5 ± 1.2	9.4 ± 2	11.8 ± 2.6	12 ±1.4	14.2 ± 1.8		3-5
o	KAW 408	660750/118400	10500	1080	2.8 ± 0.6	10.4 ± 2.2	13.1 ± 4.4				2-4-5
p	KAW160	650400/115200	1487	1160	2.7 ± 1.2		11.4 ± 2.2	11.5 ± 1.2	14.5 ± 1.2		3-5
q	KAW161	649680/115170	831	1200	2.6 ± 0.6	10.1 ± 2	11.4 ± 2	12.5 ± 1.2	16 ± 2		1-3-4
r	MCS 3	646249/118442	197	1641	3.2 ± 1.6	11.4 ± 1.8					7
s	MC 302	647034/122940	3611	1947					14.9 ± 0.2		7
t	SS9950	649620/127300	7022	2549					17 ± -		6
u	SS9816	651710/127300	9689	2474					17 ± -		6

Table III.1: Selected thermochronological dataset used in the model. Ref: 1= *Jäger et al.*, 1967; 2= *Hunziker and Bearth*, 1969; 3= *Purdy and Jäger*, 1976; 4= *Wagner et al.*, 1977; 5= *Soom*, 1990; 6= *Hetherington and Villa*, 2007; and 7= This Study.

An interpolation of compiled cooling ages from the Central Alps is given in Figure III.3. The original references for the ages used are listed in the legend of Figure III.3. The interpolation is performed using a natural-neighbor interpolation, which is a local weighted average method [*Watson*, 1999]. Only samples from the surface were used for the interpolation. The Simplon-Rhone Line appears as a major discontinuity in the cooling age pattern for all thermochronometers. As described by *Vernon et al.* [2008], the interpolations of AFT and ZFT ages (Fig. III.3a,b) highlight the fact that the youngest ages (i.e., 1-3 Ma for AFT and 6-12 Ma for ZFT) are only found in the direct footwall of the Simplon-Rhone Line.

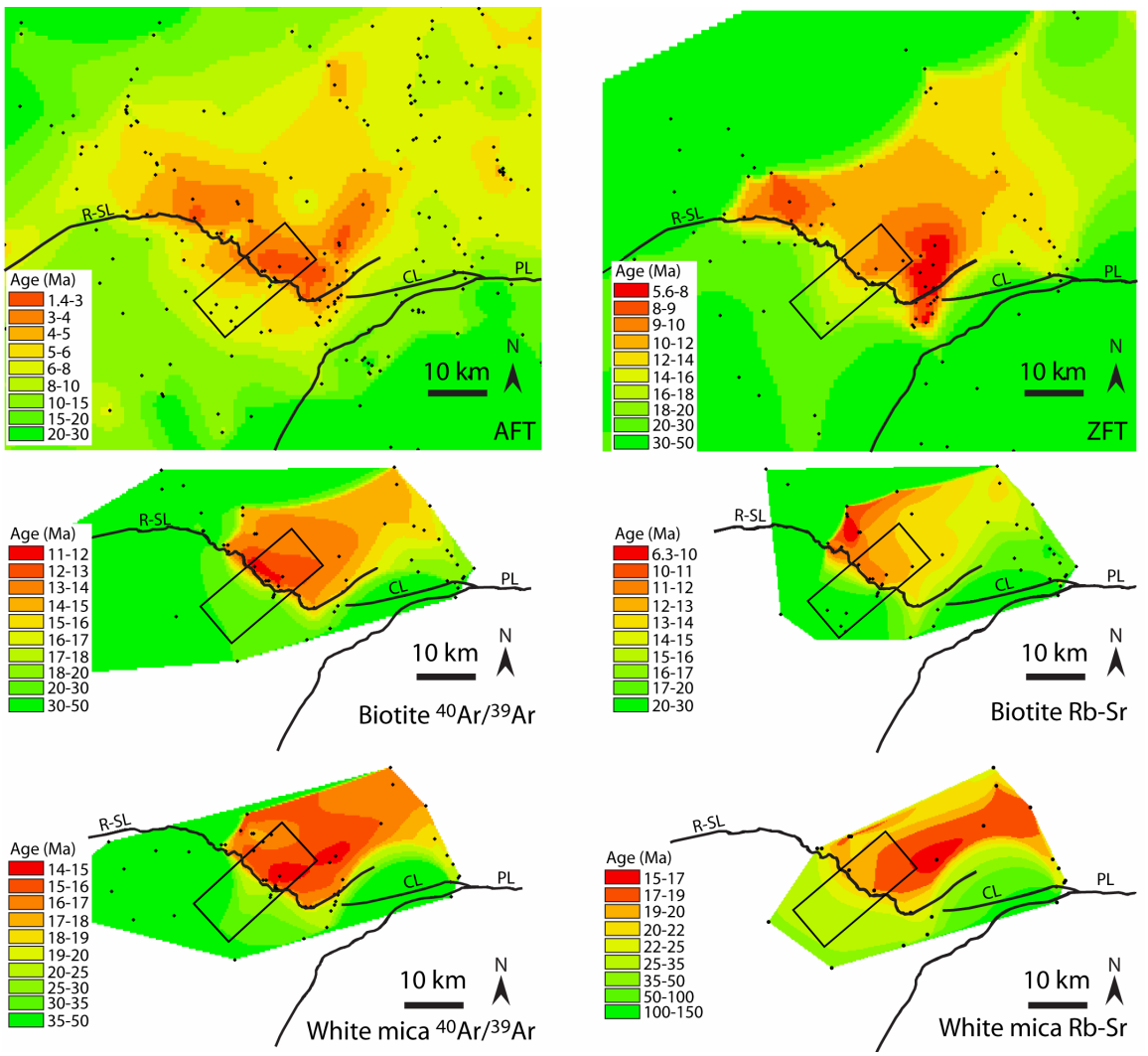

Figure III.3: Interpolated age maps for different thermochronometers. a) Apatite fission track; b) zircon fission track; c) biotite $^{40}Ar/^{39}Ar$; d) biotite Rb-Sr; e) white mica $^{40}Ar/^{39}Ar$; f) white mica Rb-Sr. R-SL: Rhone-Simplon Line, CL: Centovalli Line, PL: Periadriatic Line. The rectangle represents the study area. Ages used are from this study (Chapter II) and from a compilation of published results [*Jäger*, 1965; *Jäger et al.*, 1967; *Hunziker*, 1969; *Hunziker and Bearth*, 1969; *Purdy*, 1972; *Purdy and Jäger*, 1976; *Wagner et al.*, 1977; *Hurford*, 1986; *Michalski and Soom*, 1990; *Soom*, 1990; *Seward and Mancktelow*, 1994; *Baxter et al.*, 2002; *Keller et al.*, 2005a; *Hetherington and Villa*, 2007].

These younger ages within the footwall are likely to reflect active displacement on the SFZ at this time. For the interpolation of $^{40}Ar/^{39}Ar$ and Rb-Sr ages (Fig. III.3c,d,e,f), known or obvious crystallization ages were specifically avoided in the interpolation (for instance when white mica $^{40}Ar/^{39}Ar$ or Rb-Sr gives a younger age than biotite for the same system and the same sample). The age pattern of $^{40}Ar/^{39}Ar$ and Rb-Sr reflects the fact that reset ages are only found in the Toce Dome, which is consistent with the amphibolite facies attained there.

In Figure III.4a, we have projected the cooling ages from the study area (rectangle in Fig. III.3) into a 2D profile parallel to the slip direction across the central part of the SL. The cooling ages clearly show a significant jump across the SL for every thermochronometer, coherent with a normal sense of displacement (refer to Chapter II and *Hunziker* [1969], *Mancktelow* [1992], *Grasemann and Mancktelow* [1993] and *Steck and Hunziker* [1994]). In the footwall, with increasing distance from the SL, ages first decrease over a distance of ca. 4 km and subsequently increase (Fig. III.4a). This lateral age variation is mainly visible for high-temperature thermochronometers, such as white mica $^{40}Ar/^{39}Ar$. AFT ages do not show any singular variation. The age decrease observed at high temperature has been attributed to the effect of a distributed ductile shear within the SFZ, which is not seen at lower temperature because of a more rigid block-like behavior during exhumation along the brittle detachment [*Mancktelow*, 1992; *Grasemann and Mancktelow*, 1993]. Theoretical cooling curves, for different sample locations on either side of the SFZ, are given in Figure III.4b. Closure temperature used are listed Table III.2. In the footwall, the cooling curve for a sample close to the detachment (1.5 km) shows a break in the cooling curve at ca. 19 ± 5.6 Ma, reflecting the onset of an apparent faster cooling rate, which was attributed to the onset of faulting by *Grasemann and Mancktelow* [1993]. The apparent cooling rate then progressively slows down (Fig. III.4b).

A potential problem is the possible occurrence of excess Ar in the analyzed samples. A recent detailed study on biotite $^{40}Ar/^{39}Ar$ cooling ages, carried out by *Baxter et al.* [2002] at the contact between metapelite and amphibolite units in the central region of the SFZ, has shown a correlation of excess argon with lithology. Their biotite ages varies from 12 to 17 Ma. They suggest that $^{40}Ar/^{39}Ar$ cooling ages should be determined on several samples from each outcrop to avoid errors introduced by locally excess argon. However, our sampling strategy requires a large amount of data from different lithologies and such a detailed approach for each outcrop cannot be practically realized. Two samples with obvious excess argon obtained near Engiloch (Fig. I.3) were excluded from this study and are given in Appendix C.

Also, it is important to note that the presence of surface derived fluid infiltrating within the fault zone is an important factor that has to be considered. The work of *Morrison and Anderson* [1998] on oxygen stable isotopes demonstrates that along brittle detachments, meteoric fluid can penetrate and cool the footwall over tens of meters below the detachment. This effect would increase the cooling rate and therefore the cooling rate related to exhumation alone cannot be estimated if surface driven fluids are percolating through the fault zone. However, ongoing work on oxygen stable isotope from the central region of the SFZ [*Guerra et al.*, 2009] shows that fluids within the footwall are all buffered by the bulk rock. Therefore we do not expect that fluid percolation was significantly cooling the footwall below the detachment in this region.

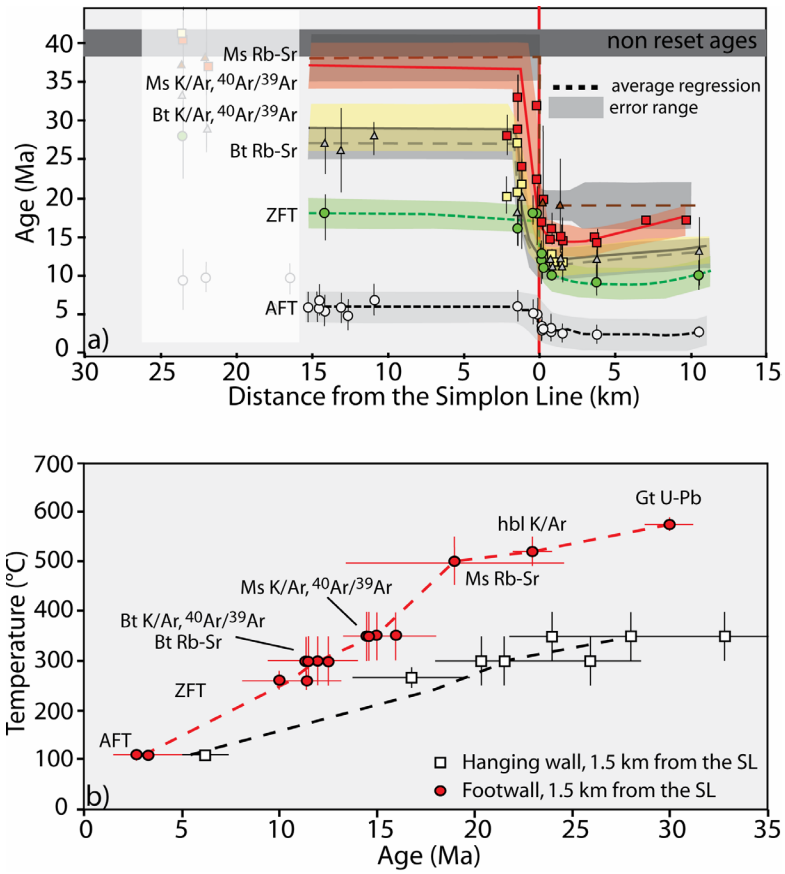

Figure III.4: Dataset description. a) Age-distance diagram given for 6 thermochronometers: AFT, ZFT, biotite Rb-Sr, biotite $^{40}Ar/^{39}Ar$ and K/Ar, white mica $^{40}Ar/^{39}Ar$ and K/Ar, white mica Rb-Sr. The regression of the observed ages and the error used in the model is also reported. b) Theoretical cooling curves across the SL for a given closure temperature (Table III.2), samples from footwall and hanging are from 1200m and 1300m elevation respectively. Errors are given at 2 sigma and ages with a 2 sigma error exceeding 30 % were not included into the model.

III.3. Approach and methods

Our objective is to analyze the thermal history on a section parallel to the transport direction of the SFZ (Fig. III.4a). This approach consists of (1) using a 2D finite element thermo-kinematic model ("Pecube") [*Braun*, 2003] to solve the heat transfer equation in a crustal block, (2) extracting T-t paths to compute ages, solving the solid state diffusion equation, (3) performing an inversion of the compiled thermochronological data using the Neighbourhood Algorithm [*Sambridge*, 1999a, b] to extract probability information on some of the model parameters (e.g. starting time for the faulting, fault velocity, etc.), and finally (4) to run forward 3D models to investigate the effects of topography on the age distribution.

III.3.1. Thermo-kinematic model

III.3.1.1. Pecube and age prediction

To model the thermal history we solve the heat transfer equation:

$$\rho c\left(\frac{\partial T}{\partial t}+v\Delta T\right)=k\nabla^2 T+H+H_s$$

where *T(x,y,z,t)* is the temperature (K), ρ is density (kg m^{-3}), *c* is heat capacity (J kg^{-1} K^{-1}), *v*(u,t) is the velocity field (m s^{-1}), *k* is the thermal conductivity (W m^{-1} K^{-1}), *H(x,y,z)* is the radioactive heat production per unit mass (W m^{-3}) and *Hs* is the shear heating (W m^{-3}). We use the same definition of the shear heating as defined in e.g. *Graham and England* [1976] and *Burg and Gerya* [2005]. It is computed as the component-wise product of the shear stress and strain rate tensors. The strain rate is calculated from the spatial derivative of the velocity field, while the stress tensor can only be approximated since the model is only kinematic. In the brittle domain, all components of the stress tensor are assumed equal to the lithostatic pressure:

$$\tau=\mu\rho gz$$

where the friction coefficient μ= tan (φ), φ is the friction angle, ρ is density (kg m^{-3}), *g* the gravitational acceleration (m s^{-2}) and *z* the depth (m).

In the ductile domain the shear stress follows a power law relationship:

$$\tau^n=\frac{\dot{\varepsilon}}{A\exp\left(\frac{-Q}{RT}\right)}$$

where $\dot{\varepsilon}$ is the strain rate (s^{-1}), *A* and *n* are intrinsic constants ($MPa^{-1}s^{-1}$), *Q* the activation energy (J/mol), and *R* the universal gas constant [e.g. *Hansen and Carter*, 1982].

Ages are then computed from the T-t histories extracted from the model. We compute ages for Rb-Sr and $^{40}Ar/^{39}Ar$ systems solving the solid state production-diffusion equation for a given geometry with the same approach outlined in *Herman et al.* [2007]:

$$\frac{\partial C}{\partial t}=D\nabla^2 C+p$$

where *C* is the concentration of Ar or Sr, *p* is their production rate. *D(t)* is the diffusion coefficient following the Arrhenius relationship:

$$\frac{D}{a^2}=\frac{D_0}{a^2}\exp\left(\frac{-E_\alpha}{RT}\right)$$

where D_0 is the diffusivity (m^2 s^{-1}), E_α is the activation energy (J mol^{-1}), *R* is the gas constant (JK^{-1} mol^{-1}), *T* is the temperature (K) and *a* is the diffusion domain radius (m). The diffusion properties used are listed in Table III.2. To compute AFT ages we use an annealing track algorithm defined by *Lutz and Omar* [1991] and *Van der Beek et al.* [1995] and adapted for ZFT by *Galbraith and Laslett* [1997], *Tagami et al.* [1998] and *Rahn et al.* [2004]. An inherited age, identical for each thermochronometer, is required as an initial condition in the model, fixing the maximum possible age. We keep this parameter *tage* as a variable.

Decay system	Mineral	Tc (°C)	References	Eα ($J\ mol^{-1}$)	Do ($m^2\ s^{-1}$)	Geometry	References
Rb-Sr	White mica	500 ± 50	*Jaeger*, 1967	104600	9E-16	cylindrical	*Jenkin*, 1997
	Biotite	300 ± 50	*Jaeger*, 1967	104600	2E-13	cylindrical	*Jenkin*, 1997
$^{40}Ar/^{39}Ar$	White mica	350 ± 50	*Jaeger*, 1967	217568	4.1E-06	cylindrical	*Hames and Bowring*, 1994
	Biotite	300 ± 50	*Jaeger*, 1967	196648	7.7E-06	cylindrical	*Harrison et al.*, 1985
Fission track	Zircon	240 ± 20	*Brandon et al.*, 1998				
	Apatite	110 ± 10	*Gleadow and Duddy*, 1981				

Table III.2: Theoretical closure temperature and diffusion parameters for the different thermochronometers used to compute ages

III.3.1.2. Initial and boundary conditions

Initial conditions, boundary conditions and configuration parameters are listed in Table III.3 and presented in Figure III.5. For both models, we use a crustal block of 30 km depth and 50 km width, defined with a grid of equally spaced nodes 1km apart. Initial conditions have been chosen based on the regional P-T distribution pattern, as established in the Toce Dome at the peak of amphibolite facies metamorphic conditions (ca. P = 7 kbar and T = 550-590°C) [*Vance and O'Nions*, 1992; *Todd and Engi*, 1997]. Assuming a lithostatic pressure, we convert pressure into depth and extend these conditions with a linear geothermal gradient to the base of the model. Resultant initial conditions are the following: 700°C temperature at the base (Tb) and 0°C at the surface (Ts), with a linear geothermal gradient of 23°C/km (Fig. III.5). The model starts at 30 Ma, which is the age obtained by *Vance and O'Nions* [1992] for the peak of metamorphism in this region and we only focus on the subsequent retrograde history.

On the two sides of the model, Neumann boundary conditions are assumed which permit no heat flow, that is

$$\frac{\partial T}{\partial t} = 0$$

The kinematics of deformation are imposed, with no lateral variation perpendicular to the profile (ie. 2D).

III.3.1.3. Definition of the kinematic models

Based on the geological observations described in paragraph III.2.2 and III.2.3, the following simplified kinematic models (Fig. III.5) are adopted: (A) an initial low-angle detachment model (Fig. III.5a,b) and (B) a rolling hinge model (Fig. III.5c,d).

III.3.1.3.1. Model A: Initial low-angle detachment

In model A, a planar fault (detachment) is prescribed in the crustal block with a constant dip of 30° (Fig. III.5a). A uniform exhumation rate is applied to the entire crustal block using a vertical velocity (*Vv*). The fault plane itself is therefore also uplifted with this vertical velocity (*Vv*) (Fig. III.5a). We allow *Vv* to vary by introducing two parameters: '*acc*' and '*tacc*'. The product "*acc***Vv*" is defined as the exhumation between *"tacc"* time and 0 Ma.

To account for displacement parallel to the fault, we define a velocity *Vf* in the footwall with a vector parallel to the fault plane (Fig. III.5a). The onset time of faulting is defined by *tγ*. We then introduce *tγ2* as the time when the fault velocity *Vf* can either increase or

decrease to a velocity *Vf2*. Finally, we also introduce a velocity gradient in the vicinity of the fault. This gradient is assumed to reflect a distributed ductile shear and is defined by two parameters *Wp* and *D*. *Wp* follows an exponential law:

$$Vf = Vf - \left(\frac{D - xf}{D} \right)^{Wp}$$

If $Wp = 0$, no gradient is applied to *Vf*, if $Wp > 0$ an exponential gradient is applied to *Vf*, whereas if $Wp = 1$ a linear gradient is applied to *Vf* over a distance *D* (Fig. III.5a). We introduce $t\alpha$ as the time when *Wp* will decreases linearly to zero, in turn simulating cooling of rocks through an apparent ductile-brittle transition. Figure III.5b presents the final velocity field used in the model A. Exhumation in the footwall is then the sum of *Vv* and the vertical component of *Vf*.

III.3.1.3.2. Model B: Rolling hinge model

In model B, we simulate a rolling hinge system accommodated by "subvertical shear" [e.g. *Axen and Bartley*, 1997]. A kinked detachment plane is prescribed in the crustal block (in red Fig. III.5c). Two faults dipping 80°, in opposite directions, define a lower and an upper hinge. They represent the two sets of antithetic brittle faults described by *Wawrzyniec et al.* [2001]. The lower kink is fixed at 15 km depth, below the upper kink, and steepens the detachment with a ramp of constant angle 30°. The upper kink, at the surface, rotates the fault plane to a flat geometry. Such opposite dips of the hinges would tend to thin the ramp in a perpendicular direction to the fault plane. Equal thickness would be conserved through the rolling hinge if we would use two hinges define by faults with a similar dip direction (i.e. east-down). However such east-down faults recording high temperature and middle pressure, as indicated by fluid inclusions, are not known in the SFZ [*Wawrzyniec et al.*, 1999; *Axen et al.*, 2001]. We then use a similar velocity field to that defined in model A (Fig. III.5c). Note that the fault velocity vector *Vf* rotates in the upper hinge to the horizontal.

In model B, no velocity gradient perpendicular to the fault is introduced (i.e. $Wp = 0$) (Fig. III.5c) for two kinematic reasons. (1) samples are uplifted along the detachment with the same velocity *Vf* and therefore will be less influenced by a perpendicular velocity gradient. Note the different exhumation paths followed by samples for the two kinematic models as delineated by dots in Fig. III.5a,c. (2) If $Wp > 0$, *Vf* along the detachment is minimized and therefore samples will not be efficiently exhumed (see vector *Vf* close to the detachment in model A Fig. III.5a,b).

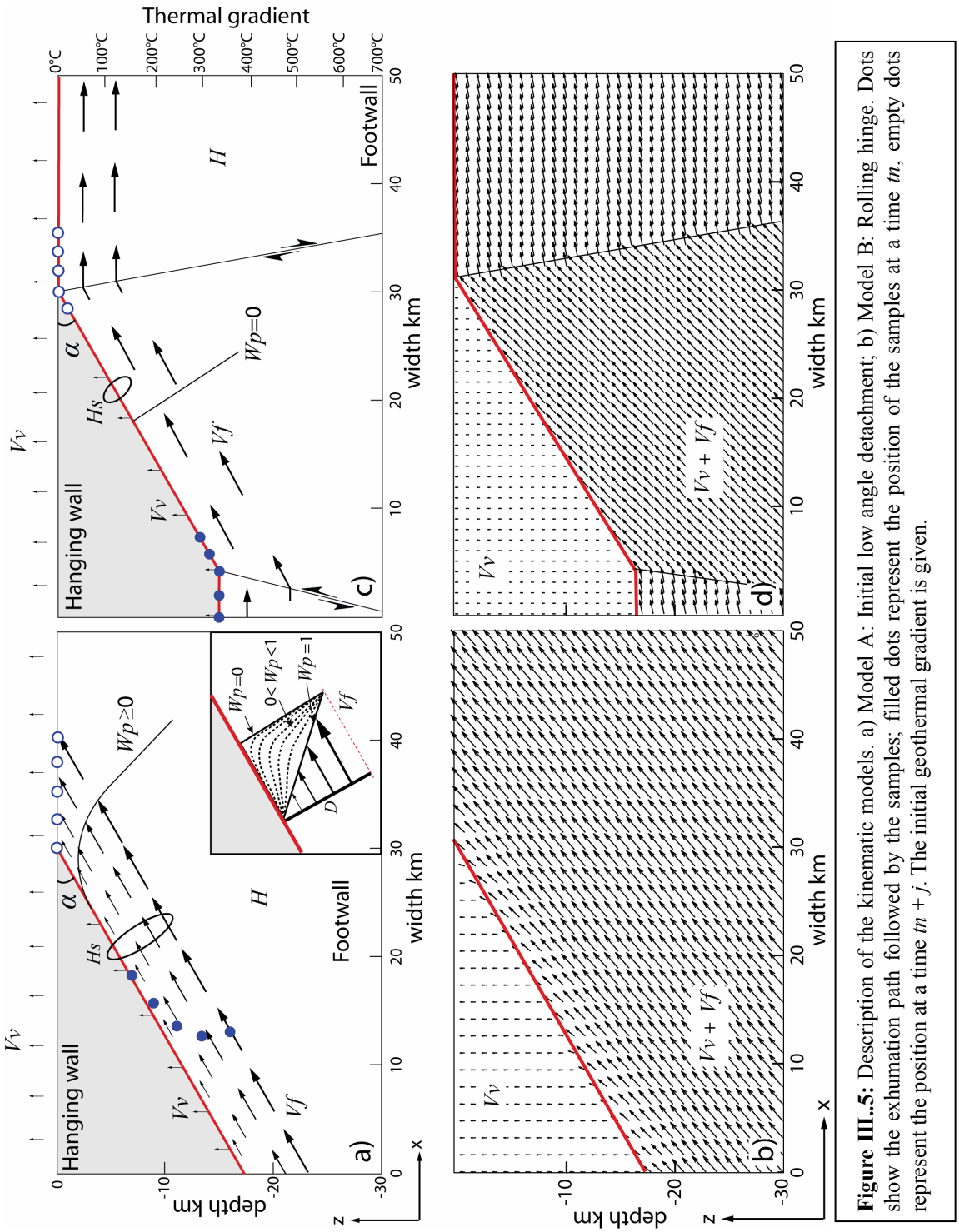

Figure III..5: Description of the kinematic models. a) Model A: Initial low angle detachment; b) Model B: Rolling hinge. Dots show the exhumation path followed by the samples; filled dots represent the position of the samples at a time *m*, empty dots represent the position at a time *m* + *j*. The initial geothermal gradient is given.

III.3.2. Neighbourhood Algorithm

We use the Neighbourhood Algorithm (NA) to constrain some of the model parameters. The NA is a two-stage numerical procedure for non-linear inversion. A detailed description of NA can be found in *Sambridge* [1999a, b]. The first search stage samples a multi-dimensional parameter space for a combination of parameters that provide satisfactory fit to the observed data.

Quality of fit to the data is assessed through an objective function that is calculated as follows:

$$\psi = \sum_{j=1}^{M} \frac{1}{n_j} \sum_{i=1}^{n_j} \frac{\sqrt{(x_i - y_i)^2}}{\sigma_i}$$

where x_i are ages sampled along an average regression of the observed data (Fig. III.4a), σ_i is the error on the average regression, y_i are ages predicted with Pecube, *M* is the number of thermochronological systems used and *n* is the number of samples in each thermochronological system. As we attempt to reproduce the trend variation of projected ages on a 2D section across the SFZ (Fig. III.4a), ages used for the inversion are sampled along a regression through each thermochronometer (see Fig. III.4a). The same weight is attributed to each set of data and therefore the same number of ages ($x_i = 31$) is sampled along the regression and the error σ_i is arbitrarily set to an identical value for each data set (variable between ± 2 and ± 3 Ma). We double the theoretical sampling in the vicinity (± 2 km) of the detachment (SL), since it is critical for our study. To obtain a significant fit, a large number of model runs are required. We use a high performance computer cluster to perform in total 10,000 models for each scenario within a reasonable time.

The second appraisal stage extracts information from the complete range of models collected, in the form of Bayesian [*Sambridge*, 1999b] measures of covariance and marginal probability density functions. The probability density function is defined as:

$$L = \exp\left[\frac{-\nu_j}{2}\psi\right]$$

where ν_j is the total number of thermochronological data (31*6) used for the search stage and ψ the misfit function calculated in the search stage. The variable model parameters solved in the inversion are listed Tables III.4 and III.5, with their corresponding possible range values. For both models we use this inverse approach to extract information on the model parameters: (1) the uniform vertical velocity *Vv* of the crustal block; (2) the parameters *acc* and *tacc* of the acceleration of *Vv*; (3) the fault velocities *Vf* and *Vf2*; (4) the timing of the fault *tγ* and *tγ2*; (5) the friction coefficient μ; (6) the gradient properties *Wp, D* and *tα* (only in the model A); and (7) the inherited age *tage*.

III.3.3. 3D model including topographic effect

To minimize the computation time, only final forward runs include the effect of a steady-state surface topography in 3D. A surface topography is added to explore age/elevation relationships and possible artifacts in the age distribution. Configuration parameters of the 3D grid are presented in Table III.5. Identical initial and boundary conditions are applied. The fault is then simulated as a fault plane within the 3D crustal block. The fit to

the data calculated in this case (Table III.6), considers the actual ages at their respective locations on the surface topography (listed in Table III.1) fitting to the 2 sigma level.

Parameters	Constant	Unit	Description
Ts	0	°C	Surface temperature
Tb	700	°C	Temperature at the base of the model
t_0	30	Ma	Starting time for the simulation
k	1.00E-06	m^2/s	Thermal diffusivity
H	1.50E-06	W/m^3	Radiogenic heat production
C	1.00E+03	J/kgK	Specific heat
ρ	2700	kg/m^3	Density
μ	variable	-	Effective friction coefficient
α	30	Degree (°)	Normal fault angle
nx,z	1581	-	Number of nodes
x	50	km	Horizontal x direction
z	30	km	Vertical z direction (Depth)
$\Delta x, \Delta z$	1	km	Grid spacing
Vvz	variable	mm/a	Vertical exhumation
acc	variable	-	Multiplication factor for *Vv*
tacc	variable	Ma	Starting time for acceleration of *Vv*
$t\gamma$	variable	Ma	Starting for the fault activity
Vfx,z	variable	mm/a	Fault velocity at time tγ
$t\gamma 2$	variable	Ma	Starting time for changing the fault velocity of *Vf*
Vf2x,z	variable	mm/a	Fault velocity at time tγ2
$t\alpha$	variable	Ma	Starting time for the localization of *Wp*
Wp	variable	-	Localization of the gradient
D	variable	km	Distance perpendicular to the fault where *Wp* is applied
tage	variable	Ma	Inherited age

Table III.3: Configuration of the model parameters.

III.4. Results

We adjust the model parameters by inverting the thermochronological data for the two kinematic models. Figures III.6 and III.10 present the results of the inversion as scatter plots in the parameter space. Each dot represents a forward model and the color scheme associated with each dot corresponds to the quality of the fit to the data set (red dot = good fit, blue dot = poor fit). Such representations highlight all plausible ranges for the model parameters. Figures III.7 and III.11 give the 1D marginal probability density functions computed for each parameter. Mean value and error calculated for each probability are given in Appendix D and do not consider bimodal distributions.

III.4.1. Model A: Initial low-angle detachment

III.4.1.1. Inversion and probability density function results

III.4.1.1.1. Timing and amount of faulting

The onset of faulting, *tγ,* is defined at 19 ± 4 Ma (Fig. III.7a). The fault velocity, *Vf,* exhibits a bimodal distribution, with maxima defined at: 2.6 ± 1mm/a and at 7 ± 1mm/a (Fig. III.6a, III.7a). The slower velocity peak is slightly more favored in the probability density function (Fig. III.7b). A variation of *Vf* is found at a time *tγ2* defined at ca. 16 ± 2 (with higher probability before 16 Ma) (Fig. III.7c) to a velocity *Vf2* of ca. 1.2 ± 0.9 mm/a (with higher probability below 1mm/a) (Fig. III.7d).
In Figure III.6c, we define three domains: (1) a steady state line where *Vf* = *Vf2*; (2) a decelerating domain (*Vf* > *Vf2)* and (3) an accelerating domain (*Vf* < *Vf2*). Most of the models leading to a good fit to the data fall within the decelerating domain, although some of them are also found for the steady state solution. Only a few acceptable models predict an increase of *Vf*. The major trend observed, therefore, predicts a reduction of the fault velocity *Vf* at ca. 16 ± 2 Ma.
A negative correlation is observed between the fault velocity, *Vf*, and the period of faster faulting (*tγ* - *tγ2*). Indeed, we notice that the faster *Vf* is*,* the later the fault starts (*tγ*) (Fig. III.6a) and the earlier the fault slows down (*tγ2*) (Fig. III.6d). Together, each set of models that results in a good fit predicts a similar amount of final fault displacement between 20 and 30 km parallel to the fault, leading to a total of 10 to 15 km vertical tectonic rock uplift (for a fault dipping at 30°).

III.4.1.1.2. Vertical velocity *Vv*

Vv is constrained to be around 0.35 ± 0.15 mm/a (Fig. III.6e, III.7e). An acceleration of *Vv* is predicted over the past 6 Ma (*tacc* in Fig. III.6f), with higher probability in the past 1 Ma (Fig. III.7f). During this period, *Vv* is multiplied by a factor, *acc,* that shows a bimodal distribution with maxima defined at 1.9 ± 0.5 and 4 ± 0.4 (Fig. III.6f, III.7g). The second peak is less favored in the probability density function (Fig. III.7g). A negative correlation is observed between *Vv* and its acceleration parameters. It appears that the faster *Vv* is, the later the acceleration occurs (Fig. III.6g) and the smaller this acceleration is (Fig. III.6h). These relationships tend to result in a similar amount of final uniform exhumation through the crustal block of ca. 11.5 km. This corresponds to the total exhumation in the hanging wall. In the footwall the vertical component of *Vf* must be added resulting in a total exhumation of ca. 21.5– 27 km.

III.4.1.1.3. Physical and geochronological properties

The exponential velocity gradient, *Wp*, is constrained by modeling to be 0.45 ± 0.15 (Fig. III.6i, III.7h) over a distance *D* of 2.5 ± 1.5 km (Fig. III.6i, III.7i). It appears in Figure III.6i that the wider *D* is, the more localized the gradient *Wp* is. This relationship always gives an overprint of the shear zone over ca. 3 km, with ~80% of the total displacement localized in the first ca. 500 m of the footwall. The time, *tα,* shows a slightly enhanced probability at ca. 11 Ma with higher probabilities also observed after 7 Ma (Fig. III.7j). The friction coefficient, *μ,* is constrained to be ca. 0.21 ± 0.05 (Fig. III.6j, III.7k).

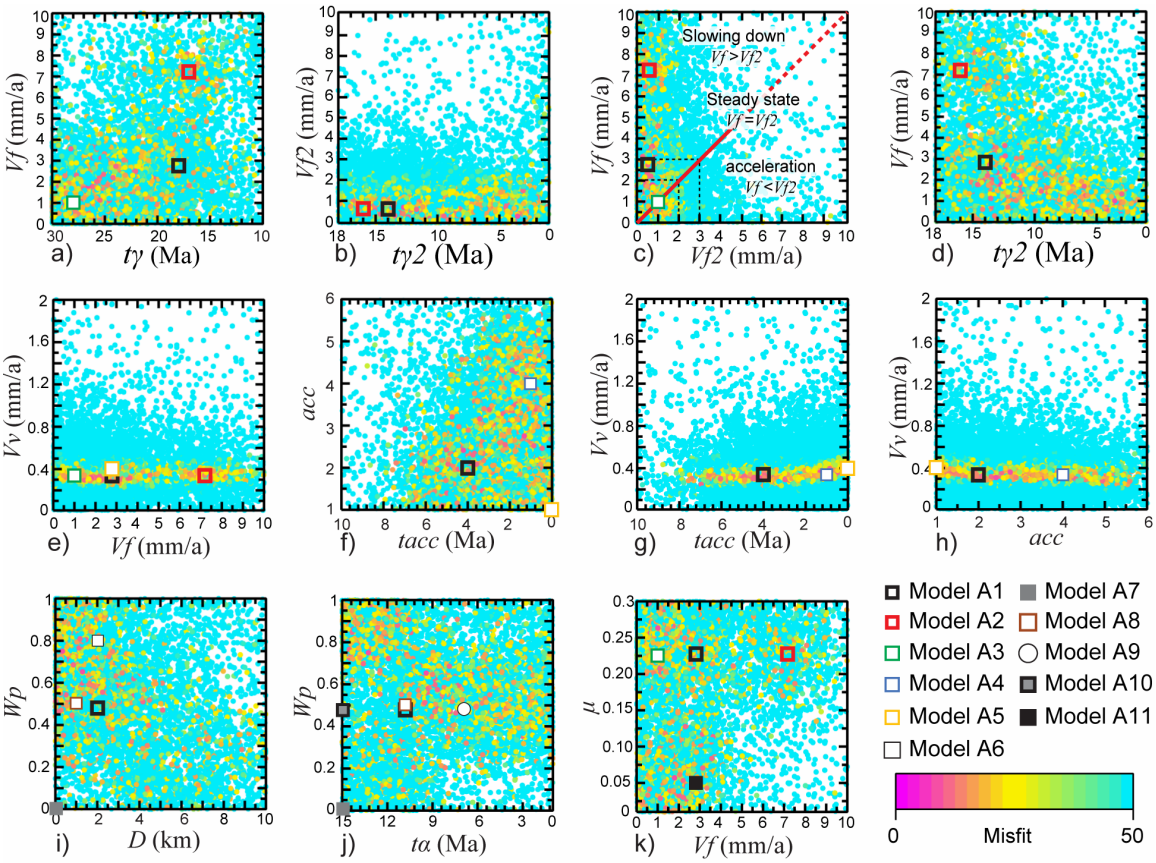

Figure III.6: Inversion results for model A. The misfit function is minimized down to a value of 8.55 for the initial low-angle detachment. Forward models A1 to A11 are also reported.

Parameters	range	A1	A2	A3	A4	A5	A6	A7	A8	A9	A10	A11
tγ	30-10	18	**17**	**28**	18	18	18	18	18	18	18	18
Vfx,z	0-10	2.8	**7.2**	**1**	2.8	2.8	2.8	2.8	2.8	2.8	2.8	2.8
tγ2	18-0	14	**16**	-	14	14	14	14	14	14	14	14
Vfx,z2	0-10	0.7	0.7	-	0.7	0.7	0.7	0.7	0.7	0.7	0.7	0.7
Vvz	0-2	0.34	0.34	0.34	0.34	**0.4**	0.34	0.34	0.34	0.34	0.34	0.34
tacc	10-0	4	4	4	**1**	**0**	4	4	4	4	4	4
acc	1-6	2	2	2	**4**	**1**	2	2	2	2	2	2
Wp	0-1	0.48	0.48	0.48	0.48	0.48	**0.8**	**0**	**0.5**	0.48	0.48	0.48
D	0-10	2	2	2	2	2	2	**0**	**1**	2	2	2
tα	15-30	10.8	10.8	10.8	10.8	10.8	10.8	10.8	10.8	**6**	**15**	10.8
μ	0-0.3	0.228	0.228	0.228	0.228	0.228	0.228	0.228	0.228	0.228	0.228	**0.005**
tage	30-100	40	40	40	40	40	40	40	40	40	40	40
Misfit		**9.490**	11.076	9.896	10.591	11.837	11.407	11.721	9.257	9.765	9.421	9.490

Table III.4: Forward models tested in model A.

Finally, an inherited age of 40 ± 6 Ma is constrained for the different thermochronometers (Fig. III.7l). This age range brackets the formation ages obtained by *Markley et al.* [1998] in the hanging wall, who obtained $^{40}Ar/^{39}Ar$ ages on syn-kinematic white micas between 36 and 41 Ma.

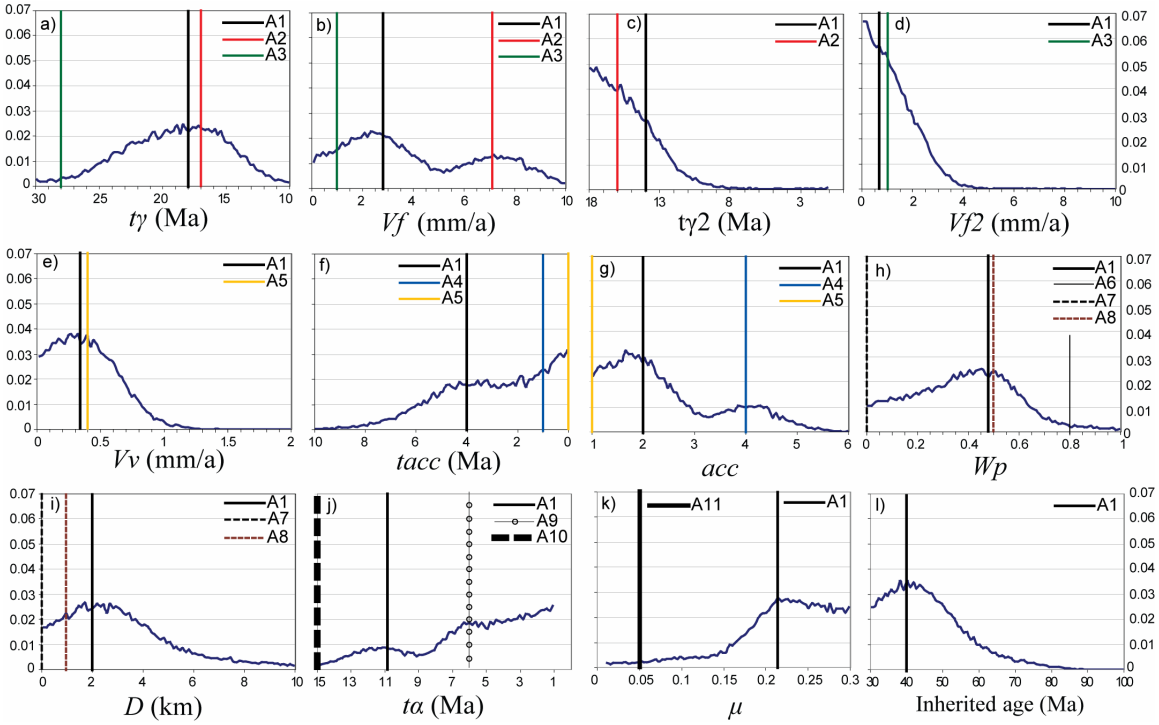

Figure III.7: Probability density functions for each parameter obtained with model A. Forward models A1 to A11 are also reported.

III.4.1.2. Forward models, predicted ages and thermal histories

We now present a suite of forward models within the parameter space. Our goal is to illustrate the sensitivity of the model to these parameters. The parameter values used in the forward models are given in Table III.4 and plotted in the parameter space in Figures III.6 and III.7.

Model A1 (Fig. III.6, III.7) presents a high probability model obtained for the inversion with an optimal misfit of 9.49 (Table III.4) and reproduces relatively well the age-distance diagram (Fig. III.8g). The fault is active from *tγ* = 18 Ma, with a fault velocity *Vf* = 2.8 mm/a, which slows down at *tγ2* = 14 Ma to 0.7 mm/a (14 Ma being the age obtained for the ductile-brittle transition in the SFZ, see Chapter II). In this model, *Vv* = 0.34 mm/a from 30 to 4 Ma and at *tacc* = 4 Ma, *Vv,* doubles (i.e. *acc* = 2) to the value *Vv* = 0.68 mm/a. We use a velocity gradient *Wp* of 0.48 over a distance D = 2 km, which corresponds to a strong localization over 480 m.

We use this model for reference and compare the successive models to it by changing only some of the parameters values. Each of these models corresponds to a set of parameters that lead to a reasonable fit to the data (χ^2 < 11.8). The models are first

presented and then discussed and compared by considering the predicted ages and thermal histories (Fig. III.8, III.9).

III.4.1.2.1. Timing and amount of faulting

In model A2 (Fig. III.6, III.7), we increase *Vf to* 7.2 mm/a (second probability peak, Fig. III.7b). To obtain a reasonable low misfit function with such a fast velocity, we need to apply it over an extremely short period of 1 Ma with *tγ* of 17 Ma and *tγ2* of 16 Ma. This is consistent with the relationships extracted from the inversion (Fig. III.6a,d). With such fast velocities, models A1 and model A2 both lead to heating of the hanging wall in the vicinity of the fault. This effect is seen in the cooling curves and the P-T curves (Fig. III.8a,b,c,d) with a deflection of the path toward higher temperature approximately at the time *tγ2* when the fast displacement stops. This increase in heat tends to reset ZFT ages in the vicinity to the SL (Fig. III.8g). Such predicted ages are still contained within the 2 sigma error margin of observed ZFT ages. In the T-t and P-t paths a faster cooling rate follows the onset of faulting *ty*. In response to *tγ2*, a slower cooling rate is observed with some delay.

In model A3 (Fig. III.6, III.7), we impose a constant fault velocity (*Vf = Vf2*) of 1 mm/a since 28 Ma. This model provides a good fit to the data (Table III.4) and perfectly reproduces the ZFT. However the probability is low if we consider the onset time of faulting *tγ* (Fig. III.7a). No additional heat can be observed in the hanging wall (Fig. III.8e,f).

These three different models, with various cooling histories, tend to a similar solution for the total amount of exhumation of ca. 21.5 to 27 km. Rocks are exhumed from similar depth and P-T conditions to that established for the peak of metamorphism for these rocks [e.g. *Vance and O'Nions*, 1992; *Todd and Engi*, 1997; *Hetherington and Le Bayon*, 2005]. However all models do not present the same probability and misfit and we favor an intermediate model as describe for model A1 (Table III.4).

III.4.1.2.2. Vertical velocity *Vv*

In the Model A4 (Fig. III.6, III.7), we test an acceleration of *Vv* (initially = 0.34 mm/a) by a factor 4 at 1 Ma (second probability peak, Fig. III.7f,g). This model also reproduces well the observed ages (Fig. III.9a) but the misfit function slightly increases (Table III.4).

In model A5 (Fig. III.6, III.7), we fix *Vv* to 0.4 mm/a without introducing any acceleration (Fig. III.7e,f,g) during the run. The resulting misfit function increases compared to model A1 and A4 (Table III.4). We observe that the predicted AFT ages from both footwall and hanging wall are too old (6.5 to 10 Ma respectively) compared to the observed ages (3.5 to 6 Ma) (Fig. III.9a). Therefore acceleration is needed in the past 6 Ma. However, we find that a steady uniform exhumation is maintained between 30 to ca. 6 Ma at ca. 0.34 mm/a.

Again, these three different models tend toward a similar solution in terms of the total amount of exhumation of ca. 11.5 km (in the hanging wall). We favor an acceleration of *Vv* at 4 Ma to twice its previous velocity (model A1) as it presents the lowest misfit and good probability.

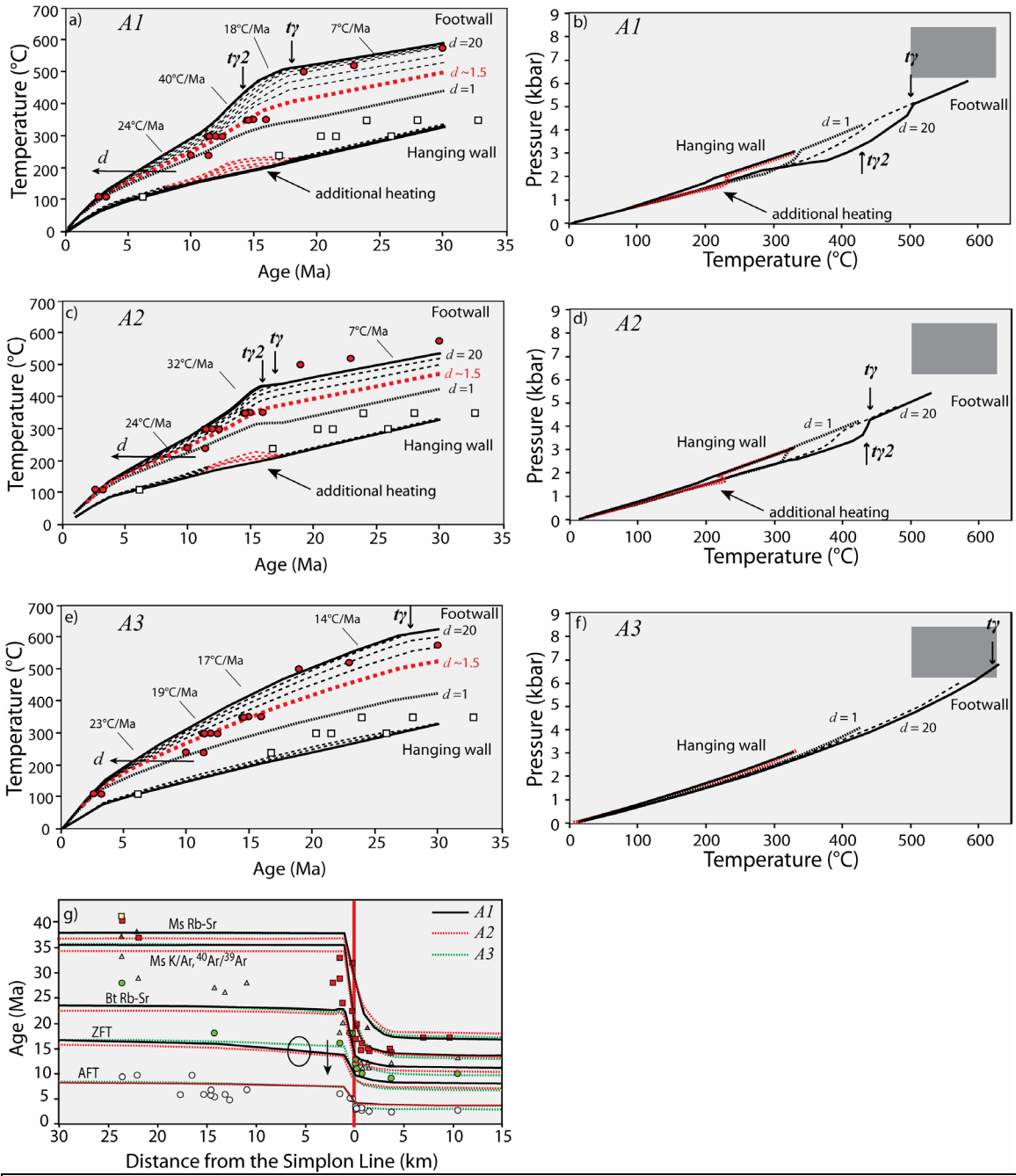

Figure III.8: Thermal history and predicted ages obtained with the model A. a) Predicted cooling history in model A1. b) Predicted P-T paths in model A1. c) Predicted cooling history in model A2. d) Predicted P-T paths in model A2. e) Predicted cooling history in model A3. f) Predicted P-T paths in model A3. g) Comparison of the predicted ages across the SFZ for the three models A1, A2 and A3. T-t and P-T paths are given for all samples that would currently be at the surface across the SFZ. We plot for reference, the theoretical cooling ages for samples located at 1.5 km distance from the SL within the footwall and hanging wall. Note that by using such a thermal model, the concept of closure temperature (*Tc*) as introduced by *Dodson* [1973] can no longer be used, as the cooling rate is not simply a function of *Tc*. d= distance from the SL; the black rectangle represent the broad P-T conditions at the peak of metamorphism established in the Toce Dome.

III.4.1.2.3. Physical and geochronological properties

In model A6 (Fig. III.6, III.7), we apply a broad near linear gradient (*Wp* = 0.8) over 2 km. The resultant misfit function increases by 17 % (Table III.4) and footwall ages in the vicinity of the fault are not well reproduced (Fig. III.9b). Similarly, in the model A7 (Fig. III.6, III.7), we do not introduce a gradient (*Wp* and *D* = 0), and this also increases the resulting misfit function by 19 % and does not perfectly reproduce the observed ages (Fig. III.9b). Therefore, a gradient over ca. 500m (as used in the reference model A1) is needed to best fit the dataset (Fig. III.9b). In model A8 (Fig. III.6, III.7), we slightly improve the misfit function by localizing the shear gradient over 250 m. Such a localized gradient (i.e. 250-500 m within a larger shear zone of 2.5 km width within the footwall) is in fact observed in the field [*Mancktelow*, 1985, 1990].
In Figure III.8, III.9b, if no distributed shear is introduced below the detachment (*Wp* = 0, model A7), ages are all similar within the footwall, reflecting a rigid block exhumation, with a similar cooling history throughout. If distributed shear is introduced (*Wp* > 0, model A1, A6, A8), then ages decrease within the footwall with increasing distance perpendicular to the detachment, showing different T-t histories and exhumation from different depths (Fig. III.8). In this case, with increasing distance from the detachment, the cooling curves (Fig. III.8a,c,e) are shifted toward younger ages (toward the left side of the X axis of the diagram). So far models A1 or A8 both perfectly reproduce the footwall ages in the vicinity of the fault with simulation of a shear zone, but they do not reproduce older ages within the Dome seen at high temperature (Fig. III.4a).
In models A9 and 10 (Fig. III.6, III.7), we consider different solutions for *tα* and we observe that the misfit function does not significantly change (Table III.4). The parameter *tα* for the ductile-brittle transition is not well constrained, as shearing is already relatively localized close to the detachment (Fig. III.6j). Similarly, in model A11 (Fig. III.6, III.7), we decrease the friction coefficient, μ, down to 0.05. The resulting misfit function is identical (Table III.4); which implies that frictional heating is also not a controlling parameter in our models.

III.4.2. Model B, Rolling hinge model

III.4.2.1. Inversion and probability density function results

In general, all parameters and probabilities are better constrained in model B because fewer parameters are being adjusted in the inversion compared to model A. Indeed the gradient parameters (*Wp*, *D* and *tα*) are not included at all in the kinematic description of model B.

III.4.2.1.1. Timing and amount of faulting

tγ presents a bimodal distribution with two maxima: one slightly more favored at ca. 27.5 ± 1 Ma and a second one at ca. 22.5 ± 1 Ma (Fig. III.10a, III.11a), which implies an older onset of faulting than in model A. *Vf* is constrained at ca. 2.7 ± 1 mm/a (Fig. III.11b). In this model *Vf* also decreases at 16 ± 2 Ma (Fig. III.10c, III.11c) to a velocity *Vf2* of 1.3 ± 0.7 mm/a (Fig. III.10d, III.11d). This is also seen in Figure III.10c, where most of the models leading to a good fit to the data set fall within the decelerating domain. Similar

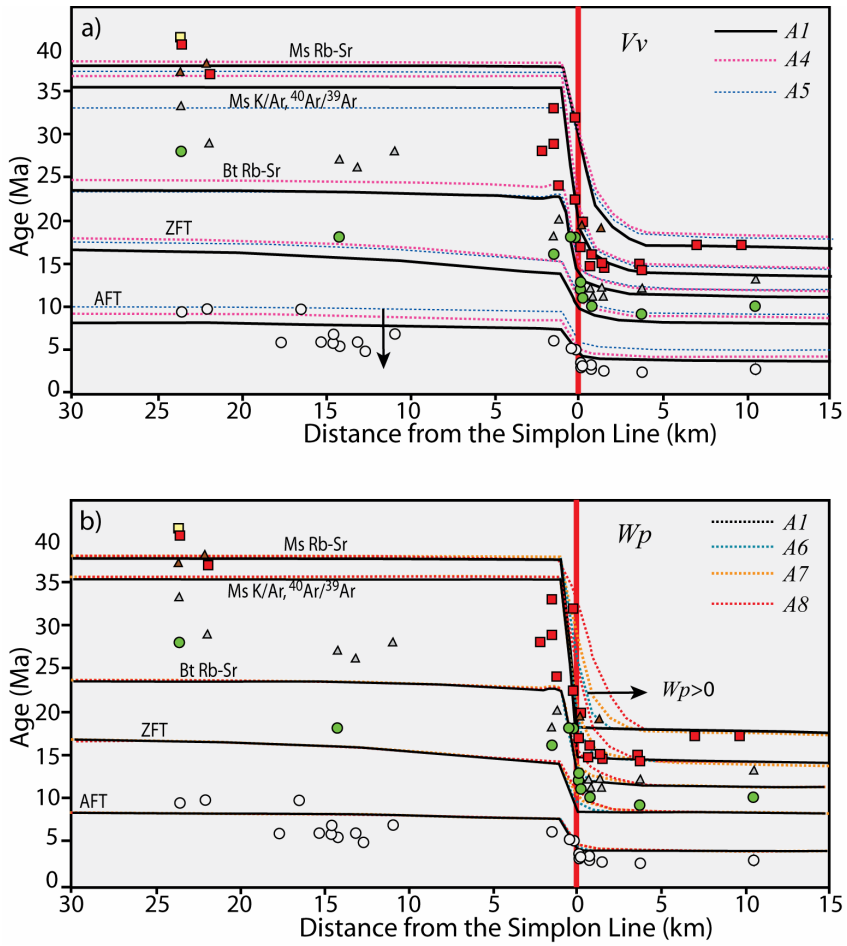

Figure III.9: Predicted ages across the SFZ. a) Comparison of various scenario for the uniform exhumation *Vv*, models A1, A4 and A5, b) comparison of various scenario of velocity gradient *Wp* in the footwall, A1, A6, A7, A8.

negative correlation can be extracted between the fault velocity *Vf* and the period of faster faulting (*tγ* - *tγ2*). The faster the fault velocity *Vf*, the later the fault starts (*tγ*) (Fig. III.10a) and the earlier the fault slows down (*tγ2*) (Fig. III.10d). Again this tends to result in a similar amount of total fault displacement of between 40 and 50 km, parallel to the fault, corresponding to a total of 20 to 25 km of vertical tectonic uplift within the footwall at the ramp level (dipping 30°). This predicted amount of tectonic rock uplift is larger than in the previous model A.

III.4.2.1.2. Vertical velocity *Vv*

As in the previous model, *Vv* is constrained at ca. 0.35 ± 0.15 mm/a (Fig. III.10e, III.11e). An acceleration of *Vv* is also predicted over the past 6 Ma (Fig. III.10f), with a high probability at 2 ± 1 Ma (Fig. III.11f). *Vv* is then multiplied by a factor, *acc,* which shows a bimodal distribution with two maxima: one slightly more favored at 1.75 ± 0.25 and one at 3 ± 0.25 (Fig. III.10f, III.11g). Similar relationships to those noted previously can be made: the faster *Vv* is, the later the acceleration occurs (Fig. III.10g) and the smaller this acceleration is (Fig. III.10h). These relationships result in a similar amount of final

uniform exhumation through the crustal block of ca. 11.5 km as previously also found in model A. This corresponds to the total exhumation within the hanging wall. Within the footwall it would lead to ca. 31.5 to 36.5 km of exhumation.

III.4.2.1.3. Physical and geochronological properties

An acceptable fit for the friction coefficient, μ, is found for the relatively high value of μ > 0.2 (Fig. III.10j). This is reflected in the probability density function (Fig. III.11h) with a slight probability peak at ca. 0.1 ± 0.025 but with the highest probability for values > 0.25.

An inherited age of 40 ± 6 Ma is implied for the different thermochronometers (Fig. III.11i), similar to the value predicted from Model A.

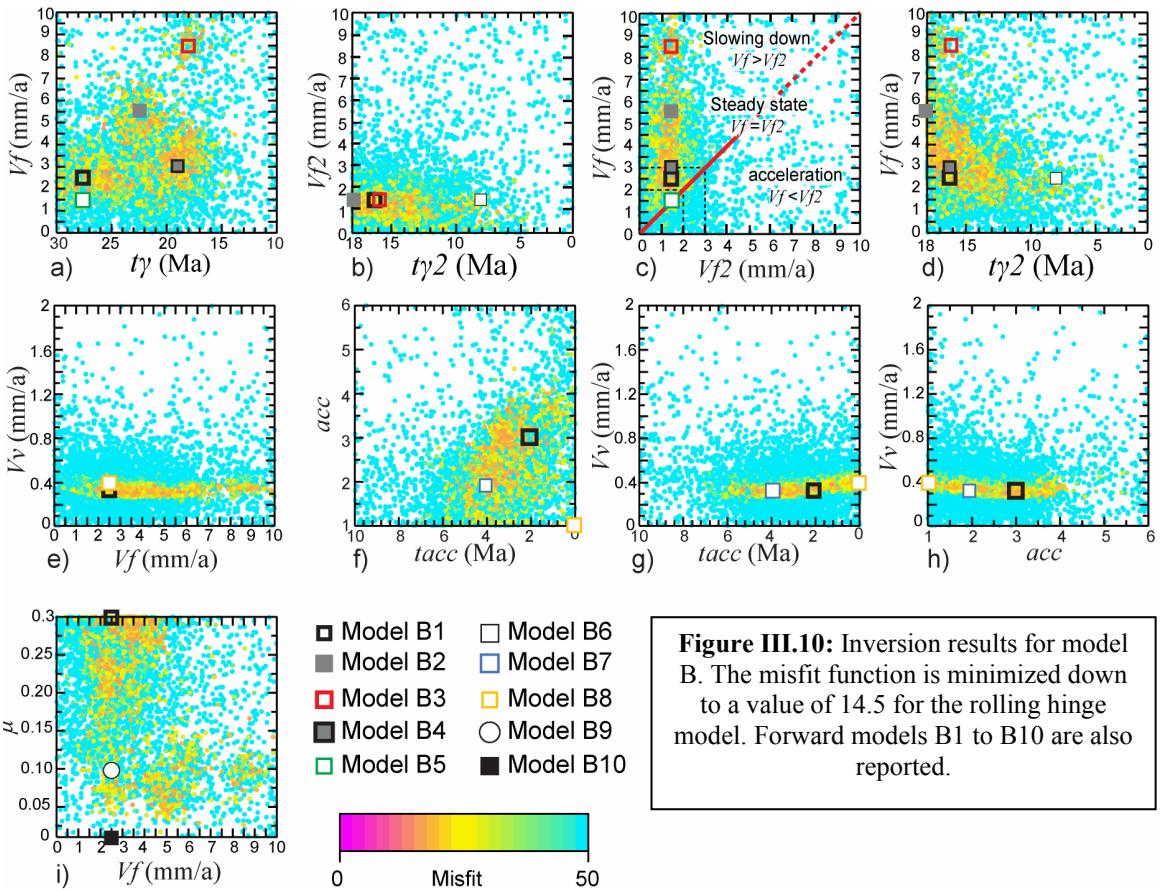

Figure III.10: Inversion results for model B. The misfit function is minimized down to a value of 14.5 for the rolling hinge model. Forward models B1 to B10 are also reported.

III.4.2.2. Forward models, predicted ages and thermal histories

We use a similar approach to the previous model A in presenting a suite of forward models to illustrate the sensitivity of the result to the model parameters. The parameter values used in the forward models are reported in Table III.5 and plotted in the parameter space in Figures III.10 and III.11. Systematically, the highest values of the misfit function are obtained with model B (15.6-18.9, Table III.5). In other words, Model A in general returns a better fit.

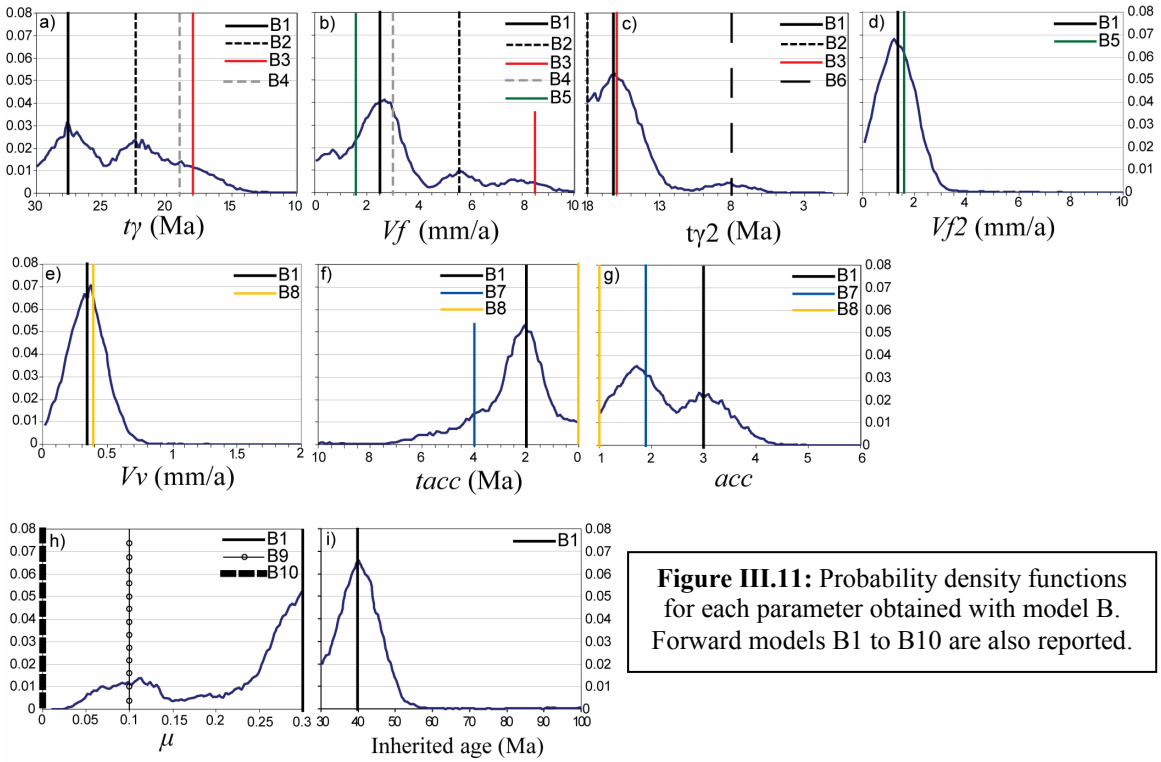

Figure III.11: Probability density functions for each parameter obtained with model B. Forward models B1 to B10 are also reported.

Parameters	range	B1	B2	B3	B4	B5	B6	B7	B8	B9	B10
tγ	30-10	27.7	**22.4**	**18**	**19**	27.7	27.7	27.7	27.7	27.7	27.7
Vfx,z	0-10	2.5	**5.6**	**8.5**	**3**	**1.6**	2.5	2.5	2.5	2.5	2.5
tγ2	18-0	16.2	**18**	**16**	16.2	-	**8**	16.2	16.2	16.2	16.2
Vfx,z2	0-10	1.4	1.4	1.4	1.4	-	1.4	1.4	1.4	1.4	1.4
Vvz	0-2	0.34	0.34	0.34	0.34	0.34	0.34	0.34	**0.39**	0.34	0.34
tacc	10-0	2	2	2	2	2	2	**4**	**0**	2	2
acc	1-6	3	3	3	3	3	3	**1.9**	**1**	3	3
μ	0-0.3	0.3	0.3	0.3	0.3	0.3	0.3	0.3	0.3	**0.1**	**0**
tage	30-100	40	40	40	40	40	40	40	40	40	40
Misfit		**15.604**	18.589	16.255	17.041	16.434	18.951	15.848	17.457	15.670	15.793

Table III.5: Forward models tested in model B.

Model B1 (Fig. III.10, III.11) represents the most likely model with an optimized misfit function of 15.6 (Table III.5). The fault is active at *tγ* = 27.5 Ma, with a fault velocity *Vf* = 2.5 mm/a, which slows down at 16 Ma to 1.4 mm/a. The uniform vertical velocity is *Vv* = 0.34 mm/a from 30 to 2 Ma and at *tacc* = 2 Ma, *Vv* increases and becomes 3 times larger (i.e. acc = 3) to 1.02 mm/a. We use this model for reference and compare different models to it by only changing some parameter values. This model predicts that ages increase within the footwall with increasing distance from the detachment (Fig. III.12g). This age variation is clearly opposite to that described in the previous model A (Fig. III.8g).

III.4.2.2.1. Timing and amount of faulting

In model B2 (Fig. III.10, III.11), we start the fault later at *tγ* = ca. 22.4 Ma (second probability peak, Fig. III.11a). To reproduce a low misfit function we need to increase the velocity *Vf* to 5.6 mm/a, over a short period of 4.4 Ma, with *tγ2* at 18 Ma. This follows the relationships extracted from Figures III.10a, d. Similarly, in model B3 (Fig. III.10, III.11), we increase this effect by starting the fault even latter at ca. 18 Ma, and by increasing *Vf* to 8.5 mm/a over a shorter period of 2 Ma, with *tγ2* at 16 Ma. Finally, in model B4 (Fig. III.10, III.11), we start the faulting at 19 Ma and slightly increase *Vf* up to 3 mm/a, without changing *tγ2*. These three models all predict higher misfit functions (Table III.5) compared to the reference model B1 and predict an additional heating of the hanging wall in the vicinity of the fault (Fig. III.12c,d) inducing a reset of the biotite Rb-Sr ages (or a ZFT reset in model B4) (Fig. III.12.g).
In model B5 (Fig. III.10, III.11), we test a constant fault velocity of 1.6 mm/a starting at 27.7 Ma and in model B6 (Fig. III.10, III.11) we only test a late onset for the velocity reduction, with *tγ2* at 8 Ma.
All these different models present an increase in ages in the footwall with increasing distance from the detachment, which leads to ages that are too old within the core of the Toce Dome (Fig. III.12g). This is also reflected in the T-t paths, where cooling curves within the footwall are shifted to older ages (toward the right side of the X axis of the diagram) with increasing distance from the detachment. The samples closest to the detachment in the footwall are exhumed from the greatest depth and the depth of exhumation is generally greater than in model A (between 31 and 36 km). Such conditions would be greater than the known peak metamorphic conditions for these rocks (Fig. III.12,b,d,f).
Samples pass through a lower hinge, which introduces a kink in the cooling curves at the time when they reach the lower hinge. From this point onward, the faster cooling rate corresponds to the onset of rock uplift along the ramp but the fault velocity, *Vf*, stays constant. Therefore the onset of a faster cooling rate in these kinematic models does not necessarily reflect onset of faulting and does not correspond to an increase in the exhumation rate, as rocks are only tectonically exhumed due to the geometry of a rolling hinge (Fig. III.1b, III.5c).

III.4.2.2.2. Vertical velocity *Vv*

In model B7 (Fig. III.10, III.11), we test an acceleration of *Vv* (initially = 0.34) by a factor 1.9 at ca. 4 Ma (first probability peak, Figure III.11g). This solution gives an equally good prediction for the observed ages (Fig. III.12h).
In model B8 (Fig. III.10, III.11), we fix *Vv* to 0.39 mm/a without adding any acceleration effect during the whole run (Fig. III.10f,g). The resulting misfit function is increased compared to the reference model B1 (Table III.5) and would also predict AFT ages that are too old within the footwall and hanging wall (Fig. III.12h).
Therefore an acceleration of *Vv* is needed in the past 4 Ma to fit AFT ages. A constant rate of exhumation is maintained between 30 and ca. 4 Ma at ca. 0.34 mm/a, but subsequently an increase in this rate is clearly required to fit the data.

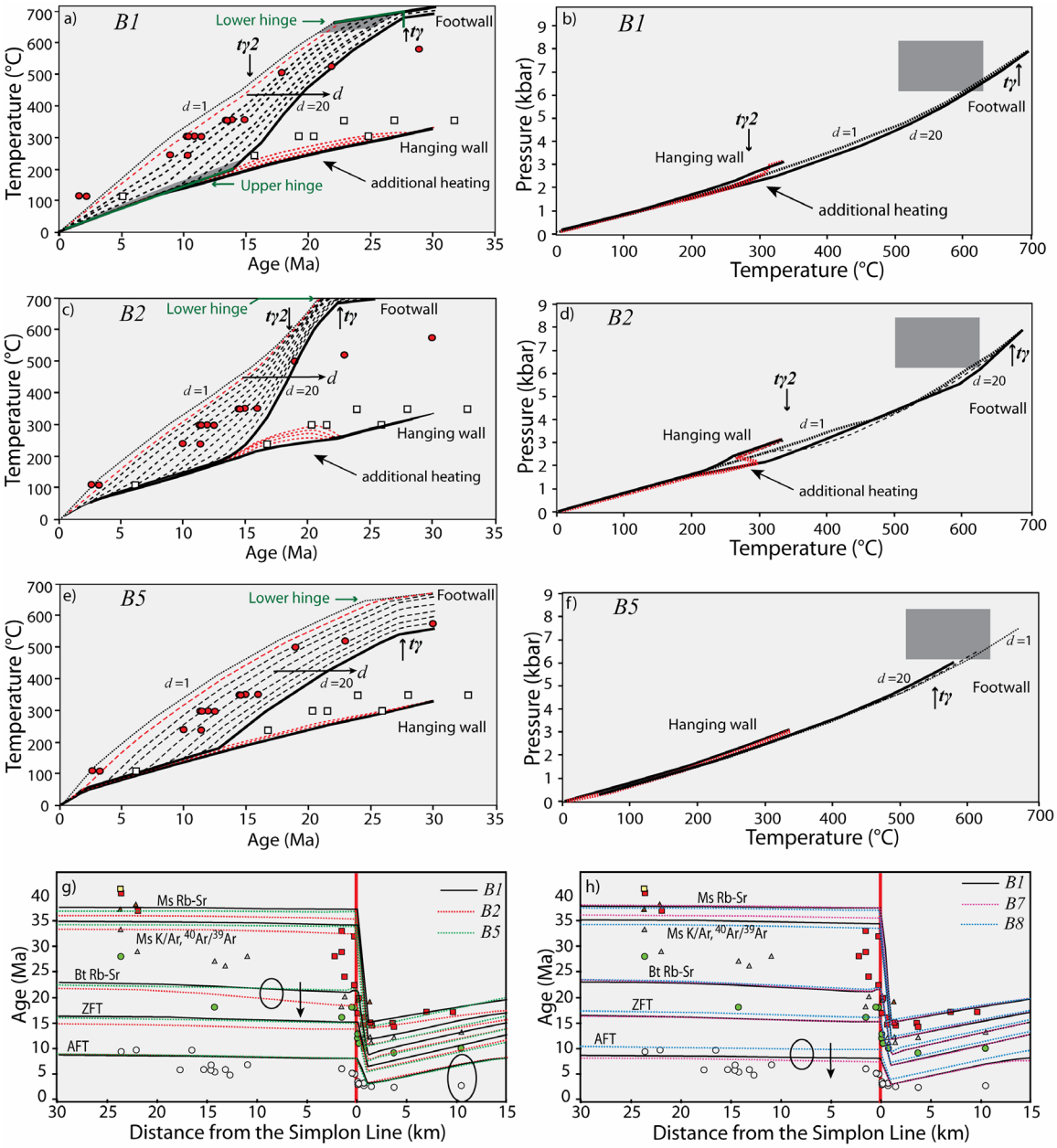

Figure III.12: Thermal history and predicted ages obtained with the model B. a) Predicted cooling history in model B1. b) Predicted P-T paths in model B1. c) Predicted cooling history in model B2. d) Predicted P-T paths in model B2. e) Predicted cooling history in model B5. f) Predicted P-T paths in model B5. g) Comparison of the predicted ages across the SFZ for the three models B1, B2 and B5. h) Comparison of the predicted ages across the SFZ for various scenarios for the uniform exhumation *Vv*, in models B1, B7 and B8. T-t and P-T paths are given for all samples that would currently be at the surface across the SFZ. We plot for reference, the theoretical cooling ages for samples located at 1.5 km distance from the SL within the footwall and hanging wall. d= distance from the SL in km; the black rectangle represents the broad P-T conditions at the peak of metamorphism established in the Toce Dome.

III.4.2.2.3. Physical and geochronological properties

In models B9 and 10 (Fig. III.10, III.11) we vary the friction coefficient, μ, in the parameter space. The resulting misfit function only changes by 1.3% (Table III.4), and frictional heating is therefore not a significant parameter in the model.

III.4.3. 3D model including the surface topography

We finally introduce a steady-state surface topography to both kinematic models to explore to what extent the age-variations observed across the SFZ are related to topography (Fig. III.4b). For both models, we first test whether the initial age decrease and subsequent age increase observed with distance into the footwall is due to a topographic effect. We then test whether the velocity gradient in *Vf* and the acceleration

Parameters	Constant	A8	A12	A13	A14	B1	B11	B12
nx,y,z	12180							
x	29							
y	14							
z	30							
Δx, Δy, Δz	1							
tγ	10-30	18	**20**	**20**	**20**	27.7	**22**	**22**
Vfx,z	0-10	2.8	**1**	**1**	**1**	2.5	**2**	**2**
tγ2	0-18	14	14	14	14	16.2	16.2	16.2
Vf2x,z	0-10	0.7	0.7	0.7	0.7	1.4	**1**	**1**
Vvz	0-2	0.34	0.34	0.34	**0.4**	0.36	0.36	**0.39**
tacc	0-10	4	4	4	**0**	2.6	2.6	**0**
acc	1-6	2	2	2	**1**	1.9	1.9	**1**
Wp	0-1	0.5	0.5	**0**	0.5	-	-	-
D	0-10	1	1	**0**	1	-	-	-
tα	15-30	10.8	10.8	10.8	10.8	-	-	-
μ	0-0.3	0.228	0.228	0.228	0.228	0.3	0.3	0.3
tage	30-100	40	40	40	40	40	40	40
Misfit		**11.956**	10.580	10.709	14.037	**34.865**	16.096	18.890

Table III.6: Forward models tested including the topography effect for model A and B.

of *Vv* required in the previous models are not simply artifacts. Corresponding misfit functions for the different forward models are reported in Table III.6 and the predicted ages are presented in Figure III.13 for only three thermochronometers (AFT, ZFT and muscovite $^{40}Ar/^{39}Ar$). The fault is simulated as a plane which does not strictly follow the Simplon Line outcrop (Fig. III.13a). This effect induces in some regions local error on the predicted ages because the actual hanging wall is simulated as being part of the footwall unit (Fig. III.13a). In this region ages are not reported to the graph and we consider this zone as a blind zone.

III.4.3.1. Model A: Initial low-angle detachment

We first use the parameters of model A8. This model includes a gradient in the velocity *Vf* and an acceleration of *Vv*. A reasonable fit to the data is found (Table III.6). In Fig. III.13b, muscovite $^{40}Ar/^{39}Ar$ ages appear to be slightly younger than observed ages. We therefore decreased the fault velocity, *Vf*, down to 1mm/a and started the fault at 20 Ma in model A12 (Table III.6). The fit is slightly improved (Table III.6), with the age-variation (Fig. III.13b) well reproduced. Therefore, the increase in the age-distance curves observed within the footwall after a distance of 5 km from the detachment can be well explained by a topographic effect in model A.

We then test a model A13 (Table III.6), where no distributed ductile shear is included (*Wp* and *D*=0). We observe (Fig. III.13c) that no older white mica $^{40}Ar/^{39}Ar$ ages very close to the detachment are reproduced. Therefore, the topography alone cannot explain the observed age decrease within the footwall and the presence of a velocity gradient is required.

Finally, in model A14 (Table III.6), we remove the acceleration of *Vv*. As seen in Figure III.13b, predicted AFT ages predicted are still too old and it follows that the topography alone cannot explain such young AFT ages. We therefore confirm the need for an acceleration in the exhumation rate throughout the whole block in Pliocene time.

We present in Figures III.13e,f,g the simulated age pattern obtained for the optimal model A12. We observe a positive correlation between elevation and predicted cooling ages for each thermochronometer, which explains the apparent age increase seen in white mica $^{40}Ar/^{39}Ar$.

III.4.3.2. Model B: Rolling hinge model

We use a similar approach for considering the effect of topography on model B. We first present model B1 with an optimal misfit function as obtained from the inversion (including an acceleration of *Vv*). A very high misfit function is obtained (Table III.6). In Figure III.13d, we observe that all predicted ages are too young. Therefore, in model B11 (Table III.6), we decreased the fault velocities *Vf* down to 2 mm/a and *Vf2* down to 1 mm/a, and we started the fault at 22 Ma. The fit is slightly improved (Table III.6). White mica $^{40}Ar/^{39}Ar$ age-variation is well reproduced, but predicted ZFT and AFT ages are too old compared to observed ages within the dome (Fig. III.13d). The age-increase is reproduced in the footwall far from the detachment, but it is also predicted for low-temperature thermochronometers, where this variation is not observed, and the age-decrease within the footwall close to the detachment is not reproduced in model B.

Figures III.13e,i,j present the simulated age pattern obtained for model B11. The positive correlation between elevation and predicted ages is still observed within the hanging wall, but in the footwall we mainly observe an increase in ages within the dome for all thermochronometers.

Finally, in model B12 (Table III.6), we do not introduce an acceleration effect. As seen in Figure III.13d, this again results in AFT ages are too old and the topography alone cannot explain such young AFT ages. As for model A, this confirms a need for increased exhumation during the Pliocene.

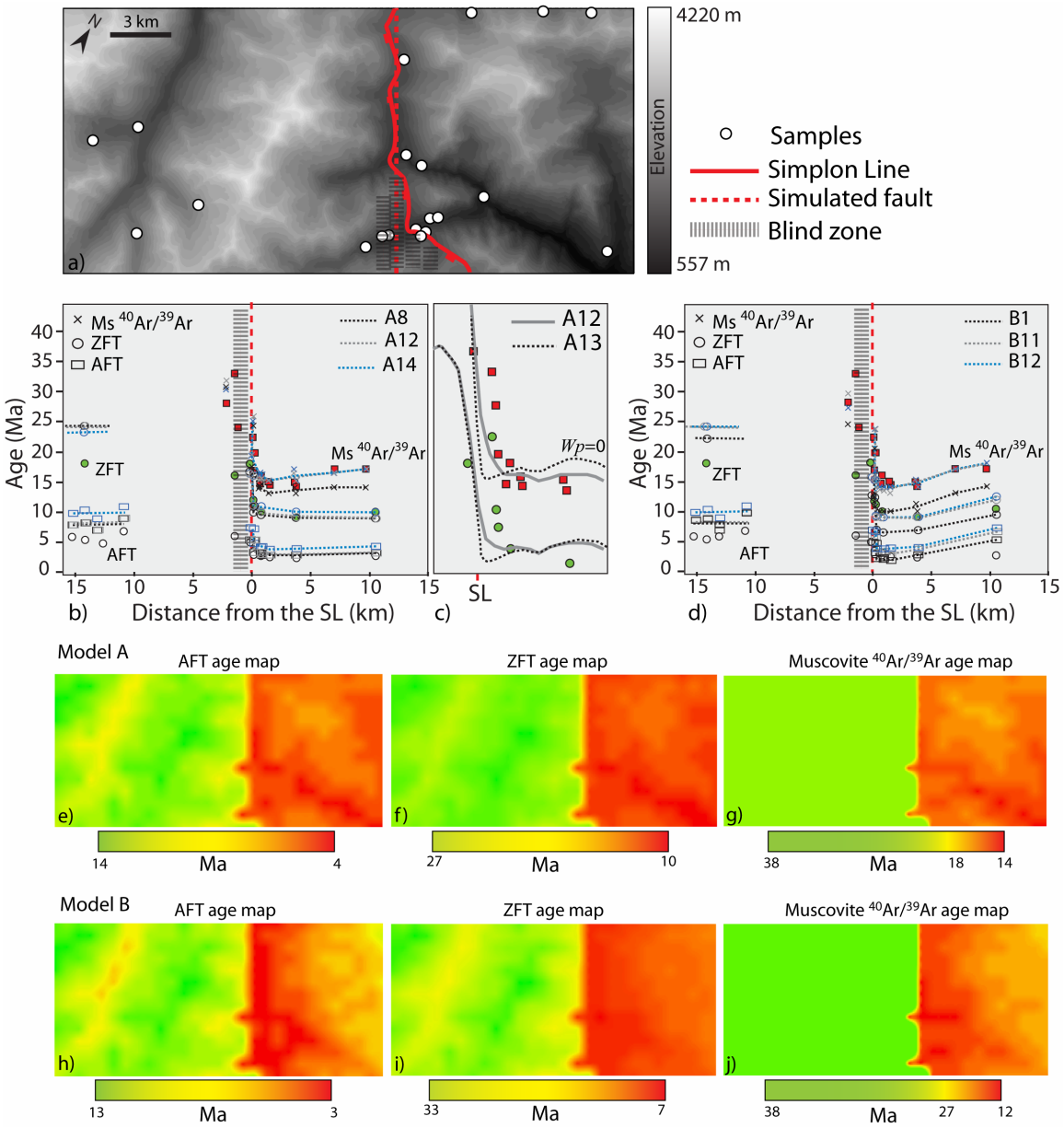

Figure III.13: Topographic effect. a) Present day topography with sample location. b) Regression through each predicted individual age for model A including the topography. c) Predicted ages with and without velocity gradient, enlarged in the vicinity of the fault zone. d) Regression through each predicted individual age for model B including the topography. e) AFT predicted age map, model A12. f) ZFT predicted age map, model A12. g) White mica $^{40}Ar/^{39}Ar$ predicted age map, model A12. h) AFT predicted age map, model B11. i) ZFT predicted age map, model B11. j) White mica $^{40}Ar/^{39}Ar$ predicted age map, model B11. The blind zone corresponds to a zone of induced error in the model where ages are not considered.

III.5. Discussion

III.5.1. Uniform exhumation rate, *Vv*

The uniform vertical velocity, *Vv*, affects the entire crustal block, independently of the kinematics involved. A similar final amount of exhumation of around 11.5 km, related to *Vv*, is therefore predicted in both models. Samples from the hanging wall (away from the footwall to avoid possible reset during exhumation) are only affected by *Vv* and only reflect this regional exhumation.

An acceleration of *Vv* is required in both models over the past 4 Ma (Fig. III.7f, III.11f). *Vv* accelerates with a factor that depends on the onset time of the acceleration: (1) it doubles if the acceleration starts at 4 Ma (recognized in both models), (2) it is 3 times larger if it starts at 2 Ma (model B), or (3) it is 4 times larger, if it starts at 1 Ma (model A). We favor the first scenario at 4 Ma as it is recognized in the two models; it also presents the highest probability and the lowest misfit function. Between 30 and 4 Ma, however, the inversion method predicts a constant exhumation rate maintained at ca 0.34 mm/a, which is very well defined in both models (Fig. III.7e, III.11e).

If we ignore this acceleration, and test a more commonly accepted exhumation rate of 0.4 mm/a, both with and without a topography effect [*Grasemann and Mancktelow*, 1993; *Schlunegger and Willett*, 1999; *Bernet et al.*, 2001] (models A5, A13 and B8, B12), then for both models A and B the predicted AFT ages would be considerably older (10 Ma) than the observed ages (6 Ma) within the hanging wall. Therefore, we are forced to introduce an acceleration of the exhumation rate in the past 4 Ma, the effect of which is only recorded by the AFT ages in our study case. Therefore for further constraint on the onset time and amount of increase of this exhumation rate, the future studies should consider such as well the use of thermochronometers of lower temperature as (U-Th)/He or OSL-thermochronology (Optically Stimulated Luminescence) [e.g. *Herman et al.*, 2008].

This acceleration of the exhumation rate in the Pliocene, as is needed uniformly within both footwall and hanging wall, can be related to an increase in the erosion rate. Indeed, a Pliocene increase of the erosional flux is also described on the regional scale in the Alps from sedimentary records in the foreland basin [*Kuhlemann et al.*, 2001; *Kuhlemann et al.*, 2002; *Kuhlemann and Kempf*, 2002; *Vernon et al.*, 2008]. Two different interpretations have been proposed for this acceleration in the erosion rate: (1) isostatic rebound of the mountain belt in response to climate changes and wetter conditions, possibly induced by intensification of the Gulf Stream in the Atlantic ocean at 4.6 Ma [*Cederbom et al.*, 2004]; and (2) climate changes augmented by the base sea level fall during the Messinian salinity crisis [*Willett et al.*, 2006], dated at 5.96 Ma [*Krijgsman et al.*, 2002].

III.5.2. Timing and amount of faulting on the Simplon Fault Zone

In both kinematic models, there is no unique solution for the onset time of faulting and for the velocities involved. The inversion results provide a range of solutions with a correlation between velocities and timing of faulting. As a result, the different solutions always predict a similar total amount of exhumation, although the cooling and exhumation rate are different for each model. Each scenario, however, does not lead to

the exact same fit to the data and does not present the same probability. Favored scenarios are now discussed.

III.5.2.1. Model A: Initial low-angle detachment

In the model A, with a low-angle detachment initiated and slipping at low-angle, the onset time of faulting is predicted to be 19 ± 4 Ma (Fig. III.7a). This age range brackets the age of 18 Ma used by *Grasemann and Mancktelow* [1993] for the starting time of the SFZ in their model. A resulting drop in the computed cooling curves is observed at the starting time *tγ* (Fig. III.8a), as well as in the P-T curves (Fig. III.8b), and obviously corresponds to the onset of a faster cooling rate.
Most of the models predict that the fault velocity decreases at ca. 16 ± 2 Ma (Fig. III.7c). The onset time of this reduction in the velocity is also reflected in the T-t and P-T paths, with a slight decrease in the cooling rate following *tγ2* (Fig. III.8a,b). This effect can be related to a decrease in the exhumation rate as rocks were exhumed through the ductile-brittle transition. This was also proposed by *Grasemann and Mancktelow* [1993]. The ductile-brittle transition is dated at ca. 14 to 14.5 Ma from $^{40}Ar/^{39}Ar$ and Rb-Sr dating on syn-kinematic white micas (Chapter II) and this age of 14.5 Ma is included within the high probability density function range for *tγ2* (Fig. III.7c). This decrease in fault velocity could also reflect an apparent decrease in the exhumation rate due to a decrease in the dip angle of the detachment during ongoing extension. However, all brittle faults observed in footwall and hanging wall with similar kinematics to that of the SFZ indicate that σ1 is always effectively vertical [*Grosjean et al.*, 2004] and there is no evidence for any rotation of these faults. Furthermore, Neogene extension in the Central Alps does not result in marked thinning of the crust, probably due to ongoing orogen-perpendicular horizontal shortening [*Mancktelow and Pavlis*, 1994] and a strong isostatic rebound effect would not be expected. For these reasons, we do not consider the decrease in exhumation rate at *tγ2* to be the effect of decreasing fault plane dip during extension.
A fast period of faulting (> 6 mm/a) over a very short period of 1 Ma from 17 to 16 Ma followed by a slower fault velocity of 0.7 mm/a (model A2, Table III.4) would yield a higher misfit function compared to other scenarios and would tend to reset ZFT in the hanging wall in the vicinity of the fault (Fig. III.8g). A steady-state solution with onset of faulting at 28 Ma and a slip rate of 1 mm/a gives a poor probability regarding the onset of faulting (Fig. III.7a). Therefore an intermediate model A1 is favored. This model gives the highest probabilities (Fig. III.7a,b) and the lowest misfit to the dataset (Table III.4). It predicts that the fault starts at 18 Ma, initially slipping at 2.8 mm/a and slows down at ca. 14 Ma to 0.7 mm/a.
The resulting overall vertical tectonic uplift is predicted to be between 10 and 15 km (for a fault plane dipping 30°). This result is similar to the 15 km of displacement obtained by *Grasemann and Mancktelow* [1993]. The resulting total amount of exhumation is ca. 22 to 27 km, corresponding to similar peak P-T conditions to those currently observed in samples at the surface.

III.5.2.2. Model B: Rolling hinge model

In model B, the onset time of faulting has a larger probable range between 30 and 18 Ma (Fig. III.11a). The starting time, *tγ*, is only reflected in the T-t curves if samples are exhumed from a lower depth than the lower hinge (Fig. III.12a,c,d). Most of the models

predict that the fault velocity decreases at ca. 16 ± 2 Ma, which also can be interpreted as reflecting the onset of localization of the deformation during the ductile-to-brittle transition leading to a decrease in the exhumation rate. Different scenarios of tectonic uplift can be extracted. A short period of fast (> 5 mm/a) faulting during 2 to 4 Ma followed by a slower fault velocity (model B2 and 3 Table III.5) yield a higher misfit function compared to the reference model B1. A steady-state solution is also possible but does not give the closest fit to the data (model B5, Table III.5). Therefore for this model we favor the scenario of model B1, which yields good probability (Fig. III.11) and an optimal misfit function (Table III.5). It predicts that the fault starts at 27.7 Ma, slips at 2.5 mm/a and slows down at ca. 16.2 Ma to 1.4 mm/a. The total vertical tectonic uplift is predicted to be between 20 and 25 km (for a fault plane dipping 30°), resulting in a total exhumation of the footwall of 31 to 36 km, which is greater than would be consistent with the estimated maximum metamorphic P-T conditions.

III.5.3. Resulting exhumation rate

Exhumation rates in the Lepontine Dome are still a matter of debate, and different rates have been proposed [e.g. *Grasemann and Mancktelow*, 1993; *Schlunegger and Willett*, 1999; *Bernet et al.*, 2001]. The onset of fast cooling rate during a retrograde history can either reflect footwall exhumation through a lower hinge [*Ketcham*, 1996] at constant fault velocity, or the onset of faster exhumation rate due to fault activity and/or increase in erosion rate [*Grasemann and Mancktelow*, 1993; *Schlunegger and Willett*, 1999]. The following given exhumation rates correspond to favored scenarios presenting the highest probability and the closest fit to the data.

III.5.3.1. Model A: Initial low-angle detachment

In model A, the onset of faulting leads to a faster cooling rate (Fig. III.8b). As the surface is fixed, rock uplift and exhumation rate are identical. In the hanging wall, the exhumation rate is equal to Vv = 0.34 mm/a between 30 and 4 Ma and increases in the Pliocene at ca. 4 Ma to ca. 0.68 mm/a. In the footwall, the exhumation rate corresponds to the sum of Vv and the vertical component of Vf. For the optimal model A1 (Table III.4) and with a fault plane of 30°, the resulting exhumation rate between 30 and 18 Ma is 0.34mm/a, between 18 and 14 Ma it increases to 1.74 mm/a, between 14 and 4 Ma it diminishes to 0.69 mm/a, and finally it accelerates during the Pliocene at ca. 4 Ma to 1.37 mm/a.

III.5.3.2. Model B: Rolling hinge model

In model B, the onset of fast cooling (Fig. III.12b) is related to the exhumation of the samples through a lower hinge. The geometry of a rolling hinge implies that the rocks uplift is horizontally transferred above the upper hinge. This does not influence the resulting exhumation rate. Even so, greater rock uplift is obtained in this model. As a result, the resulting exhumation rate is similar within footwall and hanging wall and is equal to Vv at ca. 0.34 mm/a between 30 and 4 Ma and increases to 0.68 mm/a at ca. 4 Ma. Contrary to the model A, this model does not imply an increase in the erosion rate within the footwall.

III.5.4. Comparison of the two kinematic models

The predicted age-distance curves for the two kinematics models, presented in Figures III.8g and III.12g, are significantly different within the footwall. In model A, ages decrease with increasing distance from the detachment. This age-variation reflects a distributed ductile shear over 2.5 km with a strong localization over 250-500 m below the detachment, as observed in the field [*Mancktelow*, 1985]. On the contrary, in model B, ages increase with increasing distance from the detachment. This age variation is also reflected in the T-t histories, where the cooling curves for the different sample locations within the footwall are shifted in opposite directions with increasing distance from the detachment (Figures III.8a, III.12a).

Such an age increase within the footwall of a rolling hinge system (model B) has been recognized for a long time [e.g. *Dallmeyer et al.*, 1986; *Lee and Sutter*, 1991] and has often been used to determine slip rate along low-angle detachments [e.g. *Foster et al.*, 1993; *Wells et al.*, 2000; *Brady*, 2002; *Collettini and Holdsworth*, 2004; *Brichau et al.*, 2006; *Carter et al.*, 2006; *Brichau et al.*, 2008]. The age decrease within the footwall (model A) is less commonly reported, but was clearly described for the SFZ [*Mancktelow*, 1992; *Grasemann and Mancktelow*, 1993]. In the original dataset (Fig. III.4a), both age variation trends are observed, with first a decrease of ages described over 4 km and a subsequent increase. These age variations are mainly observed for the high-temperature thermochronometers (especially white mica $^{40}Ar/^{39}Ar$).

The final 3D models show that the age increase variation can be explained with model A if the effect of surface topography is included (Fig. III.12 b). In contrast, decrease in ages with distance into the footwall cannot be explained with model B, even including surface topography. Model B reproduces well the white mica $^{40}Ar/^{39}Ar$ ages within the footwall, but it predicts ages for the low thermochronometers (AFT and ZFT) within the dome that are too old when compared to the observed ages. Therefore, only model A reproduces the full age variation observed in Figure III.4b.

Different fault velocities are involved in the two kinematic models, leading to exhumation of rocks from initially different depths. Model A exhumes rocks from ca. 20 to 25 km, consistent with peak metamorphic conditions, while model B predicts the exhumation of rocks from greater depths of ca. 31 to 36 km. Such conditions exceed the peak conditions of metamorphism, which are well established in the Toce Dome (P ~ 7 kbar and T = 550-590°C) [*Vance and O'Nions*, 1992; *Todd and Engi*, 1997; *Hetherington and Le Bayon*, 2005]. Finally, the inversion finds a closer fit (optimal misfit function) to the dataset with a kinematic model of a detachment that initiated and slipped at low-angle (model A) (Table III.4). For all these reasons, we favor the kinematic model in which the detachment initiated and slipped at a low-angle to explain the observed age pattern on the SFZ. A rolling hinge model does not seem to be applicable to the SFZ. Contrary to classic core complexes, for example from the Basin and Range province [e.g. *Spencer*, 1984; *Buck*, 1988; *Wernicke and Axen*, 1988; *Axen and Bartley*, 1997], the unroofing along the SFZ was not necessarily associated with a corresponding isostatic rebound, because unroofing related to orogen-parallel extension was compensated by ongoing orogen-perpendicular shortening [e.g. *Mancktelow and Pavlis*, 1994; *Avigad et al.*, 2001]. This conclusion differs from that of previous studies [*Wawrzyniec et al.*, 1999; *Axen et al.*, 2001; *Wawrzyniec et al.*, 2001]. They proposed that the SFZ represents a rolling hinge system accommodated by both subvertical shear and flexural failure. Their

interpretation was supported by P-T estimations from synkinematic fluid inclusions within vein filling fractures of postmylonitic structures. How can their observations be reconciled with our proposed near planar low-angle detachment?
(1) One possibility is that slip on such postmylonitic structures, corresponding to both high and low P-T conditions, was not large enough to produce significant uplift of the footwall as in a rolling hinge structure.
(2) Another possibility is that the high P-T conditions estimated for the earliest postmylonitic structures, characterizing the lower hinge, were overestimated. Their interpreted P-T conditions were based on the intersection of fluid inclusion isochores with an estimated P-T path for the samples. However, two possible intersections between isochores and the P-T path appear to be possible in their model, at either high or low P-T conditions. Only the high P-T intersection (T >500°C and P 5.5-7 kbar) was discussed in support of a rolling hinge model. It should also be noted that the P-T path used in their model is still poorly established in the Toce Dome. The peak of metamorphism appears to be well established in the literature [*Vance and O'Nions*, 1992; *Todd and Engi*, 1997; *Hetherington and Le Bayon*, 2005] but the retrograde P-T path in the Simplon region is not well known, and the interpretation of the intersection with the fluid inclusion isochores requires that the P-T history is accurately determined.
Figure III.14 presents a compilation of known P-T conditions from the Toce Dome. The only P-T path reconstructed for this region from the Toce Dome was determined by *Frank* [1983], using calibrated geothermometers and barometers. In Figure III.14 estimates for the peak of metamorphism are also given [*Vance and O'Nions*, 1992; *Todd and Engi*, 1997; *Hetherington and Le Bayon*, 2005], as are the P-T paths and isochores used in establishing the rolling hinge model of *Wawrzyniec et al.* [1999], *Axen et al.* [2001] and *Wawrzyniec et al.* [2001]. The predicted P-T-t path extracted from this study for the optimized model A1 (Table III.4) is also shown in Figure III.14. This figure illustrates the poor constraints on the retrograde P-T path in the Toce Dome. By considering a different retrograde P-T history for the SFZ, isochores determines from the fluid inclusions could intersect at lower P-T conditions, similar to those established for postmylonitic structures considered to reflect the upper hinge (T~300°C and P~2-4 kbar). As a result, the P-T conditions on the earliest postmylonitic structures could be overestimated and both sets of fractures (west-down and east-down) could have similar P-T conditions. In this case, the two opposite sets of brittle fractures observed within the footwall could instead be interpreted as conjugate sets of brittle faults developed during exhumation through the ductile-brittle transition [*Grosjean et al.*, 2004] at ca. T~300°C and P~2-4 kbar [*Wawrzyniec et al.*, 1999].

III.5.5. Implications for the foreland basin

As noted above, we consider that model A (model A1) involving a detachment of fixed and low (25-30°) initial dip, provides the best fit to thermochronological and field data from the SFZ. In this case, unroofing of the footwall requires an increase in the exhumation rate coupled with a corresponding increase in the erosion rate. There should be a signature of this increased erosion recorded within the sedimentary deposits of the foreland basin. An increase in the amount of sedimentation is indeed observed between 18 and 16 Ma [*Kuhlemann et al.*, 2001; *Kuhlemann and Kempf*, 2002], which was considered by these authors to reflect the up-doming of the Central and Eastern Alps.

This period of increased sedimentary budget fits well with the period of faster faulting on the SFZ, established in the current study to occur between 18 and 14 Ma.

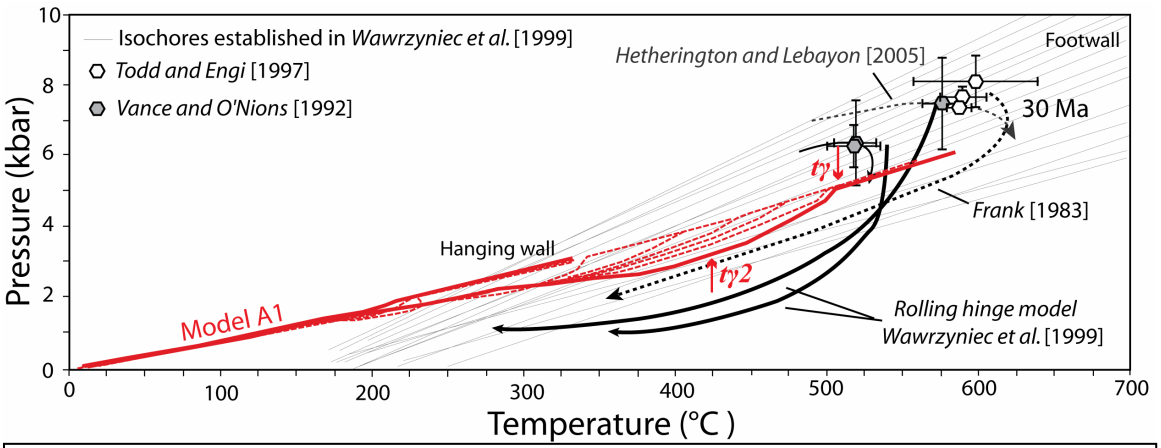

Figure III.14: Compilation for the retrograde P-T path in the Toce Dome.

III.6. Conclusions

A 2-3D thermo-kinematic model, including steady-state topography and coupled with a formal inversion method, was used to reconstruct the thermal history and the exhumation pattern across the Simplon Fault Zone in the Central Alps. Two models were tested, a detachment initiated and slipping at low-angle (25-30°), and a rolling hinge model.

The large amount of thermochronological data available from the Toce Dome was inverted to extract information on the timing and amount of faulting for both possible models. Several scenarios could explain the thermochronological dataset, with correlations between timing of faulting and fault velocities always leading to a similar amount of total relative vertical displacement between footwall and hanging wall. However these scenarios do not have the same probability and degree of fit to the data. The resulting vertical tectonic uplift is ca. 10 to 15 km in the case of an initial low-angle detachment, with the associated increase in exhumation rate and erosion rate occurring mainly between 18 and 14 Ma at a rate of ca. 1.74 mm/a in the footwall. This period of increased erosion is reflected by a corresponding increase in the sedimentary budget in the foreland basin over this time period. The rolling hinge model predicts a larger vertical tectonic uplift of 20 to 25 km but this does not involve a corresponding increase in the exhumation rate, as the rock uplift is transferred horizontally above the upper hinge. These two models predict very different T-t histories, with opposite age variation with distance into the footwall. Comparison of predicted thermochronological ages with the large existing dataset shows that a rolling hinge model does not reproduce the observed pattern of ages, predicting ages that are too old within the core of the Toce Dome. With a rolling hinge model, rocks would also be exhumed from a greater depth than the known peak conditions of metamorphism in this region. The results suggest that a rolling hinge model cannot be applied to the Simplon Fault Zone and therefore, at the local scale of the study area, no isostatic rebound is recorded on this fault structure in response to unloading. This can be explained by compensation due to orogen-perpendicular

horizontal shortening as the Simplon Fault Zone is developed during orogen-parallel extension.
Finally, a regional scale increase in the exhumation rate at ca. 4 Ma, from 0.34 mm/a to 0.68 mm/a, is established from the apatite fission-track ages. This probably reflects an increase of the erosion rate in response to large scale climate changes during the Pliocene.

IV. 3D geometry of the Simplon Fault Zone in the Central Alps

IV.1. Introduction

An interplay between large scale upright folding and low-angle faulting is typical of many detachment systems [e.g. *Malavieille*, 1987a; *Yin*, 1991; *Chauvet and Séranne*, 1994; *Mancktelow and Pavlis*, 1994; *Avigad et al.*, 2001; *Martinez-Martinez et al.*, 2002]. In such structures, generally two sets of fold orientations are described, with fold axes parallel and perpendicular to the regional extension direction. These folds strongly control the 3D geometry of exhumation, leading to the elongated domal forms described as "turtleback" [e.g. *Drewes*, 1959; *Miller*, 1991, 1992; *Holm et al.*, 1994; *Mancktelow and Pavlis*, 1994] or "metamorphic core complexes" [e.g. *Wernicke*, 1981; *Lister*, 1984; *Malavieille*, 1993]. Both sets of folds are considered to develop synchronously with extension, based on structural relationships and relative chronology [e.g. *Mancktelow*, 1992; *Yin and Dunn*, 1992; *Chauvet and Séranne*, 1994]. They are attributed either to one single or two distinct events. Possible single processes that have been proposed are: (1) emplacement of syn-extensional plutons [e.g. *Yin*, 1989; *Reynolds and Lister*, 1990; *Yin*, 1991; *Yin and Dunn*, 1992]; (2) pushing upwards by undulatory crustal roots [*Yin*, 1989, 1991]; and (3) shearing of layers originally oblique to the shear plane [*Malavieille*, 1987b]. In models proposing two distinct processes, the formation of extension-orthogonal folds is most commonly attributed to isostatic unloading in a rolling hinge system [e.g. *Spencer*, 1985; *Buck*, 1988; *Wernicke and Axen*, 1988; *Martinez-Martinez et al.*, 2002]. However, alternative mechanisms have also been proposed, such as an antithetic shear zone in the lower plate [*Reynolds and Lister*, 1990] or reverse drag induced by an unrelated deeper detachment [*Bartley and Wernicke*, 1984; *Spencer*, 1984]. Extension-parallel folds were either attributed to synchronous horizontal compression perpendicular to the extension direction [e.g. *Spencer*, 1984, 1985; *Bartley et al.*, 1990; *Chauvet and Séranne*, 1994; *Mancktelow and Pavlis*, 1994; *Avigad et al.*, 2001; *Martinez-Martinez et al.*, 2002] or to primary fault corrugations developed during fault slip [e.g. *Davis and Hardy*, 1981; *Spencer*, 1985]. In this paper, we characterize the 3D interplay between upright folding and extensional faulting in a low-angle detachment system, the Simplon Fault Zone (Fig. IV.1) [*Mancktelow*, 1985; *Mancel and Merle*, 1987; *Mancktelow*, 1990; *Steck and Hunziker*, 1994], located in the European Central Alps. This fault zone shows a complex overprint of extension-parallel and extension-orthogonal folds affecting both the brittle detachment and the ductilely deformed rocks of the footwall. This pattern has been interpreted as due to either (1) orogen-parallel extension coeval with perpendicular shortening [*Mancktelow*, 1992; *Mancktelow and Pavlis*, 1994] or to (2) two extensional stages separated by a perpendicular compressional stage [*Steck and Hunziker*, 1994]. Many studies in the Central Alps highlight the necessity of using 3D models to represent such complexly deformed regions, either using 2.5D block diagrams [e.g. *Steck*, 1984; *Mancktelow*, 1985; *Steck and Hunziker*, 1994] or full 3D models [*Maxelon*, 2004; *Maxelon and Mancktelow*, 2005; *Maxelon et al.*, 2009].

We first characterize the structural relationships between shearing and folding. Then the chronology of extension-parallel and orthogonal folds is discussed, based on relative dating using the cooling history and on direct $^{40}Ar/^{39}Ar$ dating of newly grown

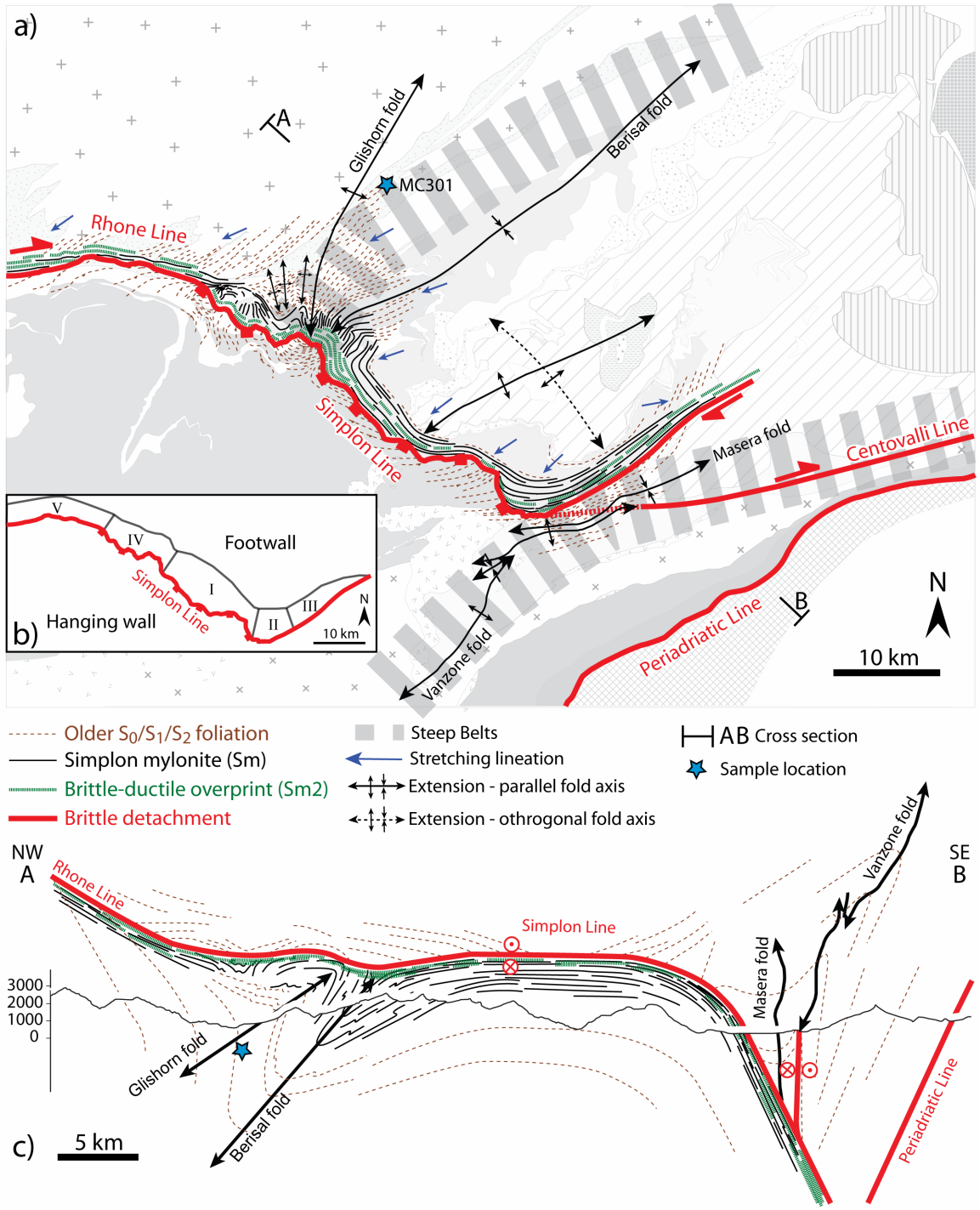

Figure IV.1: 3D geometry of the SFZ a) Structural map of the SFZ. b) Subdivision into geographical regions I to V. c) NW-SE cross section perpendicular to the extension direction.

synkinematic minerals. Finally, we model the 3D interplay between extensional faulting and folding using GeoModeller software based on the potential method [*Lajaunie et al.*, 1997; *Aug et al.*, 2004], employing a similar approach to that developed by *Maxelon* [2004], *Maxelon and Mancktelow* [2005], and *Maxelon et al.* [2009].

IV.2. Coupling between folding and extensional faulting

IV.2.1. 3D geometry of the low-angle detachment system

The Simplon Fault Zone (SFZ), located in the Central Alps, exposes an extensional ductile shear zone with subsequent brittle overprint partly localized on a brittle normal detachment (or "Simplon Line": SL) (Fig. IV.1). Clear kinematic indicators give a sense of shear top-to-SW, with the stretching direction oriented NE-SW over the entire fault zone (Fig. II.2c, IV.2a,b). In the central region (region I, Fig. IV.1b), the brittle detachment dips at a low-angle of 25-30° toward the SW. The ductile Simplon mylonites (Sm) are sub-parallel to the detachment, with a slightly lower average dip of 22° (Fig. II.2c).

In the southern area (region II and III, Fig. IV.1b), both the sub-parallel Sm mylonites and the brittle detachment dip steeply to the SSE (62° toward 155°, Fig. II.2c) within the so-called Southern Steep Belt described by *Milnes* [1974]. In this region, the overall displacement corresponds to a dextral strike-slip fault zone (Fig. II.3).

The northern region (region IV, Fig. IV.1b) presents a more complex 3D geometry. The Sm mylonites and brittle detachment are no longer parallel (Fig. IV.1a). The Sm mylonites are folded around the Berisal synform and Glishorn antiform within the Northern Steep Belt [*Milnes*, 1974], with the fold axis parallel to the regional extension direction (Fig. IV.1a) [*Steck*, 1984; *Mancel and Merle*, 1987; *Mancktelow*, 1990, 1992]. Throughout the Berisal synform, a clear reversal in the sense-of-shear (associated with a change in asymmetry of the quartz crystallographic preferred orientation) has been described from the inverted limb of the fold [*Mancel and Merle*, 1987; *Mancktelow*, 1990, 1992]. The interference between these extension-parallel folds and the SW shearing locally developed a finite constrictional strain with a predominantly linear fabric (Fig. IV.2c).

The folded Sm mylonites are transected by a narrower band of greenschist facies mylonites (Sm2) concordant with the Simplon brittle detachment (Fig. IV.2d). Sm2 is strongly developed close to the detachment itself and is also overprinted by broad scale folds [*Mancktelow*, 1992]. Both folded and transected mylonites, Sm and Sm2, are developed during retrograde metamorphic conditions, but the Sm2 mylonites are more chlorite-rich, developing more discrete shear plane (Fig. IV.2e), and are locally brecciated. They developed at lower grade, close to the ductile-brittle transition [*Mancktelow*, 1990, 1992; *Axen et al.*, 2001]. Both mylonites show identical kinematics [*Mancktelow*, 1992; *Steck and Hunziker*, 1994].

In the Rhone Valley (region V, Fig. IV.1b), the Sm mylonites and brittle detachment are parallel and show a change in strike, with the fault zone oriented E-W (Fig. IV.1). As a result, the displacement along the Rhone Valley is dominantly dextral strike-slip with a slight normal component, with the stretching lineation consistently pitching ca. 20° SW within the foliation plane (Fig. II.2c).

IV.2.2. Extension-orthogonal folding

Within the footwall, the dip of the Sm mylonites flattens with increasing distance from the detachment, leading to an overall domal shape (the so-called Toce Dome [*Preiswerk*, 1921; *Wenk*, 1955; *Steck and Hunziker*, 1994]) with a fold axis perpendicular to the regional extension direction [e.g. *Mancktelow*, 1990; *Steck and Hunziker*, 1994]. This

domal shape is reflected in the SE (regions II and III, Fig. IV.1b), by opposite plunge directions of the stretching lineation within the foliation plane (Fig. II.2c) [*Mancktelow*, 1985]. This domal shape described in the ductile mylonites is not seen in the latest brittle history, with the brittle striation always nearly horizontal (Fig. II.2c). This implies that the regional up-doming had effectively ceased before this late brittle overprint.

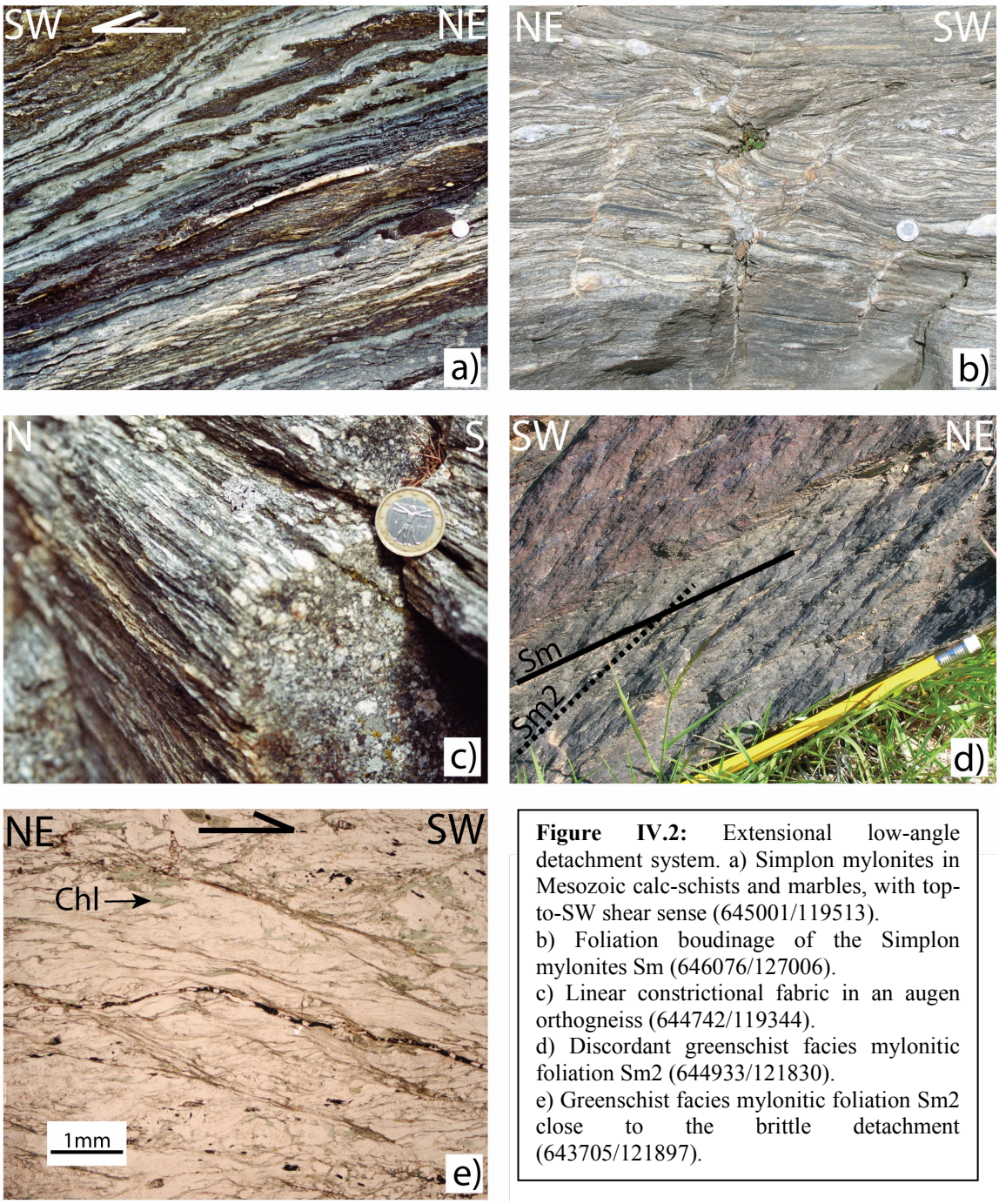

Figure IV.2: Extensional low-angle detachment system. a) Simplon mylonites in Mesozoic calc-schists and marbles, with top-to-SW shear sense (645001/119513).
b) Foliation boudinage of the Simplon mylonites Sm (646076/127006).
c) Linear constrictional fabric in an augen orthogneiss (644742/119344).
d) Discordant greenschist facies mylonitic foliation Sm2 (644933/121830).
e) Greenschist facies mylonitic foliation Sm2 close to the brittle detachment (643705/121897).

IV.2.3. Extension-parallel folding

In regional syntheses of deformation in the Central Alps, these structures are described as the "*D4* phase" or as "SE vergent backfold" structures [e.g. *Milnes et al.*, 1981; *Maxelon and Mancktelow*, 2005]. The wavy to open folds (Fig. IV.3a,b) are generally upright to moderately overturned to the SE, with a new axial planar cleavage only locally developed (Fig. IV.3c). They were developed during retrograde metamorphic conditions and are restricted to the Northern (Glishorn, Berisal folds) and Southern Steep Belts (Vanzone, Masera folds). Figure IV.4 presents the measured orientations of the *D4* fold axes and axial planes. In the Northern Steep Belt, the backfolds are oriented SW-NE, with the mean orientation of fold axes plunging shallowly at 12° toward 234° (Fig. IV.4a,b). This orientation is effectively parallel to the stretching lineation, which has a mean orientation plunging 19° toward 240° (Fig. IV.4a). Axial planes are more variable in dip and dip direction (Fig. IV.4b). In style, these folds are generally open with a rounded hinge geometry (Fig. IV.3a,b).

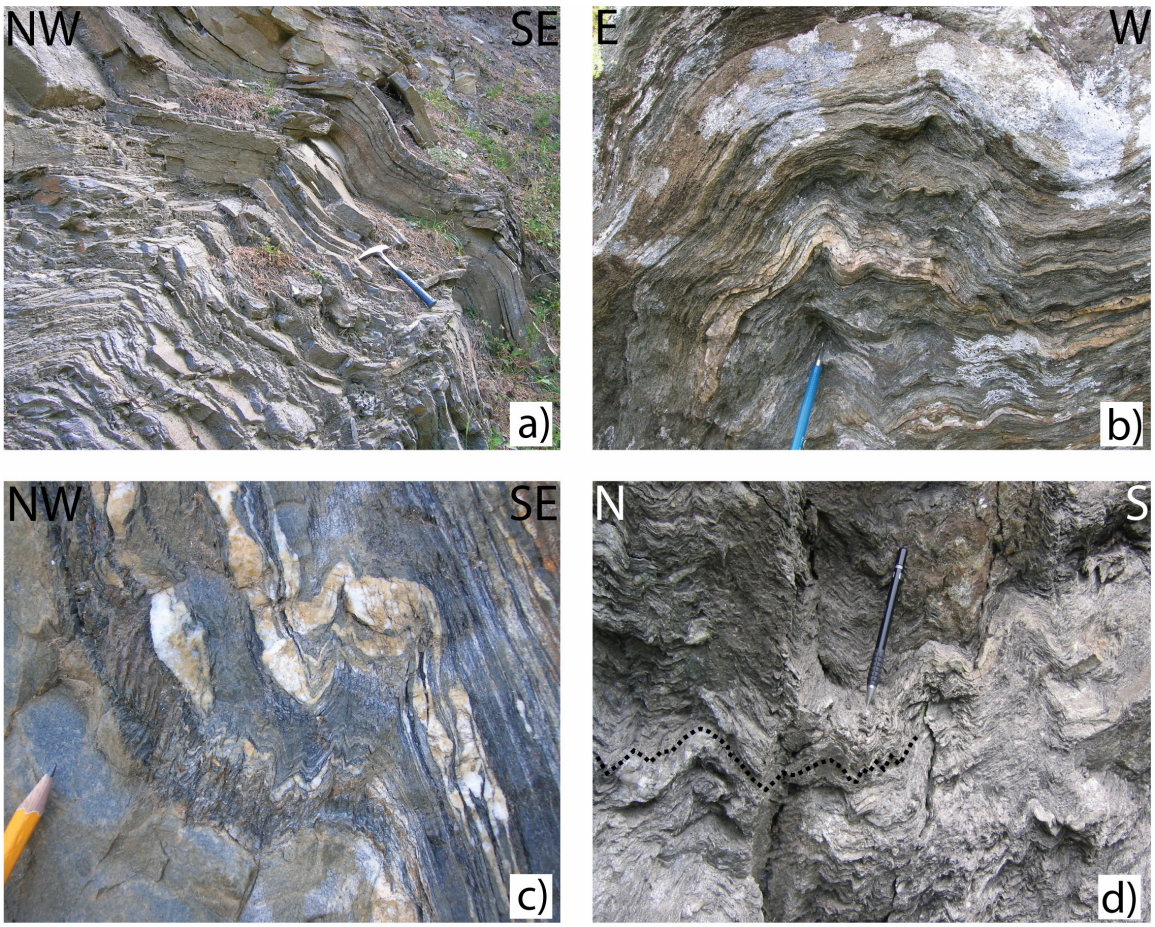

Figure IV.3: Extension-parallel folds (D_4 backfolds). a,b) D_4 open parasitic folds (641204/127695 – 642748/119806). c) S_4 crenulation cleavage (646136/130530). d) Masera kink-like parasitic folds (668781/109542).

In the Southern Steep Belt, the Masera backfold is an open synform, with common parasitic folds showing a chevron or kink-like geometry (Fig. IV.3d), whereas the

Vanzone backfold is a tight antiform (Fig. II.3a). The backfolds have steep axial planes striking WSW-ENE and a mean orientation of fold axes plunging shallowly, with an average of 7° toward 259° (Fig. IV.4c,d). Further to the SW, the axial planes rotate into a SW-NE strike direction [e.g. *Keller et al.*, 2005a].

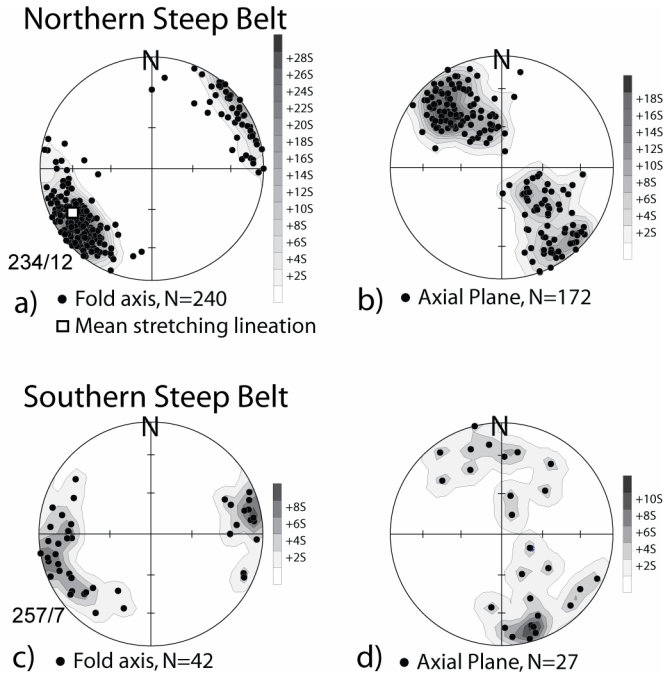

Figure IV.4: Field measurements related to D_4 backfolds in the Northern and Southern Steep Belt, given with the corresponding density contours.
Lower hemisphere, equal area projection, maximum values for fold axis.

IV.2.4. The regional Alpine structural history and the SFZ overprint

The main fabric observed in the Central Alps corresponds to an earlier fabric $S_{(0)/1/2}$ (Fig. IV.1a,c), previously acquired during two major regional deformation phases *D1* and *D2* [e.g. *Milnes et al.*, 1981; *Steck*, 1984; *Grujic and Mancktelow*, 1996; *Maxelon and Mancktelow*, 2005]. The first phase of deformation observed, *D1*, corresponds to the development of a NW-vergent nappe stack. It develops an intense isoclinal folding on a kilometer scale associated with the development of an S_1 axial plane cleavage (Fig. IV.5a). *D1* is followed by tight to isoclinal post-nappe refolding on a regional scale, *D2* (e.g. the Monte Leone and Wandfluhhorn folds), associated with the development of an S_2 axial plane cleavage (Fig. IV.5b,c). The *D2* fold axes are SW-NE oriented, parallel to the trend of the orogen [e.g. *Maxelon and Mancktelow*, 2005] and associated with prograde metamorphism. A third deformation phase, *D3* [e.g. *Maxelon and Mancktelow*, 2005], is also observed but it is only poorly represented in the Simplon region. It causes wavy to open folding of the whole tectonostratigraphy, with axial planes commonly trending NW-SE to N-S, leading to the so-called "cross-folds" [e.g. *Steck*, 1998]. This phase develops a weak crenulation lineation, sometimes also associated with a weak crenulation cleavage S_3 (Fig. IV.5d).
Overprinting relationships of these pre-existing deformation phases are observed within both footwall and hanging wall and are variably developed (Fig. IV.6). Such structures have been modeled previously in the regional 3D study of *Maxelon and Mancktelow* [2005].

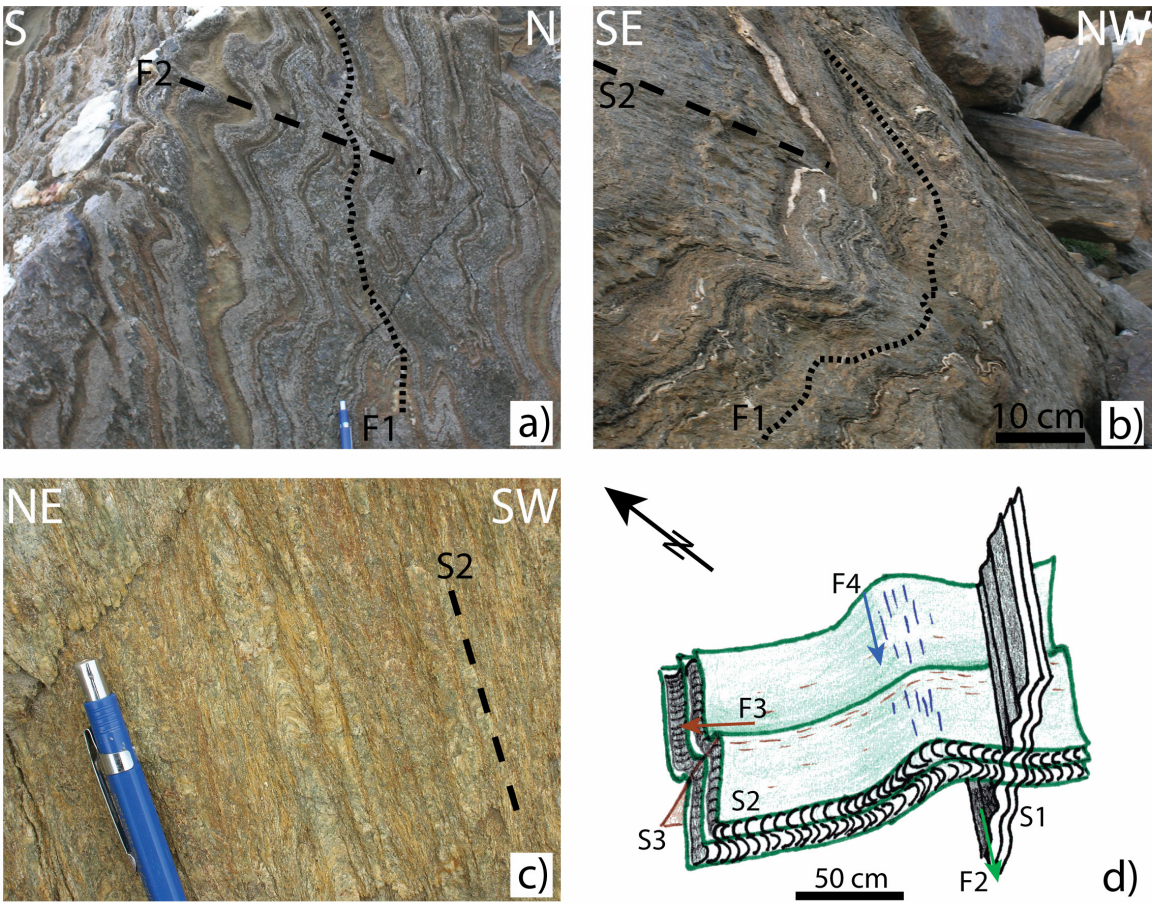

Figure IV.5: Pre-existent deformation structures. a) F1 folds refolded by F2 (649898/123263) b) F1 folds refolded by F2, with development of an S_2 axial plane schistosity (649384/123073) c) S_2 crenulation cleavage overprinting the main S_1 foliation (635033/122807). d) Synthetic sketch of the principal deformation phases observed on an outcrop scale (635083/122450).

In the footwall in the vicinity of the SFZ (i.e. within ~3 km of the SL), *D2* folds (F2) associated with an axial cleavage, S_2, are well preserved, as for example seen at the Simplon Pass (Fig. IV.6a). In this area, garnet porphyroblasts that grew during the Lepontine metamorphism have been dated at ca. 30 Ma [*Vance and O'Nions*, 1992]. These garnets clearly overgrow both F2 folds and S_2, implying prograde development of the S_2 fabric (Fig. IV.6b). In the same general outcrop (along a SW-NE profile), the same S_2 fabric is clearly overprinted by retrograde top-to-SW shearing, leading to the formation of asymmetric pressure shadows developed on garnet porphyroclasts. Such structures are interpreted to reflect transposition of the previous S_2 fabric into the Simplon shear zone. For the first few kilometres into the footwall, the new Simplon mylonitic Sm fabric and the previous S_2 foliation are therefore effectively parallel (Fig. IV.6), and a distinction between Sm and S_2 is not straightforward. Indeed, *Steck* [1990] argued that the Simplon mylonites, Sm, were nothing else than a more strongly deformed zone within a wide *D2* shear zone observed within both the footwall and the hanging wall.

However, in the central region (region I, Fig. IV.1b), the SL clearly crosscuts the fabric $S_{(0)/1/2}$ of the hanging wall and a clear discontinuity between footwall and hanging wall

could be established. Toward the SE (region II and III, Fig. IV.1b), foliation planes within footwall and hanging wall have a parallel strike and no clear geometrical discontinuity in the structural trend is observed. As a result, the prolongation of the SFZ in this region was controversial and *Keller et al.* [2005a] have argued that the SFZ did not continue to the SE and that the footwall and hanging wall fabrics were indistinguishable.
It is thus clear that the SFZ low-angle detachment system affects an already complexly deformed region, showing overprinting relationships between several deformation phases, and this results in an overall complex 3D geometry (Fig. IV.7). In this Chapter we mainly focus on the interplay between extensional faulting and upright folding corresponding to the most recent deformation phase, *D4*, affecting this complexly deformed region. However, characterization of the SFZ fabric (Sm and Sm2) in comparison to the older $S_{1/2}$ fabric is also relevant in an attempt to distinguish these two structures.

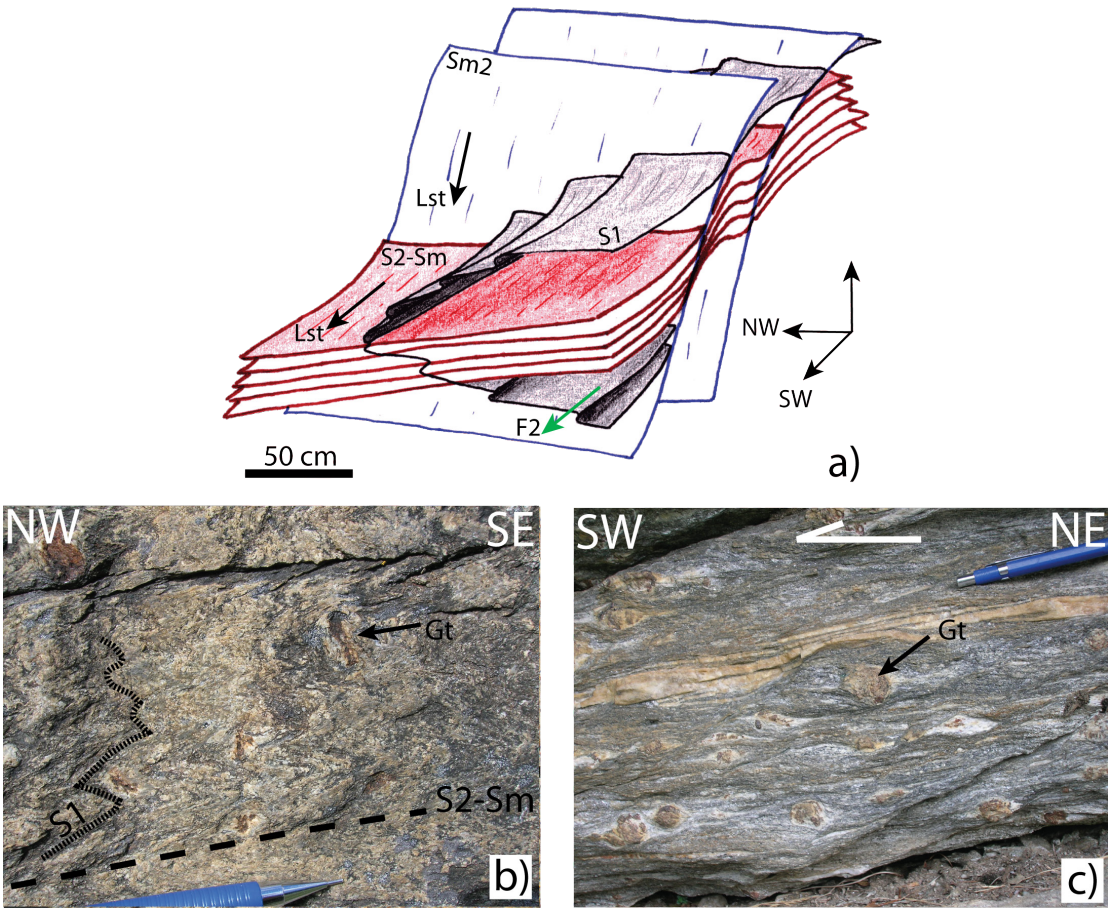

Figure IV.6: Overprint of earlier deformation structures by the SFZ. a) Synthetic sketch showing the reactivation of a pre-existent $S_{1/2}$ fabric on an outcrop scale (647034/122940). b) F2 folds overprinted by the growth of garnet at peak metamorphic conditions (647034/122940). c) Retrograde top-to-SW shearing with asymmetric pressure shadows developed on stretched garnet porphyroclasts (647034/122940).

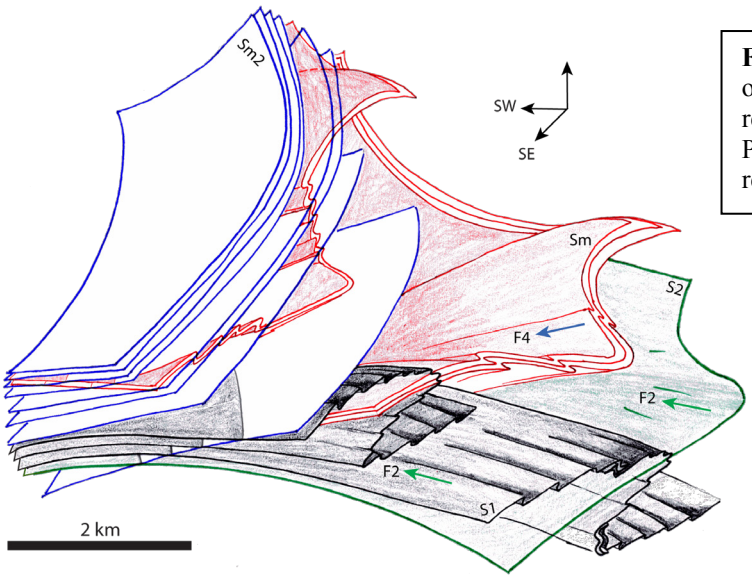

Figure IV.7: Synthetic sketch of the complexly deformed region around the Simplon Pass, showing the overprinting relationships.

IV.3. Chronological constraints

IV.3.1. Previous studies

IV.3.1.1. The Simplon Fault Zone

In Chapters II and III, the timing of the SFZ was discussed. Results obtained with a 2-3D thermo-kinematic model suggest that the onset of faulting was at 19 ± 4 Ma and continued until at least 3 Ma, as is also reflected in the discontinuous cooling history across the SFZ (Fig. II.12). Using $^{40}Ar/^{39}Ar$ and Rb-Sr methods on syn-kinematic phengites in low-grade mylonites from the NW region, the brittle-ductile transition has been dated to occur between 14.5 and 10 Ma. The same methods applied to muscovite growing in the neck of foliation boudinage within high-grade mylonites from the SE region, returned a similar age of ca. 14.5 Ma. Illite from clay gouge in the brittle detachment was previously dated at ca. 5 to 7 Ma with the K/Ar method [*Zwingmann and Mancktelow*, 2004]. A continuous evolution of the SFZ from the ductile to brittle field during the Miocene is thus well established.

IV.3.1.2. Extension-orthogonal folds

The decrease in dip of the foliation plane into the footwall, corresponding to a broad 'fold' with an axis perpendicular to the extension direction, has been interpreted to be coeval with shear zone activity and to reflect either a strain gradient through the shear zone [*Mancktelow*, 1992; *Mancktelow and Pavlis*, 1994] or a rolling hinge structure [*Wawrzyniec et al.*, 1999; *Wawrzyniec et al.*, 2001].

IV.3.1.3. Extension-Parallel folds or *D4* backfolds

Backfolds from the Southern and Northern Steep Belt are not generally considered to be coeval structures [e.g. *Steck and Hunziker*, 1994; *Maxelon and Mancktelow*, 2005]. The steep fabric of the Southern Steep Belt is crosscut by pegmatite and aplite dykes dated at ca. 25 Ma [e.g. *Romer et al.*, 1996]. *Pettke et al.* [1999] also reported direct muscovite $^{40}Ar/^{39}Ar$ dating from undeformed gold veins that crosscut the axial plane of the Vanzone

antiform. The age of these veins decreases toward the NE, varying from 32 Ma in the Brusson area to 24.5 Ma closer to the Simplon detachment. These results give a minimum age for the end of significant Vanzone fold activity and the Southern Steep Belt is therefore interpreted to develop in the Oligocene, prior to 25 Ma.
In the Northern Steep Belt, the age of the Berisal and Glishorn backfolds is less well established. *Steck and Hunziker* [1994] noted that the 12 Ma biotite Rb-Sr iso-age line is folded around the Berisal and Glishorn folds. These structures are therefore interpreted to be younger than 12 Ma, and were associated with the young exhumation of the Aar massif established from fission-track cooling ages [e.g. *Michalski and Soom*, 1990]. However, no direct dating was previously available to confirm the age of these structures in the Northern Steep Belt. These backfolds could represent either (1) perpendicular shortening developed synchronously with orogen-parallel extension [*Mancktelow*, 1992; *Mancktelow and Pavlis*, 1994] or (2) perpendicular shortening postdating an early Oligocene stage of extensional ductile shear and more-or-less synchronous with the latest Miocene brittle detachment [e.g. *Mancel and Merle*, 1987; *Steck and Hunziker*, 1994].
In this Chapter, we provide new chronological constraints on the relative and absolute timing of the extension-parallel and extension-orthogonal folding.

IV.3.2. Results

IV.3.2.1. Relative chronology

The cooling history established in Chapters II and III can provide constraints on the relative timing of both sets of folds.

IV.3.2.1.1. Extension-orthogonal folds

In the SE section (region III, Fig. IV.1b), a slight jump in $^{40}Ar/^{39}Ar$ and Rb-Sr cooling ages is observed across the SFZ between 17 Ma and 14 Ma (Fig. II.12c). This is attributed to a slight differential displacement between footwall and hanging wall, introduced by the regional up-doming of the footwall during the penetrative ductile shear, as indicated by the change in plunge direction of the stretching lineation (Fig. II.2c). However, no significant jump in cooling ages is seen with the low-temperature fission track thermochronometer after 14 Ma (Fig. II.12c). This can be explained if the late brittle dextral strike-slip movement on the SFZ postdates the regional up-doming of the footwall, which may have ceased at the time of the brittle-ductile transition around 14 Ma.

IV.3.2.1.2. Extension-parallel folds

Figure IV.8 presents an inverse distance weighted (IDW) interpolation of compiled cooling ages for biotite Rb-Sr and zircon fission track (ZFT) thermochronometers from the Central Alps. In contrast to the Natural Neighbors interpolation used in Chapter III, the IDW reveals more local variations. The main difference reflects the different method employed to compute the weighting of scattered samples used for the interpolation. In the IDW, the interpolating surface is a linear weighted average of scattered samples, with the weight assigned to each sample diminishing as the distance of the sample from the interpolation point increases. In the Natural Neighbors interpolation, the samples used to

interpolate the surface values for each cell are identified and weighted using a Delauney triangulation, with the weight assigned to each sample proportional to the area of the triangle.
The dataset used is similar to Chapter III and references are listed in Figure III.3. Ages used are not corrected for elevation.
The Rb-Sr biotite age interpolation (Fig. IV.8a) does not reflect folding of the iso-age lines, as described by *Steck and Hunziker* [1994] in the Northern Steep Belt. This interpolation mainly reflects the reset age zone, with the boundary corresponding to the limit of amphibolite facies metamorphism in the Toce Dome. The zircon fission track thermochronometer is more appropriate for considering variation in cooling age for such different metamorphic conditions. Indeed, the zircon fission track (ZFT) age interpolation shows an interesting cooling pattern (Fig. IV.8b). In the Northern Steep Belt, the iso-age lines for 15, 14, 13 and 12 Ma are folded around the Berisal fold, reflecting the fact that the backfolds in this region are younger than 12 Ma. This result is very similar to the interpetation proposed by *Steck and Hunziker* [1994] but it is best verified with the ZFT thermochronometer.

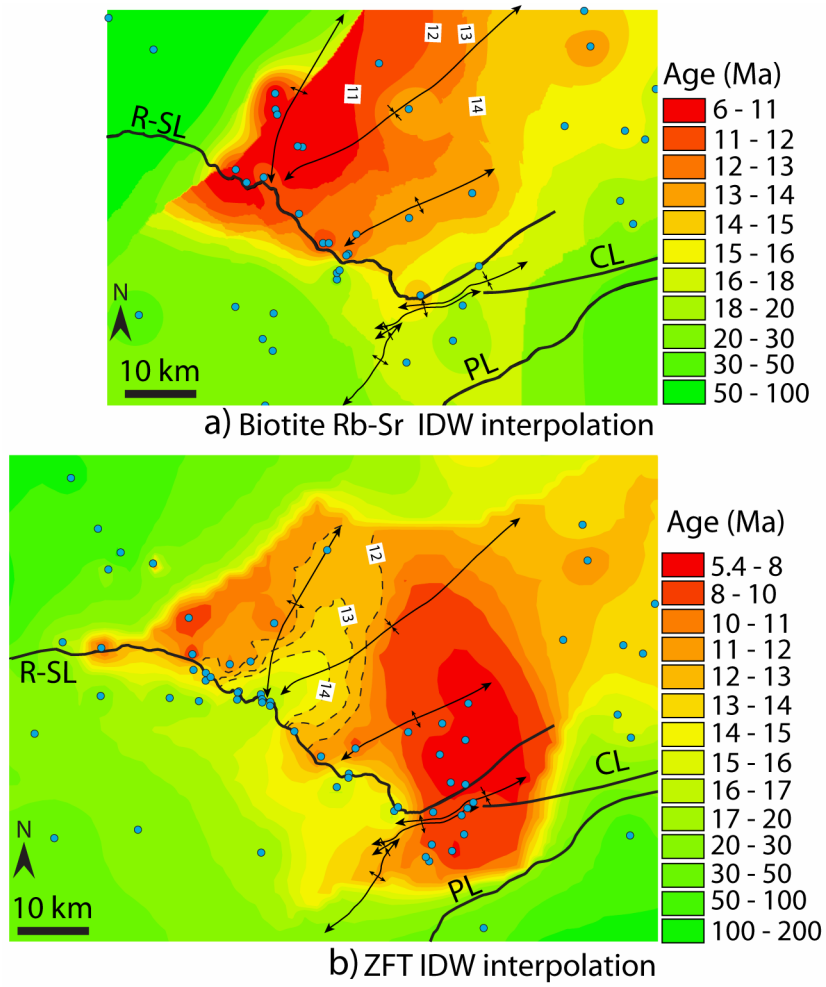

Figure IV.8: Interpolation of biotite Rb-Sr and ZFT cooling ages in the Central Alps

IV.3.2.2. Direct dating of S_4 axial plane cleavage

In the Northern Steep Belt near Mörel (Fig. I.3), sample MC301 (Fig. IV.1a) comes from the metapelite cover of the Gotthard massif, within the greenschist facies region. The metapelite shows a strongly developed steep crenulation cleavage (Fig. IV.9a,b). The relationship of this cleavage to the previous fabric ($S_{(0)/1}$) indicates that the sample lies on the southern limb of an antiform (the Glishorn antiform; Fig. IV.9a,b). This crenulation cleavage corresponds in style and orientation to the S_4 axial plane schistosity of the backfolds. In thin section (Fig. IV.9b), the main fabric ($S_{(0)/1}$) is defined by thin white micas of ca. 10 to 80 µm width and 80 to 200 µm length. Large biotite porphyroblasts (>500 µm) grew over S_1 during an upper greenschist facies metamorphic overprint. S_1 is affected by a strong crenulation cleavage (S_4) mainly defined by thin flakes of white micas of ca. 10-20 µm width and 60 to 130 µm length. This crenulation cleavage clearly postdates the growth of the biotite porphyroblasts (Fig. IV.9b).

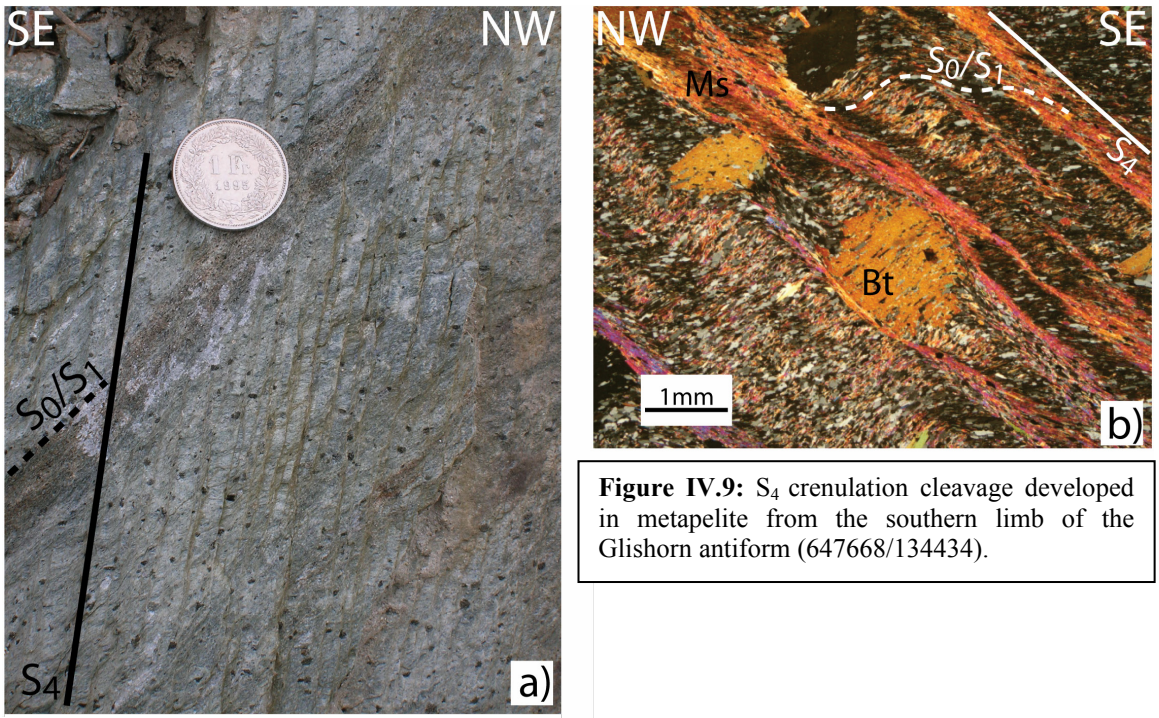

Figure IV.9: S_4 crenulation cleavage developed in metapelite from the southern limb of the Glishorn antiform (647668/134434).

Mica compositions are given in Table IV.1. Both generations of white micas (S_1 and S_4) have similar muscovite compositions, with comparable Tschermak substitution (Fig. IV.10). This suggests that they both grew under similar P-T conditions [*Guidotti*, 1973].
Biotite and muscovite were separated for single grain laser $^{40}Ar/^{39}Ar$ dating. The two generations of muscovite, S_1 and S_4, could not be isolated. Analytical methods for $^{40}Ar/^{39}Ar$ are described in Appendix A and results are presented in Table IV.2 and Figure IV.11.
Biotite yields a plateau age of 13.3 ± 0.93 Ma (Fig. IV.11a), as confirmed by the inverse isochron diagram given in Figure IV.11b. Muscovite yields a younger plateau age of 10.4 ± 0.13 Ma.

Sample	White mica				Biotite	
MC301	S1		S4			
	n=16	2σ	n=19	2σ	n=10	2σ
SiO_2	46.63	0.60	46.72	0.46	36.40	0.23
TiO_2	0.36	0.06	0.38	0.03	1.58	0.09
Cr_2O_3	0.02	0.01	0.02	0.02	0.02	0.02
Al_2O_3	33.32	0.78	33.00	0.78	17.58	0.25
FeO	3.40	0.14	3.34	0.19	19.36	0.19
MnO	0.01	0.01	0.01	0.01	0.14	0.04
MgO	1.41	0.20	1.45	0.17	10.45	0.04
CaO	0.01	0.01	0.01	0.01	0.01	0.02
Na_2O	0.65	0.09	0.61	0.08	0.15	0.03
K_2O	9.42	0.23	9.39	0.26	9.25	0.21
Total	95.23	0.43	94.93	0.26	94.94	0.29

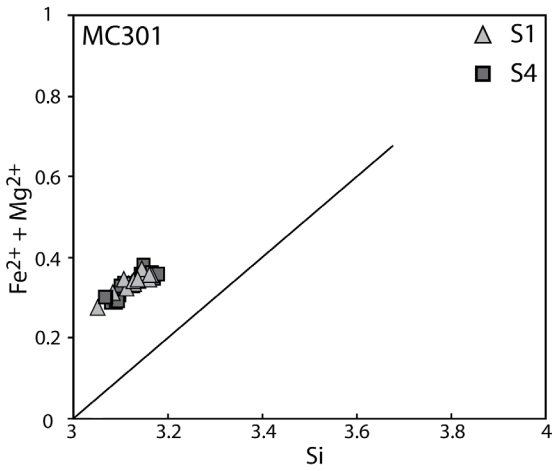

Left, Table IV.1: Representative mica compositions for sample MC301
Right, Figure IV.10: Tschermak substitutions for the analyzed muscovite S_1 and S_4.

In this greenschist facies region, where rocks did not reach more than 350°C, pre-Alpine micas are only partially reset (Chapter II). Micas growing under such conditions can therefore yield crystallization ages (see discussion Chapter II). Indeed, late Miocene ages are obtained for this sample, with biotite giving an older age than muscovite, which would not be expected for cooling ages. We therefore interpret both muscovite and biotite ages as crystallization ages. The biotite provides a maximum age of 13 Ma for the S_4 crenulation cleavage development. Note that the muscovite age could correspond either to S_1 or S_4. However in thin section (Fig. IV.9b), only the muscovite growing within the crenulation cleavage S_4 postdates the biotite and thus the crenulation most likely developed around 10 Ma. This 10 Ma result therefore provides an absolute age for backfold development in the Northern Steep Belt.

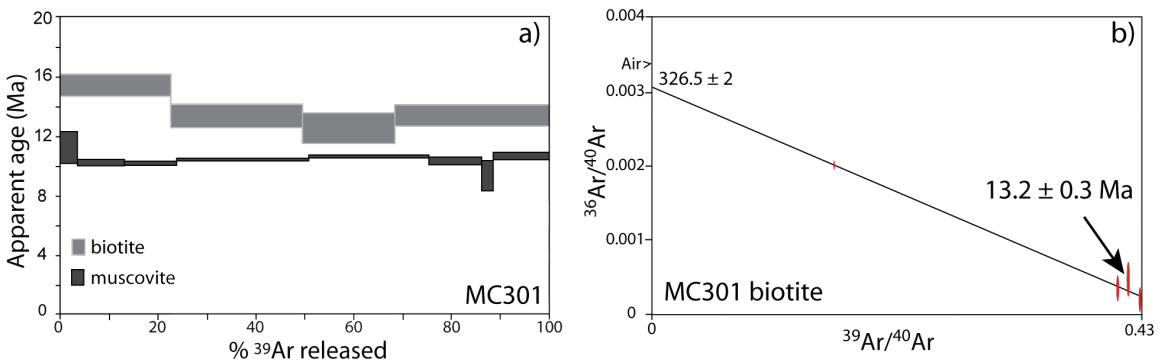

Figure IV.11: $^{40}Ar/^{39}Ar$ spectra and inverse isochron diagram

Sample	Type	Location	Elevation (m)	Mineral	$^{40}Ar/^{39}Ar$ age ± 2σ (Ma)	Description
MC301	Metapelite	647668/134434	879	Muscovite	10.4 ± 0.13	Plateau age
				Biotite	13.3 ± 0.93	Plateau age

Table IV.2: $^{40}Ar/^{39}Ar$ ages

IV.4. 3D geometric modeling

The geometry of the SFZ in 3D was modeled using the computer program GeoModeller (Intrepid Geophysics, www.intrepid-geophysics.com), which is based on the mathematical expression of a geological surface using the potential method [*Lajaunie et al.*, 1997; *Aug et al.*, 2004].

Two types of input data are used: (1) interfaces (lithology, stratification, foliation, fault, axial plane) considered as equipotential lines or planes of a fictive scalar field; and (2) geological measurements (dip, dip direction, polarity) corresponding to the orientation of the interface, with a sense given by the polarity. Such measurements are considered as the gradient (i.e. derivative) of the potential. Faults are included and modeled as a discontinuity in the potential field.

We followed a similar approach to that developed by *Maxelon and Mancktelow* [2005] and *Maxelon et al.* [2009]. The foliation field model was built using a large database of foliation measurements. To visualize this foliation field model in 3D, an arbitrary structural level needs to be fixed. All foliation measurements are given with a polarity relative to the *D4* phase of backfolds in the Northern and Southern Steep Belts and to the SFZ overprint. Folds are specifically included in the models, with the axial planes established both from direct field measurements and from the axial trace on the surface topography. An interpreted position of the fold hinge must be fixed at some depth and the hinge geometry can be estimated by comparison with observed smaller-scale parasitic folds. However, folds will be automatically generated by the 3D modeling and do not have to be explicitly included, although it can help to extend the geometry into regions where few foliation measurements are available. Such computer-generated, interpolated 3D models help to visualize the complex deformation pattern and to critically assess controversial field relationships.

In model 1 (Fig. IV.12), we first focus on the footwall of the SFZ. The goal is to visualize the last deformation phase affecting the tectonostratigraphic pile, including the effect of both extensional faulting and upright folding. To this end, we only consider the dominant fabric of the Simplon region, that is $S_{1/2}$ and Sm in the vicinity of the fault zone. These foliation measurements are presented in Figure IV.12a to show the density of orientation data available. The axial plane geometry of the Berisal and Glishorn extension-parallel folds (Fig. IV.12b) is first created using the field measurements presented in Figure IV.4. Only the hinge for the Berisal synform is simulated. The foliation field model of the dominant fabric within the footwall is then calculated, with foliation measurements given a polarity relative to the two extension-parallel folds (Berisal synform and Glishorn antiform). To visualize the resulting foliation field model, we arbitrarily fix a structural level with one single point within the footwall (orange dot Fig. IV.12a). The result is

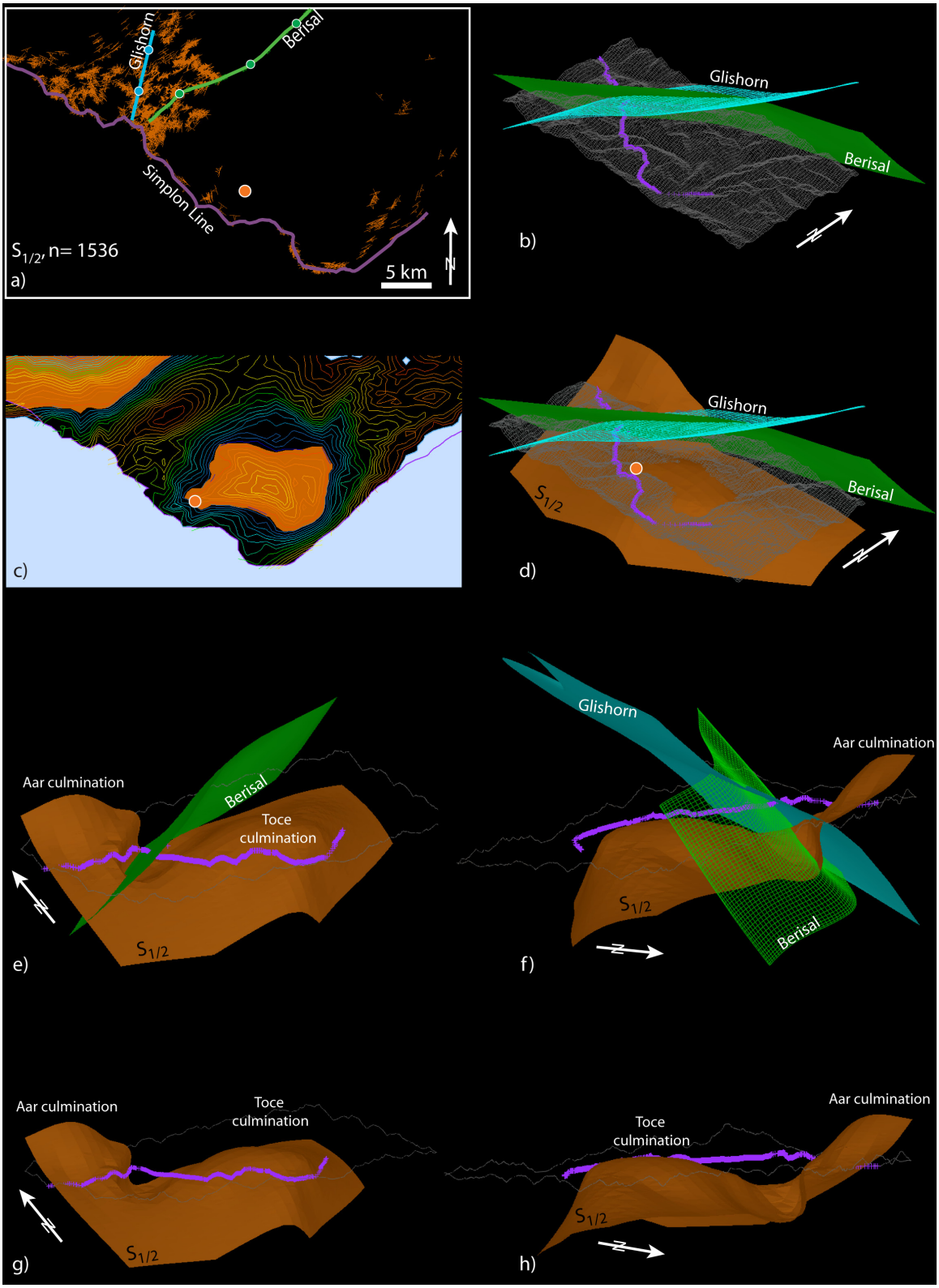

Figure IV.12: Model 1: $S_{1/2}$ and last deformation phase (*D4*) geometry within the footwall. a) Input data on the topography surface (foliation measurements and interface points). b) 3D reconstruction of the backfold system. c) Foliation field model of $S_{1/2}$ fabric on the topographic surface. d, e, f, g, h) 3D geometry of the foliation field model for $S_{1/2}$ from different viewpoints.

given in Figure IV.12c in map view and in Figures IV.12d,e,f,g,h in 3D for one single foliation plane. The Simplon Line trace on the topography is also shown for reference. This model reproduces the 3D geometry of the axial plane fabric of older deformation phases (D_1 and D_2) deformed by the combined effect of SW extension and upright folding during unroofing. The geometric model reveals two structural culminations referred as the Aar and Toce culminations [e.g. *Steck and Hunziker*, 1994] in the footwall of the SFZ. We observe in Figure IV.12c that S_2 is parallel to the SL in the Toce culmination, but is clearly folded by the backfolds in region IV (Fig. IV.1b) and discordant to the SL. In region V, in front of the Aar culmination, S_2 is clearly crosscut by the SL, and similarly in region III, in the SE, S_2 is again not parallel to the SL. As discussed in Chapter II, in this area, the SL clearly obliquely crosscuts the southern limb of the *D2* Wandfluhorn fold.

In model 2 (Fig. IV.13), we now add the fault zone geometry, including the brittle detachment and foliation planes Sm and Sm2, which are all considered as equipotential interfaces. The input data are the fault zone orientations Sm and Sm2 presented in Figure II.2c and reported Figure IV.13a, which again is only to show the density of the dataset. The detachment itself could be directly measured in several locations (e.g. Zwischbergen, Fig. I.3) and determined as well by geomorphological criteria, such as topographic dip slopes. In region I (Fig. IV.1b), the dip of the SL is confirmed to be between 25° (Zwischbergen, Fig. I.3) and 30° (Engiloch, Fig. I.3). A foliation field model of the SFZ is calculated and given in map view in Figure IV.13b. The Sm2 low grade fabric shows the same strike as the detachment, whereas Sm is clearly folded in the Northern Steep Belt, analogous to as S_2 (Fig. IV.12c). The resulting model of this foliation field is given in 3D in Figures IV.13c,d,e,d and in cross-section parallel to the extension direction in Figure IV.13f. We note that the foliation Sm has a domal geometry affected by two sets of folds, with both extension-parallel (Berisal and Glishorn) and extension-perpendicular fold axes. It is also seen that the Simplon mylonitic foliation Sm is parallel to the previous $S_{1/2}$ fabric in the vicinity of the SFZ (Fig. IV.13e,f). However, in two regions clearly different orientations of the previous the fabric $S_{1/2}$ and Sm are observed: (1) in region V, in front of the Aar culmination, and (2) in region III to the SE (Fig. IV.13e). In region III, Sm is parallel to the SL and the Sm2 fabric, while S_2 is crosscut by the SL (Fig. IV.12c). Therefore, in this region Sm and S_2 can be distinguished within the footwall as two different planar fabrics. The ductile-brittle overprint associated with the low-grade Sm2 foliation and the discrete brittle detachment (SL) are parallel and do not show any domal shape, but they are affected by wavy folds (Fig. IV.13g,h), with fold axes parallel to the regional extension direction. The two steep axial planes of the Masera and Vanzone folds in the SE region (Fig. IV.14b) from the field measurements presented in Figure IV.4. In this model, the hinge of the Masera and Vanzone backfold is simulated. The dominant foliation $S_{1/2}$ is also given, with a polarity reflecting the vergence of these folds. The resulting foliation field model is presented in Figure IV.14c in map view and in Figure IV.14d in cross section, through the Southern Steep Belt and perpendicular to the extension direction. Figures IV.14e,f,g,h present the 3D model of the foliation field in the hanging wall and its relationship with the SFZ. It is clearly seen that in the central region the hanging wall fabric is cross cut by the Simplon detachment. The Southern Steep Belt is plainly revealed in the hanging wall of region II and III, with the $S_{1/2}$ fabric folded around the Vanzone Antiform.

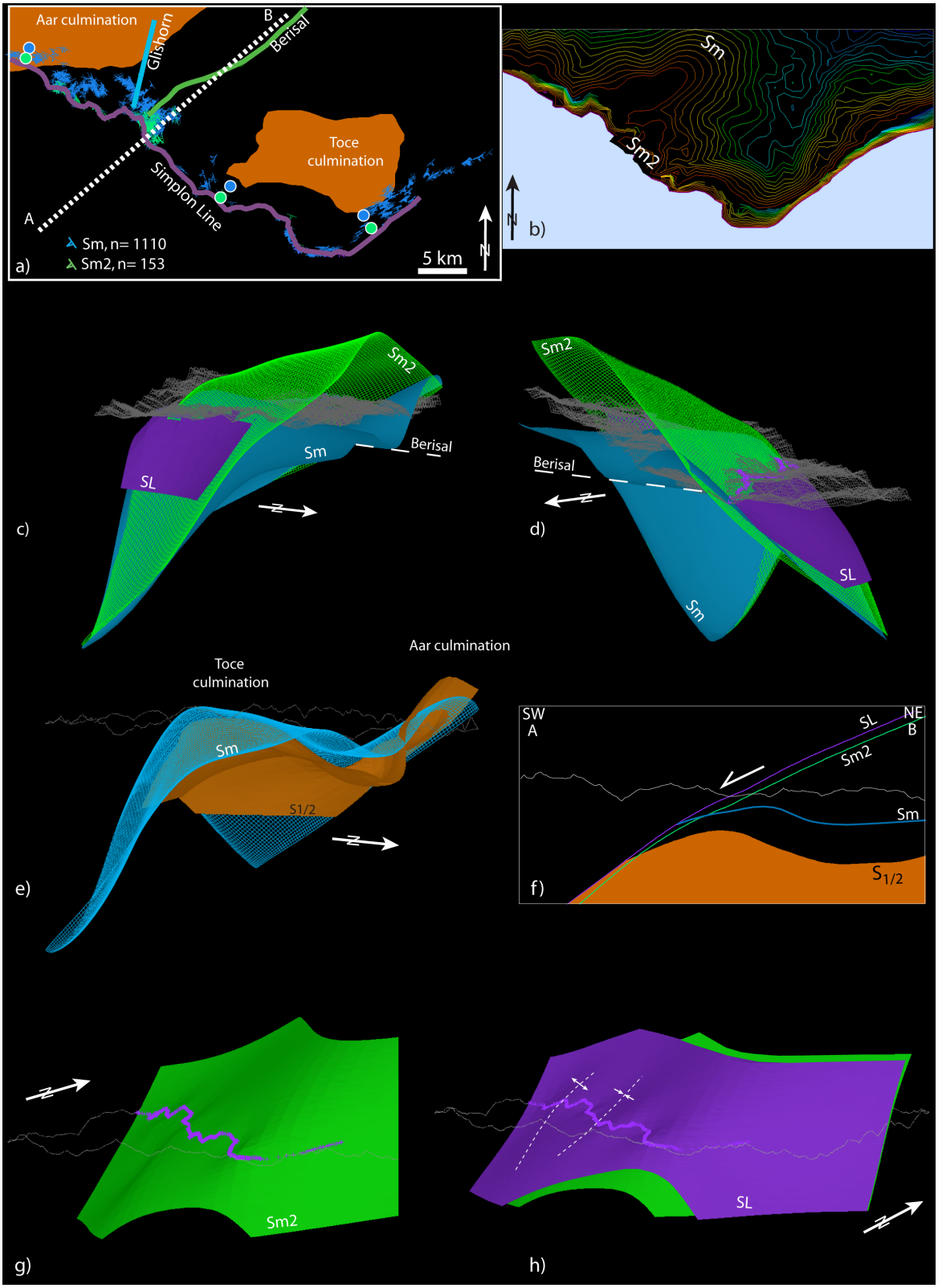
Aar culmination
Glishorn
B
Berisal
Toce
culmination
Simplon Line
A
Sm, n= 1110
Sm2, n= 153
a)
5 km
N
Sm
Sm2
b)
Sm2
Sm
Berisal
SL
c)
Sm2
Berisal
SL
Sm
d)
Toce
culmination
Aar culmination
Sm
S1/2
e)
SW
A
SL
NE
B
Sm2
Sm
S1/2
f)
Sm2
g)
SL
h)

Figure IV.13 preceding page: Model 2: Simplon Fault Zone geometry. a) Input data on the topography surface using two sets of foliation measurements and interface points. b) Foliation field model of the SFZ on the topography surface. c, d) 3D geometry of the foliation field model for the SFZ from two opposite views. e) 3D geometry of the penetrative mylonites, Sm, showing the reactivation the pre-existent fabric $S_{1/2}$ in the core of the Dome (Toce culmination) and the crosscutting relationship in the Aar culmination. f) Section parallel to the extension direction showing the fault zone geometry. The Simplon mylonites Sm shows a domal shape. g) Wavy folds with axes parallel to the extension direction affecting Sm2. h) Wavy folds with axes parallel to the extension direction affecting the brittle

In this region, the strike of the hanging wall fabric is parallel to the strike of the SFZ (Fig. IV.14c). However, in Figure IV.14d, in cross section, the two fabrics are not strictly parallel. The northern limb of the Masera synform has a shallower dip than the SFZ toward the NW. Therefore a discordant relationship in this region is still observed and confirms the continuation of the SFZ (and more discrete SL) within the Isorno Valley.
The model also predicts that the fault zone crosscuts the southern limb of the Vanzone antiform (Fig. IV.14d,f,g). The interpretation of such a geometry is discussed further below. Model 3 in addition considers the overprint of the last deformation phase within the hanging wall by using the dominant fabric $S_{1/2}$ reported in Figure IV.14a. We first create
By including the dominant foliation measured in the Simplon region we could therefore model the regional Toce Dome geometry, reflecting the coupled effect of the SFZ and the overprint of the Southern and Northern Steep Zones (Fig. IV.12). This model also reveals the 3D fault zone geometry (Fig. IV.13) and its relationships with the earliest fabric within the footwall and hanging wall (Fig. IV.13, IV.14).
Finally, model 4 considers the foliation field of the dominant fabric ($S_{1/2}$ and Sm in the vicinity of the SFZ) within the entire Lepontine Dome. The Dome is limited to the SW by the Simplon Line and to the south by the Centrovalli and Periadriatic Lines.
We use an extensive database of foliation measurements within the Lepontine Dome by combining the compilation from this study with that of *Maxelon* [2004]. The data are presented Figure IV.15a. To reduce the computation time, this model is only realized using the foliation measurements and does not explicitly include additional predefined folds. As a result, the model is best defined in regions where many data are available and folds structures will be most clearly visualized in these regions. The resulting foliation field model is presented in Figure IV.15b in map view and in Figures IV.15c,d in 3D. The major 3D structure in this large scale model is the Toce Dome, which is evidently the most exhumed part the Lepontine Dome, with this exhumation related to its position within the footwall of the SFZ. This model highlights the importance of the SFZ for the exhumation of the Lepontine Dome. Faults are included in this regional model, which predicts a continuation of the Centovalli Line within the Bognanco Valley and still further west. Of course this geometry is a result of the tendency for the modelling software to extrapolate the known geometry in the Ossola Valley and is not directly constrained by field measurements further west. Nevertheless, brittle faulting in this region has indeed been described by *Bistacchi et al*. [2000].

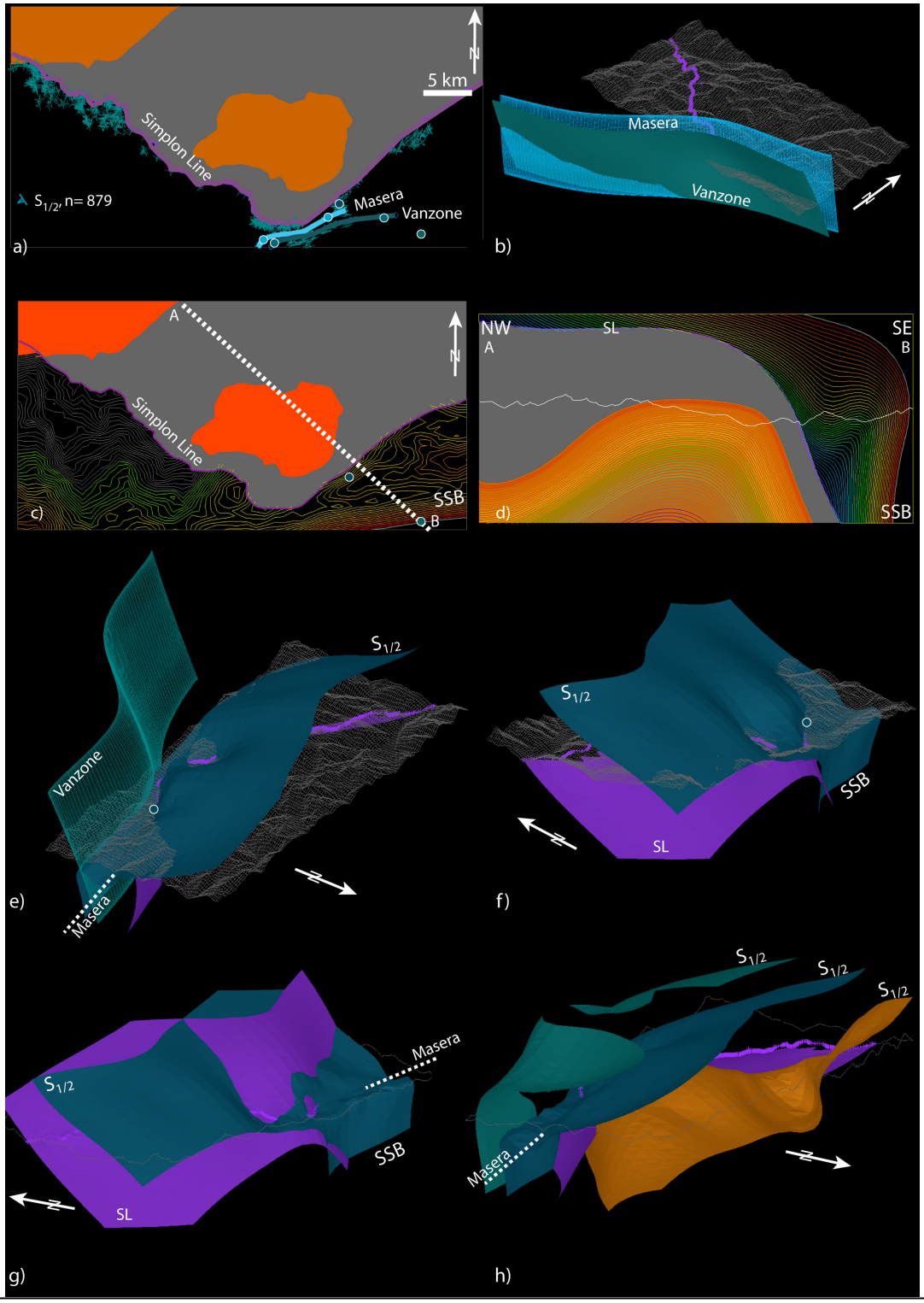

Figure IV.14: Model 3: Hanging wall geometry. a) Input data on the topography surface (foliation measurements and interface points). b) 3D reconstruction of the backfold system. c) Foliation field model of $S_{1/2}$ fabric on the topographic surface. d) Foliation field model of $S_{1/2}$ fabric on a section perpendicular to the general extension. e, f, g, h) 3D geometry of the foliation field model $S_{1/2}$ from different viewpoints.

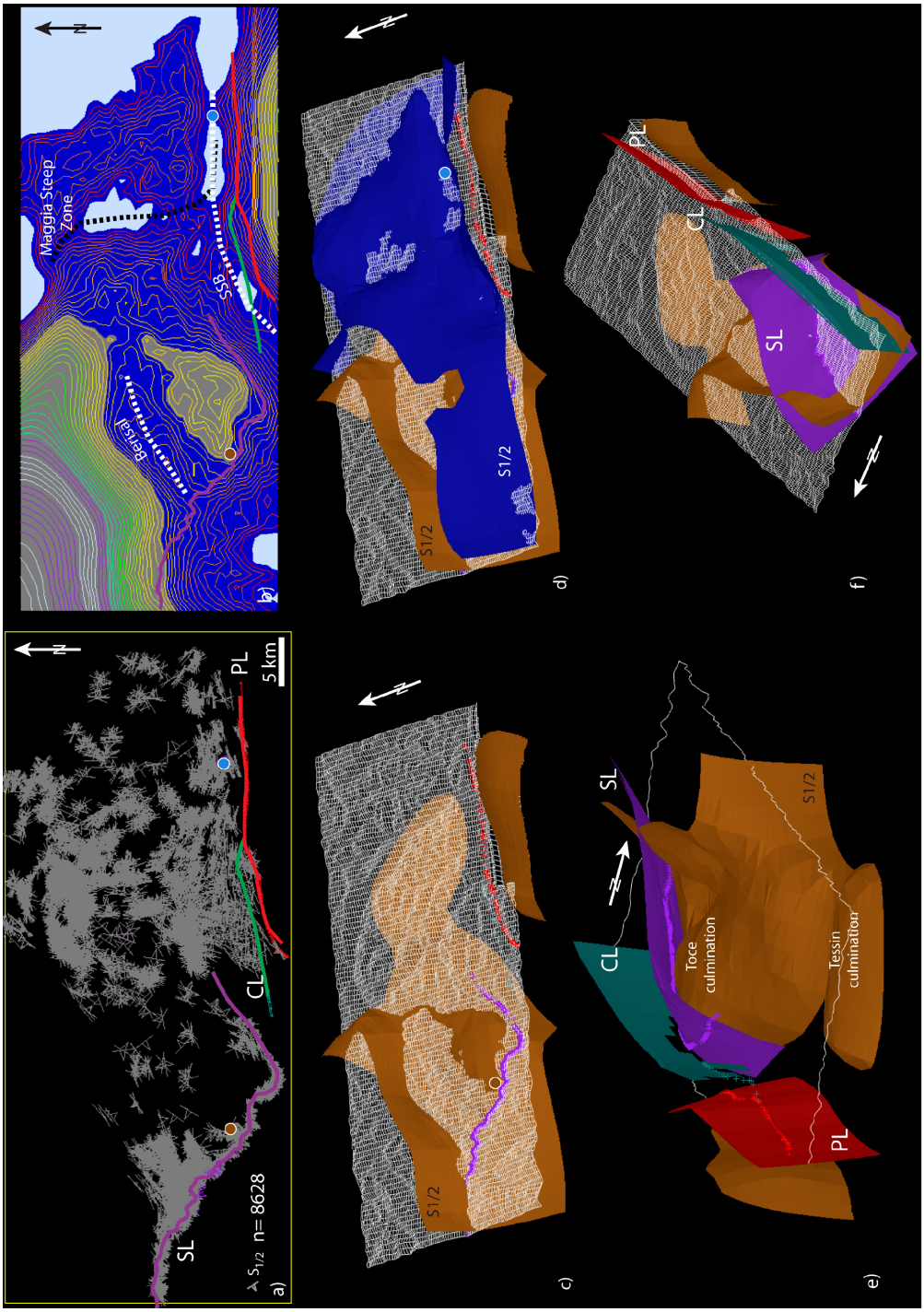

Figure IV.15: Model 4: Lepontine Dome geometry. a) Input data on the topography surface (foliation measurements and interface points). b) Foliation field model of $S_{1/2}$ fabric on the topographic surface. c,d) 3D geometry of the foliation field model $S_{1/2}$. e,f) 3D geometry of the Simplon Line (SL), Centovalli Line (CL) and Periadriatic Line (PL) system.

IV.5. Discussion

IV.5.1. Extension-parallel folding

IV.5.1.1. The Northern Steep Belt

The extension-parallel folds in the Northern Steep Belt affecting the footwall of the low-angle detachment system have been interpreted to be younger than 12 Ma [*Steck and Hunziker*, 1994]. Relative dating based on folded interpolated iso-age lines for zircon fission track confirms this interpretation. In addition, new mica $^{40}Ar/^{39}Ar$ absolute dating constrains the crenulation cleavage S_4 development to be ca. 10 Ma. In Chapter II it was already established that 10 Ma approximately corresponds to the time of brittle fracturing on the SFZ. It was also argued that the SFZ represents a continuous period of exhumation from the ductile to the brittle field, over a time range from 19 to at least 3 Ma, with the ductile-to-brittle transition dated at ca. 14.5-14 Ma.

The 3D geometric modeling clearly shows that the ductile mylonitic foliation Sm is strongly folded and transected by the more brittle detachment and greenschist facies mylonitic foliation Sm2. If the fold developed at 10 Ma, it would fold the already exhumed ductile mylonites Sm, but would be coeval with the more brittle-ductile Sm2 mylonites and the brittle detachment. Indeed the 3D geometric modeling shows that both the brittle detachment and the greenschist facies mylonites are affected by wavy extension-parallel folds.

These results suggest that the extension-parallel folds in this region were generated synchronously with the late exhumation history of the SFZ but did not start with the onset of deformation at ca. 19 Ma, in contrast to what was initially proposed by *Mancktelow* [1992] and *Mancktelow and Pavlis* [1994]. If such structures would develop as the result of one of the single processes listed in introduction (Sect. IV.1), we would expect the folds to develop synchronously with the onset of faulting. Such up-right folds clearly reflect two independent processes, with active folding occurring while the extensional faulting was still in progress. The late overprint of such horizontal NW-SE shortening on a continuously sheared top-to-SW fabric produced a constrictional finite strain, as locally observed (Fig. IV.2c).

IV.5.1.2. The Southern Steep Belt

The kinematics and mechanics of steepening of the SFZ in the south are more difficult to establish. The Southern Steep Belt and the Vanzone antiform are considered to have developed prior to 25 Ma [e.g. *Steck and Hunziker*, 1994; *Romer et al.*, 1996; *Pettke et al.*, 1999], before the onset of the SFZ. However, it is likely that some late perpendicular shortening overprinted this southern region as well. For example, the Masera synform shows a more open hinge geometry compared to the tight Vanzone antiform. No direct dating constraining the age of the Masera synform is available, but it is possible that the open Masera synform results from late shortening producing this open fold in the northern, relatively flat limb of the Vanzone antiform and causing a tightening both of the Vanzone antiform and of the pre-existing Southern Steep Belt (Fig. IV.16).

The SFZ could either be generated as (1) a shallow normal fault crosscutting the Southern Steep Belt (Fig. IV.16a,c), later steepen during the ongoing tightening (Fig. IV.16b,d), or (2) with an initial steeper geometry in the south, parallel to the initial steep fabric (Fig.

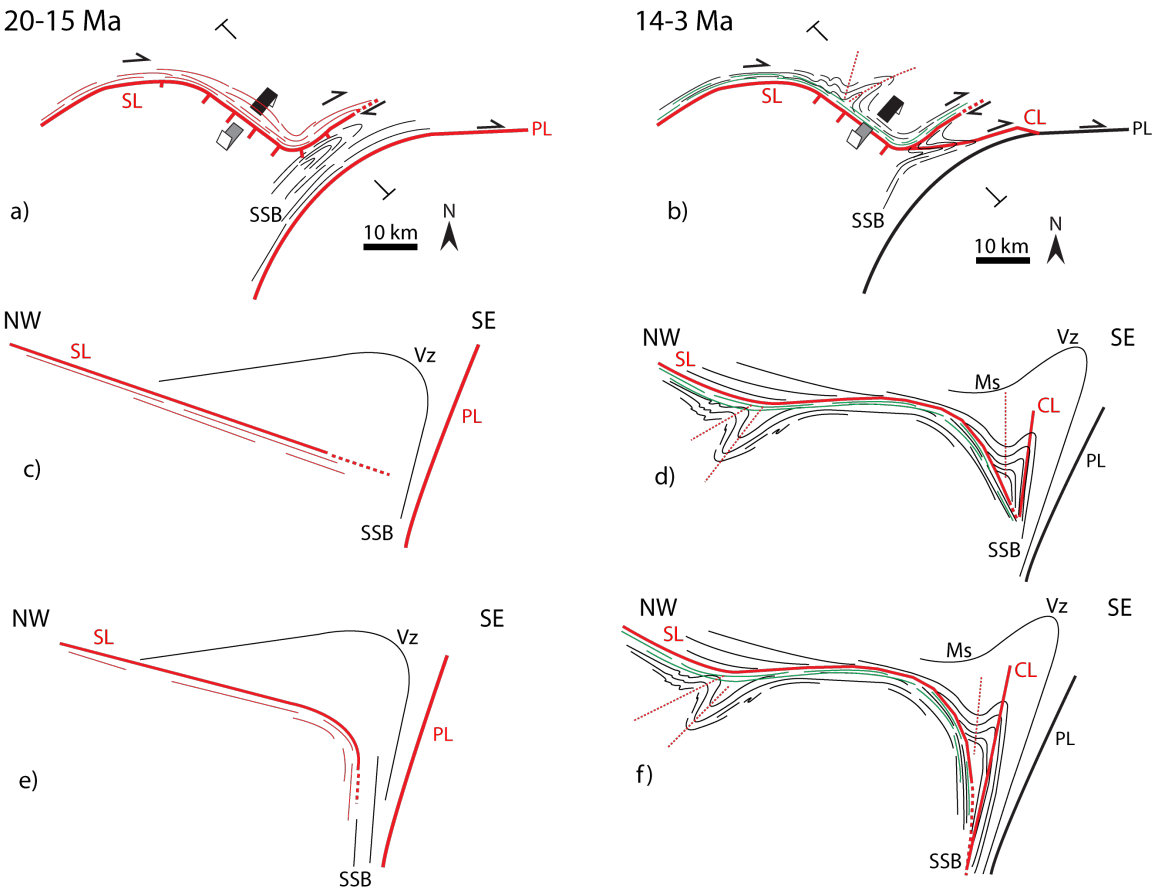

Figure IV.16: Synthetic sketches of the SFZ evolution relative to the Southern Steep Belt. a) Schematic structural map of the SFZ between 20 and 15 Ma. b) Schematic structural map of the SFZ between 14 and 3 Ma. c) Synthetic NW-SE cross section of a shallow SFZ crosscutting the Southern Steep Belt between 20 and 15 Ma. d) NW-SE cross section of the shortening and steepening of the SFZ between 14 and 3 Ma, with transecting relationship to the Southern Steep Belt. e) Synthetic NW-SE cross section of the SFZ with an initial steep geometry in the south between 20 and 15 Ma. f) NW-SE cross section of shortening and steepening of the SFZ between 14 and 3 Ma, with parallel relationship to the Southern Steep Belt. SSB: Southern Steep Belt; PL: Periadriatic Line; SL: Simplon Line; CL: Centovalli Line; Vz: Vanzone backfold; Ms: Masera backfold. Active structures are in color.

IV.16a,e) that subsequently underwent further shortening and steepening (Fig. IV.16b,f). The first solution would imply a present day geometry of the SL crosscutting the southern limb of the Vanzone fold (Fig. IV.16d). The second model would instead imply that the SL is parallel to the foliation in the Southern Steep Belt at depth (Fig. IV.16.f). The geometric modeling (Fig. IV.14) favors SL initiation as a low-angle normal fault crosscutting the pre-existing Southern Steep Belt. However, this geometry results from the extrapolation of the surface field geometry to depth, and is not well constrained at depth. The orientation is likely to vary with depth, but there are no additional measurements (e.g. from tunnels or boreholes) that could be included to more precisely constrain the geometric model. Therefore, the initial geometry of the SFZ related to the preexisting Southern Steep Belt cannot currently be solved. In both cases, a later

tightening of the whole detachment fault system to the south is likely, synchronous with amplification of the Masera synform and with the development of the Glishorn and the Berisal backfolds in the Northern Steep Zone.
The presence of such active perpendicular shortening in the late denudation history of the low-angle detachment system would also contribute to the domal uplift. Therefore, the relative displacement established in Chapter III from the thermo-kinematic model may need to be reduced, as we do not consider the effects of this 3D shortening in the current thermal model.

IV.5.2. Extension-orthogonal folds

The decrease in dip of the foliation within the dome, with a fold axis perpendicular to the extension direction, has been attributed by *Mancktelow* [1992] and *Mancktelow and Pavlis* [1994] to a strain gradient away from the shear zone, reflecting the distributed ductile shear within the footwall, and by *Wawrzyniec et al.* [1999] and *Wawrzyniec et al.* [2001] to represent a rolling hinge structure. The 3D geometric modeling suggests that only the Simplon mylonite foliation, Sm, reflects this domal shape and it is not seen in the form of the brittle detachment. It should also be noted that the exhumation pattern predicted with a rolling hinge model does not fit the observed cooling ages within the footwall, as discussed in Chapter III.
The dome is interpreted to have been generated between 17 and 14 Ma, as indicated by the cooling history of Figure II.12c. This time clearly corresponds to that when the Simplon ductile shear zone was active. Therefore, we also consider that this dome formation reflects a strain gradient way through the shear zone, as initially proposed by *Mancktelow* [1992] and *Mancktelow and Pavlis* [1994], with the lower temperature history of exhumation reflecting a more rigid-block behavior.

IV.5.3. Relationship to the previous *D2* deformation phase

The relative geometry of the SFZ to the previous fabric is also characterized. The SL clearly crosscuts the older $S_{1/2}$ fabric of the hanging wall from the Rhone Valley to the Isorno Valley, with an evident 3D geometrical discontinuity at the detachment. This confirms our interpretation and structural mapping presented in Chapter II.
Within the footwall, the ductile mylonitic foliation, Sm, and the earlier S_2 foliation are parallel, reflecting reactivation of S_2 in the vicinity of the SFZ, as presented in Figure IV.6. However, the two fabrics can be clearly differentiated at the limits of the study area to the NW (region V, Rhone Valley) and SE (region III, Isorno Valley). In these regions, the dextral ductile shear is parallel to the brittle detachment and overprints the discordant *D2* fabric. Therefore, for both structural and geometrical reasons, S_2 and Sm cannot be considered to be the same coeval foliation. Instead, Sm clearly overprints S_2 and must be younger.

IV.6. Conclusion

The Simplon low-angle detachment system is affected by upright folding with axes both parallel and perpendicular to the regional extension direction. This leads to a complex 3D denudation history of the footwall. In this Chapter, new constraints on the relative and absolute timing of such up-right folds are provided, coupled with a 3D geometric model of the interplay between extensional faulting and folding.

In the Northern Steep Belt, relative chronology using the zircon fission-track cooling ages and absolute mica $^{40}Ar/^{39}Ar$ dating suggests that the development of the extension-parallel folds are synchronous with the late exhumation history over the last 10 Ma. This generates coeval wavy folds of the greenschist facies mylonite and of the brittle detachment itself. On the contrary, published ages on crosscutting veins and dykes demonstrate that the Vanzone antiform and the Southern Steep Belt forming its southern limb must have developed before ca. 25 Ma and therefore prior to the onset of faulting related to the SFZ. However, younger tightening of the Vanzone fold, with the development of the open Masera synform, may have subsequently steepened the SFZ. The Simplon ductile mylonites form a dome with an axis perpendicular to the extension direction. The cooling history indicates that dome formation occurred between 17 and 14 Ma, at the time of penetrative ductile shearing that is reflected in a strain gradient into the footwall. This domal shape is not seen in the shape of the lower temperature brittle detachment, consistent with a more rigid-block exhumation below the ductile-brittle transition.

It is therefore proposed that the upright folds affecting the low-angle detachment system are the result of two distinct events: (1) extension-perpendicular fold generated synchronously with the onset of ductile shear and reflecting a strain gradient through the shear zone, and (2) extension-parallel folds generated over the last 10 Ma during the later more brittle exhumation history and caused by perpendicular horizontal shortening due to ongoing convergence across the Alps.

V. Discussion and conclusions

The Simplon Fault Zone (SFZ) is one of the major low-angle detachment systems that led to large scale exhumation in the European Alps. A detailed structural study coupled with (1) thermochronology and geochronology with direct (micro-) structural control, (2) thermo-kinematic modeling (Pecube, [*Braun*, 2003]) with a formal inversion algorithm (Neighbourhood Algoritm, [*Sambridge*, 1999a, b]) and (3) 3D geometric modeling (GeoModeller, [e.g. *Maxelon and Mancktelow*, 2005]) allowed the spatial and temporal evolution of this low-angle detachment system to be investigated in detail. The results of this study are summarized below.

V.1. Loss and/or transfer of the SFZ displacement

Within the regions II and III (Fig. II.2b), a continuation of the SFZ as a dextral shear zone during transition from ductile to brittle behavior could be established (Fig. II.2a). The SFZ crosscuts the SE limb of the *D2* Wandfluhorn fold and its S_2 axial plane schistosity (Fig. II.2a and IV.12c). In this region, S_2 (within both the footwall and hanging wall) and Sm are clearly distinct, demonstrating from direct observation that they cannot correspond to the same structure [e.g. *Steck*, 1990, 2008]. The displacement in region III drastically decreases over a distance of some 20 km in going from region II to III. Only a minor brittle overprint can still be distinguished near the region of Lago Larechio (Fig. I.3). In the central section, the displacement is estimated at between 10 and 15 km (from the thermal modeling), whereas the limb of the Wandfluhorn fold is only displaced by ca. 2 km. In the hanging wall of region II and III, near Domodossola (Fig. I.3), the main S_2 fabric is crosscut by the SFZ (Fig. IV.14) and this fabric does not show strong evidence for dextral shearing in the immediate vicinity of the fault. The displacement on the brittle Centrovalli Line cannot be large enough to transfer all displacement of the SFZ (10 to 15 km) to the Periadriatic Line. In addition, the hinges of the Masera and Vanzone folds could be mapped almost continuously across the Ossola Valley, as was already established by the previous study of *Keller et al.* [2005a] and *Keller et al.* [2006]. Therefore, a direct connection, via the Centovalli Line, to dextral movement on the Periadriatic Line, as proposed in several earlier studies, is not supported by field observations.
In region IV, the SFZ continues into the Rhone Valley but the ductile-to-brittle shear and brittle deformation is less localized than in regions I, II and III, reflecting a more upper crustal level of the detachment system. A cooling history was established across the SFZ using both published and new fission-track ages combined with $^{40}Ar/^{39}Ar$ cooling ages obtained from recrystallized white mica within the high-grade Simplon mylonites. A jump in zircon fission-track cooling ages could be established in region IV over a broad deformation zone of a few kilometers width (1 to 3 km). In region II and III the cooling history suggest no relative displacement between FW and HW seen after 14 Ma. This is consistent with a strike-slip fault activity. Finally, 3D geometric models also confirm of a clear structural discontinuity from the Rhone Valley to the Isorno Valley.

The zircon fission-track cooling ages along the entire NW-SE strike of the Simplon Line (in the segment with a strictly normal component, regions I and IV), show a similar jump between footwall and hanging wall (Fig. II.5) and stretching lineations and striations are invariably parallel plunging toward 240° (Fig. II.2c). This suggests a similar relative displacement between footwall and hanging wall and argues against

an anti-clockwise rotation of the hanging wall, which would imply an increase of relative displacement northwestward with an anti-clockwise rotation of the stretching lineation [*Keller et al.*, 2006].
Further NE along the Rhone Valley, a continuation of some dextral motion localized within ductile-to-brittle dextral shear zones occurred between ca. 15 and 12 Ma, at least until the Grimsel Pass [*Rolland*, personal communication]. Such structures can be correlated as a dextral ductile-brittle shear zone network accommodating a small part of the major dextral strike-slip further NE into the Rhone Valley.

V.2. Age of the SFZ

In essence, the age debate with regard to the SFZ centres on whether the brittle SL is associated or not with a high-grade Miocene mylonitic shear zone. Direct dating of the late ductile shearing history was successful in regions III and IV (Fig. II.2b). In region III, absolute dating was possible using $^{40}Ar/^{39}Ar$ and Rb-Sr on newly grown minerals in the late undeformed neck of foliation boudinage and in Riedel veins (Fig. II.3d). Muscovite growth gave a $^{40}Ar/^{39}Ar$ age of 14 Ma (Fig. II.10) and Rb-Sr on cogenetic calcite/muscovite pairs give an age of 14.5 Ma (Fig. II.11). Such veins formed at temperature of ca. 340ºC, corresponding to conditions of the brittle-ductile transition and below (or close to) the closure temperature of white mica. These veins are formed during ongoing dextral shear and represent the ductile-to-brittle transition of the SFZ (Fig. II.3h). In the Rhone Valley (region V) near Visp (Fig. I.3), phyllonites with similar kinematics to the SFZ, which developed in the Aar massif and its cover, were dated between 14 and 10 Ma with $^{40}Ar/^{39}Ar$ on syn-kinematic phengite, and at ca. 14.5 Ma with Rb-Sr microsampling between a stretched feldspar prophyroclast.
A compilation and interpolation of new thermochronological ages (apatite and zircon fission track and muscovite and biotite $^{40}Ar/^{39}Ar$), together with a large amount of published ages, was carried out for the Simplon region (Fig. III.3 and IV.8). These thermochronological ages from the central region were used in a thermo-kinematic model coupled with Neighborood Algorithm inversion to reconstruct the thermal and exhumation history along the low-angle detachment system. This model predicts that the onset of faulting occurred at 19 ± 4 Ma. It also predicts the presence of a strong distributed shear zone within the footwall over ~2.5 km (*D* in Fig. III.5a and III.7i). This is consistent with the field observation of a broad kilometer-wide zone of mylonites immediately adjacent to the Simplon Line, as described by *Mancktelow* [1985, 1990]. The Simplon Line is therefore also directly associated with the ductile deformation.
Brittle faulting in the Simplon region was already established in the Simplon region to have been active between 11 and 5 Ma, from dating of clay gouge or vein filling fractures with K/Ar and $^{40}Ar/^{39}Ar$ methods [e.g. *Pettke et al.*, 1999; *Zwingmann and Mancktelow*, 2004; *Hetherington and Villa*, 2007]. We did not attempt to specifically check when the fault stops, and we therefore arbitrarily stopped the fault at the present day in the thermo-kinematic models. However the jump in apatite fission-track ages argues for a continuation of faulting until at least 3 Ma. For further constraints on the latest activity of the fault, thermochronometers of lower temperature, such as (U-Th)/He ages should be considered.

Therefore by using (1) geochronology with direct (micro-) structural control on the mineral growth, and (2) the reconstitution of the exhumation history using the large amount of available cooling ages in a thermo-kinematic model coupled with and inversion algorithm, it is established that there was a continuous exhumation history from the ductile to the brittle field in the Neogene, from 19 to 3 Ma. This result confirms the model previously proposed by *Mancktelow* [1985] and *Grasemann and Mancktelow* [1993] and is not in agreement with the development of a two stage exhumation process [*Steck*, 1990; *Steck and Hunziker*, 1994; *Steck*, 2008], where a late Miocene brittle detachment captures a "fossil" Oligocene shear zone.
Of course these results do not exclude the existence of a previous Oligocene major D_2 shear zone in the Simplon region, which could be widespread within both footwall and hanging wall and active before 26 Ma [*Romer et al.*, 1996]. However, in the Miocene, this previous fabric is reactivated and/or transposed in the central region of the SFZ by the ductile Simplon mylonites with a clear overprint over 2.5 km.

V.3. Kinematics of exhumation

In Chapter III, two thermo-kinematic models were tested to explain the exhumation pattern of the SFZ: (1) an initial low-angle detachment [*Mancktelow*, 1985; *Grasemann and Mancktelow*, 1993] and (2) a rolling hinge model [*Wawrzyniec et al.*, 1999; *Axen et al.*, 2001; *Wawrzyniec et al.*, 2001]. Both models lead to very different thermochronological patterns. The model of a detachment with initial shallow dip predicts no variation of ages in the footwall, except with the introduction of a shear zone, which in this case will give decreasing ages into the footwall. This model requires an increase of the erosion rate in the footwall and such a signature should be recorded in the foreland basin as an increase of the sedimentary charge [e.g. *Kuhlemann et al.*, 2001]. A rolling hinge model, instead, predicts an increase of cooling ages within the footwall with increasing perpendicular distance from the detachment. This model does not involve any increase of the erosion rate, and can exhume deep rocks without having any signature within the foreland basin in term of sedimentary budget.
The thermochronological dataset from the Simplon region is well reproduced with an initially low-angle detachment dipping 30º and including the effects of topography and of a distributed ductile shear into the footwall. A rolling hinge model, however, does not reproduce the thermochronological pattern observed in the central region and predicts ages that are too old within the core of the Toce Dome. The rolling hinge model also predicts faster relative displacement between footwall and hanging wall and rocks from the footwall are exhumed from depths and corresponding metamorphic conditions that are greater than the peak metamorphic conditions actually observed.
A rolling hinge model is therefore not considered to be appropriate for the SFZ. Besides, 3D geometric models of the SFZ (Fig. IV.13) show that only the Simplon mylonitic foliation (Sm) defines a domal shape. The brittle detachment itself is not rotated through an upper hinge. This supports the interpretation that an initial low-angle detachment geometry is more appropriate. The model with a low-angle detachment predicts an increase in the erosion rate mainly between 18 and 14 Ma, which is reflected in a corresponding increase in the sedimentary budget in the foreland basin over this time period [e.g. *Spiegel et al.*, 2000; *Kuhlemann et al.*, 2001; *Kuhlemann et al.*, 2002; *Kuhlemann and Kempf*, 2002].

V.4. Exhumation rate and relative displacement

Different rates of exhumation have been proposed for the Simplon region and are still controversial [e.g. *Grasemann and Mancktelow*, 1993; *Schlunegger and Willett*, 1999; *Bernet et al.*, 2001]. The thermo-kinematic model used in this work is coupled with a formal inversion algorithm that tests all possible solutions against the set of observed thermochronological ages input as data. Several solutions for exhumation rates through time can be extracted from the observed ages. However, the total amount of exhumation and the relative displacement between footwall and hanging wall is always effectively the same. 1D probabilities are extracted from the inversion and provide further constraints on the exhumation rate (Fig. III.7).

V4.1. Uniform exhumation rate in the Central Alps

A uniform acceleration of the exhumation rate within both footwall and hanging wall (i.e. irrespective of any coeval fault displacement) is required over the past 4 Ma, in the Pliocene, to reproduce the young apatite fission-track ages. This uniform acceleration of exhumation rate most likely reflects an increase in the regional erosion rate, which has been independently reported in the Alps [e.g. *Kuhlemann et al.*, 2001; *Kuhlemann et al.*, 2002; *Kuhlemann and Kempf*, 2002; *Vernon et al.*, 2008] and proposed to be due to the effect of climate changes or the Messinian crisis [e.g. *Cederbom et al.*, 2004; *Willett et al.*, 2006].

The total amount of fault-independent regional exhumation over the past 4 Ma is 2.6 ± 0.19 km. Different scenarios for the acceleration can be extracted from the modeling, but always with a negative relationship between exhumation rate and onset time, so that the total amount of exhumation remains effectively the same. A doubling of the exhumation rate at 4 Ma is the preferred solution as it is recognized in both kinematic models with a high probability. In this model, the exhumation rate is then:

(1) 30 to 4 Ma: 0.34 mm/a

(2) 4 to 0 Ma: 0.68 mm/a.

For a better constraint on the onset time and amount of increase of the exhumation rate, future studies should also consider the use of lower temperature thermochronometers such as (U-Th)/He or OSL-thermochronology (Optically Stimulated Luminescence) [*Herman et al.*, 2008].

V.4.2. Rate of tectonic exhumation in the Toce Dome

Considering the model of a low-angle detachment, the final vertical relative displacement obtained between footwall and hanging wall is between 10 and 15 km at the most. This relative displacement established in the current study is somewhat less than the value of round 15 km previously determined by *Grasemann and Mancktelow* [1993]. Most models predict that the fault velocity slows down at 16 ± 2 Ma, which would, within error, correspond to the age established for the brittle transition.

However, once again, more than one scenario for exhumation can be extracted from the models, with negative correlation between exhumation rate and the period of faulting.

A fast period of faulting (> 6 mm/a) over a very short period of 1 Ma from 17 to 16 Ma followed by a slower fault velocity of 0.7 mm/a (model A2) yields a rather high misfit function and tend to reset ZFT ages in the hanging wall in the vicinity of the fault (Fig. III.8g). A steady-state solution with onset of faulting at 28 Ma and a slip rate of 1 mm/a gives a poor probability regarding the onset of faulting (Fig. III.7a). Therefore, the following model, with a rather slow rate of tectonic exhumation (model

A1), is proposed as the most likely, because it has the highest probability and the closest fit to the dataset:
(1) 30 to 18 Ma: 0.34 mm/a
(2) 18 Ma onset of faulting
(3) 18 to 14 Ma: 1.74 mm/a
(4) 14 to 4 Ma: 0.69 mm/a
(5) 4 to 0 Ma: 1.37 mm/a.
This objective probabilistic method involving formal inversion of a wide range of potential models highlights the problem of establishing one unique exhumation rate or slip rate based solely on a data set of thermochronological ages. In traditional approaches using age-altitude or age-distance profiles, the extent of possible solutions is not carefully considered and errors in the estimation of the geothermal gradient are not considered.

V.5. Interplay between faulting and folding

Both extension-parallel and extension-perpendicular folds affect the low-angle detachment system. The extension-parallel or *D4* backfolds [e.g. *Milnes et al.*, 1981] in region IV develop during the last stage of exhumation at ca. 10 Ma (Fig. IV.11). They strongly fold the already exhumed Simplon mylonites, Sm, leading to a finite constrictional fabric, and are coeval with the more discrete lower grade Sm2 fabric and brittle detachment, which are only affected by open wavy folds (Fig. IV.13).
The Toce Dome is the most exhumed part of the Lepontine Dome (Fig. IV.15) and this exhumation is clearly correlated with the SFZ activity. However, the backfolds also contribute to the last stage of exhumation since ca. 10 Ma. The effect of such backfolding at ca. 10 Ma was not considered in the thermal model of this study (Chapter III). Considering them would tend to decrease the necessary amount of relative displacement due to orogen-parallel movement on the SFZ. Therefore, the fact that the SFZ is responsible for 15 km vertical displacement should be taken as a strict maximum.
The relationship between SFZ and the Southern Steep Belt (Fig. IV.1) is still not unequivocally established. It is proposed here that the SFZ already initiated as a dextral strike slip fault parallel to the general steep fabric and was later further steepened during ongoing tightening of the Steep Belt, with the formation of the open Masera synform (Fig. IV.16). To better establish these relationships, additional constraints on the absolute age of such structures are necessary.
The Simplon mylonites, Sm, also define a domal shape with an axis perpendicular the regional extension (Fig. IV.1). However, the later brittle movements do not show this domal shape. This is reflected by (1) the difference in plunge of the stretching lineation and striation (Fig. II.2c), (2) the cooling history between 17 and 14 Ma (Fig. II.12c), and (3) by the 3D geometric model of the SFZ (Fig. IV.13). This dome of the Simplon mylonites is interpreted to reflect the strain gradient through the footwall shear zone, as previously suggested by *Mancktelow* [1992] and *Mancktelow and Pavlis* [1994].

The evolution of the SFZ can be reconstituted as follow:
(1) Onset of normal ductile shear at ca. 18 Ma forming the Toce dome culmination between 18 to 14 Ma.
(2) Continuous exhumation of these mylonites through the ductile-to-brittle transition around 14 Ma.
(3) Subsequent perpendicular shortening of the fault zone resulting in the folding of the mylonites and steepening of the fault zone in the SE then active as a strike-slip fault.
(4) Final and still continuous brittle deformation leading to a more rigid-block like exhumation of the footwall.
Such 3D evolution of a low-angle detachment system (≤ 30°) has led to the finite juxtaposition of ductile and brittle deformation with a shallow dip, today observed within a section reflecting different structural crustal levels from NW to SE of the detachment system. This syn-orogenic extensional system has led to the exhumation and present day geometry of the Toce dome which represents the most strongly exhumed region of the Lepontine Dome.

V.6. Conclusions of this study

V.6.1. General implications

(1) This study proposes that the finite state of deformation, with the juxtaposition of a brittle fault against ductile mylonites within the footwall of a low-angle detachment, can be explained by a continuous exhumation history from the ductile to the brittle field.
(2) The kinematic modeling in this study provides a thermochronological signature to distinguish a low-angle detachment from a rolling hinge within a non-migmatitic gneiss dome.
(3) The SFZ is shown to best fit a model with an initial low-angle detachment geometry, and provides an example for such a low-angle detachment developed during continued overall convergence.
(4) This study highlights the importance of the 3D field geometry, due to the interplay between faulting and folding, in establishing the finite exhumation pattern in gneiss domes.

Although the existence of low-angle detachment systems on a crustal scale is highly debated, especially with regard to the mechanical problem of their initiation and slip at shallow dip, such structures are observed in the field and must be considered. As a good example of such a structure, the Simplon Fault Zone presents a telescoped crustal section of a single major low-angle fault system, initially dipping ≤ 30º and developed during continued convergence. In 1987, seismic (explosion and vibroseis) profiles were made in the Western Alps as part of the project NFP/PNR-20. The profile W3 (from Stalden to Zermatt), west of the Simplon region, is well situated to record any possible continuation at depth of the low-angle detachment fault. *Marchant et al.* [1993], interpret the reflector 3G, marked by reflector discontinuities outlined by circles in Figure V.1, as representing the Simplon detachment. Considering the depth of this reflector 3G and the horizontal distance from the outcrop of the SL (parallel to displacement direction), we would get an angle between 15 and 30º in regions I and IV. This fits very well with the observations and interpretations of this thesis, which proposes that the Simplon Fault Zone, from the beginning to the end of its history, a crustal scale low-angle detachment system.

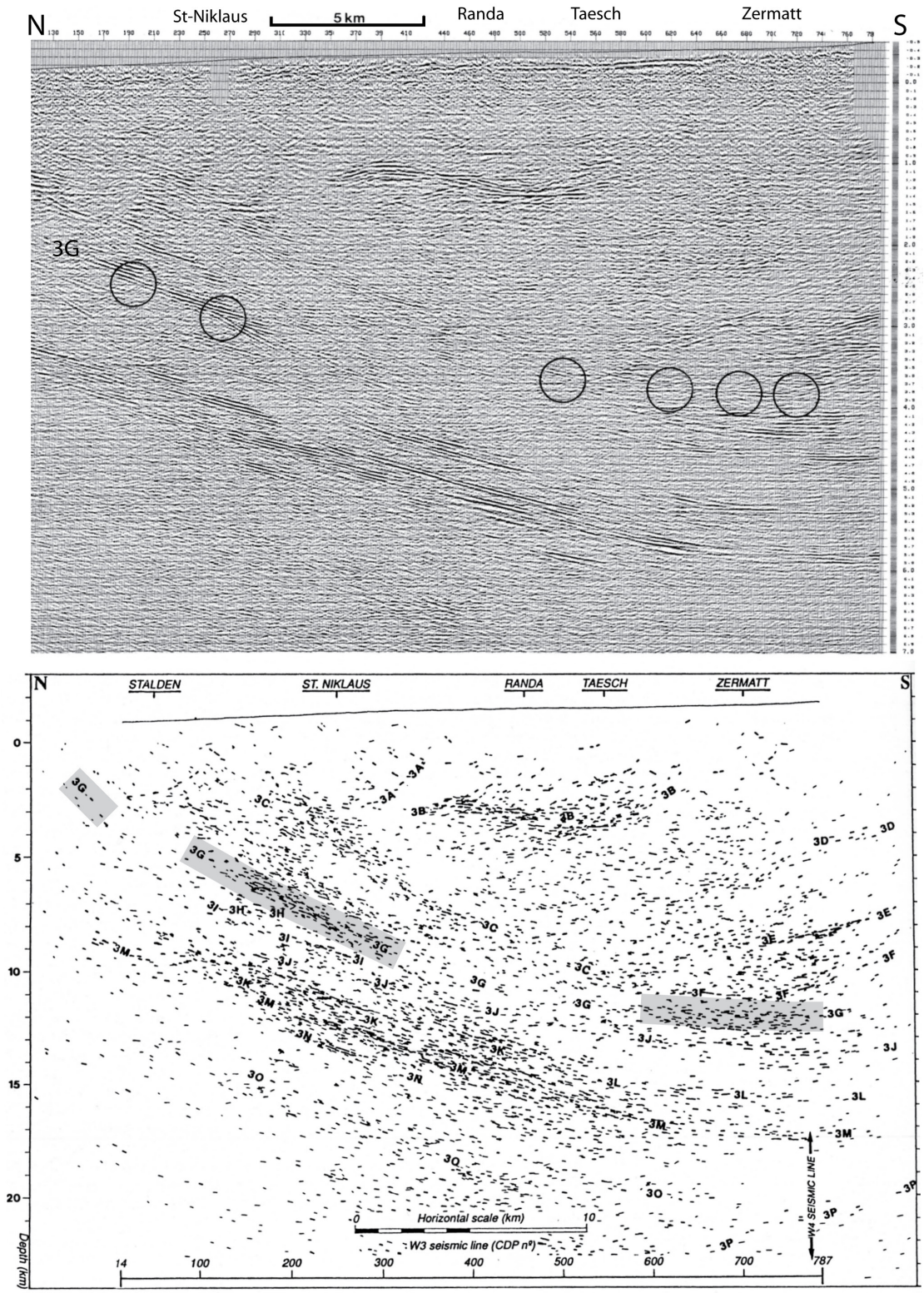

Figure V.1: Interpretation of deep seismic lines (profile W3 NFP/PNR-20) [*Marchant et al.*, 1993]. a) Conventional migration of line W3. Black circles indicate the interpreted Rhone-Simplon Line reflector. b) Geometric depth migration of line W3. Grey color highlights the reflector 3G interpreted as the Rhone-Simplon Line.

V.6.2. Alpine geodynamic implications

In the Alps, there are several examples of extensional systems developed during ongoing convergence in the Oligo-Miocene. In the Eastern Alps, for example, normal faults such as the Brenner Fault Zone [e.g. *Behrmann*, 1988; *Selverstone*, 1988; *Fugenschuh et al.*, 1997] are associated with major dextral and sinistral strike slip faults. These structures have been interpreted as reflecting a large scale extrusion toward the east [*Ratschbacher et al.*, 1991a, b], which started in the Oligocene and continued during the Miocene to Pliocene (Fig. V.2a).

In the eastern Central Alps, in the Bergell region, the Forcola normal fault [e.g. *Meyre et al.*, 1998] occupies a symmetric position to the SFZ and contributes, at smaller scale, to the exhumation of the eastern part of the Lepontine Dome. This fault zone postdates the Novate intrusion [*Liati et al.*, 2000] and, according to *Ciancaleoni and Marquer* [2008], was active from ca. 25 to 16 Ma. The sinistral Engadine fault [e.g. *Schmid and Froitzheim*, 1993] and dextral brittle faulting along the Periadriatic Line (25 to 15 Ma) [*Schmid et al.*, 1989] are broadly coeval and the association of the Forcola fault with these structures has also been interpreted as related to northeastward lateral extrusion [e.g. *Ciancaleoni and Marquer*, 2008] (Fig. V.2a).

In the Central and Western Alps, the SFZ is the major Neogene extensional fault zone. However, many smaller scale brittle orogen-parallel normal faults have also been recognized within the footwall and hanging wall [e.g. *Bistacchi and Massironi*, 2000; *Wawrzyniec et al.*, 2001; *Champagnac et al.*, 2004; *Grosjean et al.*, 2004]. Strike-slip fault systems coeval with the SFZ are generally dextral in sense: the Rhone, Centovalli, and Periadriatic Lines, and more localized dextral shear zone networks within the external Aar massif [*Rolland*, personal communication]. Figure V.2a presents a summary of the ages of these structures in the Oligo-Miocene. The dextral motion observed along the Rhone valley is described as continuing toward the Mont Blanc massif and beyond ([e.g. *Hubbard and Mancktelow*, 1992] and references therein), with a total horizontal offset estimated at ca. 10 km by *Burkhard* [1988]. In the Western Alps, the Ospizio brittle fault [*Bistacchi and Massironi*, 2000] is the only major sinistral strike-slip fault described.

Different kinematic models have been proposed to explain the mechanism of orogen-parallel extension in the Central and Western Alps.
(1) Large scale extension due to general collapse of the orogen [*Dewey*, 1988].
(2) A transpressive mechanism due to oblique convergence and transfer of movement on the Rhone Line to the Periadriatic Line [*Steck*, 1990; *Hubbard and Mancktelow*, 1992; *Schmid and Kissling*, 2000] or within the Toce Dome [*Mancktelow*, 1992; *Mancktelow and Pavlis*, 1994].
(3) Oblique indentation of a bent Adriatic indenter leading to the formation of a curved continuous wedge of backfolds in the south and to differential shortening between the footwall (FW) and hanging wall (HW) in the north [*Keller et al.*, 2006] (Fig. I.6d).
(4) Southwestward lateral extrusion with the opening of the Ligurian sea acting as a free boundary, resulting from the onset of anticlockwise rotation of the Adriatic indenter [*Champagnac et al.*, 2006].

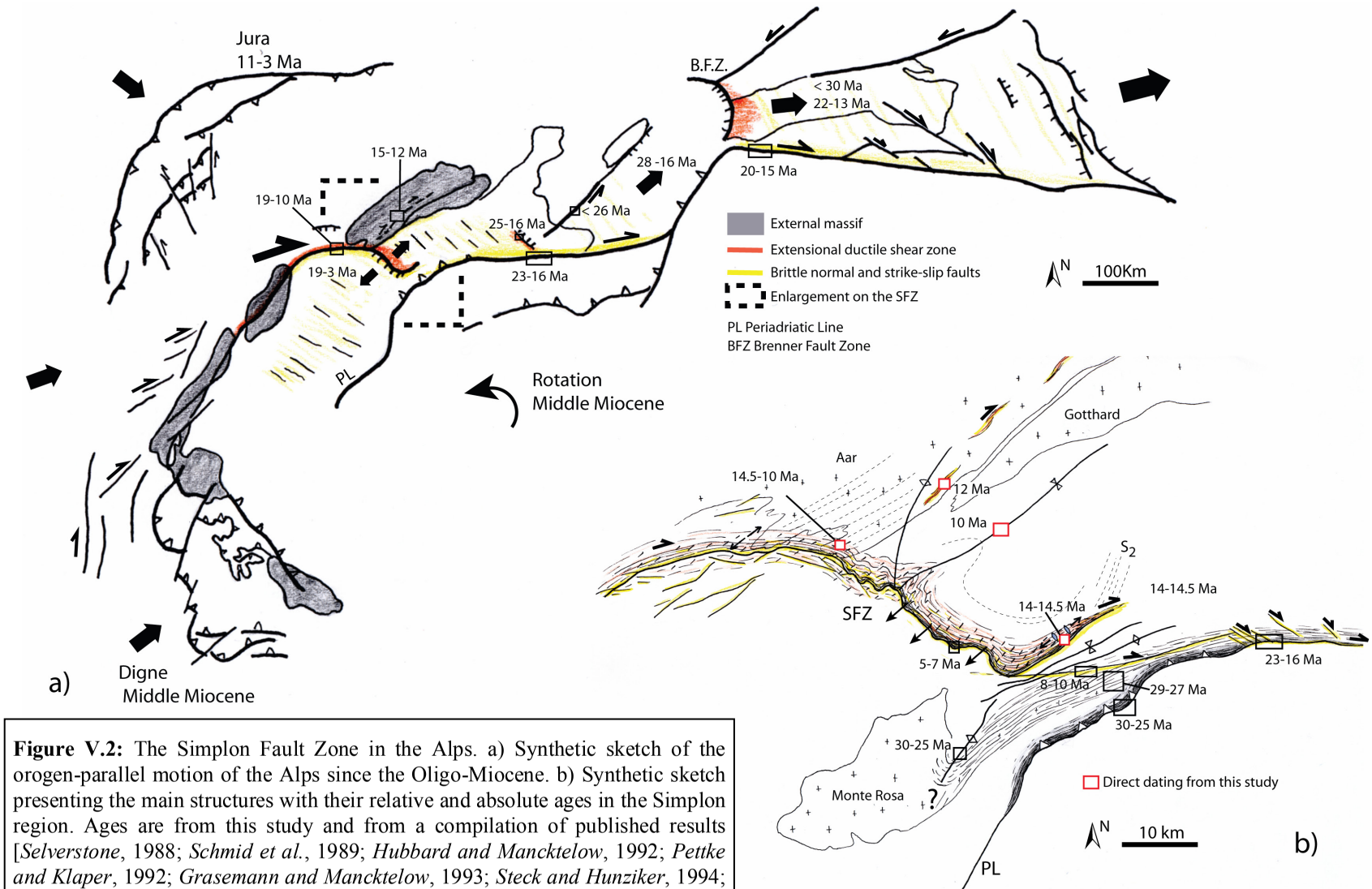

Figure V.2: The Simplon Fault Zone in the Alps. a) Synthetic sketch of the orogen-parallel motion of the Alps since the Oligo-Miocene. b) Synthetic sketch presenting the main structures with their relative and absolute ages in the Simplon region. Ages are from this study and from a compilation of published results [*Selverstone*, 1988; *Schmid et al.*, 1989; *Hubbard and Mancktelow*, 1992; *Pettke and Klaper*, 1992; *Grasemann and Mancktelow*, 1993; *Steck and Hunziker*, 1994; *Romer et al.*, 1996; *Fugenschuh et al.*, 1997; *Lickorish et al.*, 2002; *Müller et al.*, 2002; *Zwingmann and Mancktelow*, 2004; *Ciancaleoni and Marquer*, 2008; *Rolland*, personal communication].

Large scale extension due to general collapse (model (1) above) cannot be considered as appropriate, because the SFZ is clearly developed during ongoing convergence, as discussed in Chapter IV. The invariable stretching lineation and the similar relative displacement between footwall and hanging wall suggested by zircon fission-track ages in region I and IV argue against model (3), which proposes differential shortening between footwall and hanging wall leading to anticlockwise rotation of the hanging wall block. Model (4), involving lateral extrusion toward the SW, lacks the major middle Miocene sinistral faults recording ca. 10 km necessary to accommodate the extrusion.

For these reasons, model (2) above, involving large scale transpressive motion due to oblique collision, is proposed as the principal mechanism during Miocene convergence and exhumation. This oblique motion has locally being accommodated by the SFZ extensional system acting as a transfer zone and leading to gneiss dome exhumation during ongoing convergence. Middle Miocene anticlockwise rotation of the Adriatic indenter is implied in other published studies [e.g. *Collombet et al.*, 2002; *Lickorish et al.*, 2002] and could result in the onset of oblique collision (Fig. V.2a).
However, structural arguments do not support a transfer of the full ca. 10 km offset on the Rhone Line to the Periadriatic Line, with only a small part possibly transferred under brittle conditions to the Centovalli Line (Fig. V.2b). Instead a clear termination of the shear zone is described within the Isorno Valley (Fig. V.2b) with loss of the displacement and of the overprint.

Appendix A: Methodology

Fission track methodology

The separation of zircon and apatite grains was achieved by conventional crushing, Wilfley table, magnetic and heavy liquid techniques [*Seward*, 1989]. Apatites and zircons were analyzed using the external detector method. Zircon grains were mounted in teflon and polished. Samples were etched in NaOH-KOH eutectic melt at 210°C for 20-23h. Apatite grains were mounted on glass slides using epoxy glue and polished. Samples were etched in 7% HNO_3 for 50s at 21°C. Irradiation were carried out at the ANSTO facility, Lucas Heights (Australia), and at the radiation center Oregon state University, Corvallis (USA) with a nominal neutron flux of 1.0×10^{16} neutrons cm^{-2} for apatite and 1.0×10^{15} neutrons cm^{-2} for zircon. Mica detectors were etched after irradiation to reveal induced tracks using 40% HF at room temperature for 50min. Microscopic analysis was carried out using a Zeiss Axioplan2 optical microscope with a computer-driven stage and FTstage 4 software from *Dumitru*, [1995]. The magnification used was 1250x for apatite and 1600x (oil) for zircon. All ages were determined using the zeta approach [*Hurford and Green*, 1983] with a zeta value of 341 ± 6 for CN5/apatite, and of 130 ± 0.6 for CN1/zircon. At least 20 grains were counted for each sample except for MC32 where only 7 grains could be analyzed.

$^{40}Ar/^{39}Ar$ methodology

Samples were crushed, and then washed in an ultrasonic bath for 10min successively with water, alcohol and distilled water. Single grains of muscovite and biotite, and aggregates of phengite with a grain size between 800-500µm were separated by hand-picking under a binocular microscope. To avoid inclusions or alteration, transparent grains and aggregates were selected. Samples were irradiated in the nuclear reactor at McMaster University in Hamilton (Canada). $^{40}Ar/^{39}Ar$ analysis was carried out by single-grain analysis with a 50 W SYNRAD CO_2 continuous laser. Isotopic ratios were measured using a VG3600 mass spectrometer, working with a Daly detector system, at the University of Nice (Géosciences Azur, France). The typical blank values for extraction and purification of the laser system are in the range 4.2–8.75, 1.2–3.9 cm^3 STP for masses 40 and 39, respectively. Two samples MC22 and MC36 were analysed in a step-heating experiment with a double-vacuum high-frequency furnace. Decay constants are those of *Steiger and Jäger* [1977] ($5.543e10^{-10}$ y^{-1}). Isotopic measurements are corrected from isotopic interferences of K, Ca and Cl, mass discrimination and atmospheric argon contamination. Uncertainties on individual apparent ages are given at the 1 sigma level and do not include the error on the $^{40}Ar^*/^{39}Ark$ ratio of the monitor (± 0.2%). Uncertainties on plateau ages and integrated ages are given at the 2 sigma level and do not include the error on the age of the monitor. A plateau age is defined when at least 70% of the ^{39}Ar is released and there are a minimum of three successive steps in the plateau. Using the laser on single grains has the advantage of avoiding mixed population ages but it produces a lower signal than with the furnace method. This is the reason why big mica flakes (800-500µm) were chosen in this study and why, in some specific cases when the white micas were too small, a population of several individual grains was analyzed.

Rb-Sr microsampling methodology

Micro-sampling was first carried out by cutting blocks parallel to the Simplon stretching lineation, from which polished thick sections ~50µm thick were prepared using Crystalbond glue which can be reheated and liquefied [cf. *Müller et al.,* 2000a, b]. White micas fibers growing between broken porphyroclasts and calcite-white micas in textural contact inside the veins were cut with a microscope-mounted microdrill. Micro-samples were collected under a binocular microscope after heating the thick section. The samples were then cleaned in an ultrasonic bath for 10min in successively acetone (x2), methanol, and IR-distilled water (x3), and subsequently weighed using a microbalance.

The white micas were leached twice to ensure separation of silicates from residual carbonates with 250µl of ~4M acetic acid in an ultrasonic bath (10min) and on a warm plate at 120°C (~ 2h). After being rinsed with 200µl of water, they were leached with 250µl of 1M HCl on a warm plate at 120°C for ~ 5min. Subsequently, the samples were rinsed with 300µl of water and weighed afterward to calculate the real mass and density. After addition of a mixed ^{84}Sr-^{85}Rb tracer solution, the silicate samples were then dissolved in closed teflon vials at 120°C with 600µl HF and 30µl HNO_3 for about 2-3 days. After evaporation, samples were equilibrated overnight with 600µl 6M HCl at 120°C, followed with 10min in the ultrasonic bath. Calcite samples were dissolved in closed teflon vials at 120°C with 400µl of 1 M HCl for about 1 day after addition of a ^{84}Sr-^{85}Rb tracer. Rb and Sr were purified using micro-columns of 0.377 ml of cation resin as a first step, and the broad Sr cut was further purified using a 50µl SrSpec column.

Isotopic analyses were carried out using thermal ionization mass spectrometry (TIMS), namely a Thermo-Finnigan Triton mass spectrometer (Open University, UK) for Sr and a VG354 at Royal Holloway University of London for Rb, in both cases using a Ta-emitter solution on zone-refined outgassed Re filaments [*Birck et al*., 1986]. Sr blanks were 31.6 and 40 pg and no blank correction was necessary; repeated analysis of SRM987 yielded 0.710280 ± 0.000010 (2 SD). Constants were those from *Steiger and Jäger* [1977].

Oxygen isotope methodology

Quartz and white mica in textural contact inside each vein where isolated by cutting with a millimetre thick saw and the grain size then reduced to ~1-2 mg by crushing. Grains were subsequently washed in an ultrasonic bath for 10min in successively acetone (x2), methanol, and IR-distilled water (x2). Samples were then leached in 10% HCl at room temperature for ~1h30 to ensure separation from residual carbonates. The samples were then rinsed twice in an ultrasonic bath for 10min with IR-distilled water. Samples have been carefully chosen to avoid inclusions with a binocular microscope. Duplicate measurements were made of the oxygen isotopes on 5 white mica and quartz samples for each vein at the University of Lausanne. Samples were loaded in a Pt-trail in a F2 saturated chamber 12 hours prior to CO_2 laser extraction. The CO_2-laser fluorination line is equipped with a Finnigan MAT 253 for normal dual inlet and carrier gas analyses.

Microprobe analysis

Major elements analyses of minerals have been done at the ETH Zurich using a "JEOL-8200 WDS/EDS microanalyser" microprobe. Beam conditions were: an acceleration voltage of 15 kv and $2*10^{-8}$ A. Counting time was 20s on the peak for each element. The detection limit is superior to 0.01 wt% for each element. The probe diameter was between 0 and 5 μm depending on grain size.

Appendix B: Fission track dataset

ETH-327-2	MCS3	--- TRACKKEY 4.2.g ---	*counted: 4 Feb. 07*
Zircon	FW-Engiloch	Orthogneiss Monte Leone	x10 x1.6 x100 Marion Campani microscope 1

	Area:		
Cryst.:	1144		
30			
Ns:	RhoS:		
617	13.794		
Ni:	RhoI:		
1826	40.822		
Pooled:	0.338	11.2	± 0.6
Mean:	0.365	12.1	± 0.9
Central:	0.345	11.4	± 0.9
Weigh.I:	0.339	11.3	
Weigh.II:	0.37	12.3	

Chi-sq.: 63.74 **P (%):** 0.02

Dispersion: 0.28

a: 3.896 **b:** 0.249 **r:** 0.79

Irr.: 327-10 **Glass:** CN_1

Nd: 1655 **RhoD:** 5.116422

Zeta: 129.99 ± 0.6 **U.:** 279.04 (± 68 %)

Goodness: n. d.

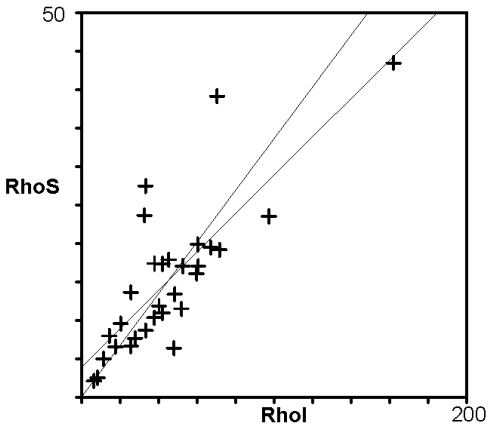

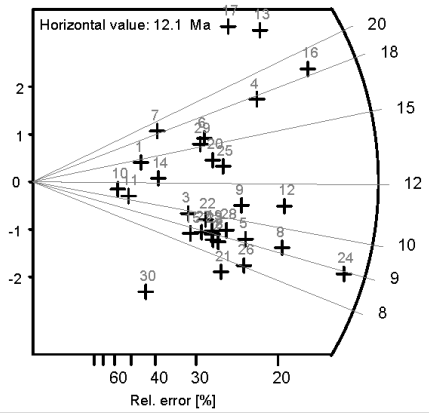

kurt.: 2.28 skew.: 1.48

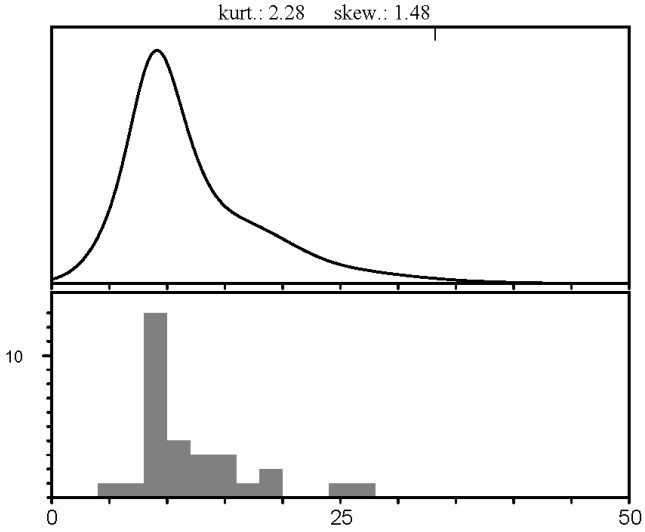

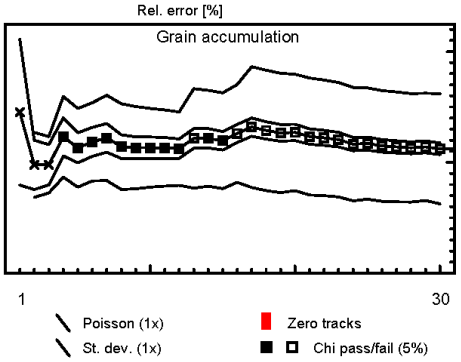

ETH-327-6	MCS8	--- TRACKKEY 4.2.g ---	*counted: 19 Feb. 07*
Zircon	VispValley	Calc-Schist	x10 x100 x1.6 Marion Campani microscope 1

Cryst.: 20 ***Area:*** 840
Ns: 597 ***RhoS:*** 18.177
Ni: 884 ***RhoI:*** 26.915

Pooled:	0.675	20.5	± 1.2
Mean:	0.672	20.4	± 1.7
Central:	0.655	19.9	± 1.6
Weigh.I:	0.717	21.8	
Weigh.II:	0.70	21.2	

Chi-sq.: 40.41 ***P (%):*** 0.29
Dispersion: 0.25
a: -2.792 ***b:*** 0.784 ***r:*** 0.89
Irr.: 327-10 ***Glass:*** CN_1
Nd: 1655 ***RhoD:*** 4.688497778
Zeta: 129.99 ± 0.6 ***U.:*** 203.09 (± 59 %)
Goodness: n. d.

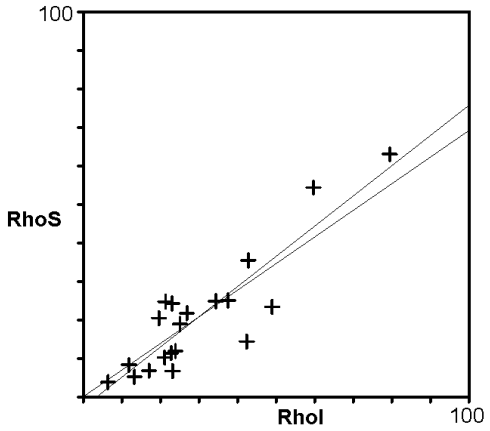

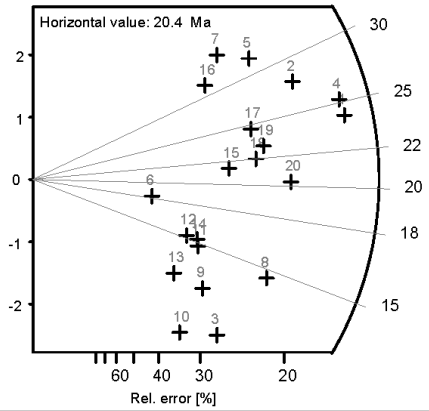

kurt.: -0.77 skew.: 0.32

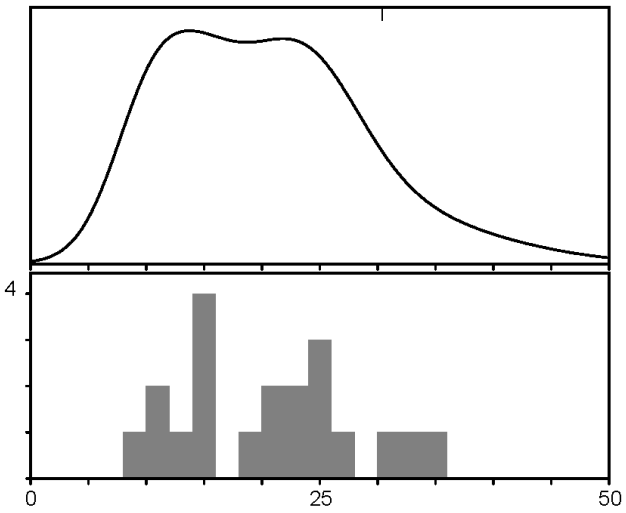

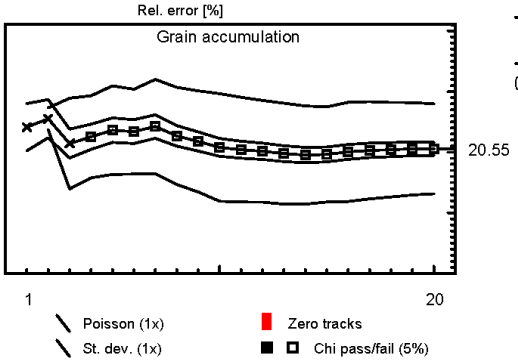

ETH-327-8	MCS12	--- TRACKKEY 4.2.g ---	*counted: 20 Feb. 07*

Zircon | Visp | Calc-Schist | x10 x100 x1.6 oil | Marion Campani microscope 1

Cryst.: ***Area:***
26 980
Ns: ***RhoS:***
449 11.718
Ni: ***RhoI:***
925 24.14

Pooled:	0.485	14.1	± 0.9
Mean:	0.484	14.0	± 0.9
Central:	0.484	14.0	± 0.9
Weigh.I:	0.486	14.1	
Weigh.II:	0.50	14.5	

Chi-sq.: 27.65 ***P (%):*** 32.4

Dispersion: 0.11

a: 1.744 ***b:*** 0.403 ***r:*** 0.77

Irr.: 327-10 ***Glass:*** CN_1

Nd: 1655 ***RhoD:*** 4.462648889

Zeta: 129.99 ± 0.6 ***U.:*** 180.04 (± 47 %)

Goodness: n. d.

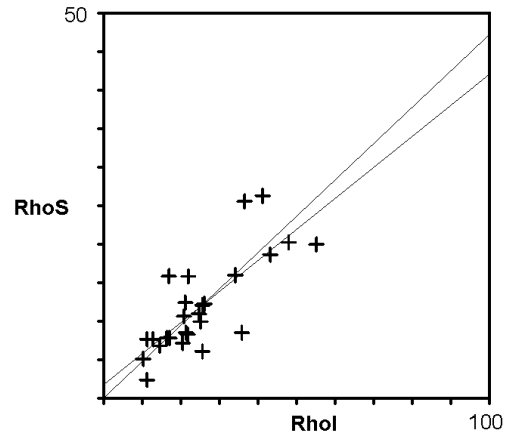

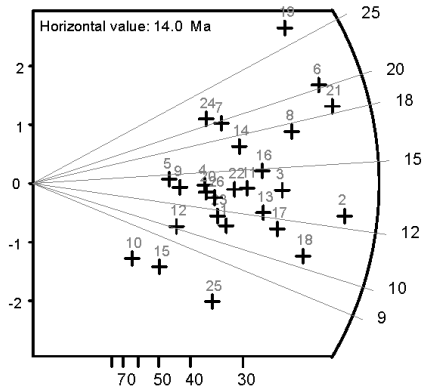

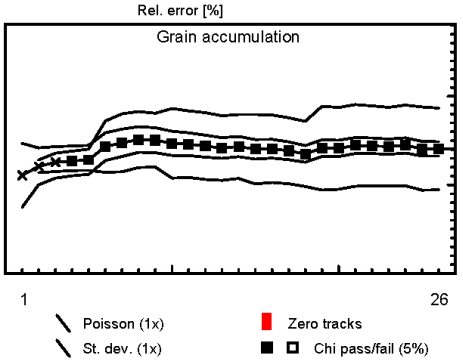

kurt.: 1.29 skew.: 0.77

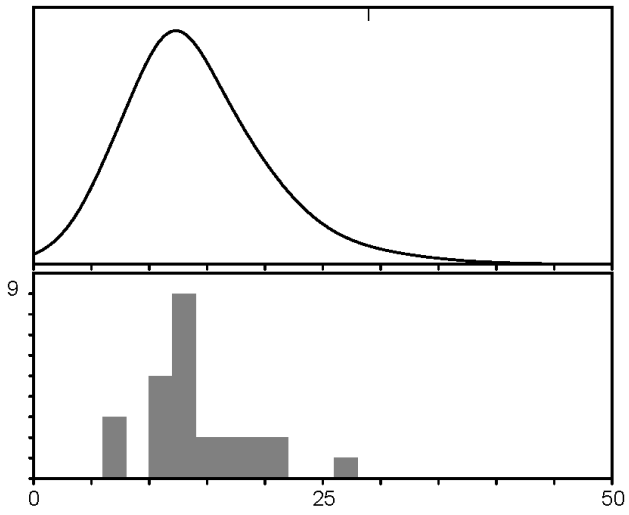

ETH-327-14	MC32	--- TRACKKEY 4.2.g ---	*counted: 27 Mar. 07*

Zircon | SimplonPass FW Monte Leone | orthogneiss | x10 x100 x1.6oil | Marion Campani microscope 1

Cryst.:	***Area:***
7	155
Ns:	***RhoS:***
120	19.8
Ni:	***RhoI:***
215	35.476

Pooled:	0.558	13.7	± 1.6
Mean:	0.517	12.7	± 1.1
Central:	0.558	13.7	± 1.6
Weigh.I:	0.583	14.3	
Weigh.II:	0.54	13.4	

Chi-sq.: 2.77 ***P (%):*** 83.74

Dispersion: 0.00

a: -4.752 ***b:*** 0.694 ***r:*** 0.99

Irr.: 327-10 ***Glass:*** CN_1

Nd: 1655 ***RhoD:*** 3.785102222

Zeta: 129.99 ± 0.6 ***U.:*** 298.97 (± 58 %)

Goodness: n. d.

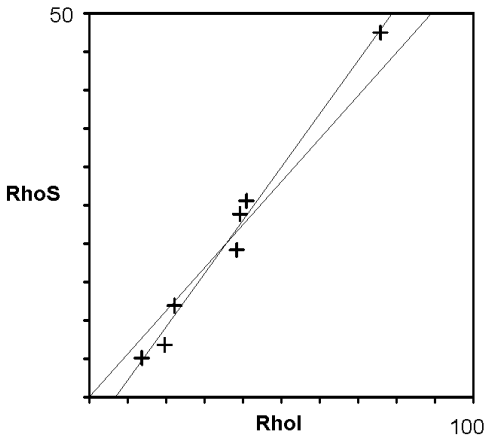

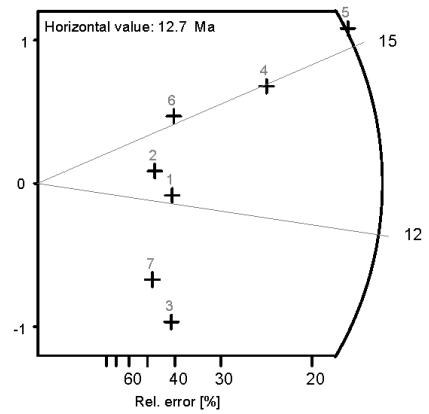

kurt.: -1.40 skew.: -0.65

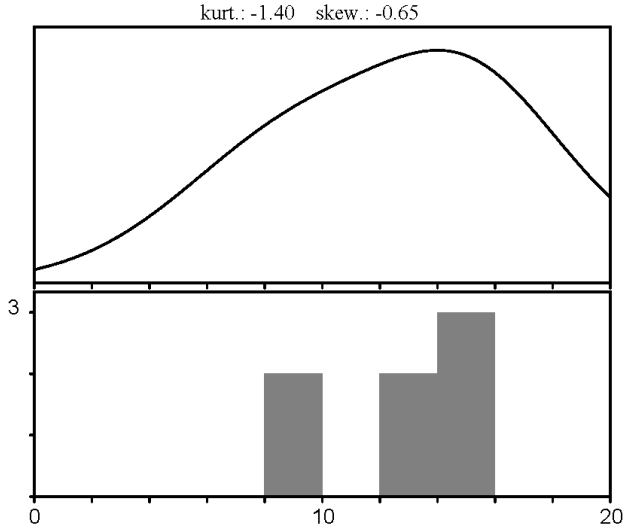

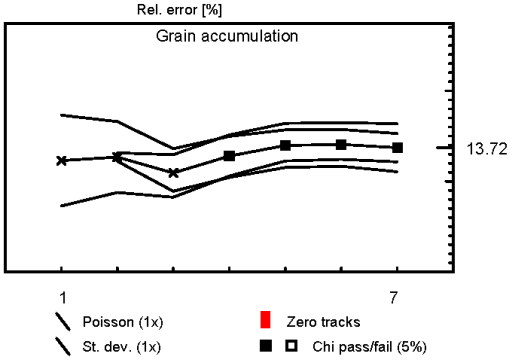

Poisson (1x) Zero tracks
St. dev. (1x) Chi pass/fail (5%)

ETH-327-13	MC33	--- TRACKKEY 4.2.g ---	*counted: 6 Feb. 07*

Zircon | HW Monte Leone | Orthogneiss | x10 x100x1.6 oil | Marion Campani microscope 1

Cryst.: 26 ***Area:*** 1102
Ns: 808 ***RhoS:*** 18.752
Ni: 1232 ***RhoI:*** 28.593

Pooled:	0.656	16.6	± 0.9
Mean:	0.694	17.6	± 1.2
Central:	0.651	16.5	± 1.0
Weigh.I:	0.647	16.4	
Weigh.II:	0.69	17.4	

Chi-sq.: 38.22 ***P (%):*** 4.4
Dispersion: 0.15
a: 1.408 ***b:*** 0.581 ***r:*** 0.89
Irr.: 327-10 ***Glass:*** CN_1
Nd: 1655 ***RhoD:*** 3.909913451
Zeta: 129.99 ± 0.6 ***U.:*** 239.62 (± 65 %)
Goodness: n. d.

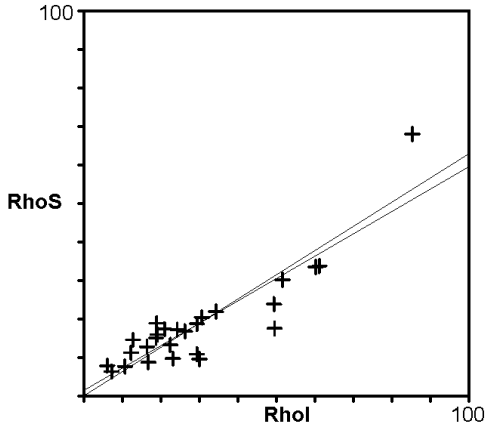

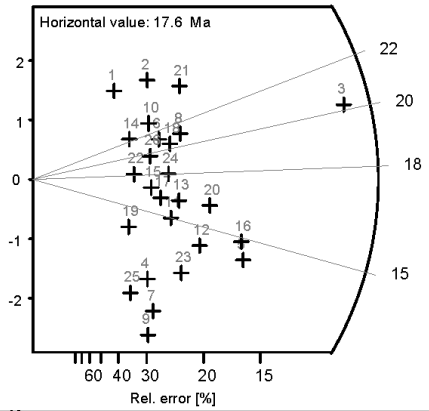

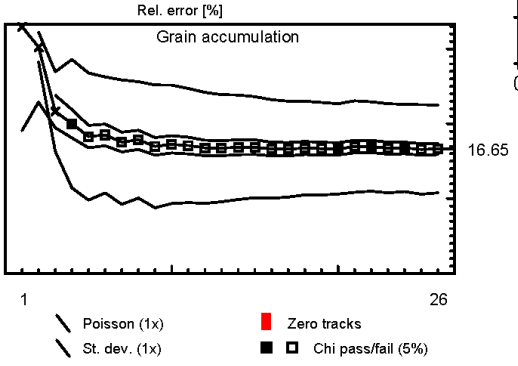

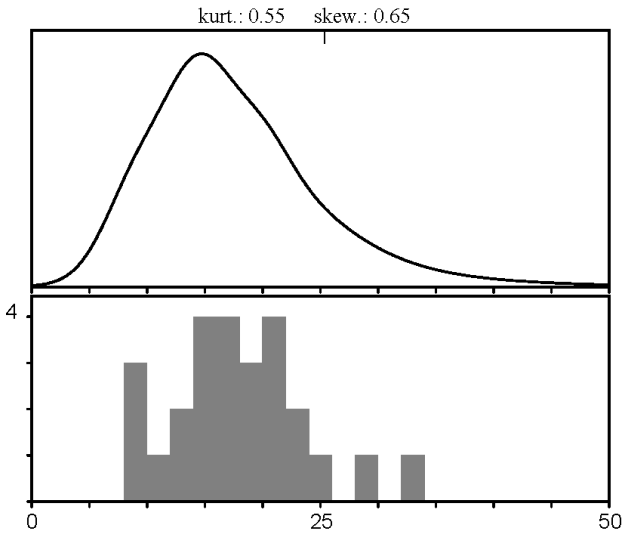

ETH-344-22	MC269	--- TRACKKEY 4.2.g ---	*counted: 19 Sep. 07*
Zircon	Visp Valley	sandstone	Marion microscope 1

Cryst.: 20 ***Area:*** 981
Ns: 481 ***RhoS:*** 12.54
Ni: 1138 ***RhoI:*** 29.669

Pooled:	0.423	11.5	± 0.7
Mean:	0.444	12.1	± 0.9
Central:	0.427	11.6	± 0.8
Weigh.I:	0.424	11.6	
Weigh.II:	0.45	12.2	

Chi-sq.: 29.25 ***P (%):*** 6.22
Dispersion: 0.17
a: 3.579 ***b:*** 0.307 ***r:*** 0.8
Irr.: 344 ***Glass:*** CN_1
Nd: 2833 ***RhoD:*** 4.1991353
Zeta: 129.99 ± 0.6 ***U.:*** 229.37 (± 51 %)
Goodness: n. d.

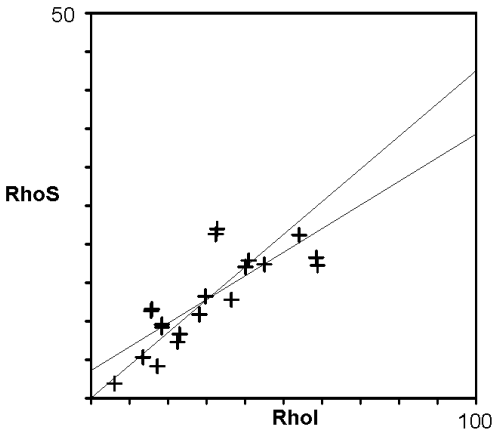

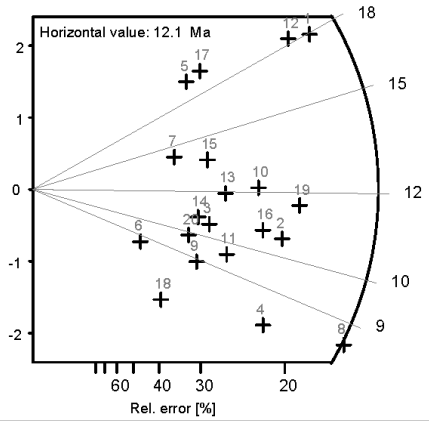

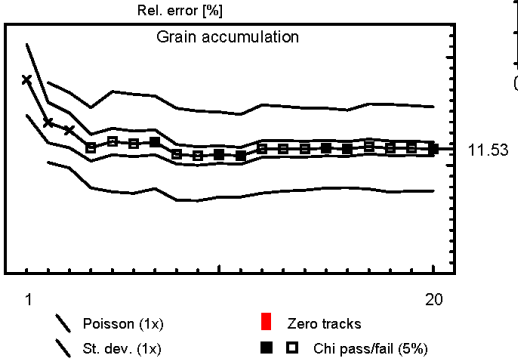

kurt.: -0.23 skew.: 0.91

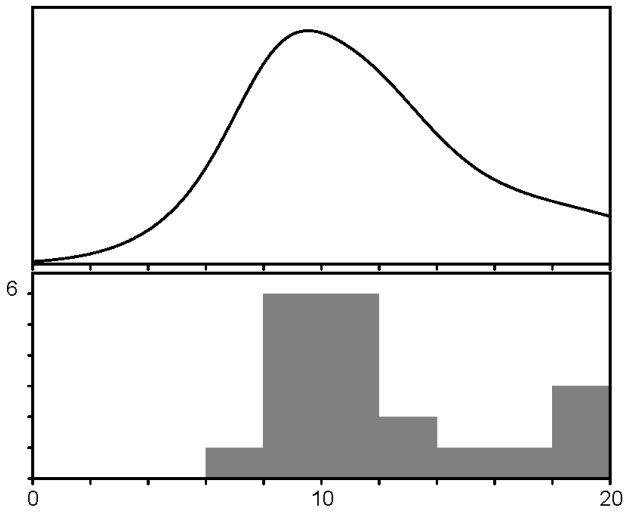

ETH-344-26 MC282 --- TRACKKEY 4.2.g --- *counted: 17 Sep. 07*

Zircon Simplon Pass quartzite x10 x100 x1.6oil Marion Campani Microscope 1

	Area:		
Cryst.:	741		
Ns:	RhoS:		
344	11.873		
Ni:	Rhol:		
625	21.572		
Pooled:	0.55	14.4	± 1.0
Mean:	0.667	17.5	± 2.3
Central:	0.572	15.0	± 1.5
Weigh.I:	0.575	15.0	
Weigh.II:	0.64	16.9	

Chi-sq.: 43.73 **P (%):** 0.1

Dispersion: 0.33

a: 6.606 **b:** 0.283 **r:** 0.47

Irr.: 344 **Glass:** CN_1

Nd: 2833 **RhoD:** 4.029045

Zeta: 129.99 ± 0.6 **U.:** 171.57 (± 47 %)

Goodness: n. d.

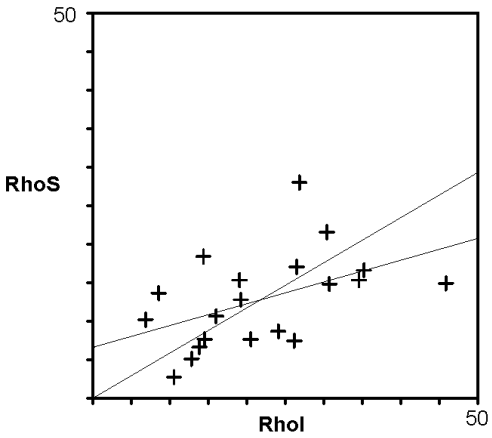

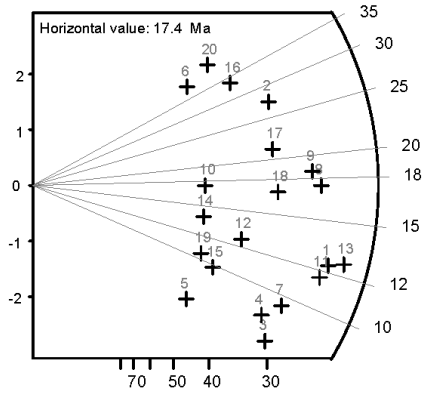

kurt.: 0.89 skew.: 1.34

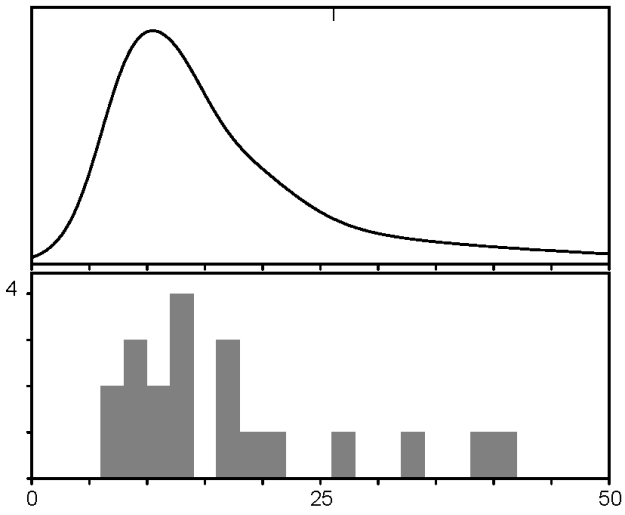

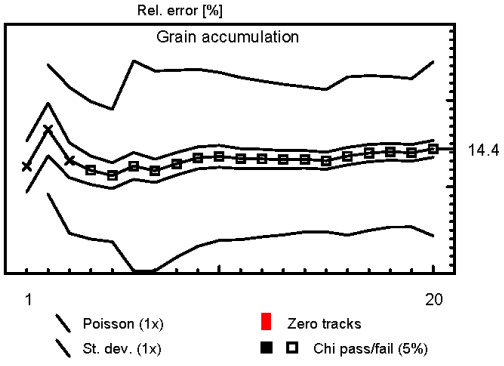

ETH-364-11 MC454 = MC283 --- TRACKKEY 4.2.g --- *counted: 12 Jul. 08*

Zircon | Simplon Pass, Gd St Bernard | paragneiss | x10x100x1.6 oil | Marion Campani, microscope 1

Cryst.: 21 ***Area:*** 520
Ns: 266 ***RhoS:*** 13.083
Ni: 492 ***RhoI:*** 24.198

Pooled:	0.541	17.4	± 1.4
Mean:	0.575	18.5	± 1.5
Central:	0.539	17.4	± 1.5
Weigh.I:	0.542	17.5	
Weigh.II:	0.58	18.7	

Chi-sq.: 22.56 ***P (%):*** 31.09
Dispersion: 0.16
a: 2.252 ***b:*** 0.446 ***r:*** 0.82
Irr.: eth364 ***Glass:*** CN_1
Nd: 3150 ***RhoD:*** 4.968306426
Zeta: 129.99 ± 0.6 ***U.:*** 162.0 (± 59 %)
Goodness: n. d.

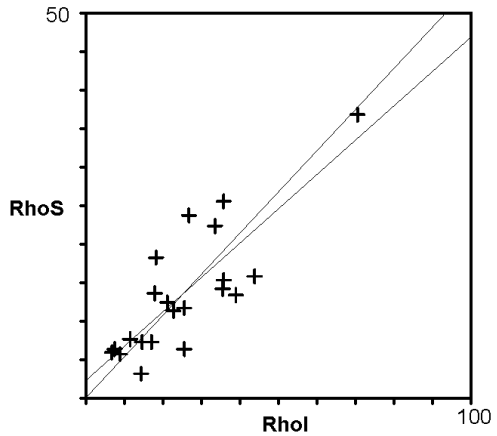

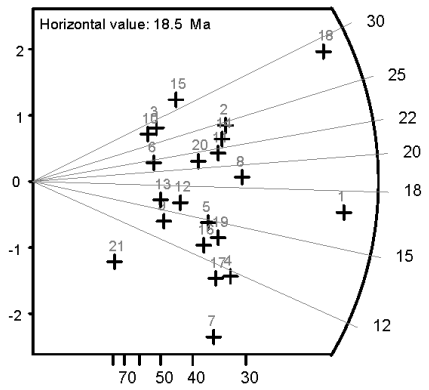

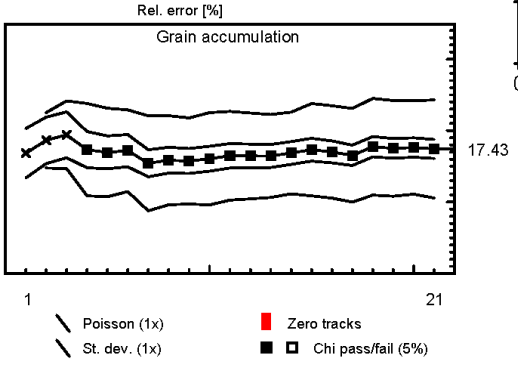

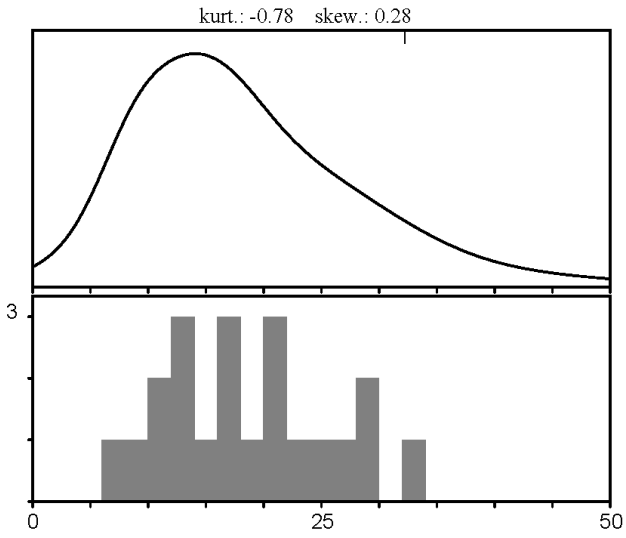

ETH-364-33 MC335 --- TRACKKEY 4.2.g --- *counted: 16 Jul. 08*

Zircon | Gamsen Mamontain | Quartzite | x10x100x1.6 oil | Marion Campani microscope 1

Cryst.:	***Area:***
20	679
Ns:	***RhoS:***
300	11.3
Ni:	***RhoI:***
677	25.5

Pooled:	0.443	11.0	± 0.8
Mean:	0.462	11.5	± 1.1
Central:	0.437	10.9	± 1.1
Weigh.I:	0.436	10.8	
Weigh.II:	0.48	11.8	

Chi-sq.: 30.86 ***P (%):*** 4.18

Dispersion: 0.26

a: 4.488 ***b:*** 0.29 ***r:*** 0.84

Irr.: eth364-2 ***Glass:*** CN_1

Nd: 2419 ***RhoD:*** 3.827473042

Zeta: 129.99 ± 0.6 ***U.:*** 264.73 (± 126 %)

Goodness: n. d.

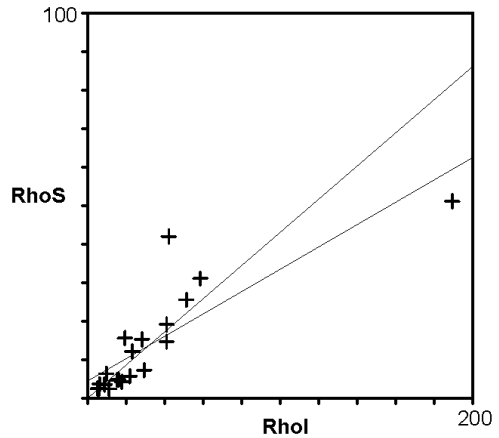

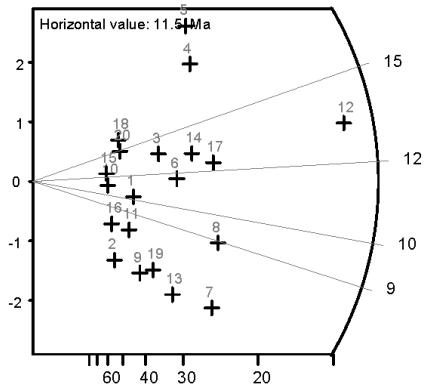

kurt.: 1.31 skew.: 1.09

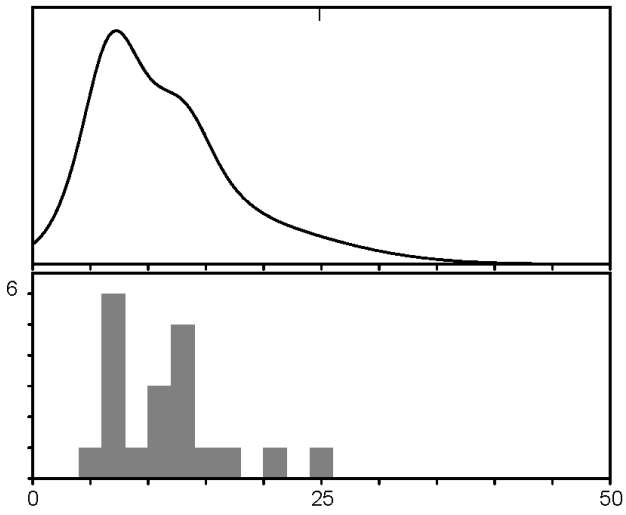

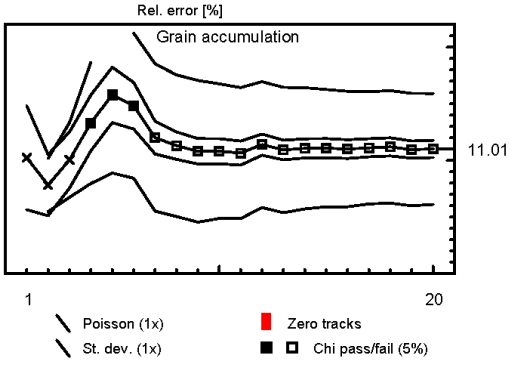

ETH-364-18	MC475	--- TRACKKEY 4.2.g ---	*counted: 13 Jul. 08*

Zircon

Gebidum FW Monte Leone	Orthogneiss	x10x100x1.6 oil	Marion Campani microscope 1

Cryst.: 21 ***Area:*** 542
Ns: 243 ***RhoS:*** 11.466
Ni: 595 ***RhoI:*** 28.076

Pooled:	0.408	12.2	± 1.0
Mean:	0.469	14.0	± 1.4
Central:	0.416	12.4	± 1.2
Weigh.I:	0.423	12.6	
Weigh.II:	0.46	13.8	

Chi-sq.: 29.24 ***P (%):*** 8.31
Dispersion: 0.22
a: 5.713 ***b:*** 0.231 ***r:*** 0.61
Irr.: eth364 ***Glass:*** CN_1
Nd: 3150 ***RhoD:*** 4.581751551
Zeta: 129.99 ± 0.6 ***U.:*** 203.73 (± 48 %)
Goodness: n. d.

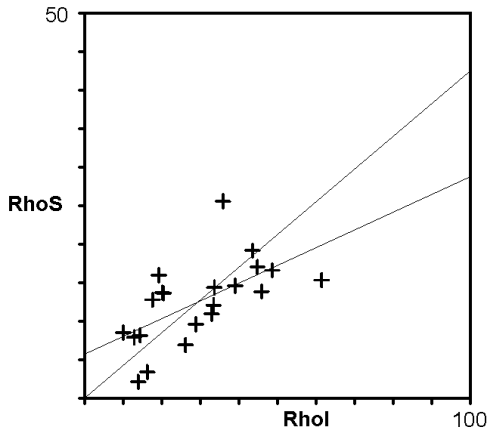

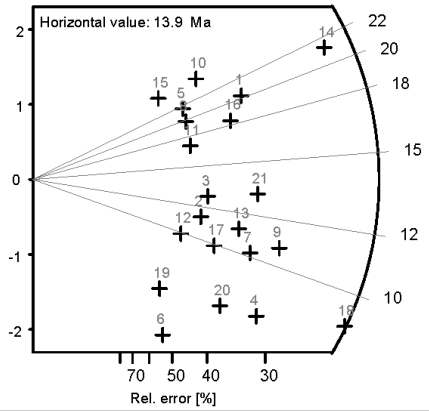

kurt.: -1.05 skew.: 0.46

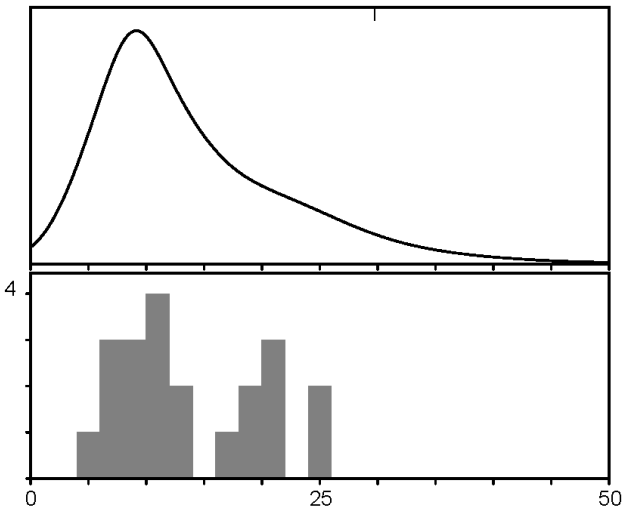

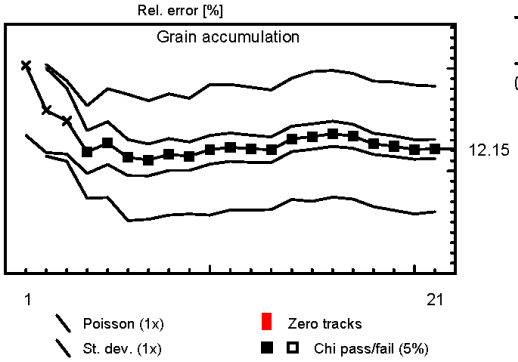

ETH-364-23	MC476	--- TRACKKEY 4.2.g ---	*counted: 14 Jul. 08*	
Zircon	Gebidum Mamontain	Quartzite	x10x100x1.6 oil	Marion Campani

Cryst.: 28 ***Area:*** 848
Ns: 439 ***RhoS:*** 13.24
Ni: 626 ***RhoI:*** 18.88

Pooled:	0.701	18.3	± 1.2
Mean:	0.762	19.8	± 1.5
Central:	0.7	18.2	± 1.5
Weigh.I:	0.726	18.9	
Weigh.II:	0.77	20.0	

Chi-sq.: 41.57 ***P (%):*** 3.63
Dispersion: 0.24
a: 3.096 ***b:*** 0.557 ***r:*** 0.7
Irr.: eth364-2 ***Glass:*** CN_1
Nd: 2419 ***RhoD:*** 4.014382487
Zeta: 129.99 ± 0.6 ***U.:*** 155.25 (± 55 %)
Goodness: n. d.

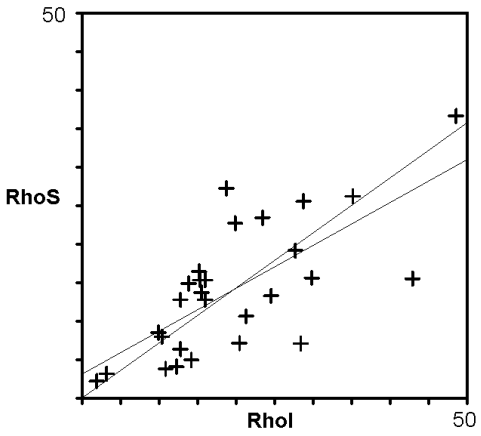

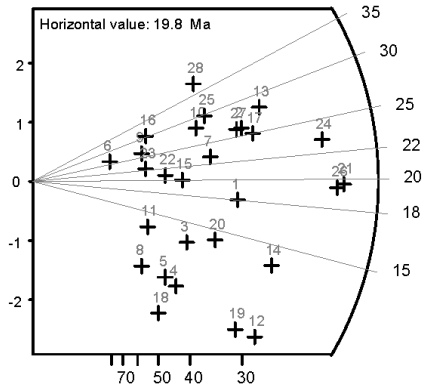

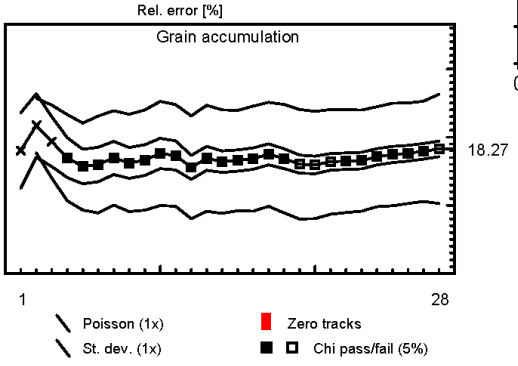

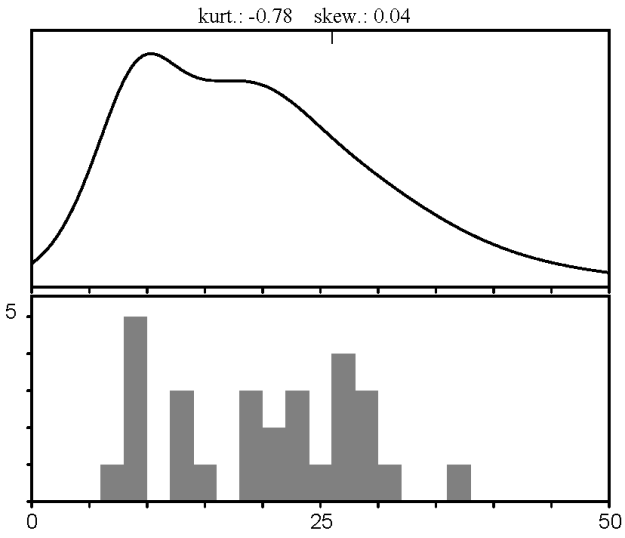

ETH-364-28	MC477	--- TRACKKEY 4.2.g ---	*counted: 15 Jul. 08*
Zircon	Gebidum Gd St Bernard	paragneiss	x10x100x1.6 oil	Marion Campani microscope 1

Cryst.:	***Area:***		
22	855		
Ns:	***RhoS:***		
462	13.82		
Ni:	***RhoI:***		
682	20.401		
Pooled:	0.677	17.3	± 1.1
Mean:	0.679	17.3	± 1.2
Central:	0.677	17.2	± 1.1
Weigh.I:	0.714	18.2	
Weigh.II:	0.69	17.7	

Chi-sq.: 20.58 ***P (%):*** 48.47

Dispersion: 0.04

a: -3.473 ***b:*** 0.866 ***r:*** 0.82

Irr.: eth364-2 ***Glass:*** CN_1

Nd: 2419 ***RhoD:*** 3.924454358

Zeta: 129.99 ± 0.6 ***U.:*** 170.14 (± 38 %)

Goodness: n. d.

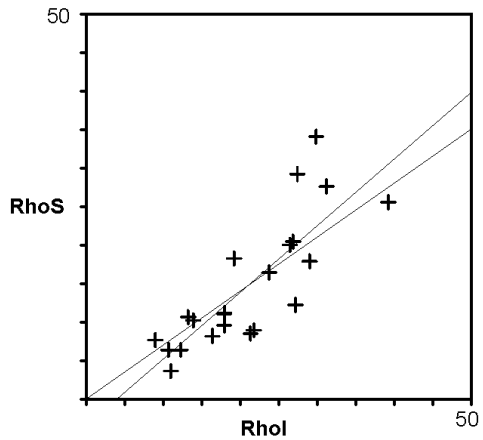

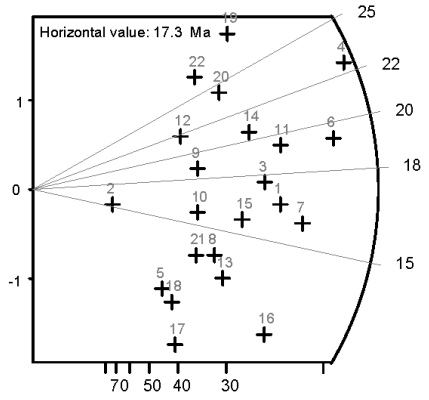

kurt.: -0.22 skew.: 0.48

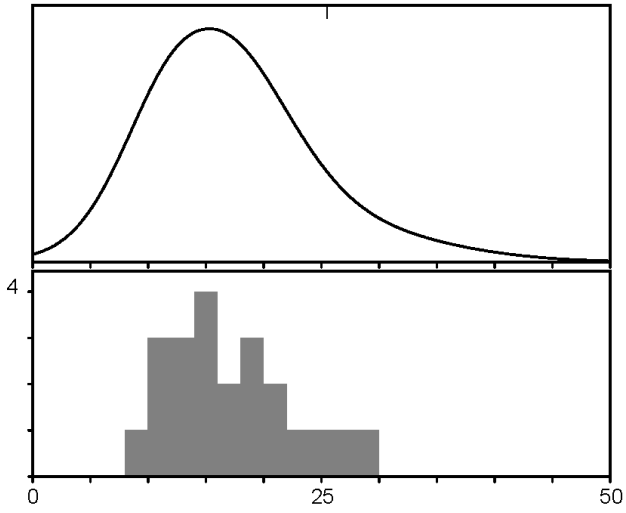

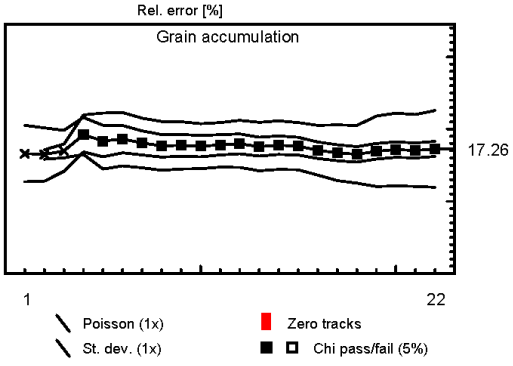

ETH-367-5	MC480	--- TRACKKEY 4.2.g ---	*counted: 18 Jul. 08*	
Zircon	Zeneggen mamontain	Quartzite	x10x100x1.6 oil	Marion Campani microscope 1

Cryst.: 20 ***Area:*** 594
Ns: 426 ***RhoS:*** 18.342
Ni: 896 ***RhoI:*** 38.578

Pooled:	0.475	14.2	± 0.9
Mean:	0.481	14.3	± 1.1
Central:	0.473	14.1	± 1.1
Weigh.I:	0.493	14.7	
Weigh.II:	0.49	14.8	

Chi-sq.: 27.08 ***P (%):*** 10.29
Dispersion: 0.18
a: -1.247 ***b:*** 0.512 ***r:*** 0.9
Irr.: eth367 ***Glass:*** CN_1
Nd: 2777 ***RhoD:*** 4.592849586
Zeta: 129.99 ± 0.6 ***U.:*** 267.32 (± 60 %)
Goodness: n. d.

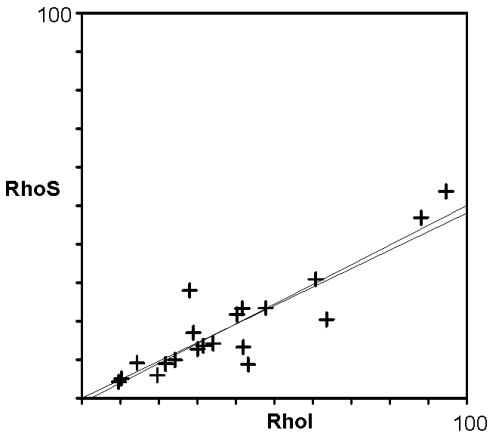

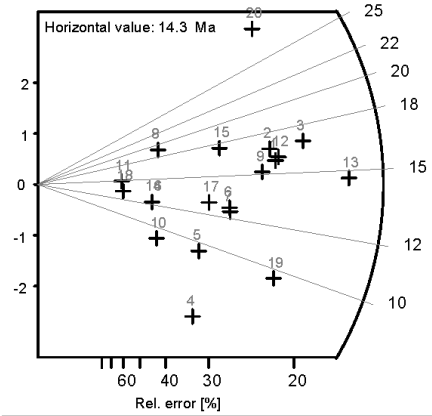

kurt.: 4.67 skew.: 1.46

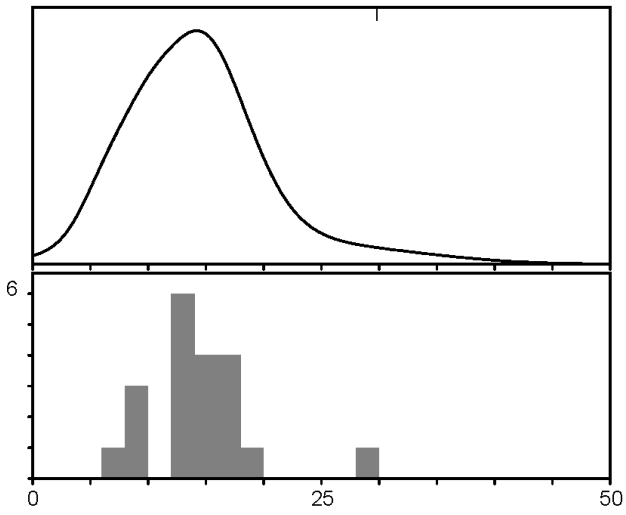

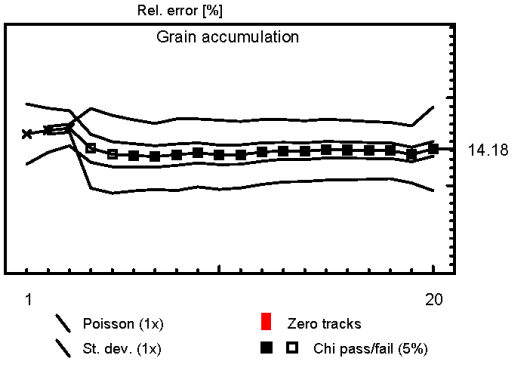

ETH-364-38	MC481	--- TRACKKEY 4.2.g ---	*counted: 17Jul. 08*
Zircon	Vispertermien Gd St Bernard	paragneiss	x10x100x1.6 oil	Marion Campani microscope 1

Cryst.:	***Area:***
24	1095
Ns:	***RhoS:***
429	10.02
Ni:	***RhoI:***
758	17.704

Pooled:	0.566	13.7	± 0.9
Mean:	0.565	13.7	± 0.8
Central:	0.566	13.7	± 0.9
Weigh.I:	0.561	13.6	
Weigh.II:	0.58	14.0	

Chi-sq.: 18.0 ***P (%):*** 75.74

Dispersion: 0.04

a: 1.116 ***b:*** 0.487 ***r:*** 0.86

Irr.: eth364-2 ***Glass:*** CN_1

Nd: 2419 ***RhoD:*** 3.734532614

Zeta: 129.99 ± 0.6 ***U.:*** 151.58 (± 56 %)

Goodness: n. d.

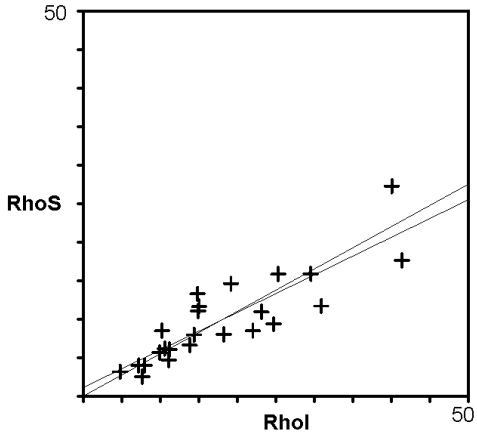

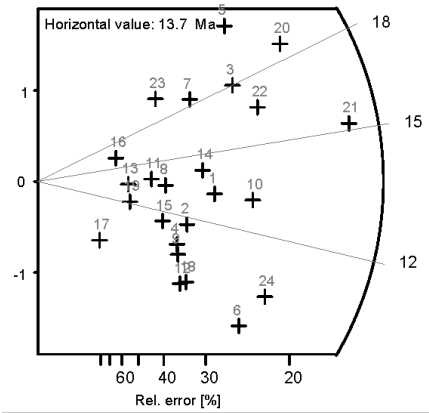

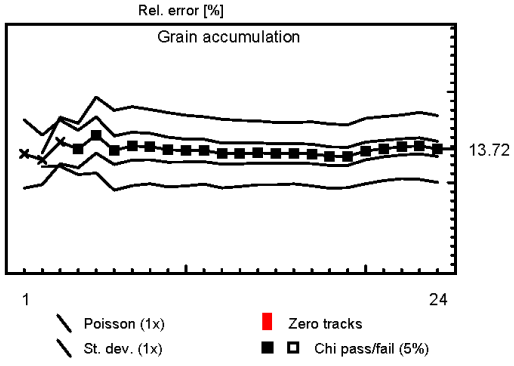

kurt.: -0.57 skew.: 0.52

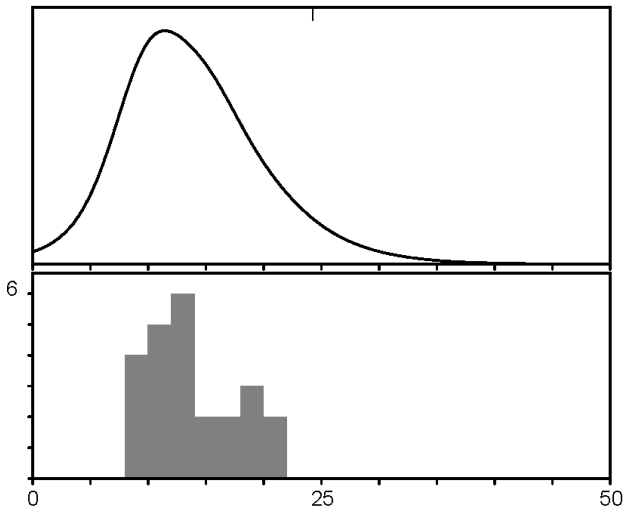

ETH-367-17	MC482	--- TRACKKEY 4.2.g ---	*counted: 29 Jul. 08*	
Zircon	Rhone Valley Mamontain	Quartzite	x10x100x1.6 oil	Marion Campani microscope 1

Cryst.: ***Area:***
22 536
Ns: ***RhoS:***
268 12.788
Ni: ***RhoI:***
759 36.216

Pooled:	0.353	9.9	± 0.7
Mean:	0.369	10.3	± 1.0
Central:	0.347	9.7	± 1.0
Weigh.I:	0.38	10.6	
Weigh.II:	0.39	10.9	

Chi-sq.: 38.26 ***P (%):*** 1.2

Dispersion: 0.30

a: 1.332 ***b:*** 0.324 ***r:*** 0.71

Irr.: eth367 ***Glass:*** CN_1

Nd: 2777 ***RhoD:*** 4.31160618

Zeta: 129.99 ± 0.6 ***U.:*** 282.75 (± 56 %)

Goodness: n. d.

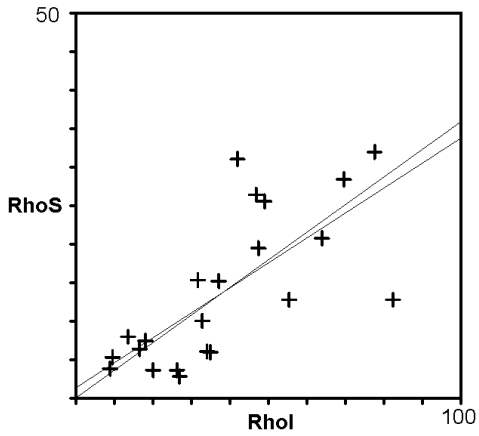

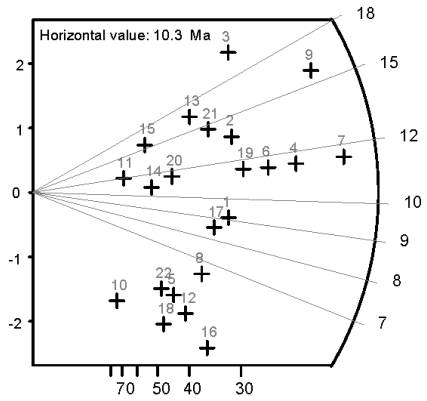

kurt.: -0.58 skew.: 0.18

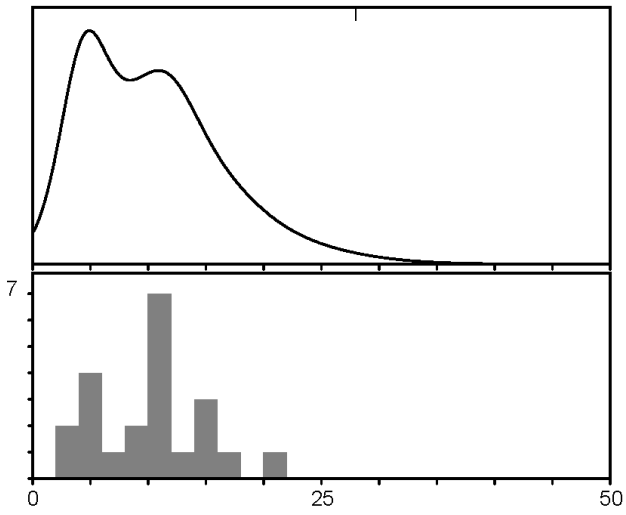

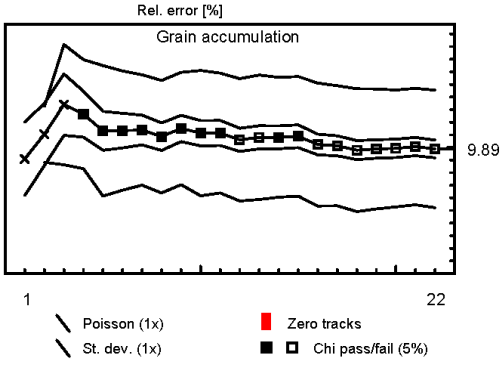

ETH-364-9	MC500	--- TRACKKEY 4.2.g ---	*counted: 6 Jun. 08*

Zircon | Bognanco FW Monte Leone | orthogneiss | x10x100x1.6 oil | Marion Campani microscope 1

Cryst.:	***Area:***		
20	497		
Ns:	***RhoS:***		
811	41.734		
Ni:	***RhoI:***		
2130	109.609		
Pooled:	0.381	12.9	± 0.6
Mean:	0.385	13.0	± 0.6
Central:	0.381	12.9	± 0.6
Weigh.I:	0.393	13.3	
Weigh.II:	0.39	13.1	

Chi-sq.: 23.18 ***P (%):*** 22.96

Dispersion: 0.08

a: -12.23 ***b:*** 0.5 ***r:*** 0.8

Irr.: eth364 ***Glass:*** CN_1

Nd: 3150 ***RhoD:*** 5.210164974

Zeta: 129.99 ± 0.6 ***U.:*** 665.27 (± 21 %)

Goodness: n. d.

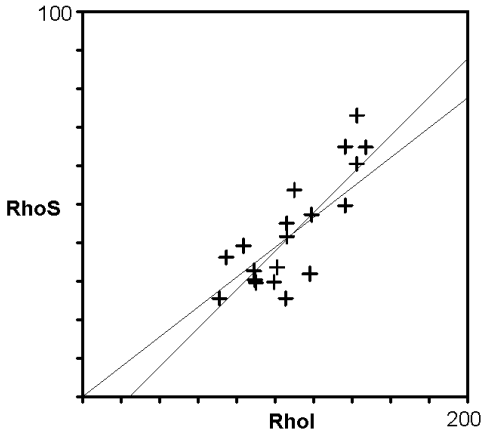

kurt.: -1.01 skew.: -0.11

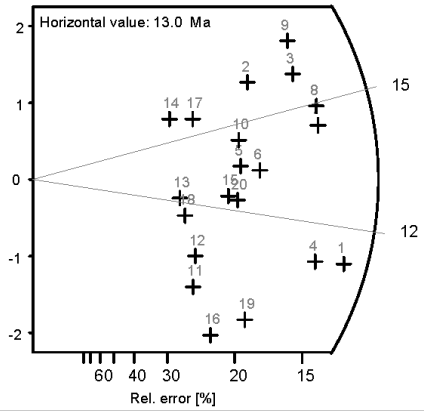

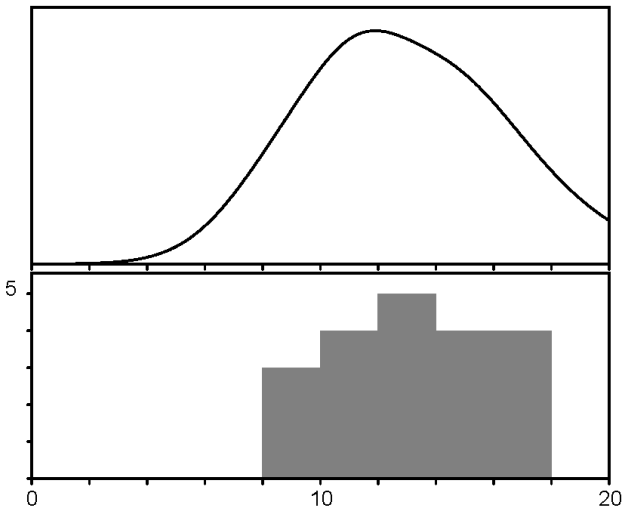

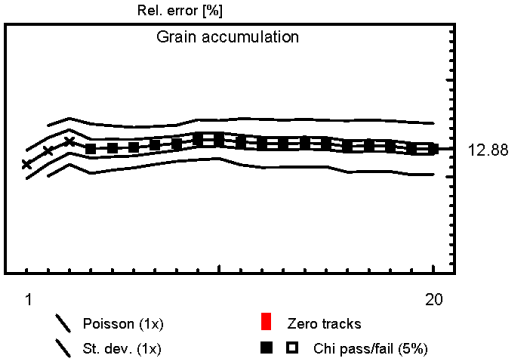

ETH-364-4	MC501	--- TRACKKEY 4.2.g ---	*counted: 5 Jun. 08*	
Zircon	Bognanco HW Camughera-Monc	Orthogneiss	x10x100x1.6 oil	Marion Campani microscope 1

Cryst.: 20	***Area:*** 541		
Ns: 867	***RhoS:*** 40.987		
Ni: 1679	***RhoI:*** 79.374		
Pooled:	0.516	18.3	± 0.8
Mean:	0.53	18.8	± 1.2
Central:	0.519	18.4	± 1.0
Weigh.I:	0.524	18.6	
Weigh.II:	0.54	19.0	

Chi-sq.: 32.09 ***P (%):*** 3.05

Dispersion: 0.13

a: 7.04 ***b:*** 0.436 ***r:*** 0.82

Irr.: eth364 ***Glass:*** CN_1

Nd: 3150 ***RhoD:*** 5.470420863

Zeta: 129.99 ± 0.6 ***U.:*** 464.72 (± 41 %)

Goodness: n. d.

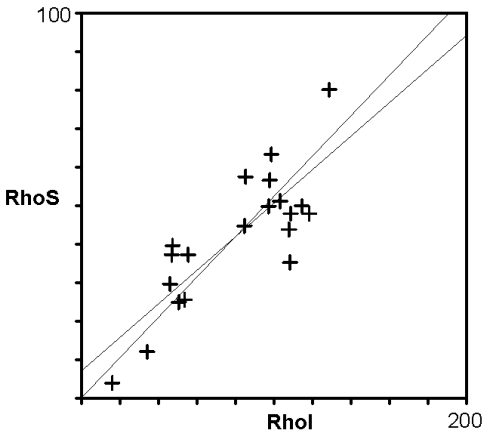

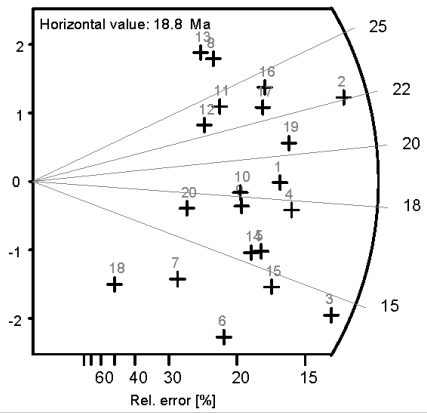

kurt.: -0.32 skew.: 0.26

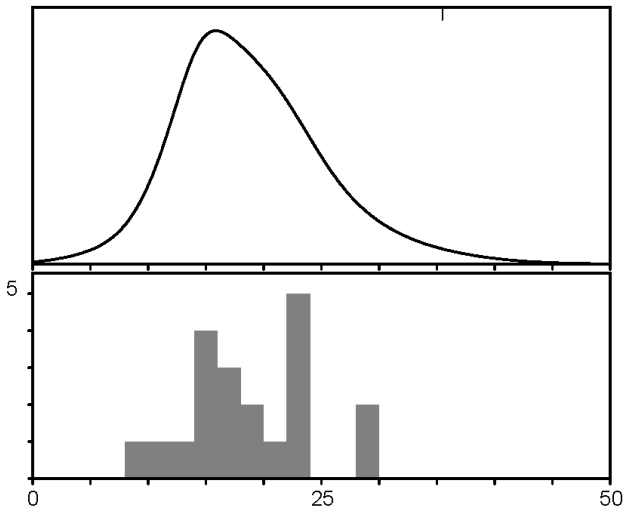

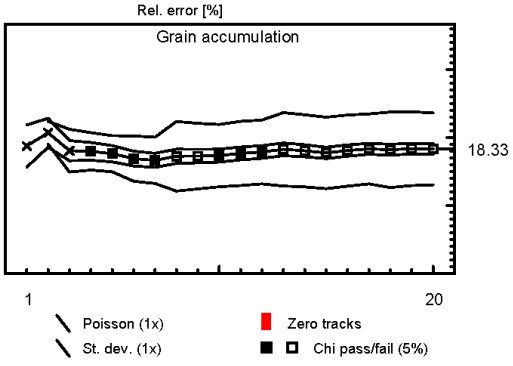

ETH-367-15	MC519	--- TRACKKEY 4.2.g ---	*counted: 28 Jul. 08*

Zircon | Simplon pass Mamontain | Quartzite | x10x100x1.6 oil | Marion Campani microscope 1

Cryst.: 20 ***Area:*** 724
Ns: 360 ***RhoS:*** 12.717
Ni: 617 ***Rhol:*** 21.796

Pooled:	0.583	16.5	± 1.1
Mean:	0.648	18.3	± 1.3
Central:	0.584	16.5	± 1.1
Weigh.I:	0.577	16.3	
Weigh.II:	0.63	17.7	

Chi-sq.: 12.88 ***P (%):*** 84.46
Dispersion: 0.01
a: 4.076 ***b:*** 0.399 ***r:*** 0.83
Irr.: eth367 ***Glass:*** CN_1
Nd: 2777 ***RhoD:*** 4.36178106
Zeta: 129.99 ± 0.6 ***U.:*** 159.24 (± 53 %)
Goodness: n. d.

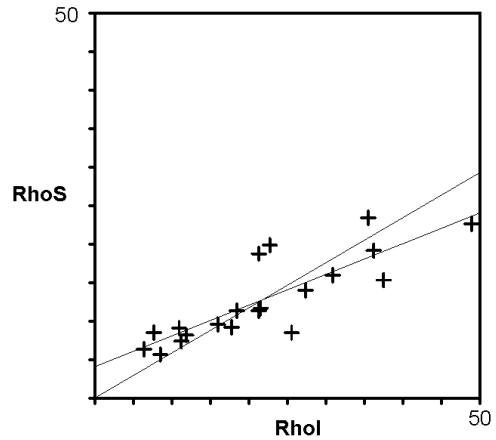

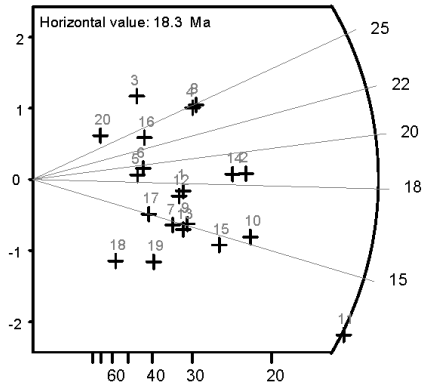

kurt.: 0.20 skew.: 0.81

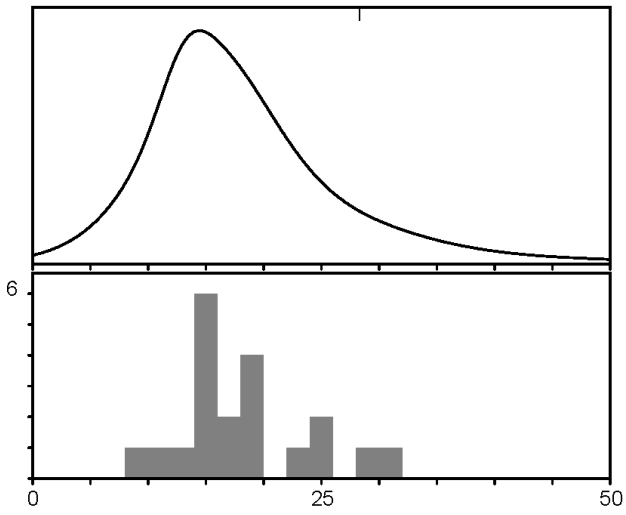

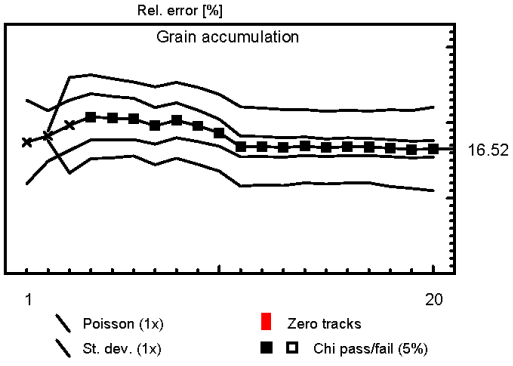

ETH-367-8	MC520	--- TRACKKEY 4.2.g ---	*counted: 19 Jul. 08*
Zircon	Simplon Pass Gd St Bernard	paragneiss	x10x100x1.6 oil	Marion Campani microscope 1

Cryst.: 21 ***Area:*** 677
Ns: 351 ***RhoS:*** 13.26
Ni: 538 ***RhoI:*** 20.324

Pooled:	0.652	19.0	± 1.4
Mean:	0.688	20.1	± 1.6
Central:	0.651	19.0	± 1.7
Weigh.I:	0.669	19.5	
Weigh.II:	0.70	20.4	

Chi-sq.: 30.09 ***P (%):*** 6.84
Dispersion: 0.23
a: 2.815 ***b:*** 0.535 ***r:*** 0.72
Irr.: eth367 ***Glass:*** CN_1
Nd: 2777 ***RhoD:*** 4.492392545
Zeta: 129.99 ± 0.6 ***U.:*** 159.87 (± 50 %)
Goodness: n. d.

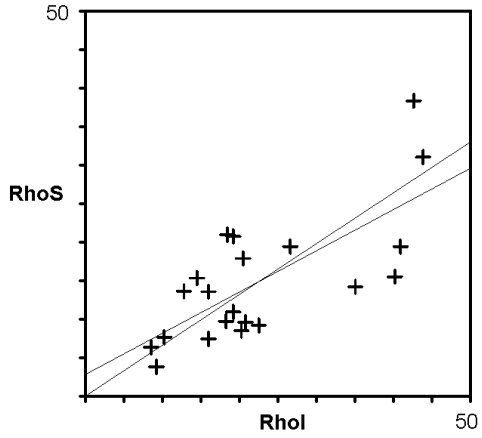

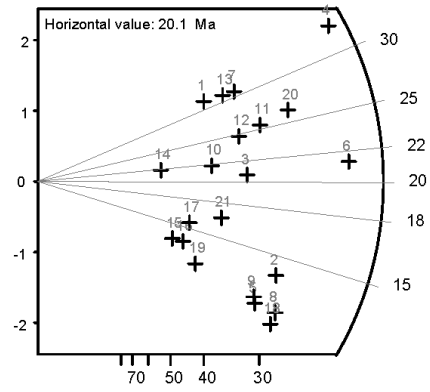

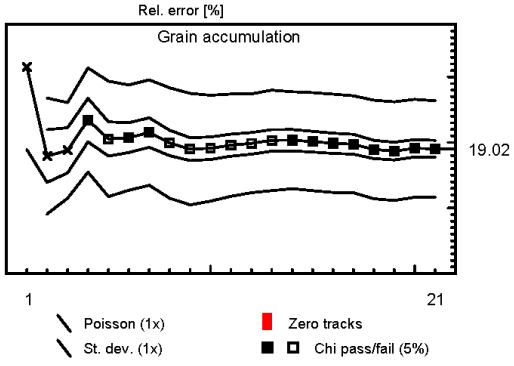

kurt.: -1.26 skew.: 0.41

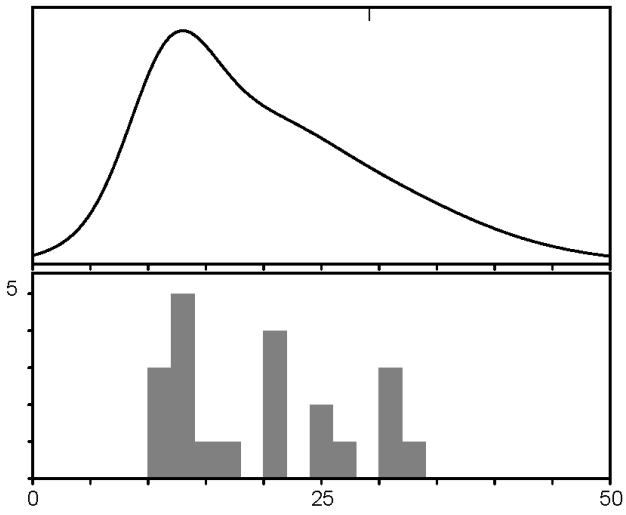

ETH-326-2-3	MCS3	--- TRACKKEY 4.2.g ---	*counted: oct-2006*

Apatite | Engiloch | ML unit | x10x100x1.25 | Marion Campani Microscope1

Cryst.:	***Area:***
40	2330
Ns:	***RhoS:***
19	0.131
Ni:	***RhoI:***
1621	11.142

Pooled:	0.012	2.9	± 0.7
Mean:	0.02	4.9	± 1.3
Central:	0.013	3.2	± 0.8
Weigh.I:	0.026	6.5	
Weigh.II:	0.05	12.7	

Chi-sq.: 59.42 ***P (%):*** 1.91

Dispersion: 0.44

a: 0.073 ***b:*** 0.009 ***r:*** 0.39

Irr.: eth326 ***Glass:*** CN_5

Nd: 7924 ***RhoD:*** 14.45

Zeta: 341.47 ± 6.41 ***U.:*** 7.96 (± 117 %)

Goodness: n. d.

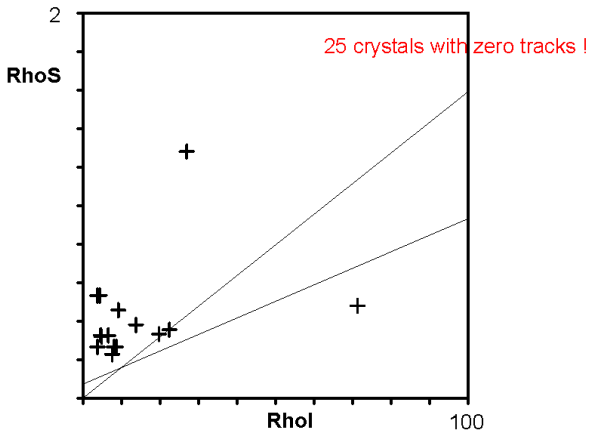

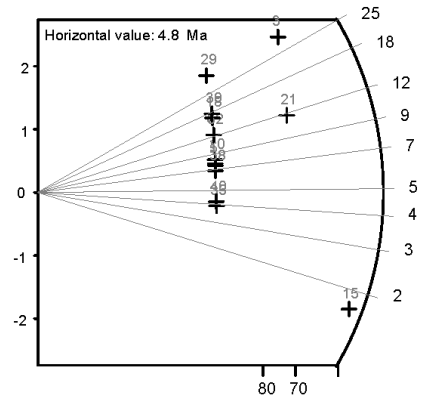

kurt.: 4.59 skew.: 2.14

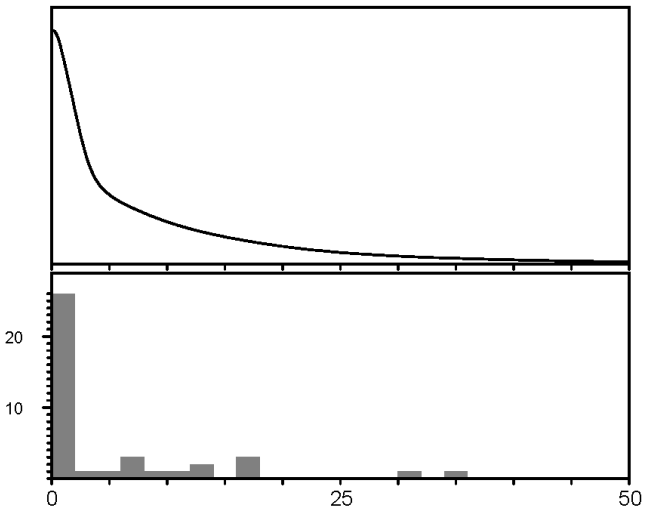

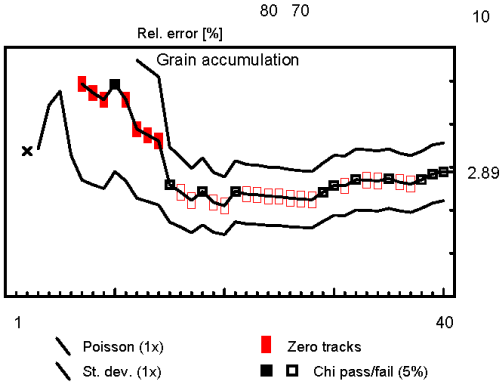

ETH-326-11-12 MC33 --- TRACKKEY 4.2.g --- *counted: 3 Nov. 06*

Apatite SimplonPass Berisal gneiss 10x100x1.25 Marion Microscope1

Cryst.: 35	***Area:*** 2236		
Ns: 31	***RhoS:*** 0.222		
Ni: 1417	***RhoI:*** 10.149		
Pooled:	0.022	4.3	± 0.8
Mean:	0.028	5.6	± 1.2
Central:	0.022	4.4	± 0.9
Weigh.I:	0.042	8.2	
Weigh.II:	0.05	9.8	

Chi-sq.: 46.25 ***P (%):*** 7.85

Dispersion: 0.40

a: 0.23 ***b:*** 0.001 ***r:*** 0.02

Irr.: eth326 ***Glass:*** CN_5

Nd: 7924 ***RhoD:*** 11.55

Zeta: 341.47 ± 6.41 ***U.:*** 10.09 (± 48 %)

Goodness: n. d.

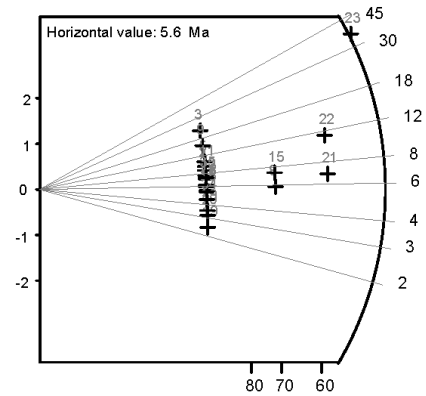

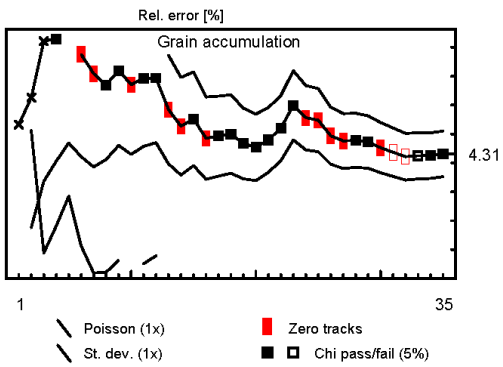

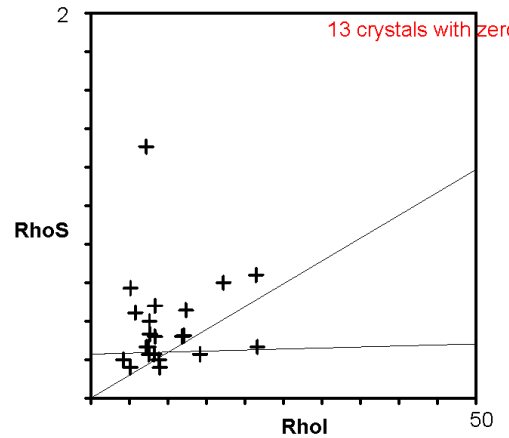

kurt.: 8.38 skew.: 2.50

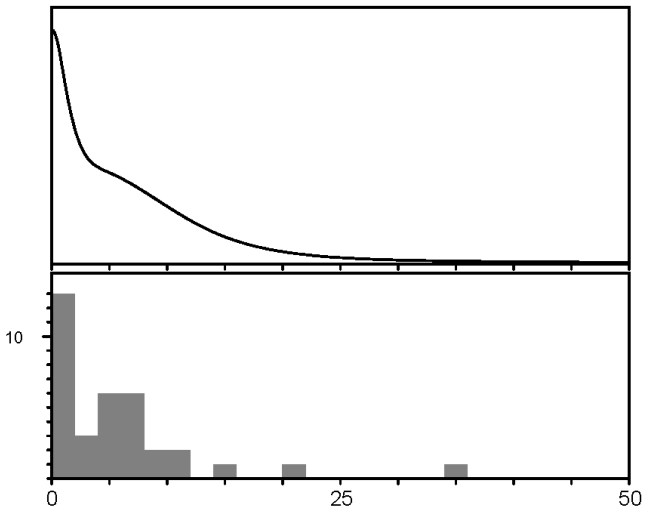

eth-365-19-20	MC475	--- TRACKKEY 4.2.g ---	*counted: 27 Sep. 08*

Apatite | Gebidum | Monte Lone Ortogneiss | x10x1.25x100 | Marion Campani microscope 1

Cryst.:	***Area:***		
20	1310		
Ns:	***RhoS:***		
20	0.245		
Ni:	***RhoI:***		
780	9.536		
Pooled:	0.026	5.3	± 1.2
Mean:	0.034	7.0	± 1.6
Central:	0.026	5.3	± 1.2
Weigh.I:	0.034	7.0	
Weigh.II:	0.04	9.0	

Chi-sq.: 14.75 ***P (%):*** 73.81

Dispersion: 0.00

a: 0.219 ***b:*** 0.003 ***r:*** 0.09

Irr.: eth365 ***Glass:*** CN_5

Nd: 8084 ***RhoD:*** 11.99913705

Zeta: 341.47 ± 6.41 ***U.:*** 8.88 (± 45 %)

Goodness: n. d.

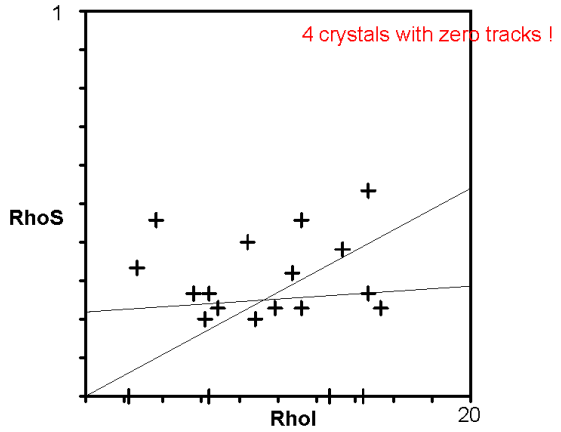

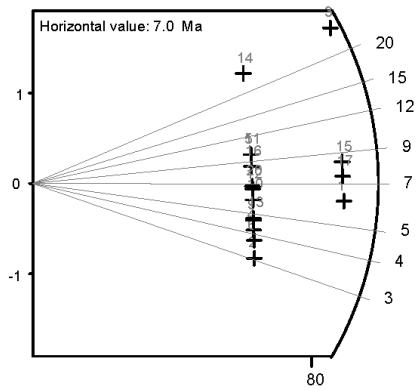

kurt.: 3.54 skew.: 1.85

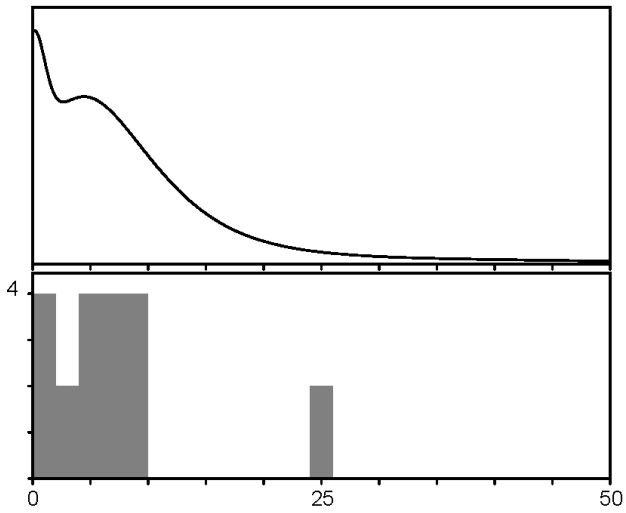

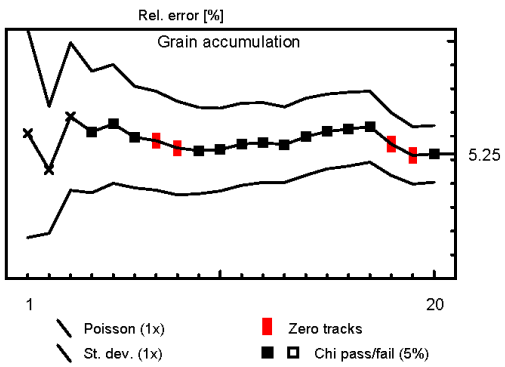

ETH-365-2	MC500	--- TRACKKEY 4.2.g ---	*counted: 14 Sep. 08*	
Apatite	Bognanco	Monte Leone orthogneiss	x10x1.25x100	Marion Campani microscope 1

Cryst.: ***Area:***
20 1802
Ns: ***RhoS:***
21 0.187
Ni: ***RhoI:***
1740 15.464

Pooled:	0.012	3.0	± 0.7
Mean:	0.013	3.3	± 0.9
Central:	0.012	3.0	± 0.7
Weigh.I:	0.015	3.6	
Weigh.II:	0.02	5.4	

Chi-sq.: 17.25 ***P (%):*** 57.32
Dispersion: 0.00
a: 0.04 ***b:*** 0.008 ***r:*** 0.61
Irr.: eth365 ***Glass:*** CN_5
Nd: 8084 ***RhoD:*** 14.3837774
Zeta: 341.47 ± 6.41 ***U.:*** 12.28 (± 82 %)
Goodness: n. d.

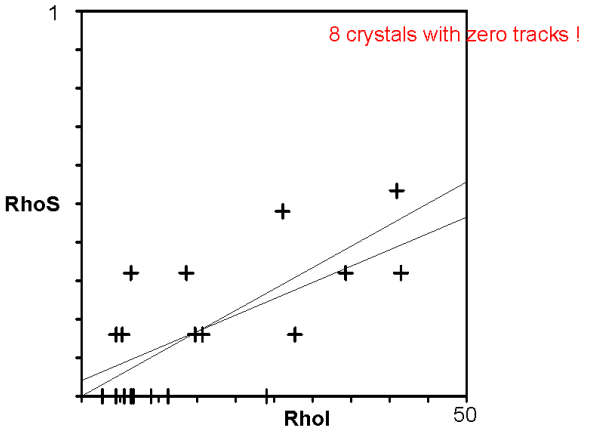

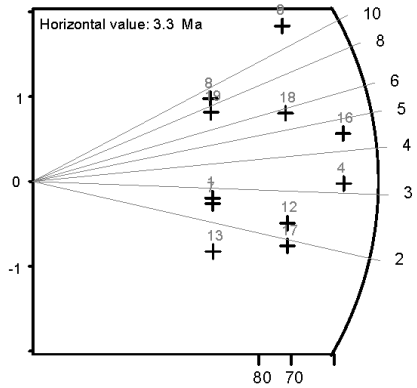

kurt.: 0.64 skew.: 1.28

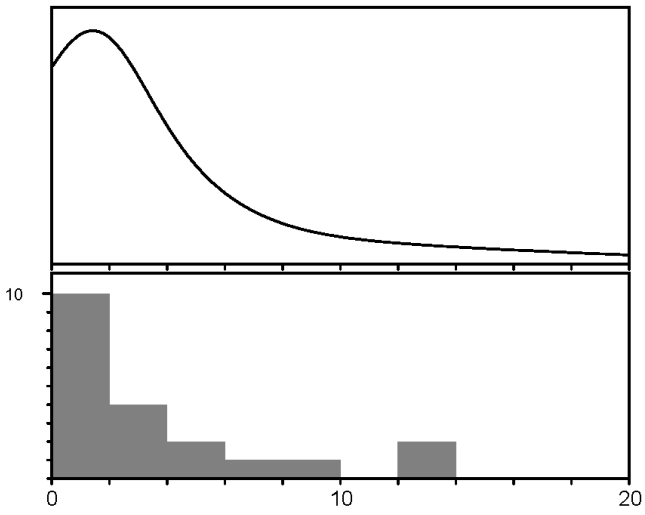

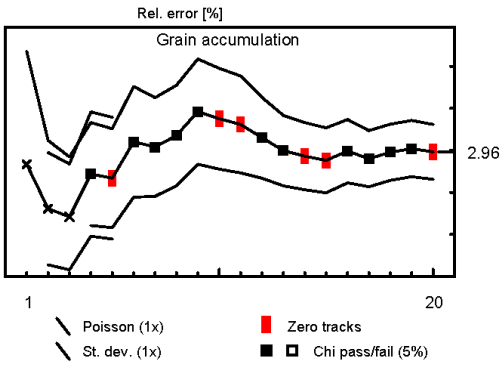

ETH-365-5	MC501	--- TRACKKEY 4.2.g ---	*counted: 22 Sep. 08*	
Apatite	Bognanco	CamugheraMoncucco granite	x10x1.25x100	Marion Campani microscope 1

Cryst.: 21 ***Area:*** 1621
Ns: 48 ***RhoS:*** 0.474
Ni: 2078 ***Rhol:*** 20.531

Pooled:	0.023	5.5	± 0.8
Mean:	0.031	7.5	± 1.5
Central:	0.023	5.5	± 0.8
Weigh.I:	0.024	5.7	
Weigh.II:	0.04	8.9	

Chi-sq.: 18.04 ***P (%):*** 58.47
Dispersion: 0.01
a: 0.146 ***b:*** 0.018 ***r:*** 0.88
Irr.: eth365 ***Glass:*** CN_5
Nd: 8084 ***RhoD:*** 14.0431145
Zeta: 341.47 ± 6.41 ***U.:*** 15.84 (± 144 %)
Goodness: n. d.

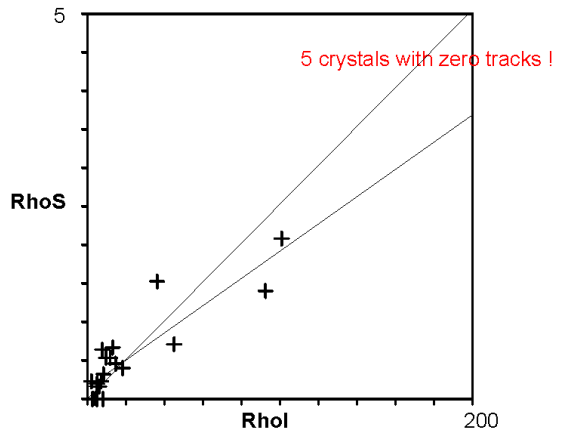

kurt.: 1.98 skew.: 1.21

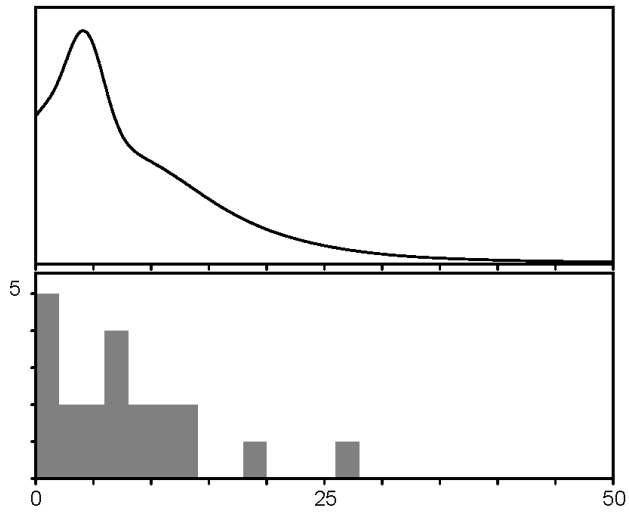

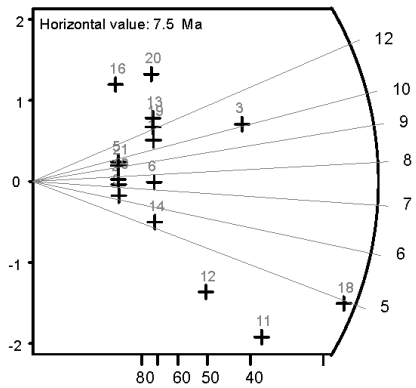

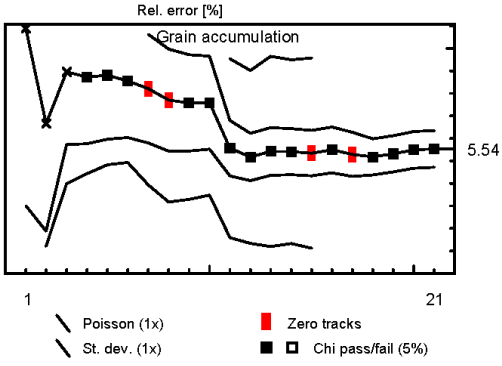

Appendix C: $^{40}Ar/^{39}Ar$ analytical dataset

Step	T(°C)	40/39	38/39	37/39	36/39	36/40	$^{39}K/^{38}Cl$	$^{37}Ca/^{39}K$	39%	%40*	40*/39K	Age (Ma)	±
MC22 Muscovite			J: 0.003774										
1	725	17.19	0.0229	0.00000	0.050810	0.002956	-	4.5E-06	0.58	14.9	2.543	17.235	1.7
2	800	7.41	0.0156	0.00000	0.017684	0.002388	-	8.5E-07	3.63	31.2	2.297	15.573	0.56
3	875	2.77	0.0129	0.00000	0.002285	0.000822	-	6.4E-08	43.72	76.3	2.097	14.223	0.13
4	1000	2.34	0.0127	0.00000	0.000946	0.000403	-	1.1E-07	68.25	88.4	2.054	13.935	0.1
5	1075	2.17	0.0125	0.00000	0.000350	0.000161	-	8.7E-08	98.1	95.4	2.052	13.918	0.06
6	1150	6.03	0.015	0.00108	0.014237	0.002360	-	4.0E-02	99.21	32.1	1.916	13.003	0.78
7	1275	7.57	0.0161	0.00000	0.017985	0.002377	-	8.3E-06	99.52	31.5	2.372	16.078	1.43
8	1450	5.32	0.0143	0.00000	0.011966	0.002249	-	5.4E-06	100	35.2	1.859	12.612	1.17
												Total age: 14.1 Ma	± 0.2
MC36 Phengite			J: 0.003818										
1	410	2.49	0.01342	0.000000	0.000531	0.000213	-	2.89E-07	5.23	93.6	2.308	15.825	0.28
2	430	1.67	0.01359	0.000000	0.000161	0.000097	-	1.52E-07	15.2	97.1	1.592	10.933	0.17
3	456	1.56	0.01235	0.000000	0.000024	0.000016	-	1.60E-07	24.65	99.5	1.523	10.458	0.23
4	496	1.74	0.01238	0.000000	0.000031	0.000018	-	6.93E-08	46.48	99.4	1.699	11.667	0.09
5	530	1.98	0.01265	0.000000	0.000000	0.000000	-	4.44E-08	80.59	100.0	1.918	13.164	0.07
6	546	2.11	0.01248	0.000000	0.000000	0.000000	-	1.30E-07	92.28	100.0	2.087	14.318	0.2
7	576	2.29	0.01202	0.000000	0.000126	0.000055	-	4.92E-07	95.36	98.3	2.224	15.255	0.46
8	640	3.18	0.01259	0.000000	0.000332	0.000104	-	4.97E-07	98.41	96.9	3.056	20.927	0.53
9	1555	14.51	0.01803	0.000000	0.002443	0.000168	-	9.51E-07	100	95.0	13.779	92.488	1.23
												Total age: 14.2 Ma	± 2.7
MC36 duplicated			J: 0.003774										
1	650	12.32	0.53200	0.010400	0.029543	0.002398	-	1.17E-01	0.33	31.0	3.852	26.042	3.83
2	725	1.84	0.01800	0.005740	0.001263	0.000687	-	6.44E-02	4.98	80.5	1.46	9.913	0.26
3	815	1.54	0.01270	0.002590	0.000171	0.000111	-	2.92E-02	33.23	97.0	1.473	10.002	0.09
4	900	1.97	0.01260	0.002870	0.000086	0.000044	-	3.23E-02	92.61	98.9	1.929	13.086	0.05
5	975	2.21	0.01290	0.002740	0.000516	0.000234	-	3.08E-01	98.93	94.4	2.065	14.01	0.18
6	1050	9.64	0.01840	0.115000	0.003682	0.000382	-	1.29	99.74	90.1	8.715	58.39	1.26
7	1200	36.25	0.04260	0.743000	0.017034	0.000470	-	8.41	100	88.4	32.387	208.064	3.83
												Total age: 13 Ma	± 2.9
MC111 Muscovite			J: 0.003545										
1	449	11.71	0.01940	0.000523	0.030608	0.002615	-	1.76E-03	0.73	23.4	2.714	17.277	2.48
2	485	2.83	0.01290	0.000192	0.000703	0.000248	-	6.46E-04	9.71	92.7	2.601	16.558	0.22
3	514	2.62	0.01310	0.000000	0.000128	0.000049	-	2.32E-08	26.35	98.6	2.555	16.267	0.19
4	549	2.58	0.01290	0.000000	0.000000	0.000000	-	1.48E-08	52.34	100.0	2.559	16.291	0.22
5	581	2.55	0.01270	0.000009	0.000000	0.000000	-	3.03E-05	65.61	100.0	2.522	16.057	0.19
6	590	2.54	0.01230	0.000000	0.000000	0.000000	-	1.03E-07	69.4	100.0	2.517	16.03	0.43
7	1222	2.55	0.01280	0.000000	0.000000	0.000000	-	1.28E-08	100	100.0	2.521	16.05	0.2
												Total age: 16.22 Ma	± 0.17
MC276 Muscovite			J: 0.003463										
1	465	6.3	0.01470	0.006590	0.011274	0.001789	-	2.74E-02	1.23	48.8	3.067	19.061	2.18
2	559	2.75	0.01290	0.000000	0.001863	0.000676	-	2.12E-08	49.72	80.6	2.207	13.737	0.11
3	600	2.22	0.01240	0.000000	0.000000	0.000000	-	3.97E-08	75.59	100.0	2.203	13.713	0.18
4	652	2.18	0.01200	0.000000	0.000000	0.000000	-	6.49E-08	91.44	100.0	2.167	13.49	0.24
5	1555	2.19	0.01220	0.000016	0.000000	0.000000	-	6.72E-05	100	100.0	2.177	13.55	0.36
												Total age: 13.7 Ma	± 0.32

Step	T(°C)	40/39	38/39	37/39	36/39	36/40	$^{39}K/^{38}Cl$	$^{37}Ca/^{39}K$	39%	%40*	40*/39K	Age (Ma)	±
MC283 Muscovite			J: 0.003463										
1	405	2.89	0.01090	0.000000	0.001787	0.000619	-	3.69E-07	3.03	81.7	2.333	14.584	0.67
2	460	3.54	0.01230	0.000000	0.000175	0.000049	-	7.23E-08	18.54	98.5	3.457	21.565	0.18
3	505	3.91	0.01240	0.000000	0.000000	0.000000	-	2.76E-08	59.18	100.0	3.881	24.194	0.09
4	533	3.44	0.01220	0.000000	0.000000	0.000000	-	4.37E-08	84.85	100.0	3.412	21.287	0.14
5	576	3.59	0.01160	0.000288	0.000000	0.000000	-	1.84E-03	96.4	100.0	3.561	22.207	0.28
6	1000	3.84	0.01060	0.019200	0.000562	0.000147	-	1.23E-01	100	95.9	3.651	22.765	0.96
												Total age: 22.5 Ma ± 1.8	
MC286 Muscovite			J: 0.003465										
1	320	15.37	0.01030	0.000000	0.012187	0.000793	-	6.51E-07	1.54	76.7	11.777	71.962	1.11
2	382	11.39	0.01130	0.000000	0.004822	0.000423	-	6.29E-07	3.13	87.6	9.96	61.042	1.29
3	430	13.68	0.01240	0.000000	0.002188	0.000160	-	5.30E-08	21.99	95.3	13.022	79.403	0.28
4	460	15.54	0.01240	0.000000	0.000221	0.000014	-	3.27E-08	52.61	99.6	15.46	93.885	0.27
5	465	10.43	0.01270	0.000000	0.000281	0.000027	-	5.54E-08	70.7	99.2	10.325	63.244	1.89
6	472	10.68	0.01100	0.000000	0.001138	0.000107	-	2.55E-07	74.64	96.9	10.33	63.269	1.06
7	500	9.42	0.01200	0.000000	0.000958	0.000102	-	2.73E-07	78.31	97.0	9.118	55.965	0.92
8	1555	12.84	0.01220	0.000000	0.000000	0.000000	-	4.63E-08	100	100.0	12.823	78.216	0.28
												Total age: 78.8 Ma ± 8.3	
MC287 Muscovite			J: 0.003471										
1	365	5.64	0.00980	0.000000	0.011057	0.001962	-	6.19E-07	3.1	42.4	2.365	14.749	1.74
2	388	4.17	0.01120	0.000000	0.003143	0.000753	-	2.82E-07	9.92	77.9	3.225	20.082	0.77
3	405	3.91	0.01150	0.000000	0.001858	0.000475	-	1.26E-07	25.16	86.0	3.343	20.812	0.38
4	426	4.02	0.01140	0.000000	0.001974	0.000492	-	2.06E-07	34.49	85.5	3.412	21.236	0.55
5	461	3.62	0.01150	0.000000	0.001332	0.000368	-	1.23E-07	50.11	89.2	3.204	19.948	0.26
6	500	3.53	0.01150	0.000000	0.001192	0.000338	-	1.27E-07	65.29	90.1	3.15	19.618	0.43
7	1555	3.3	0.01240	0.000000	0.000417	0.000126	-	5.54E-08	100	96.3	3.154	19.642	0.16
												Total age: 19.9 Ma ± 0.58	
MC288 Muscovite			J: 0.003477										
1	426	4.06	0.01370	0.006360	0.006155	0.001518	-	2.63E-02	10.42	56.6	2.281	14.252	0.43
2	480	2.44	0.01240	0.000475	0.000443	0.000182	-	1.97E-03	50.36	94.8	2.301	14.373	0.1
3	530	2.4	0.01220	0.000000	0.000000	0.000000	-	3.57E-08	81	100.0	2.386	14.903	0.12
4	584	2.37	0.00988	0.000000	0.000000	0.000000	-	3.39E-07	84.23	100.0	2.357	14.722	0.52
5	1555	2.37	0.01220	0.000000	0.000064	0.000027	-	6.94E-08	100	99.2	2.34	14.618	0.2
												Total age: 14.6 Ma ± 0.34	
MC289 Muscovite			J: 0.003478										
1	393	7.03	0.00000	0.000000	0.017371	0.002472	-	1.35E-06	2.78	27.7	1.931	12.075	5.54
2	420	4.38	0.00319	0.000000	0.004627	0.001055	-	7.06E-07	8.1	69.1	3.011	18.797	3.16
3	460	3.17	0.01200	0.000000	0.001636	0.000516	-	6.34E-08	67.34	84.9	2.673	16.695	0.4
4	480	2.94	0.00970	0.000000	0.000161	0.000055	-	1.60E-07	90.77	98.4	2.869	17.915	0.77
5	512	2.93	0.00000	0.000000	0.000000	0.000000	-	1.20E-06	93.91	100.0	2.908	18.156	4.57
6	1111	2.87	0.00351	0.000000	0.000000	0.000000	-	6.18E-07	100	100.0	2.843	17.754	2.58
												Total age: 17.1 Ma ± 0.69	

Step	T(°C)	40/39	38/39	37/39	36/39	36/40	$^{39}K/^{38}Cl$	$^{37}Ca/^{39}K$	39%	%40*	40*/39K	Age (Ma)	±
MC290 Muscovite			J: 0.003477										
1	275	13.97	0.00000	0.000000	0.038996	0.002792	-	1.96E-06	0.54	17.6	2.436	15.224	5.64
2	390	5.25	0.01050	0.000000	0.008112	0.001546	-	5.10E-07	2.59	54.4	2.824	17.632	1.54
3	415	4.74	0.01230	0.000000	0.005714	0.001206	-	1.21E-07	11.27	64.4	3.023	18.874	0.61
4	440	3.55	0.01250	0.000000	0.001596	0.000449	-	5.62E-08	29.94	86.8	3.052	19.054	0.2
5	480	3.67	0.01280	0.000000	0.001818	0.000495	-	2.54E-08	71.32	85.4	3.109	19.403	0.12
6	530	3.35	0.01140	0.000000	0.000530	0.000158	-	1.91E-07	76.83	95.3	3.167	19.768	0.57
7	1555	3.17	0.01240	0.000000	0.000093	0.000029	-	4.54E-08	99.99	99.1	3.109	19.407	0.12
												Total age: 19.3 Ma ±	0.15
MC291 Muscovite			J: 0.003477										
1	433	5.37	0.01010	0.000000	0.009249	0.001723	-	2.61E-07	9.63	50.2	2.68	16.736	1.39
2	470	2.95	0.01190	0.000000	0.000817	0.000277	-	1.13E-07	31.97	92.0	2.702	16.87	0.58
3	517	2.75	0.01070	0.000000	0.000667	0.000242	-	1.37E-07	50.36	93.0	2.541	15.87	0.87
4	522	2.83	0.00802	0.000000	0.001322	0.000468	-	3.49E-07	57.95	86.4	2.429	15.175	1.12
5	590	2.64	0.01130	0.000000	0.000350	0.000133	-	1.04E-07	83.34	96.2	2.526	15.772	0.47
6	653	2.6	0.00826	0.000000	0.000000	0.000000	-	3.56E-07	90.79	100.0	2.579	16.107	1.1
7	1555	2.54	0.00588	0.004780	0.000663	0.000262	-	2.03E-02	100	92.5	2.333	14.574	0.71
												Total age: 16 Ma ±	0.55
MC292 Muscovite			J: 0.003472										
1	380	10.22	0.01680	0.000000	0.000006	0.002268	-	1.53E-07	8.39	33.4	3.392	21.126	0.86
2	400	3.63	0.01270	0.000000	0.001721	0.000474	-	6.17E-08	29.17	86.1	3.098	19.302	0.22
3	420	3.56	0.01260	0.000000	0.001991	0.000559	-	6.29E-08	49.58	83.6	2.953	18.405	0.23
4	440	3.18	0.01260	0.000069	0.001235	0.000388	-	4.56E-04	78.03	88.6	2.794	17.417	0.21
5	478	2.88	0.01350	0.001500	0.000786	0.000272	-	9.88E-03	86.55	92.0	2.626	16.374	0.52
6	1555	2.91	0.01230	0.000000	0.000287	0.000099	-	9.66E-08	100	97.1	2.797	17.436	0.38
												Total age: 18.2 Ma ±	1.1
MC301 Biotite			J: 0.003468										
1	400	6.21	0.01870	0.000000	0.012896	0.002078	-	2.23E-07	22.61	40.4	2.501	15.586	0.73
2	540	2.44	0.01730	0.000000	0.001031	0.000422	-	1.87E-07	49.58	89.3	2.17	13.528	0.78
3	622	2.39	0.01590	0.000000	0.001182	0.000494	-	2.68E-07	68.43	85.8	2.038	12.711	1.02
4	2400	2.33	0.01750	0.000178	0.000510	0.000218	-	7.84E-04	100	93.8	2.175	13.561	0.7
												Total age: 13.8 Ma ±	1.9
MC301 Muscovite			J: 0.003471										
1	421	1.97	0.01210	0.000000	0.000552	0.000281	-	1.94E-07	3.54	91.9	1.789	11.169	1.07
2	470	1.69	0.01180	0.000000	0.000151	8.94E-05	-	7.22E-08	13.15	97.4	1.627	10.157	0.22
3	512	1.67	0.01150	0.000000	0.000106	6.36E-05	-	6.50E-08	23.83	98.2	1.619	10.111	0.14
4	578	1.68	0.01230	0.000000	1.44E-05	0.0000100	-	2.57E-08	50.86	99.7	1.66	10.362	0.09
5	605	1.71	0.01220	0.00039	0.0000000	0.0000000	-	1.53E-03	75.38	100.0	1.693	10.57	0.1
6	620	1.73	0.01170	0.00055	0.000237	0.000136	-	2.15E-03	86.18	96.1	1.645	10.271	0.26
7	655	1.76	0.00919	0.001690	0.000877	0.000497	-	6.61E-03	88.55	85.7	1.485	9.277	1.02
8	1555	1.74	0.01070	8.6E-05	6.35E-05	3.64E-05	-	3.36E-04	100	99.0	1.698	10.602	0.25
												Total age: 10.4 Ma ±	0.16
MC302 Muscovite			J: 0.003467										
1	350	135.4	0.14200	0.000000	0.118603	0.000876	-	1.13E-05	0.13	74.3	100.72	538.763	72.2
2	370	4.4	0.01850	0.005650	0.033393	0.007605	-	3.73E-02	0.48	-123.0	-5.442	0	0
3	433	3.94	0.01300	0.001230	0.0033080	0.00084	-	8.13E-03	16.94	75.4	2.941	18.243	0.34
4	473	2.43	0.01250	0.001190	0.0000332	0.0001371	-	7.87E-03	69.95	99.6	2.395	14.867	0.08
5	493	2.48	0.01200	0.001100	0.000479	0.000193	-	7.28E-03	82.28	94.4	2.313	14.362	0.25
6	1555	2.49	0.01210	0.000581	0.0000186	0.0000100	-	3.85E-03	100	99.8	2.457	15.251	0.22
												Total age: 16.1 Ma ±	1.2

Step	T(°C)	40/39	38/39	37/39	36/39	36/40	$^{39}K/^{38}Cl$	$^{37}Ca/^{39}K$	39%	%40*	40*/39K	Age (Ma)	±
MC430 Phg. Matrix			J: 0.003537										
1	382	8.94	0.02840	0.019100	0.038867	0.004344	-	6.69E-02	0.06	-27.2	-2.463	0	0
2	438	2.52	0.01400	0.004290	0.003067	0.001217	-	1.50E-02	1.13	64.4	1.598	10.167	0.76
3	495	1.8	0.01270	0.003890	0.000000	0.000000	-	1.38E-02	6.18	100.0	1.771	11.264	0.21
4	545	1.96	0.01250	0.001820	0.000000	0.000000	-	6.44E-03	23.85	100.0	1.933	12.288	0.1
5	580	1.98	0.01250	0.002370	0.000000	0.000000	-	8.41E-03	39.11	100.0	1.952	12.41	0.08
6	620	1.98	0.01240	0.004000	0.000000	0.000000	-	1.42E-02	67.5	100.0	1.951	12.408	0.05
7	642	2	0.01250	0.017000	0.000071	0.000036	-	6.05E-02	77.96	99.2	1.961	12.465	0.12
8	1300	2.09	0.01250	0.024200	0.000073	0.000035	-	8.61E-02	99.99	99.3	2.054	13.058	0.05
												Total age: 12.4 Ma ± 0.38	
MC430 Phg. Porphyroclast			J: 0.003537										
1	410	21.93	0.01280	0.000000	0.001624	0.000074	-	7.11E-08	16.42	97.8	21.466	132.034	0.88
2	438	21.65	0.01230	0.000000	0.001243	0.000057	-	9.66E-08	28.51	98.3	21.291	131.001	0.76
3	459	19.09	0.01210	0.000000	0.001015	0.000053	-	4.68E-08	53.48	98.4	18.792	116.107	0.56
4	479	15.82	0.01220	0.000369	0.000489	0.000031	-	1.27E-03	72.35	99.1	15.67	97.329	0.78
5	509	14.04	0.01570	0.003360	0.000620	0.000044	-	1.15E-02	82.68	98.7	13.851	86.292	0.84
6	574	12.38	0.01260	0.003390	0.000382	0.000031	-	1.16E-02	91.77	99.1	12.265	76.619	1.01
7	1300	13.85	0.01080	0.000000	0.000000	0.000000	-	1.44E-07	100	100.0	13.848	86.277	0.7
												Total age:107.9 Ma ± 19	
MC499 Biotite			J: 0.003533										
1	400	8.64	0.01276	0.009680	0.022338	0.002589	-	3.23E-02	0.18	24.2	2.062	13.096	23.4
2	460	3.75	0.01360	0.000849	0.004480	0.001193	-	2.84E-03	11.53	65.0	2.417	15.341	0.47
3	508	2.6	0.01310	0.000376	0.000694	0.000266	-	1.26E-03	33.26	92.2	2.376	15.085	0.13
4	549	2.46	0.01270	0.000697	0.000155	0.000063	-	2.33E-03	44.96	98.2	2.389	15.166	0.24
5	634	2.46	0.01280	0.001490	0.000019	0.000010	-	4.99E-03	63.86	99.8	2.428	15.412	0.18
6	1200	2.46	0.01270	0.003280	0.000119	0.000049	-	1.10E-02	100	98.6	2.399	15.231	0.11
												Total age: 15.2 Ma ± 0.14	
MC506 Muscovite			J: 0.003544										
1	435	7.15	0.01470	0.000129	0.012657	0.001769	-	4.40E-04	2.56	48.2	3.423	21.749	0.79
2	480	5.45	0.01390	0.000088	0.006837	0.001255	-	3.01E-04	8.85	63.2	3.422	21.748	0.46
3	518	3.98	0.01260	0.000000	0.002146	0.000539	-	2.75E-08	22.81	84.2	3.33	21.162	0.2
4	560	4	0.01270	0.000000	0.002044	0.000511	-	1.68E-08	45.73	85.0	3.375	21.452	0.18
5	600	3.93	0.01310	0.000000	0.001795	0.000456	-	2.55E-08	60.8	86.6	3.383	21.5	0.34
6	704	3.52	0.01230	0.000000	0.000636	0.000181	-	1.46E-08	87.08	94.7	3.308	21.025	0.15
7	1300	3.43	0.01240	0.000000	0.000121	0.000035	-	2.98E-08	100	99.0	3.374	21.443	0.19
												Total age: 21.3 Ma ± 0.16	
MC516 Muscovite			J: 0.003541										
1	449	5.48	0.01320	0.000000	0.003482	0.000636	-	2.46E-08	13.16	81.4	4.435	28.112	0.36
2	490	3.57	0.01280	0.000000	0.001149	0.000322	-	3.22E-08	23.22	90.6	3.208	20.382	0.26
3	529	4.13	0.01300	0.000000	0.002594	0.000628	-	2.48E-08	36.26	81.6	3.347	21.255	0.38
4	559	3.26	0.01250	0.000015	0.000146	0.000045	-	5.09E-05	89.37	98.7	3.194	20.289	0.1
5	580	3.37	0.01180	0.000000	0.000000	0.000000	-	1.08E-07	92.38	100.0	3.346	21.251	0.42
6	1300	3.52	0.01210	0.000000	0.000000	0.000000	-	4.26E-08	100	100.0	3.5	22.224	0.24
												Total age: 21.6 Ma ± 2	

Step	T(°C)	40/39	38/39	37/39	36/39	36/40	$^{39}K/^{38}Cl$	$^{37}Ca/^{39}K$	39%	%40*	40*/39K	Age (Ma)	±
MC346 Muscovite			J: 0.003463										
1	460	3.37	0.01290	0.000000	0.003488	0.001036	-	5.77E-08	32.69	70.3	2.354	14.647	0.25
2	505	2.39	0.01160	0.000000	0.000274	0.000115	-	8.12E-08	55.93	96.7	2.298	14.299	0.29
3	1555	2.38	0.01240	0.000000	0.0002080	0.0000874	-	4.34E-08	99.99	97.5	2.31	14.376	0.11
												Total age: 14.4 Ma ±	0.18
MC366 Muscovite			J: 0.003463										
1	400	6.26	0.01460	0.00000	0.01245	0.00199	-	9.48E-08	12.19	41.7	2.583	16.028	0.44
2	430	3.42	0.01320	0.00000	0.00344	0.00100	-	3.15E-08	48.84	70.5	2.387	14.817	0.22
3	442	2.55	0.01250	0.00000	0.00040	0.00015	-	4.85E-08	72.66	95.5	2.41	14.964	0.17
4	460	2.8	0.01120	0.00000	0.00138	0.00049	-	2.76E-07	76.85	85.4	2.369	14.706	0.74
5	1555	2.97	0.01260	0.00238	0.00165	0.00056	-	1.54E-02	100	83.7	2.455	15.242	0.13
												Total age: 15.1 Ma ±	0.36
MC420 Biotite			J: 0.003533										
1	470	20.88	0.02210	0.00263	0.010804	0.000517	-	8.80E-03	13.37	84.8	17.717	109.541	0.76
2	524	10.79	0.02010	0.00241	0.000933	0.000086	-	8.08E-03	37.08	97.5	10.504	65.741	0.42
3	554	9.62	0.02010	0.00212	0.000343	0.000036	-	7.10E-03	47.68	99.0	9.505	59.592	0.39
4	585	9.8	0.02010	0.00272	0.000276	0.000028	-	9.12E-03	57.38	99.2	9.703	60.817	0.37
5	625	9.76	0.01990	0.00388	0.000497	0.000051	-	1.30E-02	65.1	98.5	9.606	60.216	0.43
6	720	9.18	0.02010	0.00915	0.000726	0.000079	-	3.07E-02	77.06	97.7	8.957	56.213	0.46
7	1400	9.3	0.02030	0.03980	0.000893	0.000096	-	1.34E-01	100	97.3	9.041	56.727	0.24
												Total age: 66.8 Ma ±	9.8
MC420 Phengite			J: 0.003536										
1	483	1.67	0.01370	0.001720	0.000723	0.000433	-	5.99E-03	6.94	87.4	1.433	9.116	0.15
2	526	1.75	0.01260	0.000740	0.000088	0.000050	-	2.58E-03	14.77	98.5	1.696	10.788	0.12
3	582	2.23	0.01240	0.000233	0.000007	0.000010	-	8.14E-04	70.1	99.9	2.203	14	0.07
4	603	2.32	0.01230	0.000238	0.000000	0.000000	-	8.31E-04	88.65	100.0	2.3	14.609	0.1
5	645	2.4	0.01220	0.000247	0.000000	0.000000	-	8.63E-04	93.04	100.0	2.375	15.084	0.25
6	780	2.54	0.01320	0.001180	0.000324	0.000128	-	4.13E-03	94.75	96.3	2.417	15.352	0.48
7	1300	2.44	0.01220	0.000000	0.000000	0.000000	-	5.60E-08	99.99	100.0	2.417	15.354	0.21
												Total age: 13.7 Ma ±	1.8
MC422 Phengite			J: 0.003536										
1	434	10.22	0.03060	0.018400	0.027976	0.002734	-	6.41E-02	0.08	19.9	2.013	12.797	17.3
2	499	6.89	0.01510	0.010900	0.009961	0.001445	-	3.81E-02	0.78	57.7	3.957	25.065	4.32
3	582	2.15	0.01330	0.002580	0.001046	0.000485	-	8.97E-03	6.44	85.8	1.822	11.588	0.17
4	680	2.09	0.01230	0.001560	0.000043	0.000021	-	5.42E-03	29.58	99.4	2.048	13.014	0.08
5	734	2.35	0.01230	0.001200	0.000004	0.000010	-	4.18E-03	86.22	100.0	2.327	14.78	0.05
6	735	2.45	0.01230	0.001370	0.000000	0.000000	-	4.78E-03	92.44	100.0	2.425	15.403	0.19
7	772	2.5	0.01210	0.008210	0.000000	0.000000	-	2.86E-02	93.91	100.0	2.48	15.752	0.43
8	1200	2.47	0.01240	0.012400	0.000000	0.000000	-	4.30E-02	99.99	100.0	2.445	15.527	0.17
												Total age: 14.4 Ma ±	0.95
MC423 Phengite			J: 0.003535										
1	510	2.17	0.01560	0.001230	0.002673	0.001234	-	4.38E-03	2.86	63.9	1.358	8.64	0.59
2	584	1.62	0.01280	0.000052	0.000003	0.000010	-	1.84E-04	14.76	99.9	1.596	10.148	0.12
3	650	1.68	0.01230	0.000263	0.000000	0.000000	-	9.34E-04	38.21	100.0	1.657	10.537	0.12
4	685	1.76	0.01230	0.000422	0.000000	0.000000	-	1.50E-03	58.17	100.0	1.732	11.015	0.1
5	741	1.81	0.01210	0.000837	0.000019	0.000011	-	2.98E-03	73.61	99.7	1.774	11.281	0.27
6	1350	1.86	0.01260	0.005270	0.000000	0.000000	-	1.88E-02	99.99	100.0	1.84	11.694	0.08
												Total age: 11 Ma ±	0.71

Ages not presented in the study and complicated either by partial reset, mixture ages or fluid percolation with excess Ar

Simplon Pass in the vicinity of the fault zone (Sm2) in middle grade mylonites (footwall)

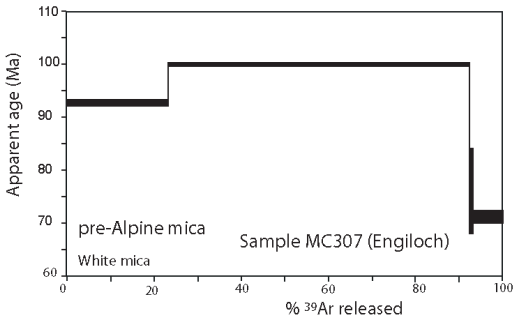

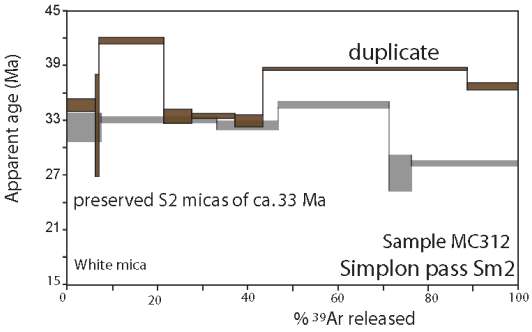

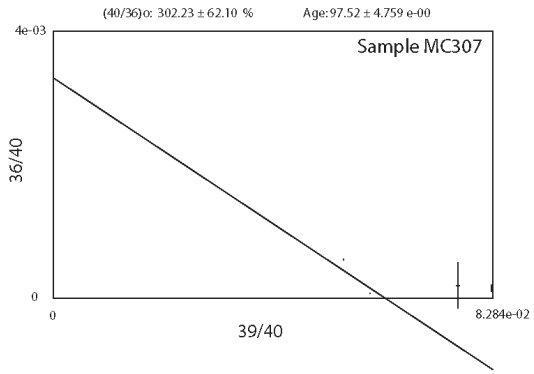

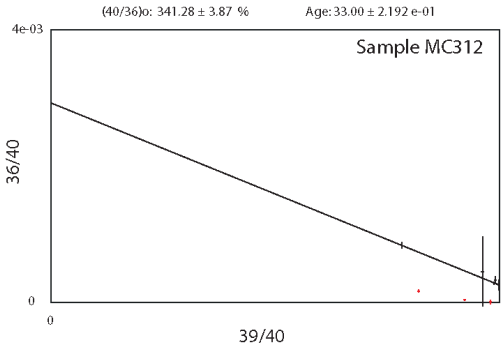

Rhone Valley in low-grade mylonites (footwall)

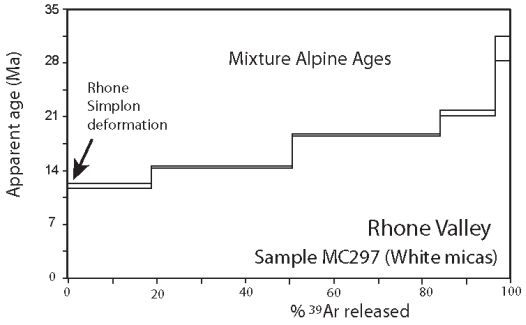

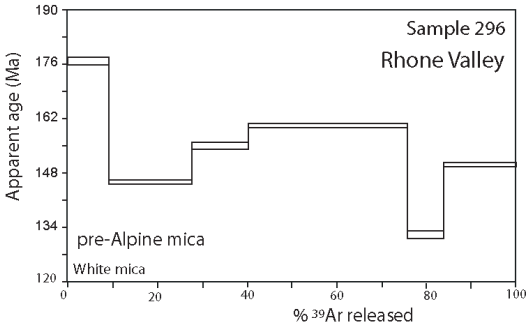

Appendix D: Probability density functions

Model A

Parameter	Mean	Stn err
Vv	0.40	0.24
μ	0.22	0.06
D	3.13	2.11
Wp	0.40	0.21
tage	45.97	11.02
Vf	3.97	2.62
tα	24.19	3.63
tγ2	14.91	2.63
tγ	19.25	4.09
acc	2.39	1.08
tacc	2.96	2.11
Vf2	1.24	0.95

Model B

Parameter	Mean	Stn err
Vv	0.35	0.15
μ	0.20	0.09
-	-	-
-	-	-
tage	39.81	5.56
vf	2.77	1.93
-	-	-
tγ2	15.17	2.69
tγ	22.57	3.39
acc	2.44	0.79
tacc	2.66	1.48
Vf2	1.29	0.68

References

Abbott, R. E., J. N. Louie, S. J. Caskey, and S. Pullammanappallil (2001), Geophysical confirmation of low-angle normal slip on the historically active Dixie Valley fault, Nevada, *Journal of Geophysical Research-Solid Earth*, *106*(B3), 4169-4181.

Amstutz, A. (1954), Pennides dans l'Ossola et problème des racines, in *Archives des sciences physiques et naturelles,* Genève, p. 411.

Andersen, T. B., and B. Jamtveit (1990), Uplift of deep crust during orogenic extensional collapse: a model based on field studies in the Sogn-Sunnfjord region of Western Norway, *Tectonics*, *9*(5), 1097-1111.

Argand, E. (1911), Les nappes de recouvrement des Alpes Pennines et leurs prolongements structuraux, *Matériaux pour la carte Géologique de la Suisse, 31*,1-26.

Armstrong, R. L., E. Jäger, and P. Eberhardt (1966), A comparison of K/Ar and Rb/Sr ages on Alpine biotites, *Earth and Planetary Science Letters*, *1*, 13-19.

Aug, C., J. P. Chiles, G. Courrioux, and C. Lajaunie (2004), 3D geological modelling and uncertainty: the potential-field method, paper presented at 7th International Geostatistics Congress, Springer, Banff, Canada, Sep 26-Oct 01.

Avigad, D., A. Ziv, and Z. Garfunkel (2001), Ductile and brittle shortening, extension-parallel folds and maintenance of crustal thickness in the central Aegean (Cyclades, Greece), *Tectonics*, *20*(2), 277-287.

Axen, G. J., and J. M. Bartley (1997), Field tests of rolling hinges: existence, mechanical types, and implications for extensional tectonics, *Journal of Geophysical Research-Solid Earth*, *102*(B9), 20515-20537.

Axen, G. J., J. Selverstone, and T. Wawrzyniec (2001), High-temperature embrittlement of extensional Alpine mylonite zones in the midcrustal ductile-brittle transition, *Journal of Geophysical Research-Solid Earth*, *106*(B3), 4337-4348.

Bartley, J. M., and B. P. Wernicke (1984), The Snake Range decollement interpreted as a major extensional shear zone, *Tectonics*, *3*(6), 647-657.

Bartley, J. M., J. M. Fletcher, and A. F. Glazner (1990), Tertiary extension and contraction of lower-plate rocks in the Central Mojave metamorphic core complex, Southern California, *Tectonics*, *9*(3), 521-534.

Baxter, E. F., D. J. DePaolo, and P. R. Renne (2002), Spatially correlated anomalous $^{40}Ar/^{39}Ar$ "age" variations in biotites about a lithologic contact near Simplon Pass, Switzerland: a mechanistic explanation for excess Ar, *Geochimica et Cosmochimica Acta*, *66*(6), 1067-1083.

Bearth, P. (1956a), Zur Geologie der Wurzelzone östlich des Ossolatales *Eclogae Geologicae Helvetiae*, *49*, 267-278.

Bearth, P. (1956b), Geologische Beobachtungen im Grenzgebiet der Lepontinischen und Penninischen Alpen, *Eclogae Geologicae Helvetiae*, *49*, 279-290.

Bearth, P. (1958), Ueber eine Wechsel der Mineralfazies in der Wurzelzone des Penninikums, *Schweizerische Mineralogische Und Petrographische Mitteilungen*, *38*, 363-373.

Bearth, P. (1967), Die Ophiolite der Zone von Zermatt-Saas Fee, 132, *Beiträge zur Geologischen Karte der schweiz*, Bern.

Bearth, P. (1972), Geologischer Atlas der Schweiz. 1:25000. Blatt: Simplon (Atlasblatt 61). *Schweizerischen geologischen Kommission*, Basel.

Behrmann, J. H. (1988), Crustal-scale extension in a convergent orogen: the Sterzing-Steinach mylonite zone in the Eastern Alps, *Geodinamica Acta*, *2*(2), 63-73.
Bernet, M., M. Zattin, J. I. Garver, M. T. Brandon, and J. A. Vance (2001), Steady-stale exhumation of the European Alps, *Geology*, *29*(1), 35-38.
Berthé, D., P. Choukroune, and P. Jegouzo (1979), Orthogneiss, mylonite and non coaxial deformation of granites: example of the South Armorican shear zone, *Journal of Structural Geology*, *1*(1), 31-42.
Birck, J. L. (1986), Precision K-Rb-Sr isotopic analysis: application to Rb-Sr Chronology, *Chemical Geology*, *56*, 73-83.
Bistacchi, A., and M. Massironi (2000), Post-nappe brittle tectonics and kinematic evolution of the North-Western Alps: an integrated approach, *Tectonophysics*, *327*(3-4), 267-292.
Block, L., and L. H. Royden (1990), Core complex geometries and regional scale flow in the lower crust, *Tectonics*, *9*(4), 557-567.
Brady, R. J. (2002), Very high slip rates on continental extensional faults: new evidence from (U-Th)/He thermochronometry of the Buckskin Mountains, Arizona, *Earth and Planetary Science Letters*, *197*(1-2), 95-104.
Brandon, M. T., M. K. Roden-Tice, and J. I. Garver (1998), Late Cenozoic exhumation of the Cascadia accretionary wedge in the Olympic Mountains, northwest Washington State, *Geological Society of America Bulletin*, *110*(8), 985-1009.
Braun, J. (2002), Estimating exhumation rate and relief evolution by spectral analysis of age-elevation datasets, *Terra Nova*, *14*(3), 210-214.
Braun, J. (2003), Pecube: a new finite-element code to solve the 3D heat transport equation including the effects of a time-varying, finite amplitude surface topography, *Computers and Geosciences*, *29*(6), 787-794.
Brichau, S., U. Ring, R. A. Ketcham, A. Carter, D. Stockli, and M. Brunel (2006), Constraining the long-term evolution of the slip rate for a major extensional fault system in the central Aegean, Greece, using thermochronology, *Earth and Planetary Science Letters*, *241*(1-2), 293-306.
Brichau, S., U. Ring, A. Carter, R. Bolhar, P. Monié, D. Stockli, and M. Brunel (2008), Timing, slip rate, displacement and cooling history of the Mykonos detachment footwall, Cyclades, Greece, and implications for the opening of the Aegean Sea basin, *Journal of the Geological Society*, *165*, 263-277.
Buck, W. R. (1988), Flexural rotation of normal faults, *Tectonics*, *7*(5), 959-973.
Burg, J. P., J. Van Den Driessche, and J. P. Brun (1994), Syn- to post-thickening extension: mode and consequences, *Comptes Rendus de l'Académie des Sciences Série II*, *319*(2), 1019-1032.
Burg, J. P., and T. V. Gerya (2005), The role of viscous heating in Barrovian metamorphism of collisional orogens: thermomechanical models and application to the Lepontine Dome in the Central Alps, *Journal of Metamorphic Geology*, *23*(2), 75-95.
Burkhard, M. (1988), L'Helvétique de la bordure occidentale du massif de l'Aar (évolution tectonique et métamorphique), *Eclogae Geologicae Helvetiae*, *81*, 63-114.
Carter, T. J., B. P. Kohn, D. A. Foster, A. J. W. Gleadow, and J. D. Woodhead (2006), Late-stage evolution of the Chemehuevi and Sacramento detachment faults from apatite (U-Th)/He thermochronometry - evidence for mid-Miocene accelerated slip, *Geological Society of America Bulletin*, *118*(5-6), 689-709.

Cederbom, C. E., H. D. Sinclair, F. Schlunegger, and M. K. Rahn (2004), Climate-induced rebound and exhumation of the European Alps, *Geology*, *32*(8), 709-712.
Champagnac, J. D., C. Sue, B. Delacou, and M. Burkhard (2004), Brittle deformation in the inner NW Alps: from early orogen parallel extrusion to late orogen-perpendicular collapse, *Terra Nova*, *16*(4), 232-242.
Champagnac, J. D., C. Sue, B. Delacou, P. Tricart, C. Allanic, and M. Burkhard (2006), Miocene lateral extrusion in the inner western Alps revealed by dynamic fault analysis, *Tectonics*, *25*(3), 26.
Chauvet, A., and M. Séranne (1994), Extension-parallel folding in the Scandinavian Caledonides: implications for late-orogenic processes, *Tectonophysics*, *238*(1-4), 31-54.
Chopin, C., and P. Monié (1984), A unique magnesiochloritoid-bearing, high-pressure assemblage from the Monte Rosa, Western Alps: petrologic and ^{40}Ar-^{39}Ar radiometric study, *Contributions to Mineralogy and Petrology*, *87*(4), 388-398.
Ciancaleoni, L., and D. Marquer (2008), Late Oligocene to early Miocene lateral extrusion at the eastern border of the Lepontine dome of the Central Alps (Bergell and Insubric areas, Eastern Central Alps), *Tectonics*, *27*(4), 22.
Collettini, C., and R. E. Holdsworth (2004), Fault zone weakening and character of slip along low-angle normal faults: insights from the Zuccale fault, Elba, Italy, *Journal of the Geological Society*, *161*, 1039-1051.
Collombet, M., J. C. Thomas, A. Chauvin, P. Tricart, J. P. Bouillin, and J. P. Gratier (2002), Counterclockwise rotation of the western Alps since the Oligocene: new insights from paleomagnetic data, *Tectonics*, *21*(4), 15.
Colombi, A. (1989), Métamorphisme et géochimie des roches mafiques des Alpes Ouest-Centrales (géoprofil Viege-Domodossola-Locarno), *Mémoire Géologique de Lausanne*, *4*.
Coney, P. J., and T. A. Harms (1984), Cordilleran metamorphic core complexes: Cenozoic extensionalrelics of Mesozoic compression, *Geology*, *12*(9), 550-554.
Cooper, F. J., J. P. Platt, and E. S. Platzman (2006), Rotation of syn-kinematic dikes in the northern Snake Range decollement mylonite zone, *Eos Transactions, American Geophysical Union, 86*(52), Fall Meeting Supplement, Abstract T13B-0448.
Dallmeyer, R. D., A. W. Snoke, and E. H. McKee (1986), The Mesozoic-Cenozoic tectonothermal evolution of the Ruby Mountains, East Humboldt Range, Nevada: a Cordilleran metamorphic core complex, *Tectonics*, *5*(6), 931-954.
Davis, G. A. (1988), Rapid upward transport of mid-crustal mylonitic gneisses in the footwall of a Miocene detachment fault, Whipple Mountains, southeastern California, *Geologische Rundschau*, *77*(1), 191-209.
Davis, G. H., and P. J. Coney (1979), Geologic development of the Cordilleran metamorphic core complexes, *Geology*, *7*(3), 120-124.
Davis, G. H., and J. J. Hardy (1981), The Eagle pass detachment, southeastern Arizona: product of mid-Miocene listric normal faulting in the Southern Basin and Range, *Geological Society of America Bulletin*, *92*(10), 749-762.
Davis, G. H. (1983), Shear-zone model for the origin of metamorphic core complexes, *Geology*, *11*(6), 342-347.
Deutsch, A., and R. H. Steiger (1985), Hornblende K-Ar ages and the climax of Tertiary metamorphism in the Lepontine Alps (South-Central Switzerland): an old problem reassessed, *Earth and Planetary Science Letters*, *72*(2-3), 175-189.
Dewey, J. F. (1988), Extensional collapse of orogens, *Tectonics*, *7*(6), 1123-1139.

Dodson, M. H. (1973), Closure temperature in cooling geochronological and petrological systems, *Contributions to Mineralogy and Petrology*, *40*(3), 259-274.
Drewes, H. (1959), Turtleback faults of Death-Valley, California: a reinterpretation, *Geological Society of America Bulletin*, *70*(12), 1497-1508.
Dumitru, T. A. (1995), A new computer automated microscope stage system for fission track analysis, *Nuclear Tracks and Radiation Measurements*, *21*, 575-580.
Dunkl, I., B. Grasemann, and W. Frisch (1998), Thermal effects of exhumation of a metamorphic core complex on hanging wall syn-rift sediments: an example from the Rechnitz window, Eastern Alps, *Tectonophysics*, *297*, 31-50.
Dunlap, W. J. (1997), Neocrystallization or cooling? $^{40}Ar/^{39}Ar$ ages of white micas from low-grade mylonites, *Chemical Geology*, *143*, 181-203.
Echtler, H., and J. Malavieille (1990), Extensional tectonics, basement uplift and Stephano-Permian collapse basin in a late Variscan metamorphic core complex (Montagne Noire, Southern Massif-Central), *Tectonophysics*, *177*, 125-138.
Foster, D. A., A. J. W. Gleadow, S. J. Reynolds, and P. G. Fitzgerald (1993), Denudation of metamorphic core complexes and the reconstruction of the transition zone, West-Central Arizona: constraints from apatite fission-track thermochronology, *Journal of Geophysical Research-Solid Earth*, *98*(B2), 2167-2185.
Frank, E., and A. Stettler (1979), K-Ar and ^{39}Ar-^{40}Ar systematics of white K-mica from an Alpine metamorphic profile in the Swiss Alps, *Schweizerische Mineralogische Und Petrographische Mitteilungen*, *59*, 375-394.
Frank, E. (1983), Alpine metamorphism of calcareous rocks along a cross-section in the Central Alps: occurrence and breakdown of muscovite, margarite and paragonite, *Schweizerische Mineralogische Und Petrographische Mitteilungen*, *63*, 37-93.
Frey, M., J. Hunziker, W. Frank, J. Bocquet, G. V. Dal Piaz, E. Jäger, and E. Niggli (1974), Alpine metamorphism of the Alps: a review, *Schweizerische Mineralogische Und Petrographische Mitteilungen*, *54*, 247-290.
Frey, M., and R.F. Mahlmann (1999), Alpine metamorphism of the central Alps, *Schweizerische Mineralogische Und Petrographische Mitteilungen*, *79,* 135-154.
Friedman, I.P. and J.R. O'Neil (1977), Compilation of stable isotope fractionation factors of geochemical interest. in *Data of geochemistry,* edited by M. Fleischer, U.S. Geological Survey.
Fugenschuh, B., D. Seward, and N. Mancktelow (1997), Exhumation in a convergent orogen: the western Tauern window, *Terra Nova*, *9*(5-6), 213-217.
Galbraith, R. F. (1981), On statistical-models for fission-track counts, *Journal of the International Association for Mathematical Geology*, *13*(6), 471-478.
Galbraith, R. F., and G. M. Laslett (1997), Statistical modelling of thermal annealing of fission tracks in zircon, *Chemical Geology*, *140*(1-2), 123-135.
Gautier, P., J. P. Brun, and L. Jolivet (1993), Structure and kinematics of upper Cenozoic extensional detachment on Naxos and Paros (Cyclades Islands, Greece), *Tectonics*, *12*(5), 1180-1194.
Gawlick, H. J., W. Frisch, A. Vecsei, T. Steiger, and F. Bohm (1999), The change from rifting to thrusting in the Northern Calcareous Alps as recorded in Jurassic sediments, *Geologische Rundschau* , *87*, 644-657.
Gleadow, A. J. W., and I. R. Duddy (1981), A natural long-term track annealing experiment for apatite, *Nuclear Tracks and Radiation Measurements*, *5*(1-2), 169-174.

Glodny, J., A. Kuhn, and H. Austrheim (2008), Diffusion versus recrystallization processes in Rb-Sr geochronology: isotopic relics in eclogite facies rocks, Western gneiss region, Norway, *Geochimica et Cosmochimica Acta*, *72*(2), 506-525.

Graham, C. M., and P. C. England (1976), Thermal regimes and regional metamorphism in vicinity of overthrust faults: an example of shear heating and inverted metamorphic zonation from southern California, *Earth and Planetary Science Letters*, *31*(1), 142-152.

Grasemann, B., and N. S. Mancktelow (1993), 2-dimensional thermal modeling of normal faulting: the Simplon Fault Zone, Central Alps, Switzerland, *Tectonophysics*, *225*(3), 155-165.

Grosjean, G., C. Sue, and M. Burkhard (2004), Late Neogene extension in the vicinity of the Simplon Fault Zone (Central Alps, Switzerland), *Eclogae Geologicae Helvetiae*, *97*(1), 33-46.

Grujic, D., and N. S. Mancktelow (1996), Structure of the northern Maggia and Lebendun nappes, Central Alps, Switzerland, *Eclogae Geologicae Helvetiae*, *89*(1), 461-504.

Guerra, I., et al. (2009), Fluid-rock interaction along the Simplon fault zone (central western Alps): constraints from oxygen and carbon stable isotope geochemistry, *Geophysical Research Abstracts European Geological Union, 11*, Abstract 2009-8969.

Guidotti, C. V. (1973), Compositional variation of muscovite as a function of metamorphic grade and assemblages in metapellites from N.W. Maine, *Contributions to Mineralogy and Petrology*, *42*, 33-42.

Hansen, F., and N. Carter (1982), Creep of selected crustal rocks at 1000MPa, *Eos Transactions, American Geophysical Union,63*, Fall Meeting Supplement, p. 437.

Heinrich, C. A. (1986), Eclogite facies regional metamorphism of hydrous mafic rocks in the Central Alpine Adula nappe, *Journal of Petrology*, *27*(1), 123-154.

Herman, F., J. Braun, and W. J. Dunlap (2007), Tectonomorphic scenarios in the Southern Alps of New Zealand, *Journal of Geophysical Research-Solid Earth*, *112*, B04201.

Herman, F., E. Rhodes, and J. Braun (2008), Steady-state relief in the Southern Alps of New Zealand during the last glacial cycle, *Eos Transactions, American Geophysical Union, 89* (53), Fall Meeting Supplement, Abstract T41C-03.

Herwartz, D., C. Munker, E. E. Scherer, T. J. Nagel, J. Pleuger, and N. Froitzheim (2008), Lu-Hf garnet geochronology of eclogites from the Balma Unit (Pennine Alps): implications for Alpine paleotectonic reconstructions, *Swiss Journal of Geosciences*, *101*, S173-S189.

Hetherington, C. J., and R. Le Bayon (2005), Bulk rock composition: a key to identifying invisible prograde reactions in zoned garnet, *Schweizerische Mineralogische Und Petrographische Mitteilungen*, *85*(1), 57-67.

Hetherington, C. J., and I. M. Villa (2007), Barium silicates of the Berisal complex, Switzerland: a study in geochronology and rare-gas release systematics, *Geochimica et Cosmochimica Acta*, *71*(13), 3336-3347.

Holm, D. K., R. J. Fleck, and D. R. Lux (1994), The Death-Valley turtlebacks reinterpreted as Miocene-Pliocene folds of a major detachment surface, *Journal of Geology*, *102*(6), 718-727.

House, M. A., B. P. Wernicke, K. A. Farley, and T. A. Dumitru (1997), Cenozoic thermal evolution of the Central Sierra Nevada, California, from (U-Th)/He thermochronometry, *Earth and Planetary Science Letters*, *151*(3-4), 167-179.

Hubbard, M., and N. S. Mancktelow (1992), Lateral displacement during Neogene convergence in the Western and Central Alps, *Geology*, *20*(10), 943-946.
Hunziker, J. (1969), Rb-Sr Altersbestimmungen aus den Walliser Alpen Hellglimmer- und Gesamtgesteinsalterswerte, *Eclogae Geologicae Helvetiae*, *62*(2), 527-542.
Hunziker, J., and P. Bearth (1969), Rb-Sr Altersbestimmungen aus den Walliser-Alpen: Biotitalterswerte und ihre Bedeutung für die Abkühlungsgeschichte der alpinen Metamorphose, *Eclogae Geologicae Helvetiae*, *62*, 205-222.
Hurford, A. J., and P. F. Green (1983), The zeta-age calibration of fission-track dating, *Isotope Geoscience*, *1*, 285-317.
Hurford, A. J. (1986), Cooling and up-lift patterns in the Lepontine Alps south central Switzerland and age of vertical movement on the Insubric fault line, *Contributions to Mineralogy and Petrology*, *92*(4), 413-427.
Jäger, E. (1965), Rb/Sr age determination on minerals and rocks from the Alps, *Sci. Terre*, *10*, 395-406.
Jäger, E., E. Niggli, and E. Wenk (1967), Rb-Sr Altersbestimmungen an Glimmern der Zentralpen, *Beiträge zur Geologischen Karte der schweiz, 134*
John, B. E. (1987), Geometry and evolution of a mid-crustal extensional fault system: Chemehuevi Mountains, southeastern California, in *Continental extensional tectonics*, edited by M. P. Coward, J. F. Dewey and P. L. Hancock, pp. 313-335 Geological Society of London Special Publications
Jolivet, L., J. P. Brun, P. Gautier, S. Lallemant, and M. Patriat (1994), 3D-kinematics of extension in the Aegean region from the early Miocene to the present, insights from the ductile crust, *Bulletin de la Société Géologique de France*, *165*(3), 195-209.
Keller, L. M., M. Hess, B. Fugenschuh, and S. M. Schmid (2005a), Structural and metamorphic evolution of the Camughera - Moncucco, Antrona and Monte Rosa units southwest of the Simplon line, Western Alps, *Eclogae Geologicae Helvetiae*, *98*(1), 19-49.
Keller, L. M., R. Abart, S. M. Schmid, and C. De Capitani (2005b), Phase relations and chemical composition of phengite and paragonite in pelitic schists during decompression: a case study from the Monte Rosa nappe and Camughera-Moncucco unit, Western Alps, *Journal of Petrology*, *46*(10), 2145-2166.
Keller, L. M., B. Fugenschuh, M. Hess, B. Schneider, and S. M. Schmid (2006), Simplon Fault Zone in the Western and Central Alps: mechanism of Neogene faulting and folding revisited, *Geology*, *34*(4), 317-320.
Ketcham, R. A. (1996), Thermal models of core-complex evolution in Arizona and New Guinea: implications for ancient cooling paths and present-day heat flow, *Tectonics*, *15*(5), 933-951.
Kirschner, D. L., H. Masson, and M. A. Cosca (2003), An $^{40}Ar/^{39}Ar$, Rb/Sr, and stable isotope study of micas in low-grade fold-and-thrust belt: an example from the Swiss Helvetic Alps, *Contributions to Mineralogy and Petrology*, *145*(4), 460-480.
Kozur, H. (1989), The evolution of the Meliata-Hallstatt ocean and its significance for the early evolution of the Eastern Alps and Western Carpathians, *Symposium at the International Geological Congress: Paleogeography and Paleoceanography of Tethys*, Elsevier Science Bv.
Kretz, R. (1983), Symbols for rock-forming minerals, *American Mineralogist, 68,* 277-279
Krijgsman, W., M. M. Blanc-Valleron, R. Flecker, F. J. Hilgen, T. J. Kouwenhoven, D. Merle, F. Orszag-Sperber, and J. M. Rouchy (2002), The onset of the

Messinian salinity crisis in the Eastern Mediterranean (Pissouri Basin, Cyprus), *Earth and Planetary Science Letters*, *194*(3-4), 299-310.
Kuhlemann, J., W. Frisch, I. Dunkl, and B. Szekely (2001), Quantifying tectonic versus erosive denudation by the sediment budget: the Miocene core complexes of the Alps, *Tectonophysics*, *330*(1-2), 1-23.
Kuhlemann, J., W. Frisch, B. Szekely, I. Dunkl, and M. Kazmer (2002), Post-collisional sediment budget history of the Alps: tectonic versus climatic control, *International Journal of Earth Sciences*, *91*(5), 818-837.
Kuhlemann, J., and O. Kempf (2002), Post-Eocene evolution of the North Alpine foreland basin and its response to Alpine tectonics, *Sedimentary Geology*, *152*(1-2), 45-78.
Lacassin, R. (1988), Large-scale foliation boudinage in gneisses, *Journal of Structural Geology*, *10*(6), 643-647.
Lajaunie, C., G. Courrioux, and L. Manuel (1997), Foliation fields and 3D cartography in geology: principles of a method based on potential interpolation, *Mathematical Geology*, *29*(4), 571-584.
Lardeaux, J. M., G. Gosso, J. R. Kienast, and B. Lombardo (1982), Metamorphism and deformation in Sesia-Lanzo site (Western Alps) and eclogitization of continental-crust, *Bulletin de la Société Géologique de France*, *24*(4), 793-800.
Lee, J., and J. F. Sutter (1991), Incremental $^{40}Ar/^{39}Ar$ thermochronology of mylonitic rocks from the Northern Snake Range, Nevada, *Tectonics*, *10*(1), 77-100.
Liati, A., D. Gebauer, and M. Fanning (2000), U-Pb SHRIMP dating of zircon from the Novate granite (Bergell, Central Alps): evidence for Oligocene-Miocene magmatism, Jurassic/Cretaceous continental rifting and opening of the Valais trough, *Schweizerische Mineralogische und Petrographische Mitteilungen*, *80*(3), 305-316.
Lickorish, W. H., M. Ford, J. Burgisser, and P. R. Cobbold (2002), Arcuate thrust systems in sandbox experiments: a comparison to the external arcs of the Western Alps, *Geological Society of America Bulletin*, *114*(9), 1089-1107.
Lister, G. S. (1984), Metamorphic core complexes of Cordilleran type in the Cyclades, Aegean Sea, Greece, *Geology*, *12*(4), 221-225.
Lister, G. S., and G. A. Davis (1989), The origin of metamorphic core complexes and detachment faults formed during Tertiary continental extension in the Northern Colorado river region, USA, *Journal of Structural Geology*, *11*(1-2), 65-94.
Lugeon, M. (1901), Les grandes nappes de recouvrement des Alpes du Chablais et de la Suisse, *Bulletin de la Société Géologique de France*, *22*, 723-826.
Lutz, T. M., and G. Omar (1991), An inverse method of modeling thernmal histories from apatite fission-track data, *Earth and Planetary Science Letters*, *104*(2-4), 181-195.
Malavieille, J. (1987a), Extensional shearing deformation and kilometer-scale a-type folds in a Cordilleran metamorphic core complex (Raft River Mountains, Northwestern Utah), *Tectonics*, *6*(4), 423-448.
Malavieille, J. (1987b), Kinematics of compressional and extensional ductile shearing deformation in a metamorphic core complex of the Northeastern Basin and Range, *Journal of Structural Geology*, *9*(5-6), 541-554.
Malavieille, J., P. Guihot, S. Costa, J. M. Lardeaux, and V. Gardien (1990), Collapse of the thickened Variscan crust in the French Massif-Central: Mont Pilat extensional shear zone and St. Etienne late Carboniferous basin, *Tectonophysics*, *177*, 139-149.

Malavieille, J. (1993), Late orogenic extension in mountain belts: insights from the Basin and Range and the late Paleozoic Variscan belt, *Tectonics*, *12*(5), 1115-1130.
Mancel, P., and O. Merle (1987), Kinematics of the northern part of the Simplon Line (Central Alps), *Tectonophysics*, *135*(4), 265-275.
Mancktelow, N. (1985), The Simplon Line: a major displacement zone in the Western Lepontine Alps, *Eclogae Geologicae Helvetiae*, *78*(1), 73-96.
Mancktelow, N. S. (1987), Quartz textures from the Simplon fault zone, southwest Switzerland and north Italy, *Tectonophysics*, *135*(1-3), 133-153.
Mancktelow, N. (1990), The Simplon Fault Zone, *Beiträge zur Geologischen Karte der schweiz* , NF *163*.
Mancktelow, N. S. (1992), Neogene lateral extension during convergence in the Central Alps: evidence from interrelated faulting and backfolding around the Simplonpass (Switzerland), *Tectonophysics*, *215*(3-4), 295-317.
Mancktelow, N. S., and T. L. Pavlis (1994), Fold-fault relationships in low-angle detachment systems, *Tectonics*, *13*(3), 668-685.
Mancktelow, N. S., and B. Grasemann (1997), Time-dependent effects of heat advection and topography on cooling histories during erosion, *Tectonophysics*, *270*(3-4), 167-195.
Marchant, R., A. Steck, A. Escher, L. Levato, H. Masson, R. Olivier, G. M. Stampfli, and J. J. Wagner (1993), An interpretation of the deep seismic lines from the Penninic Alps of Valais (Switzerland), *Bulletin de la Société Géologique de France*, *164*(3), 395-414.
Markley, M. J., C. Teyssier, M. A. Cosca, R. Caby, J. C. Hunziker, and M. Sartori (1998), Alpine deformation and $^{40}Ar/^{39}Ar$ geochronology of synkinematic white mica in the Siviez-Mischabel nappe, Western Pennine Alps, Switzerland, *Tectonics*, *17*(3), 407-425.
Martinez-Martinez, J. M., J. I. Soto, and J. C. Balanya (2002), Orthogonal folding of extensional detachments: structure and origin of the Sierra Nevada elongated dome (Betics, SE Spain), *Tectonics*, *21*(3), 1012.
Matsuhisa, Y., J. R. Goldsmith, and R. N. Clayton (1979), Oxygen isotopic fractionation in the system quartz-albite-anorthite-water, *Geochimica Et Cosmochimica Acta*, *43*(7), 1131-1140.
Maxelon, M. (2004), Developing a three-dimensional structural model of the Lower Lepontine nappes: Central Alps, Switzerland and Northern Italy, PhD thesis, ETH-Zürich.
Maxelon, M., and N. S. Mancktelow (2005), Three-dimensional geometry and tectonostratigraphy of the Pennine zone, Central Alps, Switzerland and Northern Italy, *Earth-Science Reviews*, *71*(3-4), 171-227.
Maxelon, M., P. Renard, G. Courrioux, M. Braendli, and N. Mancktelow (2009), A workflow to facilitate three-dimensional geometrical modelling of complex poly-deformed geological units, *Computers and Geosciences*, *35*(3), 644-658.
Mehl, C., L. Jolivet, and O. Lacombe (2005), From ductile to brittle: evolution and localization of deformation below a crustal detachment (Tinos, Cyclades, Greece), *Tectonics*, *24*(4), 23.
Merle, O., P. Legal, and P. Mancel (1986), Deformation and metamorphosis in the Simplon region of the Central Alps, *Eclogae Geologicae Helvetiae*, *79*(3), 705-718.
Merle, O. (1987), Deformation history in the Western Lepontine Alps, *Bulletin de la Société Géologique de France*, *3*(1), 183-190.

Meyre, C., D. Marquer, S. M. Schmid, and L. Ciancaleoni (1998), Syn-orogenic extension along the Forcola fault: correlation of Alpine deformations in the Tambo and Adula nappes (Eastern Penninic Alps), *Eclogae Geologicae Helvetiae*, *91*(3), 409-420.

Michalski, I., and M. A. Soom (1990), The Alpine thermo-tectonic evolution of the Aar and Gotthard massifs, Central Switzerland: fission track ages on zircon and apatite and K-Ar mica ages, *Schweizerische Mineralogische Und Petrographische Mitteilungen*, *70*, 373-387.

Miller, M. G. (1991), High-angle origin of the currently low-angle Badwater turtleback fault, Death-Valley, California, *Geology*, *19*(4), 372-375.

Miller, M. G. (1992), Brittle faulting induced by ductile deformation of a rheologically stratified rock sequence, Badwater turtleback, Death-Valley, California, *Geological Society of America Bulletin*, *104*(10), 1376-1385.

Milnes, A. G. (1973), Structural reinterpretation of classic Simplon tunnel section of Central Alps, *Geological Society of America Bulletin*, *84*(1), 269-274.

Milnes, A. G. (1974), Structure of Pennine zone (Central Alps): a new working hypothesis, *Geological Society of America Bulletin*, *85*(11), 1727-1732.

Milnes, A. G., M. Greller, and R. Müller (1981), Sequence and style of major post-nappe structures, Simplon-Pennine Alps, *Journal of Structural Geology*, *3*(4), 411-420.

Morrison, J., and J. L. Anderson (1998), Footwall refrigeration along a detachment fault: implications for the thermal evolution of core complexes, *Science*, *279*(5347), 63-66.

Mulch, A., M. A. Cosca, and J. Fiebig (2002), In situ $^{40}Ar/^{39}Ar$ UV laser dating of mylonitic mica fish: cooling or crystallisation ages?, *Geochimica Et Cosmochimica Acta*, *66*(15A), A532.

Mulch, A., and M. A. Cosca (2004), Recrystallization or cooling ages: in situ UV-laser $^{40}Ar/^{39}Ar$ geochronology of muscovite in mylonitic rocks, *Journal of the Geological Society*, *161*, 573-582.

Mulch, A., C. Teyssier, M. A. Cosca, and T. W. Vennemann (2006), Thermomechanical analysis of strain localization in a ductile detachment zone, *Journal of Geophysical Research-Solid Earth*, *111,* B12405.

Müller, W., D. Aerden, and A. N. Halliday (2000a), Isotopic dating of strain fringe increments: duration and rates of deformation in shear zones, *Science*, *288*(5474), 2195-2198.

Müller, W., N.S. Mancktelow, M. Meir (2000b), Rb-Sr microchrons of synkinematic mica in mylonites: an example from the DAV fault of the Eastern Alps, *Earth and Planetary Science Letters*, *180*, 385-397.

Müller, W., S. P. Kelley, and I. M. Villa (2002), Dating fault-generated pseudotachylytes: comparison of $^{40}Ar/^{39}Ar$ stepwise-heating, laser-ablation and Rb-Sr microsampling analyses, *Contributions to Mineralogy and Petrology*, *144*(1), 57-77.

Nievergelt, P., M. Liniger, N. Froitzheim, and R. F. Mahlmann (1996), Early to mid Tertiary crustal extension in the Central Alps: the Turba mylonite zone (Eastern Switzerland), *Tectonics*, *15*(2), 329-340.

Niggli, E., and C. Niggli (1965), Karten der Verbreitung einiger Mineralien der alpidischen Metamorphose in den schweizer Alpen (Stilpnomelan, AlKali-Amphibol, Chloritoid, Staurolith, Disthen, Sillimanit), *Eclogae Geologicae Helvetiae*, *58*, 335-368.

Niggli, C. (1970), Alpine metamorphose und alpine Gebirgsbildung, *Fortschung Mineralogist*, *47*, 16-26.
Norton, M. G. (1986), Late Caledonide extension in Western Norway: a response to extreme crustal thickening, *Tectonics*, *5*(2), 195-204.
Peltzer, G., and P. Tapponnier (1988), Formation and evolution of strike-slip faults, rifts, and basins during the India-Asia collision: an experimental approach, *Journal of Geophysical Research-Solid Earth and Planets*, *93*(B12), 15085-15097.
Pettke, T., and E. M. Klaper (1992), Petrology and deformation of the southeastern Gotthard massif, *Schweizerische Mineralogische Und Petrographische Mitteilungen*, *72*(2), 197-211.
Pettke, T., L. W. Diamond, and I. M. Villa (1999), Mesothermal gold veins and metamorphic devolatilization in the northwestern Alps: the temporal link, *Geology*, *27*(7), 641-644.
Platt, J. P., and R. L. M. Vissers (1989), Extensional collapse of thickened continental lithosphere: a working hypothesis for the Alboran sea and Gibraltar arc, *Geology*, *17*(6), 540-543.
Pognante, U. (1989), Tectonic implications of lawsonite formation in the Sesia zone (Western Alps), *Tectonophysics*, *162*(3-4), 219-227.
Preiswerk, H. (1921), Die zwei Deckenkulminationen Tosa-Tessin und die Tessiner Querfalte, *Eclogae Geologicae Helvetiae*, *16*, 485-496.
Purdy, J. W. (1972), K-Ar ages of coexisting mica pairs from Central Alps, *Transactions-American Geophysical Union*, *53*, 543.
Purdy, J. W., and E. Jäger (1976), K-Ar ages on rock-forming minerals from the Central Alps, in *Memoirs of the Institute of Geology and Mineralogy,* University of Padova, *30*, 1-31.
Rahn, M. K., M. T. Brandon, G. E. Batt, and J. I. Garver (2004), A zero-damage model for fission-track annealing in zircon, *American Mineralogist*, *89*(4), 473-484.
Ratschbacher, L., W. Frisch, F. Neubauer, S. M. Schmid, and J. Neugebauer (1989), Extension in compressional orogenic belts: the Eastern Alps, *Geology*, *17*(5), 404-407.
Ratschbacher, L., W. Frisch, H. G. Linzer, and O. Merle (1991a), Lateral extrusion in the Eastern Alps, part 2. Structural-analysis, *Tectonics*, *10*(2), 257-271.
Ratschbacher, L., O. Merle, P. Davy, and P. Cobbold (1991b), Lateral extrusion in the Eastern Alps, part 1. Boundary-conditions and experiments scaled for gravity, *Tectonics*, *10*(2), 245-256.
Reinecke, T. (1991), Very-high-pressure metamorphism and uplift of coesite-bearing metasediments from the Zermatt-Saas zone, Western Alps, *European Journal of Mineralogy*, *3*(1), 7-17.
Reynolds, S. J., and G. S. Lister (1990), Folding of mylonitic zones in Cordilleran metamorphic core complexes: evidence from near the mylonitic front, *Geology*, *18*(3), 216-219.
Rieder, M., G. Cavazzini, Y. S. D'Yakonov, V. A. Frank-Kamenetskii, G. Gottardi, S. Guggenheim, P. V. Koval, G. Muller, A. M. R. Neiva, E. W. Radoslovich, J. L. Robert, F. P. Sassi, H. Takeda, Z. Weiss, and D. R. Wones (1998), Nomenclature of the micas, *Canadian Mineralogist*, *36*, 905-912.
Rolland, y., M. Rossi, S. F. Cox, M. Corsini, N. Mancktelow, G. Pennacchioni, M. Fornari, and A. M. Boullier (2008), $^{40}Ar/^{39}Ar$ dating of synkinematic white mica: insights from fluid-rock reaction in low-grade shear zones (Mont Blanc Massif)

and constraints on timing of deformation in the NW external Alps, in *The internal structure of fault zones: implications for mechanical and fluid-flow properties*, edited by C. A. J. Wibberley, et al., pp. 293-315, Geological Society of London Special Publications.

Romer, R. L., U. Scharer, and A. Steck (1996), Alpine and pre-Alpine magmatism in the root-zone of the Western Central Alps, *Contributions to Mineralogy and Petrology*, *123*(2), 138-158.

Rossi, M., y. Rolland, O. Vidal, and S. F. Cox (2005), Geochemical variations and element transfer during shear-zone development and related episyenites at middle crust depths: insights from the Mont Blanc granite (French-Italian Alps), in *High-strain zones: structure and physical properties*, edited by D. Bruhn and L. Burlini, pp. 373-396, Geological Society of London Special Publications.

Rubatto, D., D. Gebauer, and M. Fanning (1998), Jurassic formation and Eocene subduction of the Zermatt-Saas-Fee ophiolites: implications for the geodynamic evolution of the Central and Western Alps, *Contributions to Mineralogy and Petrology*, *132*(3), 269-287.

Sambridge, M. (1999a), Geophysical inversion with a neighbourhood algorithm - I. Searching a parameter space, *Geophysical Journal International*, *138*(2), 479-494.

Sambridge, M. (1999b), Geophysical inversion with a neighbourhood algorithm - II. Appraising the ensemble, *Geophysical Journal International*, *138*(3), 727-746.

Schlunegger, F., and S. Willett (1999), Spatial and temporal variations in exhumation of the Central Swiss Alps and implications for exhumation mechanisms. in *Exhumation processes: normal faulting, ductile flow and erosion,* edited by U. Ring, M.T. Brandon, G.S. Lister and S. Willett, pp. 157-179, Geological Society of London Special Publications.

Schmid, S. M., A. Zingg, and M. Handy (1987), The kinematics of movements along the Insubric Line and the emplacement of the Ivrea Zone, *Tectonophysics*, *135*(1-3), 47-66.

Schmid, S. M., H. R. Aebli, F. Heller, and A. Zingg (1989), The role of the Periadriatic Line in the tectonic evolution of the Alps, in *Alpine Tectonics, edited by* M.P. Coward, D. Dietrich and R.G. Park, pp.153-171, Geological society of London special Publication.

Schmid, S. M., and N. Froitzheim (1993), Oblique slip and block rotation along the Engadine Line, *Eclogae Geologicae Helvetiae*, *86*(2), 569.

Schmid, S. M., and E. Kissling (2000), The arc of the Western Alps in the light of geophysical data on deep crustal structure, *Tectonics*, *19*(1), 62-85.

Schmid, S. M., B. Fügenschuh, E. Klissing, and R. Schuster (2004), Tectonic map and overall architecture of the Alpine orogen, *Eclogae Geologicae Helvetiae*, *97*, 93-117.

Schmidt, C., and H. Preiswerk (1908), Geologische Karte der Simplongruppe, Spezialkarte n°48 mit Erläuterungen. *Schweizerischen geologischen Kommission*, *6,* Basel.

Selverstone, J. (1988), Evidence for east-west crustal extension in the Eastern Alps: implications for the unroofing history of the Tauern window, *Tectonics*, *7*(1), 87-105.

Séranne, M., and M. Séguret (1985), Etirement ductile et cisaillement basal dans les bassins dévoniens de l'ouest Norvège, *Comptes Rendus de l'Académie des Sciences Série II*, *300*(2), 376-378.

Seward, D. (1989), Cenozoic basin histories determined by fission-track dating of basement granites, South Island, New-Zealand, *Chemical Geology*, *79*(1), 31-48.

Seward, D., and N. S. Mancktelow (1994), Neogene kinematics of the Central and Western Alps: evidence from fission-track dating, *Geology*, *22*(9), 803-806.
Sibson, R. H. (1983), Continental fault structure and the shallow earthquake source, *Journal of the Geological Society*, *140*, 741-767.
Simon-Labric, T., Y. Rolland, T. Dumont, T. Heymes, C. Authemayou, M. Corsini, and M. Fornari (2009), $^{40}Ar/^{39}Ar$ dating of Penninic front tectonic displacement (W Alps) during the lower Oligocene (31-34 Ma), *Terra Nova*, *21*(2), 127-136.
Smith, S. A. F., R. E. Holdsworth, C. Collettini, and J. Imber (2007), Using footwall structures to constrain the evolution of low-angle normal faults, *Journal of the Geological Society*, *164*, 1187-1191.
Soom, M. A. (1990), Abkühlungs- und Hebungsgeschichte der Externmassive und der penninischen Decken beidseits der Simplon-Rhone-Linie seit dem Oligozän: Spaltspurdatierungen an Apatit/Zirkon und K-Ar-Datierungen an Biotit/Muskowit (westliche Zentralalpen). PhD thesis, Universitat Bern.
Spencer, J. E. (1984), Role of tectonic denudation in warping and uplift of low-angle normal faults, *Geology*, *12*(2), 95-98.
Spencer, J. E. (1985), Miocene low-angle normal faulting and dike emplacement, Homer Mountain and surrounding areas, southeastern California and southernmost Nevada, *Geological Society of America Bulletin*, *96*(9), 1140-1155.
Spiegel, C., J. Kuhlemann, I. Dunkl, W. Frisch, H. von Eynatten, and K. Balogh (2000), The erosion history of the Central Alps: evidence from zircon fission track data of the foreland basin sediments, *Terra Nova*, *12*(4), 163-170.
Steck, A. (1980), Deux directions principales de flux synmetamorphiques dans les Alpes Centrales, *Bulletin de la Société Vaudoise des Sciences Naturelles*, *75*(358), 141-149.
Steck, A. (1984), Tertiary deformation structures in the Central Alps, *Eclogae Geologicae Helvetiae*, *77*(1), 55-100.
Steck, A. (1987), Le massif du Simplon - réflexions sur la cinématique des nappes de gneiss, *Schweizerische Mineralogische Und Petrographische Mitteilungen*, *67*, 27-45.
Steck, A. (1990), A map of ductile shear zones of the Central Alps, *Eclogae Geologicae Helvetiae*, *83*(3), 603-627.
Steck, A., and J. Hunziker (1994), The Tertiary structural and thermal evolution of the Central Alps - compressional and extensional structures in an orogenic belt, *Tectonophysics*, *238*(1-4), 229-254.
Steck, A. (1998), The Maggia cross-fold: an enigmatic structure of the lower Penninic nappes of the Lepontine Alps, *Eclogae Geologicae Helvetiae*, *91*, 333-343.
Steck, A. (2008), Tectonics of the Simplon massif and Lepontine gneiss dome: deformation structures due to collision between the underthrusting European plate and the Adriatic indenter, *Conference on Modern Methods in Structural Geology and Tectonics held in honor of Martin Burkhard*, Birkhauser Verlag Ag.
Steiger, R. H., and E. Jäger (1977), Subcommission on geochronology: convention on use of decay constants in geochronology and cosmochronology, *Earth and Planetary Science Letters*, *36*, 359-362.
Tagami, T., R. F. Galbraith, R. Yamada, and G. M. Laslett (1998), Revised annealing kinetics of fission tracks in zircon and geological implications, in *Advances in fission-track geochronology*, edited by P. v. d. Haute and F. De Corte, pp. 99-112, Springer, Gent.
Todd, C. S., and M. Engi (1997), Metamorphic field gradients in the Central Alps, *Journal of Metamorphic Geology*, *15*(4), 513-530.

Trommsdorff, V. (1966), Progressive Metamorphose kieseliger Karbonatgesteine in den Zentralapen zwischen Bernina und Simplon, *Schweizerische Mineralogische Und Petrographische Mitteilungen*, *46*, 431-460.

Trommsdorff, V. (1972), Change in T-X during metamorphism of siliceous dolomite rocks of the Central Alps, *Schweizerische Mineralogische Und Petrographische Mitteilungen*, *52*, 567-571.

Urai, J. L., R. D. Schuiling, and J. B. H. Jansen (1990), Alpine deformation on Naxos (Greece), in *Deformation Mechanisms, Rheology and Tectonics,* Edited by R. J. Knipe and E. H. Rutter, pp.509-522, Geological Society of London Special Publication.

Vance, D., and R. K. O'Nions (1992), Prograde and retrograde thermal histories from the Central Swiss Alps, *Earth and Planetary Science Letters*, *114*(1), 113-129.

Vandendriessche, J., and J. P. Brun (1989), Kinematic model of late Paleozoic extensional tectonics in the Southern French massif Central, *Comptes Rendus de l'Académie des Sciences Série II*, *309*(16), 1607-1613.

Vandendriessche, J., and J. P. Brun (1992), Tectonic evolution of the Montagne Noire (French Massif Central): a model of extensional gneiss dome, *Geodinamica Acta*, 85-99.

Vanderbeek, P., P. Andriessen, and S. Cloetingh (1995), Morphotectonic evolution of rifted continental margins: inferences from a coupled tectonic-surface processes model and fission track thermochronology, *Tectonics*, *14*(2), 406-421.

Vanderhaeghe, O., C. Teyssier, I. McDougall, and W. J. Dunlap (2003), Cooling and exhumation of the Shuswap metamorphic core complex constrained by $^{40}Ar/^{39}Ar$ thermochronology, *Geological Society of America Bulletin*, *115*(2), 200-216.

Vernon, A. J., P. A. Van der Beek, H. D. Sinclair, and M. K. Rahn (2008), Increase in late Neogene denudation of the European Alps confirmed by analysis of a fission-track thermochronology database, *Earth and Planetary Science Letters*, *270*(3-4), 316-329.

Villa, I. M. (1998), Isotopic closure, *Terra Nova*, *10*(1), 42-47.

Wagner, G. A., G. M. Reimer, and E. Jäger (1977), Cooling ages derived by apatite fission-track, mica Rb-Sr and K-Ar dating: the uplift and cooling history of the Central Alps, in *Memoirs of the Institute of Geology and Mineralogy,* University of Padova, *30*, 1-27.

Watson, D. (1999), The natural neighbor series manuals and source codes, *Computers and Geosciences*, *25*(4), 463-466.

Wawrzyniec, T., J. Selverstone, and G. J. Axen (1999), Correlations between fluid composition and deep-seated structural style in the footwall of the Simplon low-angle normal fault, Switzerland, *Geology*, *27*(8), 715-718.

Wawrzyniec, T. F., J. Selverstone, and G. J. Axen (2001), Styles of footwall uplift along the Simplon and Brenner normal fault systems, Central and Eastern Alps, *Tectonics*, *20*(5), 748-770.

Wells, M. L., L. W. Snee, and A. E. Blythe (2000), Dating of major normal fault systems using thermochronology: an example from the Raft River detachment, Basin and Range, Western United States, *Journal of Geophysical Research-Solid Earth and Planets*, *105*(B7), 16303-16327.

Wenk, E. (1955), Eine Strukturkarte der Tessineralpen, *Schweizerische Mineralogische Und Petrographische Mitteilungen*, *53*, 311-319.

Wenk, E., and H. R. Wenk (1984), Distribution of plagioclase in carbonate rocks from the Tertiary metamorphic belt of the Central Alps, Bulletin de Minéralogi*e*, *107*(3-4), 357-368.

Wernicke, B. (1981), Low-angle normal faults in the Basin and Range province: nappe tectonics in an extending orogen, *Nature*, *291*(5817), 645-648.
Wernicke, B., and G. J. Axen (1988), On the role of isostasy in the evolution of normal-fault systems, *Geology*, *16*(9), 848-851.
Wernicke, B. (1995), Low-angle normal faults and seismicity: a review, *Journal of Geophysical Research-Solid Earth*, *100*(B10), 20159-20174.
Willett, S. D., F. Schlunegger, and V. Picotti (2006), Messinian climate change and erosional destruction of the central European Alps, *Geology*, *34*(8), 613-616.
Yin, A. (1989), Origin of regional, rooted low-angle normal faults: a mechanical model and its tectonic implications, *Tectonics*, *8*(3), 469-482.
Yin, A. (1991), Mechanisms for the formation of domal and basinal detachment faults: a 3-dimensional analysis, *Journal of Geophysical Research-Solid Earth and Planets*, *96*(B9), 14577-14594.
Yin, A., and J. F. Dunn (1992), Structural and stratigraphic development of the Whipple-Chemehuevi detachment fault system, Southeastern California: implications for the geometrical evolution of domal and basinal low-angle normal faults, *Geological Society of America Bulletin*, *104*(6), 659-674.
Zwingmann, H., and N. Mancktelow (2004), Timing of Alpine fault gouges, *Earth and Planetary Science Letters*, *223*(3-4), 415-425.